Universidade Estadual de Londrina

RICARDO TADASHI KOBAYASHI

PROTOTYPE FILTER DESIGN FOR FBMC SYSTEMS VIA CONVEX OPTIMIZATION

Londrina
2019

RICARDO TADASHI KOBAYASHI

PROTOTYPE FILTER DESIGN FOR FBMC SYSTEMS VIA CONVEX OPTIMIZATION

Engineering Doctorate Program at State University of Londrina in fulfillment of the requirements for the degree of Doctor of Philosophy in Electrical Engineering.

Area: Telecommunication Systems
Supervisor: Taufik Abrão

Londrina
2019

Kobayashi, Ricardo Tadashi

Prototype Filter Design for FBMC Systems via Convex Optimization. Londrina, 2019. 242 p.

Supervisor: Taufik Abrão

Thesis (Doctor of Philosophy) – Department of Electrical Engineering – State University of Londrina

1. Telecommunications, 2. 5G, 3. FBMC Systems, 4. MIMO Systems, 5. Convex Optimization

Ricardo Tadashi Kobayashi

Prototype Filter Design for FBMC Systems via Convex Optimization

A Thesis submitted to the Electrical Engineering Doctorate Program at the State University of Londrina in fulfillment of the requirements for the degree of Doctor of Philosophy in Electrical Engineering.

Area: Telecommunication Systems

Examination Board

Dr. Cristiano Magalhães Panazio
Department of Telecom. & Control Engineering
University of São Paulo
Member

Dr. José Carlos Marinello
Department of Electrical Engineering
State University of Londrina
Member

Dr. Paulo Rogério Scalassara
Academic Department of Electrical Engineering
Federal University of Technology - Paraná
Member

Dr. Vitor Heloiz Nascimento
Department of Electronic Systems Engineering
University of São Paulo
Member

Dr. Taufik Abrão
Department of Electrical Engineering
State University of Londrina
Supervisor

Londrina,
October 25, 2019

Agradecimentos

Meus sinceros agradecimentos ao prof. Taufik Abrão pela orientação nos últimos anos.

A todos meus colegas de laboratório pelo companheirismo e auxílio no desenvolvimento das atividades ligadas a este trabalho.

À Universidade Estadual de Londrina pela estrutura e suporte providos para o desenvolvimento deste trabalho.

À Coordenação de Aperfeiçoamento de Pessoal de Nível Superior(CAPES) pelo apoio financeiro. O presente trabalho foi realizado com o apoio da CAPES - Código de Financiamento 001.

"I have always believed, and I still believe, that whatever good or bad fortune may come our way we can always give it meaning and transform it into something of value."

(Hermann Hesse)

Abstract

5G systems have been the main topic of discussion in telecommunications in the last few years. Since 5G envisions the support of a new class of demanding services, it requires a paradigm shift in current telecommunication technology. As an example, radio access via alternative waveforms other than Orthogonal Frequency-Division Multiplexing (OFDM) is feasible and has many advantages. In particular, Filter Bank MultiCarrier (FBMC) multiplexing is a promising non-orthogonal waveform due to its high-performance spectrum signature, resilience to time-frequency dispersion, and non-reliance on Cyclic-Prefix. From this perspective, this work studies FBMC as an enabler of 5G by providing an overview of FBMC systems and proposing new prototype filter designs for such multiplexing scheme. Thus, efforts are made towards designing prototype filters with the aid of SemiDefinite Programming (SDP) and Quadratically Constrained Quadratic Programming (QCQP). Initially, this work proposes short length prototype filters with near-perfect reconstruction features. Moreover, three prototype filters with low Out-of-Band energy emission and fast spectrum decay are offered to enhance the overall performance of FBMC systems. Finally, a study on the effects of the prototype filter on the symbol reconstruction of FBMC systems closes the work. Thus, this thesis offers a solid background on FBMC systems, contributing for the development of such technology and its deployment in telecommunication systems to come.

Keywords: Telecommunications, 5G, FBMC Systems, MIMO Systems, Convex Optimization

Resumo

Nos últimos anos, sistemas 5G se tornaram um dos principais tópicos de discussão em telecomunicações. Como a Quinta Geração de Telefonia Móvel prevê o suporte de uma nova gama de serviços com requisitos exigentes, espera-se uma mudança de paradigma na atual tecnologia de telecomunicações. Como exemplo, o acesso ao meio realizado através de formas de onda diferentes da Multiplexação por Divisão de Frequências Ortogonais (OFDM) é factível e possui diversas vantagens. Em particular, a multiplexação via Banco de Filtros Multiportadora (FBMC) é uma forma de onda não ortogonal promissora dado seu alto desempenho espectral, resiliência a dispersões no tempo e frequência, e não dependência de prefixos cíclicos. Desta forma, este trabalho estuda a multipelxação FBMC como tecnologia candidata a sistemas 5G, provendo uma rica discussão sobre banco de filtros e novos projetos de filtros protótipos para tal esquema de multiplexação. Logo, este trabalho concentra-se no desenvolvimento de filtros protótipo com o auxílio da Programação SemiDefinida (SDP) e Programação Quadrática com Restrições Quadráticas (QCQP). Inicialmente, este trabalho propõe filtros de baixo comprimento e características de reconstrução quase perfeitas. Além disso, três filtros protótipos com baixa emissão de energia fora de banda e rápido decaimento espectral são propostos para melhorar o desempenho global de sistemas FBMC. Finalmente, são estudados os efeitos do filtro protótipo na reconstrução de símbolos em sistemas FBMC. Desta forma, esta tese oferece um panorama sólido sobre sistemas FBMC, contribuindo para o desenvolvimento desta tecnologia e sua aplicação em sistemas de telecomunicações emergentes.

Palavras-chave: Telecomunicações, 5G, Sistemas FBMC, Sistemas MIMO, Otimização Convexa

List of abbreviations and acronyms

4G	4th Telecommunication Generation
5G	5th Telecommunication Generation
AWGN	Additive White Gaussian Noise
BEP	Bit Error Probability
BER	Bit Error Rate
BS	Base Station
CDF	Cumulative Density Function
CP	Cyclic-Prefix
cMBB	crowd Mobile BroadBand
CSI	Channel State Information
DFT	Discrete Fourier Transform
DFS	Discrete Fourier Series
DL	Downlink
DTFT	Discrete-Time Fourier Transform
DPSS	Discrete Prolate Spheroidal Sequences
EGF	Extended Gaussian Function
eMBB	enhanced Mobile BroadBand
f-OFDM	filtered Orthogonal Frequency-Division Multiplexing
FDD	Frequency-Division Duplex
FBMC-OQAM	Offset Quadrature Amplitude Modulation Filter Bank MultiCarrier
FBMC	Filter Bank MultiCarrier
FFT	Fast Fourier Transform
FPGA	Field-Programmable Gate Array
GFDM	Generalized Frequency-Division Multiplexing

HSV	Hue, Saturation, Value
IAM	Interference Approximation Method
IB	In-Band
ICI	InterCarrier Interference
IDFT	Inverse Discrete Fourier Transform
IFFT	Inverse Fast Fourier Transform
IOTA	Isotropic Orthogonal Transform Algorithm
ISI	InterSymbol Interference
ITU	International Telecommunication Union
IoT	Internet of Things
KKT	Karush-Kuhn-Tucker
LDPC	Low-Density Parity-Check Code
LLL	Lenstra-Lenstra-Lovász
LS	Least Squares
LR	Lattice Reduction
LTE	Long-Term Evolution
M2M	Machine-to-Machine
MCS	Modulation Coding Scheme
MIMO-FBMC	Multiple-Input Multiple-Output Filter Bank MultiCarrier
MIMO	Multiple-Input Multiple-Output
ML	Maximum Likelihood
MSE	Mean-Squared Error
MMSE-DFE	Minimum Mean-Squared Error Decision Feedback Equalizer
MMSE	Minimum Mean-Squared Error
mMTC	massive Machine-Type Communications
mmWaves	Millimeter Waves

MRT	Maximum Ratio Transmission
MSL	Maximum Sidelobe Level
MTC	Machine-Type communications
NMSE	Normalized Mean-Squared Error
NOMA	Non-Orthogonal Multiple Access
OFDM-OQAM	Offset Quadrature Amplitude Modulation Orthogonal Frequency-Division Multiplexing
OFDM	Orthogonal Frequency-Division Multiplexing
OFDP	Optimal Finite Duration Pulses
OQAM	Offset Quadrature Amplitude Modulation
OoB	Out-of-Band
OSIC	Ordered Successive Interference Cancellation
PAM	Pulse Amplitude Modulation
PAPR	Peak-to-Average Power Ratio
PDF	Probability Density Function
POP	Pair of Pilots
PSK	Phase-Shift Keying
QAM	Quadrature Amplitude Modulation
QCQP	Quadratically Constrained Quadratic Programming
QoS	Quality of Service
RAP	Random Access Protocol
RC	Raised-Cosine
RMS	Root Mean Square
SAR	Specific Absorption Rate
SCMA	Sparse-Code Multiple-Access
SD	Sphere Decoder
SDP	SemiDefinite Programming

SDR	Software-Defined Radio
SEP	Symbol Error Probability
SIC	Successive Interference Cancellation
SIR	Signal-to-Interference Ratio
SISO	Single-Input Single-Output
SNR	Signal-to-Noise Ratio
SOCP	Second-Order Cone Program
SRRC	Square-Root Raised Cosine
SUCR	Strongest-User Collision Resolution
TDD	Time-Division Duplex
UFMC	Universal Filtered MultiCarrier
UL	Uplink
URLLC	Ultra-Reliable Low Latency Communications
V-BLAST	Vertical Bell Labs Layered Space-Time
w-OFDM	windowed Orthogonal Frequency-Division Multiplexing
WiMAX	Worldwide Interoperability for Microwave Access
ZF	Zero-Forcing

List of Notations

$\mathbf{a}$	vectors are denoted by lower case bold letters
$\mathbf{A}$	matrices are denoted by upper case bold letters
$[\mathbf{A}]_{i,k}$	element present in the ith row and jth column of $\mathbf{A}$
$\mathbf{I}_N$	$N \times N$ identity matrix
$\mathbf{A}^{-1}$	matrix inversion
$\mathbf{A}^T$	matrix transposition
$\|\mathbf{A}\|_1$	norm-1 of $\mathbf{A}$
$\|\mathbf{A}\|_2$	norm-2 of $\mathbf{A}$
$\rho(\mathbf{A})$	spectrum (eigenvalues) of $\mathbf{A}$
$\rho_{\min}(\mathbf{A})$	smallest eigenvalue of $\mathbf{A}$
$\rho_{\max}(\mathbf{A})$	largest eigenvalue of $\mathbf{A}$
$\lfloor x \rfloor$	Nearest integer lesser than x
$\lfloor x \rceil$	Nearest integer of x
$\lceil x \rceil$	Nearest integer greater than x
j	$\sqrt{-1}$
$\mathrm{Re}\{x\}$	real part x
$\mathrm{Im}\{x\}$	imaginary x
$\|x\|$	absolute value of x
$\mathrm{sinc}(x)$	sinc function;
$u(x)$	step function
$\delta(x)$	Dirac delta function
$u(x)$	Step or Heaviside function
$Q(x)$	Q-function;
$\mathcal{H}_n(\cdot)$	Hermite function of order n
$L_\ell^i(\cdot)$	Generalized Laguerre polynomial

$\mathcal{O}_a$ IOTA operator

$\mathcal{F}$ Fourier transform

$\mathcal{F}^{-1}$ inverse Fourier transform

$\mathcal{O}(\cdot)$ Big-O notation;

$|\mathcal{S}|$ Cardinality of the set $\mathcal{S}$

List of Symbols

Chapter 2

M	number of subcarriers
K	overlap factor
L_p	length of the prototype filter
m	subcarrier index $0 \leq m \leq M-1$
n	time-slot index $n \in \mathbb{Z}$
τ_0	distance between two consecutive symbols in multicarrier systems
ν_0	distance between two consecutive subcarriers in multicarrier systems
T_s	sampling period
Δ_α	latency established at the output of a FBMC receiver
Δ_β	delay required at the input of a FBMC receiver
N_p	modulation order of PAM symbols
N_q	modulation order of QAM symbols
$d_{m,n}$	QAM symbol of the mth subcarrier and nth time-slot
$a_{m,n}$	PAM symbol of the mth subcarrier and nth time-slot
$\phi_{m,n}$	PAM phase-shift of the symbol $a_{m,n}$
$s(t)$	continuous representation of the FBMC signal
$p_{m,n}(t)$	continuous representation of the pulse deployed by $a_{m,n}$
$p(t)$	continuous representation of the prototype filter
$s[k]$	discrete representation of the multiplexed FBMC signal
$p_{m,n}[k]$	discrete representation of the pulse deployed by $a_{m,n}$
$p[k]$	discrete representation of the prototype filter
$\mathbf{L}_{\text{OFDM}}$	OFDM generator matrix $\mathbf{L}_{\text{OFDM}} \in \mathbb{R}^{2\times 2}$
$\mathbf{L}_{\text{FBMC}}$	FBMC generator matrix $\mathbf{L}_{\text{FBMC}} \in \mathbb{R}^{2\times 2}$
η_{bw}	spectral efficiency

η_{bw}^{OFDM} spectral efficiency for OFDM systems

η_{bw}^{FBMC} spectral efficiency for FBMC systems

N_T number of transmitting antennas

N_R number of receiving antennas

$\mathbf{x}_{m,n}$ approximated received signal vector for the nth time slot of a multicarrier MIMO system
$\mathbf{x}_{m,n} \in \mathbb{C}^{N_t \times 1}$

$\mathbf{H}_m$ channel matrix for the mth subchannel oof a multicarrier MIMO system
$\mathbf{H}_m \in \mathbb{C}^{N_R \times NT}$

$\mathbf{a}_{m,n}$ PAM symbol vector for the nth time slot of the mth subccarier of a multicarrier MIMO system
$\mathbf{a}_{m,n} \in \mathbb{R}^{N_T \times 1}$

$\hat{\mathbf{a}}_{m,n}$ Imaginary interference experienced by $\mathbf{a}_{m,n}$]
$\hat{\mathbf{a}}_{m,n} \in \mathbb{R}^{N_T \times 1}$

$\boldsymbol{\eta}_{m,n}$ noise vector for the nth time slot of the mth subcarrier of a multicarrier MIMO system
$\boldsymbol{\eta}_{m,n} \in \mathbb{C}^{N_T \times 1}$

Chapter 3

$\mathbf{p}$ Prototype filter vector
$\mathbf{p} \in \mathbb{R}^{L_p \times 1}$

$P\left(e^{j\omega}\right)$ DTFT of $p[k]$

$\boldsymbol{\Gamma}(\omega)$ Prolate matrix, used to evaluate the IB and OoB energies
$\boldsymbol{\Gamma}(\omega) in \mathbb{R}^{L_p \times L_p}$

$E(\omega_c)$ IB. Energy contained within the frequency range $|\omega| \leq \omega_c$

$\overline{E}(\omega_c)$ OoB. Energy contained within the frequency range $|\omega| \geq \omega_c$ of $p[k]$

MSL Maximum Sidelobe Level

SIR Signal-to-Interference Ratio

D_k temporal dispersion of $p[k]$

D_f frequency dispersion of $p[k]$

D_τ temporal dispersion of $p[k]$ normalized by the sampling period

D_ν frequency dispersion of $p[k]$ normalized by the sampling period

ξ Heisenberg factor

r Roll of factor for SRRC prototype filter

α Spreading factor for Gaussian prototype filter and EGF

N_H Number of elements used to build the Hermite prototype filter

$\overline{d}_{\ell,\alpha,\nu_0}$ EGF filter weights

$H_{4\ell}$ ℓth weight fo the Hermite prototype filter

k_ℓ Mirabbasi-Martin prototype filter weights

α_{2i} ith weight of the Optimal Finite Duration Pulses (OFDP) prototype filter

$\psi_{i,\omega_s}[k]$ ith DPSS with a stop band ω_s
$0 \leq k \leq L_p - 1$

$\boldsymbol{\psi}_{i,\omega_s}$ Column vector ith containing the sequence $\psi_{i,\omega_s}[k]$
$\boldsymbol{\psi}_{i,\omega_s} \in \mathbb{R}^{L_p \times 1}$

$w[k]$ Window used in the window-based prototype filter
$0 \leq k \leq L_p - 1$

Chapter 4

$b_{m,n}$ Pilot/preamble transmitted during the nth time-slot of the mth subcarrier

$\breve{b}_{m,n}$ Imaginary interference generated by the preamble $b_{m,n}$

$\hat{b}_{m,n}$ Imaginary interference experience during the nth time-slot of the mth subcarrier

$\hat{H}_m$ Channel estimate for the mth subcarrier

$\mathcal{R}$ Ratio between the imaginary and real part of the channel estimate

E_s Average constellation energy

N_0 Noise spectral density

η_B Frequency selectivity index

$\mathbf{Q}_m$ Orthogonal matrix obtained via QR decomposition of $\mathbf{H}_m$

$\mathbf{R}_m$ Triangular matrix obtained via QR decomposition of $\mathbf{H}_m$

$\mathbf{y}'_{m,n}$ Modified received signal array, $\mathbf{Q}_m^H \mathbf{y}_{m,n}$

$\underline{\mathbf{H}}_m$ Extended channel matrix

$\mathbf{T}_m$ Unimodular matrix obtained via the LLL algorithm

$\mathbf{H}_m$ Near-orthogonal matrix obtained via the LLL algorithm

$\mathbf{z}_m$ Symbols in the LR domain

$w_{m,\ell}$ ℓ weight of the multi-tap equalizer deployed in the mth subcarrier

L_w length of the multi-tap equalizer

$\mathbf{W}_{m,\ell}$ ℓ matrix weight of the multi-tap equalizer deployed in the mth subcarrier

$\mathbf{H}_{m,(\ell)}$ ℓth subchannel matrix of the mth subcarrier

$\mathbf{G}_{m,(\ell)}$ ℓth subchannel equalization matrix of the mth subcarrier

$\mathbf{D}_{i,\ell}$ Frequency conversion matrix

Chapter 5

N Number of weights used in the optimization problem

$\mathbf{\Psi}$ Concatenation of all the row vectors $\psi_{i,\omega_s}[k]$

c_i Prototype filter weights to be optimized

$\mathbf{c}$ Weight vector containing all the elements c_i
$\mathbf{c} \in \mathbb{R}^{N\times 1}$

$\mathbf{c}$ Outer product of $\mathbf{c}$
$\mathbf{c} \in \mathbb{R}^{N\times N}$

$\epsilon_{m,n}$ Interference generated by the symbols $a_{m,n}$ into the symbol $a_{0,0}$

$\mathcal{E}$ Set of doubles (m, n) which leads to non-zero interference elements $\epsilon_{m,n}$

$\mathbf{\Sigma}_m$ Diagonal matrix containing cosine entries used to evaluate the interference elements

$\mathbf{\Pi}_n$ Shift matrix used to evaluate the interference elements

κ Solution accuracy of a SDP solver

Chapter 6

N Number of weights used in the optimization problem

$f_i[k]$ ith sequence of the family that composes the prototype filter design presented in Chapter 6
$0 \leq k \leq L_p - 1$

$\mathbf{f}_i$ Column vector containing the sequence $f_i[k]$
$\mathbf{f}_i \in \mathbb{R}^{L_p\times 1}$

$\mathbf{F}$ Matrix containing the column vectors $\mathbf{f}_i$
$\mathbf{F} \in \mathbb{R}^{L_p\times N}$

c_i Prototype filter weights to be optimized

$\mathbf{c}$ Weight vector containing all the elements c_i
$\mathbf{c} \in \mathbb{R}^{N\times 1}$

$\epsilon_{m,n}$ Interference generated by the symbols $a_{m,n}$ into the symbol $a_{0,0}$

$\mathcal{E}$ Set of doubles (m, n) which leads to non-zero interference elements $\epsilon_{m,n}$

$\mathbf{\Sigma}_m$ Diagonal matrix containing cosine entries used to evaluate the interference elements

$\mathbf{\Pi}_n$ Shift matrix used to evaluate the interference elements

$\mathbf{Q}_0$ Matrix used to evaluate the IB energy of the proposed problem

$\mathbf{Q}_{m,n}^{(i)}$ Matrix used to evaluate the interference elements

δ_ρ Spectrum shift

ϵ_0 Maximum interference allowed in the prototype filter design of presented in Chapter 6

$\mathcal{K}$ Set of indexes of the boundaries samples used in the constraints of the optimization problem described in Chapter 6

Chapter 7

$\mathcal{A}_{N_p}$ Alphabet for N_p-Pulse Amplitude Modulation (PAM)

$f_\eta(y)$ Probability Density Function (PDF) for the additive noise

$f_{a_{m,n}}(y)$ PDF for the PAM symbols

$f_{\epsilon_{m,n}a_{m,n}}(y)$ PDF

$f_{\epsilon_0}(y)$ PDF for the interference

$f_{\epsilon_0+\eta_0}(y)$ PDF for the interference plus noise

$P_b^{\text{AWGN,PAM}}(\gamma_b)$ Bit Error Rate (BER) for PAM transmission under Additive White Gaussian Noise (AWGN)

$P_b^{\text{RAY,PAM}}(\gamma_b)$ BER for PAM transmission under Rayleigh

$P_b^{\text{AWGN,FBMC}}(\gamma_b)$ BER for FBMC transmission under AWGN

$P_b^{\text{RAY,FBMC}}(\gamma_b)$ BER for FBMC transmission under Rayleigh

List of Figures

List of Tables

List of Scripts

Contents

1 Introduction

In the last few decades, telecommunications systems have become an essential tool that changed profoundly the perception and how people interact with the world, being a mean of entertainment and critical business enabler. From this perspective, an increasing number of telecommunication users with ever-growing requirements is expected. In this sense, wireless networks will experience a growth on the number of connections due to the vast number of users and the advent of the Internet of Things (IoT), which aims to connect every embedded system to a network to the benefit of interaction. Moreover, data traffic will rise dramatically due to services such as high definition video streaming, augmented reality, and cloud storage. Specifically, global mobile data traffic will increase seven fold from 2016 to 2021, achieving the astonishing traffic of 48.3 EB/month (CISCO, 2017). Thus, wireless telecommunications is a billionaire business that will require great endeavors to drive emergent systems such as the 5th Telecommunication Generation (5G).

1.1 5G: Requirements, Services and Technologies

It is widely widespread that 5G will not be just "4G, but faster", for 5G will introduce new services with steep requirements. With this in mind, DOCOMO (2014) envisioned that 5G should require a hundredfold data rate gain compared to 4G, with a hundred more connections, 1 ms latency, and very high energy/spectral efficiency. Furthermore, reliability, coverage, and mobility requirements will also be more demanding in 5G applications. In order to provide better visualization, Figure 1.1 presents a spider plot comparing 4G and 5G requirements issued by the International Telecommunication Union (ITU).

Mainly, the aforementioned requirements emerged due to the new services to be offered by 5G. Concerning the number of connections, IoT will increase wireless network density, given the integration of a massive number of sensors and embedded systems, which will benefit, for example, home, industry, and agriculture automation (AL-FUQAHA et al., 2015). On the other hand, applications such as virtual reality require very low transmission latency (< 1 ms) in order to provide users a full sensorial experience, namely tactile internet (FETTWEIS, 2014). For obvious reasons, healthcare applications and autonomous driving will require a high degree of reliability. As mentioned previously, video streaming, augmented reality, and cloud storage are examples of services that will require very high data rates.

Energy efficiency is one of the main concerns in 5G systems. In this sense, high energy efficient wireless devices lead long life batteries, which is a critical point as mobile phones, sensors, and other embedded systems are battery-powered due to mobility features. On the other hand, Base Stations (BSs) can also benefit from high energy efficiency as

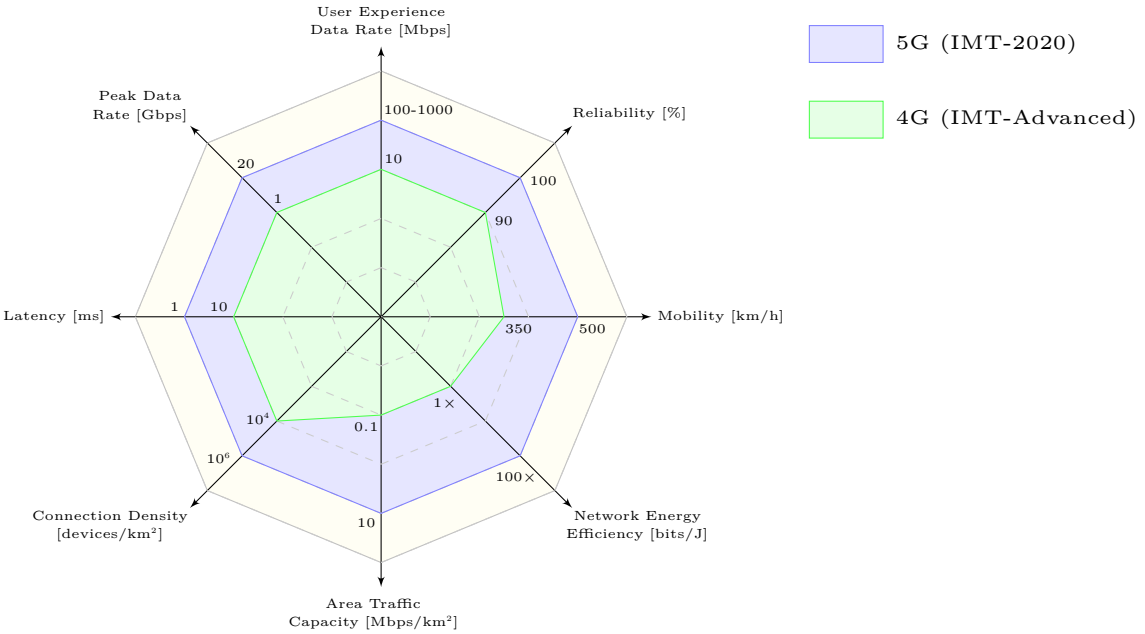

Figure 1.1 Spider chart for 4G (IMT-Advanced) and 5G (IMT-2020) requirements (DOHLER; NAKAMURA, 2016)

operational costs are not negligible and there is much room for improvements. Furthermore, BSs can be powered by renewable energy sources such as solar, wind, and fuel cells (WANG; RANGAPILLAI, 2012). Another concern involving the energy efficiency of wireless systems is the amount of electromagnetic irradiation. Despite being controversial, electromagnetic irradiation should be limited to safe values in order to prevent harmful effects on the human body (LIN, 2016). In particular, a prolonged electromagnetic exposition should not exceed the Specific Absorption Rate (SAR) of 80 mW/kg (IEEE, 2006). From this perspective, contemporary systems, such as 4G, may experience emission power peaks of 20 W in BS and 100 mW for mobile terminals (3GPP, 2016). Although there is no consensus on the relationship between prolonged electromagnetic exposition and diseases such as cancer (MICHELOZZI ALESSANDRA CAPON, 2002), such emission guidelines must be followed, constraining the amount of irradiated power.

One of the most valued resources in telecommunication systems is the spectrum. As a relatively recent example, recall the reallocation of the 700 MHz band. The 700 MHz band was used previously for TV broadcasting and gave place for mobile communications (ANATEL, 2015). Such a transition took place very slowly through a great bureaucratic effort. Nevertheless, it also rendered billionaire spectrum auctions, highlighting both the scarcity and the value of the spectrum. Hence, spectrum efficiency is definitively a priority for 5G systems due to the high rate applications and limited spectrum availability. Moreover, radio access may experience changes in order to provide flexibility, scalability, and efficiency. Despite not being considered a candidate technology, the deployment of cognitive radio concepts (HAYKIN, 2005) is plausible, as pointed out by Wang et al. (2014).

However, cognitive radios are more likely to be deployed for scheduling and interference management rather than for opportunistic spectrum usage enabled by spectrum sensing (SHAFI et al., 2017).

1.1.1 Family of Services

As presented previously, 5G services and requirements were presented qualitatively aiming to present an introduction of the overall idea behind 5G. As an example, Figure 1.1 provides an overall view of the 5G requirements. However, these requirements do not need to be simultaneously attained to comply with the aforementioned services, as each application has its priorities. In this sense, IMT-2020 categorizes 5G services into three families of applications (SHAFI et al., 2017):

- **enhanced Mobile BroadBand (eMBB):** This family of services focuses on enhancing user experience in scenarios ranging from hotspots to wide-area coverage. Hotspot scenarios will require high data rates and support to a massive number of terminals at pedestrian speed. On the other hand, high mobility is the priority for wide-area coverage applications, while data rates are less stringent than in hotspot scenarios.
- **Ultra-Reliable Low Latency Communications (URLLC):** In this case, low latency and high reliability are the main goals to leverage this set of services. Applications examples for this family are Tactile Internet, Smart Grids, Autonomous vehicles, remote medical surgery, etc.
- **massive Machine-Type Communications (mMTC):** This type of application covers wireless systems with a huge number of low-cost devices with long battery life. Despite the number of connections, mMTC does not require high data rates or low latency. However, it is worth mentioning that the traffic patterns are not fully characterized. IoT is the main application example of this family of services.

1.1.2 Requirements

Based on the aforementioned classes of services for 5G, Table 1.1 defines and summarizes the minimum requirements for 5G services according to the IMT-2020 (ITU, 2017).

Table 1.1 Minimum Requirements for 5G (IMT-2020)

Key Point	**Definition**	**Minimum Requirement**
Peak Data Rate	Maximum achievable data rate under ideal conditions	20 Gbps (DL, eMBB) 20 Gbps (UL, eMBB)
Peak spectral efficiency	Maximum data rate under ideal conditions normalized by channel bandwidth	30 bps/Hz (DL, eMBB) 15 bps/Hz (UL, eMBB)
User Experienced Data Rate	5% point of the Cumulative Density Function (CDF) of the user throughput	100 Mbps (DL, eMBB, Dense Urban) 50 Mbps (UL, eMBB, Dense Urban)
5% User Spectral Efficiency	5% point of the CDF of the normalized user throughput [1]	0.23 bps/Hz (DL, eMBB, Dense Urban) 0.15 bps/Hz (UL, eMBB, Dense Urban)
Average Spectral Efficiency	Aggregated throughput of all users divided by the channel bandwidth of a specific band divided by the number of TRxPs [2]	7.8 bps/Hz/TRxP (DL, eMBB Dense Urban) 5.4 bps/Hz/TRxP (UL, eMBB, Dense Urban)
Area Traffic Capacity	Total traffic throughput served per geographic area	10 Mbps/m^2 (DL, eMBB, Indoor hotspot)
User Plane Latency	Contribution of the radio network to the time from when the source sends a packet to when the destination receives it	1 ms (URLLC) 4 ms (eMBB)
Control Plane Latency	Transition time from an idle state to the start of continuous data transfer	20 ms (URLLC) 20 ms (eMBB)
Energy Efficiency	Capability to minimize the radio access network energy consumption in relation to the traffic capacity provided	Capability to support long sleep duration
Reliability	Capability of transmitting a given amount of traffic within a predetermined time duration with high success probability	10^{-5} (URLLC) [3]
Mobility	Maximum mobile station speed at which a defined QoS can be achieved	500 km/h (eMBB)
Mobility Interruption	Shortest time duration supported by the system during which a user terminal cannot exchange user plane packets with any base station during transitions	0 ms (eMBB, URLLC)
Bandwidth	Maximum aggregated system bandwidth	$\leq$ 100 MHz (eMBB, $fc \leq 6$ GHz) $\geq$ 1 GHz (eMBB, $fc > 6$ GHz)

[1] Normalized user throughput: number of correctly received bits over a certain period of time divided by the channel bandwidth and is measured in bit/s/Hz

[2] TRxP: Transmission reception points

[3] Success probability of transmitting 32 bytes within 1 ms in channel quality of coverage edge

1.1.3 Candidate Technologies

As observed, 5G services impose very demanding requirements. Therefore, the technology deployed in wireless systems must be rethought as an endeavor to comply with the steep requirements of 5G. In this sense, the following technologies are the leading contenders to leverage 5G systems:

- Massive Multiple-Input Multiple-Output (MIMO);
- Millimeter Waves (mmWaves);
- Random Access Protocols (RAPs);
- Non-Orthogonal Multiple Access (NOMA) and new coding schemes;
- Non-orthogonal waveforms for radio access.

1.1.3.1 Massive MIMO

Considered by many as the leading technology for 5G, massive MIMO deploys a large number of antennas in order to enhance the overall performance of communications systems over wireless channels. Due to statistical properties, the usage of a large number of antennas averages out small-scale fading (RUSEK et al., 2013), simplifying the signal processing. Furthermore, massive MIMO can be deployed to boost data transmission due to its high spatial multiplexing capability and/or to improve reliability. Another advantage is the possibility of using many low-cost power amplifiers instead of a single high power amplifier (LARSSON et al., 2014). Indeed, the idea that massive MIMO requires high precision hardware is a myth pointed out by Bjösrnson et al. (2016).

Despite its numerous qualities, massive MIMO still faces a challenging bottleneck: the pilot contamination. By deploying pilot reuse, interference arises during channel estimation. Hence dense networks are prone to pilot contamination, limiting overall performance of massive MIMO systems considerably, as only poor channel estimates are available to be deployed during signal processing.

Given the large number of antennas required by massive MIMO, the physical size of the array of antennas has always been a major concern. In this context, the operating frequency also plays an important role as the recommended antenna separation is inversely proportional to the frequency of the system. As an example, a linear array of half-length antennas projected for microwave can require an ample accommodation space, i.e., some meters. However, this problem can be circumvented with dual-polarized antennas or higher carrier frequencies, as demonstrated by Vieira et al. (2014) and Roh et al. (2014), respectively.

1.1.3.2 mmWaves

The reason behind the usage of mmWaves is the abundant spectrum available in frequencies beyond 30 GHz (RAPPAPORT et al., 2017). However, propagation in mmWaves for densely populated areas is not fully characterized (RAPPAPORT et al., 2013). Furthermore, operating in such frequencies imposes a higher path-loss and hardware impairments. Fortunately, MIMO and mmWaves can be combined to overcome some problems introduced by the latter technology. By deploying MIMO, mmWaves can overcome its expressive path loss (ROH et al., 2014). On the other hand, mmWaves enable the usage of smaller antennas, leading to higher antenna density and making it a technology to empower massive MIMO systems.

1.1.3.3 Random Access Protocols

Initially, pilot allocation among mobile terminals was assumed to be static in massive MIMO systems. Nevertheless, such allocation policy is impractical given the limited number of pilots. More recently, dynamic random pilot allocation strategy in massive MIMO has aroused great interest as it is suitable to mMTC (CARVALHO et al., 2017). Figure 1.2 depicts the types of pilot assignment according to the relation between the number of orthogonal pilots and devices.

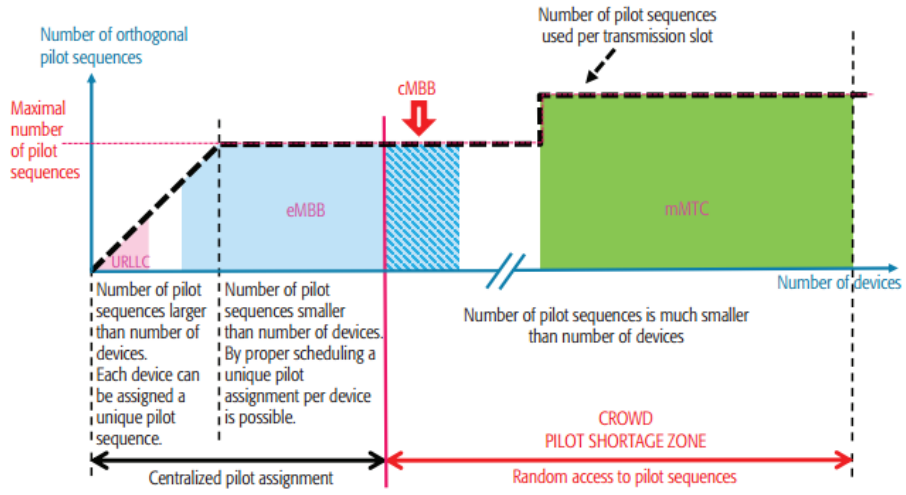

Figure 1.2 Types of pilot assignment according to the number of device (CARVALHO et al., 2017)

Figure 1.2 also classifies the pilot assignment according to the scenario of interest. URLLC prioritizes reliability and low latency while eMBB aims to provide high data rates for a moderate number of terminals. Similarly, eMBB requires high rates, but the traffic is intermittent and a large number of terminals must be supported. On the other hand, mMTC is characterized by its large number of devices served per cell, sporadic activation[4] and heavy uplink traffic.

[4]Typically with activation probability around 0.05% to 0.2%

Since only a small portion of devices is simultaneously active in mMTC, dynamic random pilot allocation can provide orthogonal pilots. Still, multiple active devices can select the same pilot, generating pilot collision and pilot contamination. Hence, RAPs must be established in order to minimize pilot collision, enhancing the performance and reliability of mMTC.

In summary, there are three types of RAP for massive MIMO systems, which are used to deal with collision resolution. First, the Spatial Capture resolution uses information of the spatial signature in order to detect pilot collision. The other option is the centralized collision resolution, which enables collision detection at the BS. Due to the centralized nature of this method, a device may only connect to the BS when there is no collision. Hence, such lack of coordination makes devices to attempt connection multiple times. On the other hand, distributed collision resolution enables devices to estimate pilot collision, improving reliability compared to the centralized topology.

In this context, the Strongest-User Collision Resolution (SUCR) (BJÖRNSON et al., 2017; MARINELLO; ABRÃO, 2019) is a promising RAP with distributed collision detection. Such a RAP estimates pilot collision based on the individual array gain of each device that wishes to connect to the BS. In this sense, devices with low individual array gains should abort the connection, as they are less reliable than other devices. However, a precise distributed decision rule to control collision is a challenging task, which poses great research opportunities. Other examples of works that explore RAP in mMTC are (HAN et al., 2017a) and (HAN et al., 2017b).

1.1.3.4 NOMA and Coding Schemes

The idea behind NOMA is the harmonious integration of different multiple-access techniques to serve users by using non-orthogonal signals (CAI et al., 2018). Since such technology envisions non-orthogonal access, extra interference and higher complexity are expected. However, such a scheme delivers a more efficient utilization of scarce resources to support more users. NOMA can be divided into three main categories: power-domain NOMA, code-domain NOMA, and multi-domain NOMA. More recently, Sparse-Code Multiple-Access (SCMA) is a NOMA scheme that has drawn attention from researchers, being successfully implemented in 5G prototypes (WANG et al., 2018; DONG et al., 2017).

Another candidate technology for 5G is the deployment of new error correcting schemes. By deploying efficient coding schemes, throughput and spectral efficiency can be significantly improved. In this sense, Low-Density Parity-Check Code (LDPC) (GALLAGER, 1962) and Polar Codes (BIOGLIO et al., 2018) are promising techniques due to their performance. Compared with 4th Telecommunication Generation (4G) turbo codes, both Polar coding and LDPC can achieve superior performance. Hence, a higher Modulation Coding Scheme (MCS) or less energy can be used on the transmission (WANG et al., 2017). Despite being promising techniques, both polar codes and LDPC present their

own drawbacks. LDPC is known for its error floor (RICHARDSON, 2003), making it less adequate for URLLC (WANG et al., 2018). On the other hand, polar code performance is particularly high for long length codes, meaning burdensome processing requirements. Nevertheless, polar code chip implementations have been investigated, being successfully able to achieve a throughput of 5 Gbps (LIU et al., 2018), pushing such technology closer and closer to feasibility.

1.1.3.5 Non-Orthogonal Waveforms

Thanks to its simple, yet elegant, implementation and ability to deal with highly selective channels, Orthogonal Frequency-Division Multiplexing (OFDM) has become the standard waveform for many contemporary telecommunication systems, including 802.11 for local area networks, 802.16 for WiMAX and 4G LTE systems (HWANG et al., 2009). Despite its mentioned advantages, 5G requirements are exceedingly steep for OFDM to deal. Services covered by mMTC, eMBB and URLLC are not homogeneous, requiring more flexible radio access through non-orthogonal waveforms. In this sense, the following deficiencies justify the need for different waveforms (GUAN et al., 2017):

- **Mixed Numerologies:** Various types of services and applications must coexist in 5G. In this sense, classical 4G uniform resource allocation is not fit for 5G, as each application needs to meet their specific requirement. As an example, URLLC needs a shorter signaling interval, while eMBB prioritize data rate and mMTC must guarantee massive connectivity.

- **Spectral Efficiency:** Since OFDM deploys a rectangular pulse shaping, it presents high sidelobes (-13 dB) and Out-of-Band (OoB) energy emission. Thus, OFDM requires extra guard band ($\approx$ 10% for 4G) in order to avoid the generation of interference to neighbor bands. Furthermore, OFDM is dependent on Cyclic-Prefix (CP) to mitigate the effect of the wireless channel delay spread. Therefore, these negative OFDM features make this multiplexing less attractive for 5G applications covered by eMBB.

- **Asynchronous Access:** In 4G, OFDM is known to require extra signaling for carrier synchronization. This is not the ideal scenario for 5G as synchronization should not require substantial overheads to enable, for example, better spectral efficiency and a massive number of connections in mMTC applications. Moreover, mMTC requires asynchronous narrowband transmissions, which cannot be handled by OFDM due to the generation of subband interference.

Despite not being a relatively new subject, radio access through alternative non-orthogonal waveforms is a hot topic due to the stringent 5G requirements. As alternatives to OFDM, Cai et al. (2018) and Wunder et al. (2014) enumerate the following options as the most promising non-orthogonal waveforms candidates for 5G:

- **Universal Filtered MultiCarrier (UFMC):** OFDM is applied in each subband followed by zero-padding and subband filtering. Despite the existence of residual interference generated by the filtering process, zero-padding elements vanish the problem as the symbol duration is shorter compared to other multiplexing schemes, *e.g.* OFDM.

- **filtered Orthogonal Frequency-Division Multiplexing (f-OFDM):** Similar to UFMC, f-OFDM also uses OFDM in multiple subbands, where main difference is the deployment of CP rather than zero-padding. Since CP mitigates the almost all the effect of the filtering tail, the residual can be treated as additive noise. One of the main advantages of f-OFDM is its well contained spectrum, and its fully backward compatibility with OFDM algorithms and signal processing techniques, making it an attractive waveform. However, f-OFDM still relies on CP and is prone to residual interference generated by the tail of the output filter.

- **windowed Orthogonal Frequency-Division Multiplexing (w-OFDM):** deploys a windowing procedure at the cyclic prefix and postfix to mitigate the OoB emission of CP-OFDM systems. Notice that the windowing procedure controls the sidelobe and the main-lobe levels, enabling reduced OoB emissions. Despite the windowing procedure being less complex than linear filtering, w-OFDM presents an inferior performance. Furthermore, w-OFDM also relies on prefixes, which increases the overall overhead of the multiplexing.

- **Generalized Frequency-Division Multiplexing (GFDM):** is the general case for single carrier Frequency-Division Multiplexing and OFDM. In summary, GFDM distributes symbols through different subcarriers and deploys a circular prototype filter on each subcarrier to form up the multiplexed signal. Since the prototype filter is circular, its tail is shorter in comparison with linear filters. Thus, GFDM is a waveform recommended for sporadic transmission.

- **Filter Bank MultiCarrier (FBMC):** In FBMC, phase-shifted staggered Pulse Amplitude Modulation (PAM) symbols are staggered, distributed through different subcarriers, filtered and combined. As a consequence, the multiplexed signal presents a very low OoB emission. Furthermore, synchronization requirements are relaxed and CP usage is not required. However, FBMC signals present intrinsic imaginary component interference. Therefore, such a multiplexing scheme is not entirely backward compatible with OFDM signal processing techniques.

1.1.4 Prototypes and Testbeds

5G prototypes and testbeds are herein presented to corroborate the effectiveness of the candidate technologies discussed throughout this section.

In particular, the first 5G prototypes were devoted to massive MIMO. From this perspective, massive MIMO was extensively studied as a mean of characterizing and making this technology feasible. In this sense, Table 1.2 shows some massive MIMO prototypes. It is noteworthy mentioning that other candidate 5G technologies were also deployed in these prototypes. For example, Roh et al. (2014) combine mmWaves with MIMO and LDPC to improve the performance of the developed system.

Table 1.2 Massive MIMO prototype systems and testbeds

System/Reference	Keypoints
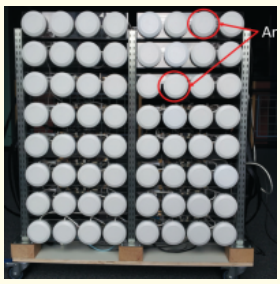 (SHEPARD et al., 2012)	Argos was the first MIMO prototype to deploy multi-user beamforming to serve user terminals with a large number of antennas. In particular, this implementation deploys a BS with 64 antennas to serve 15 users. This prototype is a modular Field-Programmable Gate Array (FPGA)-based platform, delivering a competent performance, flexibility and scalability. Furthermore, it operates under Time-Division Duplex (TDD), imposing less overhead and enabling a feasible channel estimation.
 (GAO et al., 2015)	This work discusses the channel characteristics of a cylindrical array of 128 patch antennas and a linear array of 128 vertically-polarized antennas. Authors of this work discuss the contribution of each antenna of the array in contrast to the ideal scenario where all antennas contribute equally. Furthermore, it is pointed out that large-fading and antenna configuration can affect the received/transmitted signal significantly. Hence, it is pointed out by authors that antennas present different contributions and adaptive antenna selection can improve the performance of the system considerably.
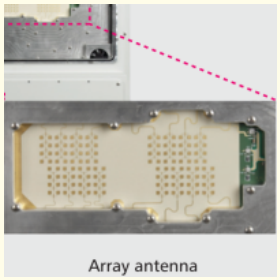 (ROH et al., 2014)	This prototype deploys a planar array of 32 antennas, OFDM multiplexing, and LDPC coding. Interestingly, mmWaves is deployed with MIMO, demonstrating that the synergistic operation of both technologies. MIMO helps mmWaves to deal with its propagation loss. On the other hand, mmWaves enables smaller arrays as antenna separation decay with frequency.
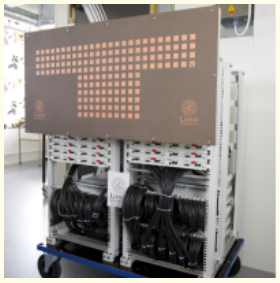 (VIEIRA et al., 2014)	LUNAMI is another FPGA/Software-Defined Radio (SDR) massive MIMO prototype. The LUNAMI BS serves ten single-antenna users with 160 half-wavelength dual-polarized antennas, OFDM multiplexing, and Zero-Forcing (ZF) or Maximum Ratio Transmission (MRT) precoding. One of the main highlights of this implementation is the size of the antennas array. Even operating in 3.7 GHz, the array of antennas occupies a relatively small area (1.2×0.6 m) due to the usage of dual-polarized antennas.

Dong et al. (2017) also presented another exciting prototype. This prototype

combines different technology in order to achieve superior performance. In particular, this prototype combines MIMO, f-OFDM multiplexing, polar codes, and NOMA access via SCMA. Performance gains are reported to be within 30% in comparison to the spectral efficiency of the baseline 4G system.

Guan et al. (2017) present a prototype to discuss radio access through non-orthogonal waveforms in 5G. In particular, the presented prototype deploys both f-OFDM and w-OFDM as a mean to support different 5G services within a given band. Since both waveforms possess well-contained spectra, less band guard is required, enabling the coexistence and efficient operation of distinct 5G applications.

1.2 FBMC Systems

FBMC waveform is regarded as a strong candidate for 5G and other wireless systems to come due to some distinctive features. One of them is the low OoB emission produced by FBMC signals (LIN; SIOHAN, 2014): a consequence of the deployment of non-rectangular pulse shaping, which enables spectrum with sidelobes as low as -60 dB. Another interesting feature is the ability of FBMC to deal with InterSymbol Interference (ISI) without relying on CP, making it a wiser choice than OFDM in terms of spectral efficiency (FARHANG et al., 2014). Also, FBMC requirements on time/frequency synchronization are more relaxed than other multicarrier schemes, as described in (CASSIAU et al., 2013). Yet another important aspect of FBMC is its compatibility with massive-MIMO systems (FARHANG et al., 2014), representing one of the main technologies to drive 5G (BOCCARDI et al., 2014). Indeed, given such promising aspects, FBMC waveform was designated as a candidate on METIS project (SCHELLMANN, 2015) and as the main choice for PHYDIAS project (VIHOLAINEN et al., 2009).

Despite offering many advantages, FBMC still presents some troublesome issues to be addressed. Due to its dependence on orthogonality in the real field, many algorithms used in other multicarrier systems need to be adapted for FBMC. Although FBMC deploys prototype filters with low spectrum leakage, they also generate imaginary interference that spans through adjacent symbols. As a result, traditional pilot-aided channel estimation cannot be proceed as in OFDM, since pilots are prone to imaginary interference at the receiver. Thus, FBMC channel estimation is carried out through specific methods such as scattered pilots (LÉLÉ et al., 2008c), coded auxiliary p silots (CUI et al., 2016), Interference Approximation Method (IAM) and Pair of Pilots (POP) (LÉLÉ et al., 2008a). Another example of incompatibility is the Tone Reservation method (RAHMATALLAH; MOHAN, 2013), used for Peak-to-Average Power Ratio (PAPR) reduction in OFDM systems, which requires system modifications to take full advantage of FBMC transmission (BULUSU et al., 2015). Finally, equalization of FBMC signals also requires extra care due to imaginary interference. Some examples of promising equalizers oriented to FBMC systems

are: the Minimum Mean-Squared Error (MMSE) per Subchannel Equalizer (IKHLEF; LOUVEAUX, 2009a), the Frequency-Sampling equalizer (IHALAINEN et al., 2011) and Minimum Mean-Squared Error Decision Feedback Equalizer (MMSE-DFE) per subchannel equalizer (BALTAR et al., 2009; CHEN; MAEHARA, 2017).

Another concern that emerges when designing an FBMC system is the choice of the prototype filter. Different prototype filters render distinct features to an FBMC signal, which should be well aligned to the aimed application. For example, when adapting themselves for opportunistic spectrum sharing, cognitive radios should minimize OoB emission in order to avoid interfering other bands (KUMAR; TYAGI, 2016). Hence, cognitive radios require waveforms with low OoB energy emission and small sidelobes. Although being less vulnerable to time/frequency channel dispersion, FBMC signals are still prone to such effects (ZHANG et al., 2017). Thus, well localized filters in both time and frequency domains are desirable. Another aspect to be taken into account is the reconstruction capability offered by the filter, as FBMC systems operate under an intrinsic interference floor dictated by the prototype filter. Unfortunately, a prototype filter cannot be designed arbitrarily, as there is a performance trade-off between the aforementioned characteristics of the filter. Prototype filters designs such as the Mirabassi-Martin (MIRABBASI; MARTIN, 2003) may provide very low sidelobes and good reconstructions features, but at the cost of very long impulse responses, which introduce high latency at the receiver. On the other hand, Optimal Finite Duration Pulses (OFDP) (VAHLIN; HOLTE, 1994) may offer good reconstruction features and short pulses, but they do not overcome the Mirabassi-Martin design in terms of sidelobe levels. From this perspective, the right choice of the prototype filter is decisive for an FBMC to operate properly in a given application.

1.3 Outline of the Work

Based on the previous section, FBMC possesses many qualities. Nevertheless, FBMC scheme is not the most popular waveform deployed in 5G prototypes. As pointed out previously, f-OFDM have been the predominant waveform deployed in 5G prototypes and field tests, mainly due to its simplicity and backward compatibility with OFDM. However, f-OFDM still possesses limitations that can be overcome by other multiplexing schemes.

Given the challenges behind FBMC systems and the convenience of the f-OFDM deployment, the former waveform has not been considered as the leading contender for 5G. From this perspective, this work studies FBMC as a mean of characterizing and improving the feasibility of FBMC for 5G systems. More specifically, this work has the following goals:

- Providing FBMC basics from the perspective of telecommunications systems;

- Studying promising prototype filters, highlighting their importance on the spectrum and symbol reconstruction qualities of FBMC signals;
- Proposing prototype filter designs to enhance the operation of FBMC systems;
- Studying the effects of prototype filters on the overall FBMC signal transmission.

Concerning the remainder of this work Chapter 2 provides a background on FBMC multiplexing, describing both the discrete and continuous formulation. Additionally, the author offers a brief discussion of FBMC systems operating over wireless channels, including some basics on Multiple-Input Multiple-Output Filter Bank MultiCarrier (MIMO-FBMC) systems. In the sequel, Chapter 3 discusses promising prototype filters and some mechanisms to evaluate their performance. Chapter 4 discusses channel estimation and symbol detection techniques for FBMC systems, which are primordial steps to reconstruct the conveyed data at the receiver side. Chapter 5 reinterprets the OFDP prototype filter design using a matrix description and SemiDefinite Programming (SDP), achieving much better symbol reconstruction performance. Inspired by the previous design, Chapter 6 proposes an extension in order to provide a prototype filter with superior spectrum performance. Nevertheless, the design proposed in Chapter 6 relaxes a non-convex Quadratically Constrained Quadratic Programming (QCQP) into a convex problem. Aiming to better describe the effects of the prototype filter on the overall FBMC multiplexing and transmission, Chapter 7 develops closed-form Bit Error Rate (BER) expressions for FBMC systems operating under Additive White Gaussian Noise (AWGN) and Rayleigh Channels. Finally, Chapter 8 closes the work by offering conclusions and final remarks. Additionally, the Appendices provide a large amount of information related to FBMC systems, including the weights of the prototype filters designed in this work, additional analysis of prototype filters, definitions of recurring functions, and Matlab scripts that cover all the signal processing deployed and developed in this work.

1.4 Submissions and Publications

This section enumerates the works developed throughout the doctorate Program, which are divided into published and accepted papers.

1.4.1 Published Papers

[P1] **Title:** "Theoretical Error for Asynchronous Multi-uUer Large-Scale MIMO Channel Estimation"
Authors: Ricardo Tadashi Kobayashi, Taufik Abrão
Journal: *IET Communications*
Publication Date: January 2017

Available on: <https://doi.org/10.1049/iet-com.2016.0738>
This paper is not directly related to this thesis

[P2] **Title:**"BER Minimisation via Optimal Power Allocation and Eigenbeamforming in MIMO Systems"
Authors: Ricardo Tadashi Kobayashi, Alex Mussi, Taufik Abrão
Journal: *Telecommunication Systems*
Publication Date: July 2018
Available on: <https://doi.org/10.1007/s11235-018-0487-4>
This paper is not directly related to this thesis

[P3] **Title:** "Improved Multi-Band Cognitive Radio Spectrum Sensing using Wavelet Spectrum Filtering"
Authors: Ricardo Tadashi Kobayashi, Aislan Gabriel Hernandes, Mário Lemes Proença, Taufik Abrão
Journal: *Journal of Circuits, Systems and Computers*
Publication Date: August 2018
Available on: <https://doi.org/10.1142/S0218126619501366>
This paper is not directly related to this thesis

[P4] **Title:** "DE/PSO-Aided Hybrid Linear Detectors for MIMO-OFDM Systems Under Correlated Arrays"
Authors: Rafael Masashi Fukuda, David William Marques Guerra, R Ricardo Tadashi Kobayashi, Taufik Abrão
Journal: *Transactions on Emerging Telecommunications Technologies*
Publication Date: August 2018
Available on: <https://doi.org/10.1002/ett.3495>
This paper is not directly related to this thesis

[P5] **Title:** "Efficient Detectors for MIMO-OFDM Systems under Spatial Correlation Antenna Arrays"
Authors: David William Marques Guerra, Rafael Masashi Fukuda, Ricardo Tadashi Kobayashi, Taufik Abrão
Journal: *Etri Journal*
Publication Date: September 2018
Available on: <https://doi.org/10.4218/etrij.2018-0005>
This paper is not directly related to this thesis

[P6] **Title:** "FBMC Prototype Filter Design via Convex Optimization"
Authors: Ricardo Tadashi Kobayashi, Taufik Abrão
Journal: *IEEE Transactions on Vehicular Technology*
Publication Date: November 2018

Available on: <https://doi.org/10.1109/TVT.2018.2879856>
This paper is connected to Chapter 6 of this thesis.

[P7] **Title:** "Near-Perfect Reconstruction Short Length Pulses for FBMC systems: Re-optimizing OFDP Design via Semi-Definite Programming"
Authors: Ricardo Tadashi Kobayashi, Alex Mussi, Taufik Abrão
Journal: *IIET Signal Processing*
Publication Date: October 2019
Available on: <https://doi.org/10.1049/iet-spr.2018.5177>
This paper is connected to Chapter 5 of this thesis.

1.4.2 Papers Accepted for Publication

[A1] **Title:** "Exact Error Probability for FBMC Systems"
Authors: Ricardo Tadashi Kobayashi, Taufik Abrão
Journal: *IEEE Transactions of Vehicular Technology*
Status: Accepted with minor revisions (August 2019)
This paper is connected to Chapter 7 of this thesis.

2 FBMC Systems

This chapter introduces a basic yet solid framework for FBMC systems, which is fundamental for the development of the remainder of this work. Initially, we discuss the FBMC multiplexing in both continuous and discrete-time domains. Since the latter is more effective for signal processing, it is carried out through the remainder of this work. In this sense, we also provide the complete block diagram for the FBMC transmultiplexing and polyphase representations. Moreover, we present the operation of FBMC systems over wireless channels, highlighting signal processing techniques deployed for retrieving the conveyed data. Closing this chapter, we offer a collection of relevant works in the context of FBMC systems.

2.1 FBMC Transmultiplexing Scheme

An FBMC signal consists of a set of staggered wand phase-shifted PAM symbols multiplexed over M subcarriers. Aiming to improve features such as low OoB emission, FBMC systems deploy per-subcarrier filtering. Despite presenting a shorter symbol interval than OFDM, FBMC symbol duration is longer. However, two staggered PAM symbols are equivalent to one Quadrature Amplitude Modulation (QAM) symbol. Thus, symbol density is the same in both OFDM and FBMC systems.

2.1.1 Continuous-Time Description

In continuous time, an FBMC signal can be compactly described by

$$s(t) = \sum_{n=-\infty}^{\infty} \sum_{m=0}^{M-1} a_{m,n} p_{m,n}(t), \tag{2.1}$$

where $p_{m,n}(t)$ is the pulse shape used by the PAM symbol $a_{m,n}$, which is contained in the set

$$\mathcal{A}_{N_p} = \{-N_p + 1, -N_p + 3, \cdots, N_p - 1\}. \tag{2.2}$$

The pulse format $p_{m,n}(t)$ used by the nth symbol of the mth subcarrier can be written as

$$p_{m,n}(t) = p\left(t - n\tau_0\right) e^{j(2\pi\nu_0 mt + \phi_{m,n})}, \tag{2.3}$$

where $p(t)$ is an even real-valued function known as the prototype filter, $\nu_0 = 1/(2\tau_0)$ the frequency separation between two adjacent subcarriers, τ_0 is the PAM signaling interval and $\phi_{m,n}$ is a phase-shift added to the PAM symbol $a_{m,n}$.

2.1.1.1 Symbol Reconstruction

In order to retrieve the conveyed data from the signal $s(t)$, the following inner product can be evaluated:

$$\tilde{a}_{m,n} = \mathrm{Re}\left\{\langle s(t), p_{m,n}(t)\rangle\right\}, \tag{2.4}$$

where the real operator is deployed as the PAM symbols are real-valued. Noticeably, perfect reconstruction requires that the set $\{p_{m,n}(t)\}$ is orthogonal in the real field, i.e.,

$$\mathrm{Re}\left\{\langle p_{m,n}(t), p_{m',n'}(t)\rangle\right\} = \delta(m-m')\delta(n-n'). \tag{2.5}$$

In summary, the reconstruction quality depends on two main factors: the prototype filter $p(t)$ and the phase-shift $\phi_{m,n}$. Initially, defining $\phi_{m,n}$ is an easier task, as explained in the following subsection. On the other hand, the choice of $p(t)$ is a much harder task, since it may assume various forms yielded by different designs. Unfortunately, prototype filters with (near)perfect symbol reconstruction do not usually lead to outstanding spectrum features, which is one of the main features of the FBMC multiplexing. Thus, a balance between spectrum features and reconstruction quality should be pursued when designing a prototype filter. In this sense, Chapters 3, 5, and 6 provide a more detailed discussion on prototype filters.

2.1.1.2 Phase-Shift

Since $\tau_0\nu_0 = 1/2$, one can observe that the pulse shapes $p_{m,n}(t)$ overlap in both frequency and time domains when forming the signal $s(t)$. Hence, in order to improve orthogonality between adjacent symbols and enable data reconstruction, $a_{m,n}$ is phase-shift by $\phi_{m,n}$. The most popular choice for phase-shift is (VIHOLAINEN et al., 2009)

$$e^{j\phi_{m,n}} = e^{j\frac{\pi}{2}(m+n)}. \tag{2.6}$$

By analyzing both Figure 2.1 and eq. (2.6), one can observe that adjacent symbols are phase-shifted by $\pi/2$ rad, minimizing ISI and InterCarrier Interference (ICI) of such symbols. Since eq. (2.6) is the standard phase-shift choice, it will be adopted throughout the remainder of this work. However, it is noteworthy mentioning that there are still other phase-shift options that deliver the same effect as eq. (2.6), e.g., eq. (23) from (SIOHAN et al., 2002).

2.1.2 Discrete-Time Description

In order to provide an efficient description, let us define the discrete-time FBMC signal using the critical sampling. Since $2\tau_0$ is the duration required to transmit M symbols, the critical sampling interval is given by

$$T_s = \frac{2\tau_0}{M}. \tag{2.7}$$

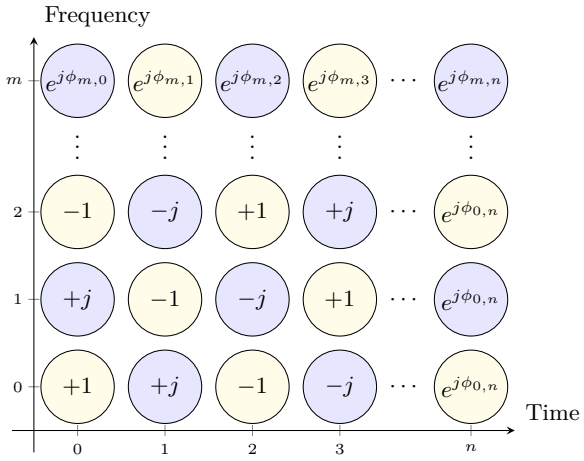

Figure 2.1 Phase-shift lattice for eq. (2.6)

Before sampling, we must turn our attention to causality and implementation aspects. First, one may recall that $p(t)$ is a symmetrical real-valued function, yielding a non causal representation. Second, $p(t)$ need to be limited in time to enable digital signal processing. In order to provide a causal representation of eq. (2.1), the prototype filter is truncated to L_p samples and it is also delayed by $(L_p-1)/2$ samples. Therefore, the discrete representation of $s(t)$ is given by

$$\begin{aligned} s[k] &= \sqrt{T_s}s\left(\left(k-\frac{L_p-1}{2}\right)T_s\right) \\ &= \sum_{n=-\infty}^{\infty}\sum_{m=0}^{M-1} a_{m,n}p_{m,n}[k], \end{aligned} \tag{2.8}$$

where

$$p_{m,n}[k] = p\left[k-n\frac{M}{2}\right]e^{j\left[\frac{2\pi}{M}m\left(k-\frac{L_p-1}{2}\right)+\phi_{m,n}\right]}. \tag{2.9}$$

Since $k-(L_p-1)/2$ is a recurring term, let us define

$$\underline{k} = k-\frac{L_p-1}{2}. \tag{2.10}$$

Since the prototype filter is limited to L_p samples, $p[k]=0$ outside the interval $[0, L_p-1]$. Moreover, typical values for L_p are $KM-1$, KM, and $KM+1$, where K is referred to as the overlapping factor.

2.1.2.1 Block Diagram

In Figure 2.2, a complete representation of an FBMC transmultiplexer is presented. In this representation, PAM symbols from different subchannels are phase shifted, expanded at a rate $M/2$, pulse-shaped by their respective subcarrier filter

$$p_m[k] = p[k]e^{j\frac{2\pi}{M}m\underline{k}} \tag{2.11}$$

and combined to form the multiplexed signal $s[k]$. At the receiver side, extra attention is required in order to guarantee causality, as a delay Δ_β must be introduced at the input of

the receiver, and a latency Δ_α arises at the estimated symbols. The relation between Δ_α and Δ_β is given by

$$L_p - 1 = \frac{M}{2}\Delta_\alpha - \Delta_\beta, \tag{2.12}$$

as demonstrated by Siohan et al. (2002) in Section II.C. Since Δ_α and Δ_β are non-negative integers, one can observe that

$$\Delta_\beta = \begin{cases} M - \bmod(L_p, KM) + 1, & L_p > KM + 1 \\ KM + 1 - L_p, & \text{otherwise} \end{cases} \tag{2.13}$$

and

$$\Delta_\alpha = \frac{2}{M}\left(L_p - 1 + D_\beta\right). \tag{2.14}$$

Furthermore, it is easy to verify that a longer prototype filter introduces a higher latency at the output of the transmultiplexer. Thus, it is desirable to deploy filters with a low overlapping factor in order to provide a latency as low as possible[1]. However, desirable spectrum and reconstruction features usually come at the expense of longer length prototype filters.

At this point, it is noteworthy mentioning that prototype filters with lengths shorter than $KM - 1$ may experience performance losses, as discussed in (VIHOLAINEN et al., 2009). On the other hand, prototype filters longer than $KM + 1$ introduce from extra latency at the output as can be observed in eq. (2.14) and (2.13). Thus, the most common values for L_p are $KM - 1$, KM, and $KM + 1$.

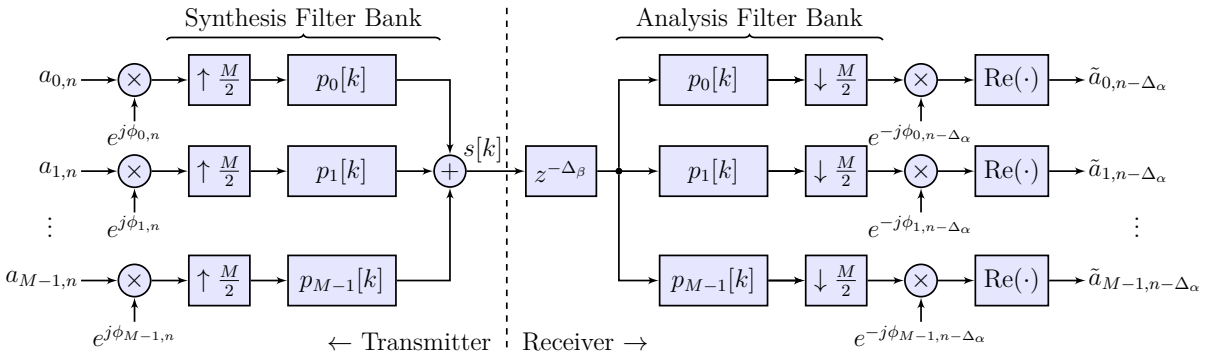

Figure 2.2 FBMC Transmultiplexer

2.1.3 Orthogonal-QAM Staggering

At this point, one might ask about the usage of QAM symbols or the spectral efficiency of the FBMC multiplexing. In order to use a QAM alphabet, one may serialize the real and imaginary parts of a QAM symbol, as depicted by the scheme presented in

[1] In certain 5G applications, such as tactile internet, low latency is a crucial feature.

Figure 2.2. Thus, a QAM symbol $d_{m,l}$ can be converted into two real-valued PAM symbols via

$$a_{m,n} = \begin{cases} \mathrm{Re}\{d_{m,l}\}, & n = 2l \\ \mathrm{Im}\{d_{m,l}\}, & n = 2l+1 \end{cases}, \tag{2.15}$$

where it is noticeable that the output symbols are at a higher rate. Figure 2.3a illustrates the procedure described by eq. (2.15), while Figure 2.3b depicts the inverse operation. Since $a_{m,n}$ is obtained from the QAM symbol, and it is phase-shifted by $\phi_{m,n}$, the resulting symbols are also referred to as Offset Quadrature Amplitude Modulation (OQAM). Thus, FBMC systems fed with QAM symbols are referred to as OFDM-OQAM while FBMC-OQAM multiplexers are fed with PAM symbols. Nevertheless, the nomenclature is not a consensus as some authors may mix these terms. Sometimes, it is preferable to use the FBMC-OQAM description since it ignores the OQAM staggering blocks and considers the input as PAM symbols.

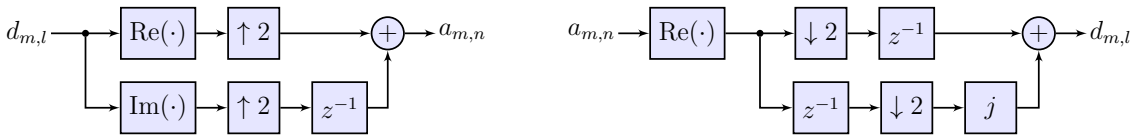

(a) OQAM staggering, complex-to-real conversion ($\mathbb{C}2\mathbb{R}$)

(b) OQAM de-staggering, real-to-complex conversion ($\mathbb{R}2\mathbb{C}$)

Figure 2.3 OQAM staggering and de-staggering blocks

The major problem of picking-up the FBMC-OQAM description is that the multiplexer is fed with $\sqrt{N_q}$-PAM symbols, while Offset Quadrature Amplitude Modulation Orthogonal Frequency-Division Multiplexing (OFDM-OQAM) and classical OFDM transmission schemes are fed by N_q-QAM symbols at a lower rate, leading to confusing comparisons. In spite of this, although FBMC-OQAM, OFDM-OQAM, and OFDM are fed with different symbol constellations, they deliver the same amount of data per frequency-time area ($\tau_0\nu_0$).

2.1.4 Time-Frequency Lattices and Bandwidth

In order to compare the spectral efficiency of the FBMC and OFDM multiplexing, let us define the generator matrix for the FBMC time-frequency lattice. For convenience, we assume $T_s = 1$, leading to

$$\mathbf{L}_{\mathrm{FBMC}} = \begin{bmatrix} M/2 & 0 \\ 0 & 1/M \end{bmatrix}. \tag{2.16}$$

Similarly, the OFDM generator matrix is given by

$$\mathbf{L}_{\mathrm{OFDM}} = \begin{bmatrix} M & 0 \\ 0 & 1/M \end{bmatrix}. \tag{2.17}$$

Each column of the generator matrices $\mathbf{L}_{\text{FBMC}}$ and $\mathbf{L}_{\text{OFDM}}$ is a unique distance between symbols spread along the time-frequency lattice. Furthermore, the matrices $\mathbf{L}_{\text{FBMC}}$ and $\mathbf{L}_{\text{OFDM}}$ are a compact representation of their respective time-frequency lattice, as depicted in Figure 2.4.

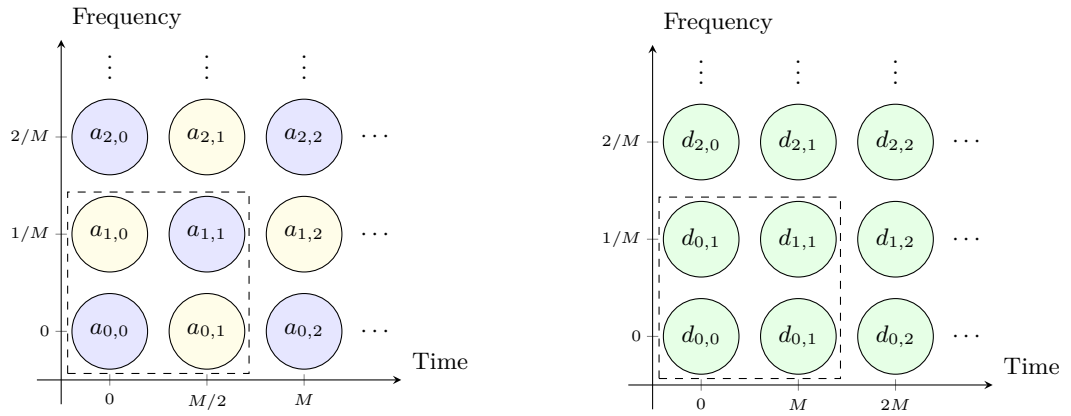

(a) FBMC Time-Frequency Lattice **(b)** OFDM Time-Frequency Lattice

Figure 2.4 FBMC and OFDM Time-Frequency Lattices

According to Sahin et al. (2014), the spectral or bandwidth efficiency is defined as the ratio between the number of bits transmitted and the respective time-frequency resource required:

$$\eta_{bw} = \frac{N_b'}{\det(\mathbf{L})}. \tag{2.18}$$

For the OFDM case, the time-frequency resource, defined by the area $\det(\mathbf{L}_{\text{OFDM}}) = 1$, covers 4 N_q-QAM symbols, as illustrated in Figure 2.4b. Thus, this leads to the efficiency

$$\eta_{bw}^{\text{OFDM}} = 4\log_2 N_q. \tag{2.19}$$

Despite being a different scheme, FBMC delivers the same efficiency as the transmission of 4 $\sqrt{N_q}$-PAM symbols requires $\det(\mathbf{L}_{\text{FBMC}}) = 1/2$ time-frequency resources

$$\eta_{bw}^{\text{FBMC}} = 4\log_2 N_q. \tag{2.20}$$

Therefore, both schemes can convey data with the same bandwidth efficiency.

It is noteworthy mentioning that the steps herein deployed to evaluate η_{bw} are valid for any multiplexing scheme, regardless of their time-frequency lattices. Examples different from OFDM and FBMC are the hexagonal-lattice schemes provided by Strohmer and Beaver (2003) and Han and Zhang (2007).

2.2 FBMC Polyphase Representation

Aiming to reduce the computational complexity of the FBMC implementation presented in Figure 2.2, let us deploy the polyphase decomposition. For a more detailed discussion on polyphase decomposition, please refer to Appendix E.

2.2.1 Polyphase Decomposition

Initially, let us apply the Z-transform on the prototype filter, leading to

$$P(z) = \sum_{k=0}^{L_p-1} p[k]z^{-k}. \tag{2.21}$$

Alternatively, eq. (2.21) can be written as

$$P(z) = \sum_{\ell=0}^{M-1} z^{-\ell} G_\ell(z^M), \tag{2.22}$$

which is the summation of M polyphase components defined as

$$G_\ell(z) = \sum_{i=0}^{K-1} z^{-i} p[\ell + iM]. \tag{2.23}$$

Before rewriting the polyphase components of the FBMC synthesis filter bank, we need to define the Z-transform of all the subcarrier filters $p_m[k]$. In this sense, one can observe that $P_m(z)$ can be written directly in terms of $P(z)$, *i.e.*,

$$P_m(z) = P\left(ze^{-j2\pi\frac{m}{M}}\right) e^{-j2\pi\frac{m}{M}\frac{L_p-1}{2}}. \tag{2.24}$$

Alternatively, one can rewrite eq. (2.24) as

$$P_m(z) = \sum_{\ell=0}^{M-1} z^{-\ell} G_\ell^{(m)}(z^M), \tag{2.25}$$

where

$$G_\ell^{(m)} = G_\ell(z) e^{j2\pi\frac{m}{M}\left(\ell - \frac{L_p-1}{2}\right)} \tag{2.26}$$

is the ℓth polyphase component of $p_m[k]$.

2.2.2 Multiplexed Signal

At this point, let us consider the output of the mth branch of the Synthesis filter of an FBMC system, depicted in Figure 2.5. Notice that the output of such a branch can be written as

$$s_m[k] = \sum_{n=-\infty}^{\infty} a_{m,n} e^{j\phi_{m,n}} p_m\left[k - n\frac{M}{2}\right] \tag{2.27}$$

and it is the filtered signal of the up-sampled phase-shifted PAM symbols.

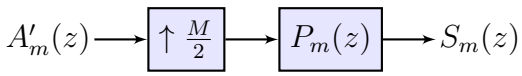

Figure 2.5 mth branch of the synthesis filter of a FBMC multiplexer

In order to analyze Figure 2.5, let us apply the Z-Transform on the output of the mth branch of the synthesis filter, which can be represented by

$$S_m(z) = A'_m\left(z^{\frac{M}{2}}\right) P_m(z), \tag{2.28}$$

where

$$A'_m(z) = \mathcal{Z}\left\{a_{m,n}e^{j\phi_{m,n}}\right\}. \tag{2.29}$$

By deploying the polyphase decomposition, *i.e.*, eq (2.25), on the prototype filter of the mth subcarrier, eq. (2.28) can be written as

$$S_m(z) = A'_m\left(z^{\frac{M}{2}}\right)\sum_{\ell=0}^{M-1} z^{-\ell}G_\ell\left(z^M\right)e^{j2\pi\frac{m}{M}\left(\ell-\frac{L_p-1}{2}\right)}. \tag{2.30}$$

Hence, Figure 2.5 can be redrawn as presented in Figure 2.6.

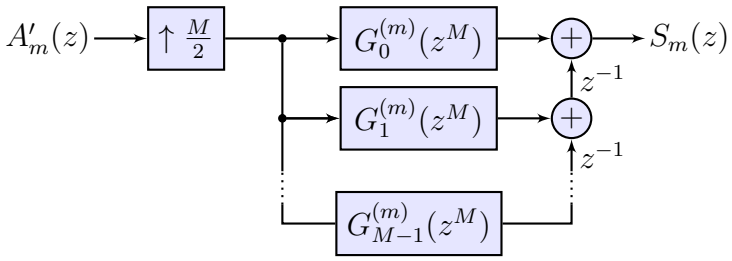

Figure 2.6 Alternative representation of Figure 2.5 after deploying the polyphase decomposition

Since our goal is reducing the computational complexity of the FBMC multiplexing, let us swap the position of the up-sampler and the prototype filter presented in Figure 2.6[2]. Hence, eq. (2.30) can be rewritten as

$$S_m(z) = \sum_{\ell=0}^{M-1} z^{-\ell}G_\ell\left(z^2\right)e^{j2\pi\frac{m}{M}\left(\ell-\frac{L_p-1}{2}\right)}A'_m\left(z\right), \tag{2.31}$$

making the phase-shifted symbols be filtered prior to up-sampling, which reduces the processing considerably. Figure 2.7 presents the modified version of the mth branch of the FBMC multiplexer.

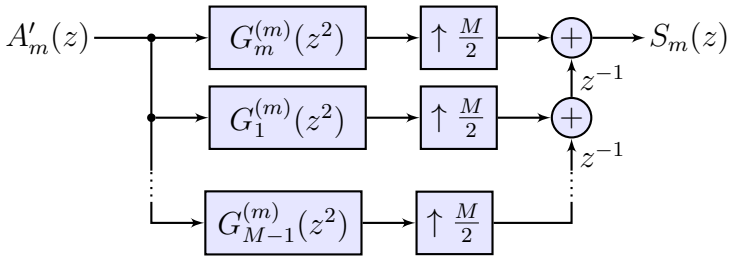

Figure 2.7 Alternative representation of Figure 2.6 after deploying the Noble identity for up-sampling

A further complexity reduction can be achieved at the output of the FBMC multiplexer, which can be obtained by adding the signals from all the subcarrier filtering branches $S_m(z)$:

$$S(z) = \sum_{m=0}^{M-1}\sum_{\ell=0}^{M-1} z^{-\ell}G_\ell\left(z^2\right)A'_m\left(z\right)e^{j2\pi\frac{m}{M}\left(\ell-\frac{L_p-1}{2}\right)}. \tag{2.32}$$

[2]This operation is known as the expansion Noble identity depicted in Figure E.8.

By rearranging the terms in eq. (2.32)

$$S(z) = \underbrace{\sum_{\ell=0}^{M-1} z^{-\ell} G_\ell\left(z^2\right)}_{\text{Polyphase net}} \underbrace{\frac{1}{M} \sum_{m=0}^{M-1} e^{j\frac{2\pi m\ell}{M}} \underbrace{\underbrace{Me^{-j2\pi\frac{m}{M}\frac{L_p-1}{2}} e^{j\phi_{m,n}}}_{\text{Scalling + phase-shift}} \underbrace{A_m(z)}_{\text{PAM symbols}}}_{\text{IDFT input}}}_{\text{IDFT}}, \tag{2.33}$$

one can observe that an Inverse Discrete Fourier Transform (IDFT) can be deployed at the input of the multiplexer to reduce the complexity of the signal. However, a factor $Me^{-j\frac{2\pi}{M}}$ must be added before the IDFT block to scale and phase-shift the PAM symbols properly. With these proper modifications, the Inverse Fast Fourier Transform (IFFT) can be deployed instead of the IDFT for a more efficient implementation.

2.2.3 Polyphase FBMC Transmultiplexer

Since the receiving structure presented previously is a mirrored version of the transmitter, the polyphase FBMC transmultiplexer can be depicted as shown in Figure 2.8. However, it is worthy mentioning that the receiving side is not strictly a mirrored version of the transmission, as a delay on the input is required.

At this point, it is noteworthy mentioning that the FBMC implementation illustrated in Figure 2.8 uses IFFT blocks in both transmission and reception, unlike OFDM, where the an Fast Fourier Transform (FFT) block is deployed in the reception. A more detailed analysis can be found in (SIOHAN et al., 2002).

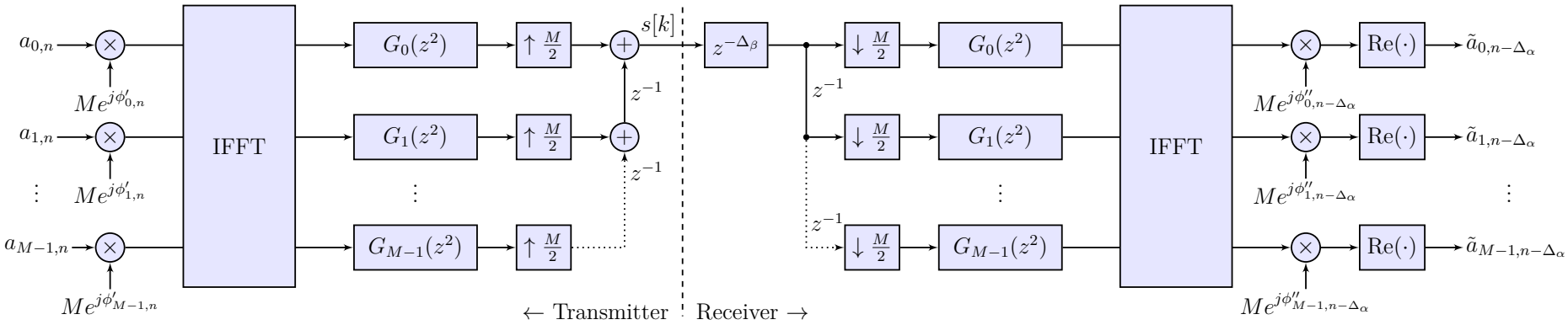

$$e^{j\phi'_{m,n}} = e^{-j2\pi\frac{m}{M}\frac{L_p-1}{2}} e^{j\phi_{m,n}}$$

$$e^{j\phi''_{m,n}} = e^{-j2\pi\frac{m}{M}\frac{L_p-1}{2}} e^{-j\phi_{m,n}}$$

Figure 2.8 Polyphase implementation of an FBMC Transmultiplexer

2.3 FBMC in Communications Systems

After a brief explanation of the FBMC multiplexing, we focus now on the deployment of such scheme in communications systems. Hence, we provide a concise description of the operation of FBMC systems over wireless channels, highlighting useful description simplifications for this scenario. Initially, a general description is presented assuming a time-varying and frequency selective channels. Simplifications are then introduced considering static frequency flat subchannels, followed by basic signal processing techniques used to recover the conveyed data. Moreover, the system model is extended for MIMO usage. Providing a detailed survey on FBMC systems is outside the scope of this work. However, we offer a small collection of relevant works related to FBMC systems, closing this chapter.

2.3.1 Basic Operation Over Flat-Rayleigh

When operating over selective channels, the received FBMC signal is written as

$$x[k] = \sum_{\ell=0}^{\infty} h[k,\ell]s[k-\ell] + \eta[k], \tag{2.34}$$

where $h[k,\ell]$ is the ℓ-th tap channel impulse response on the instant k, and $\eta[k]$ is the AWGN. If the channel is flat over each subcarrier and the coherence time is much larger than signaling interval[3], eq. (2.34) can be simplified to

$$x[k] = \sum_{n=-\infty}^{\infty} \sum_{m=0}^{M-1} H_m a_{m,n} p_{m,n}[k] + \eta[k], \tag{2.35}$$

where M is the number of subcarriers, and for each FBMC transmission frame, the mth channel frequency response is

$$H_m = \sum_{\ell=0}^{\infty} h[\ell] e^{-j\frac{2\pi}{M}m\ell}, \tag{2.36}$$

which can be evaluated efficiently by using a FFT implementation.

After passing through the receiver signal processing, the nth non-equalized symbol of the mth subcarrier is given by

$$\begin{aligned} y_{m,n} &= \langle x[k], p_{m,n}[k] \rangle \\ &\approx H_m(a_{m,n} + j\hat{a}_{m,n}) + \eta'[k], \end{aligned} \tag{2.37}$$

where $\hat{a}_{m,n}$ is the imaginary intrinsic interference and $\eta'[k]$ presents the same distribution of $\eta[k]$. At this point, it is noteworthy mentioning that $\{p_{m,n}[k]\}$ is not strictly orthogonal. Hence, one can observe the symbol $a_{m,n}$ overtakes extra interference from its neighbors. Notice that even well designed filters are prone to both real and imaginary interference. Nevertheless, prototype filters are designed to generate negligible real self-interference, whereas imaginary interference cannot be avoided.

[3] $h[k,\ell] = h[i,\ell]$, $\forall i,k$ in a complete FBMC and OFDM transmission frame

Analyzing eq. (2.37), one can observe that further processing is required to retrieve the conveyed data. At this point, symbols are distorted by the channel, requiring proper equalization to reconstruct the transmitted signal. However, to proceed with channel equalization the receiver also have to estimate the channel state for a precise frequency compensation. Since both steps are critical and demand a more in-depth development, Chapter 4 focuses on providing basics of channel estimation and equalization of FBMC systems.

Considering the present system, one can observe that the signal processing flow for the FBMC herein presented is composed by multiplexing, transmission through the wireless channel, de-multiplexing, channel estimation, equalization and symbol detection. Nevertheless, pre-equalization or precoding is a possibility. In this case, the transmitter is responsible for estimating the channel response and pre-processing the multiplexed signal, whereas the receiver has only de-multiplex and demodulated the received signal.

2.3.2 FBMC and MIMO Systems

As OFDM and other multicarrier systems, FBMC is typically associated with MIMO systems via the Vertical Bell Labs Layered Space-Time (V-BLAST) transmitting scheme (WOLNIANSKY et al., 1998). V-BLAST is the most popular choice due to its simplicity, as such a scheme consists of feeding each transmitting antenna with an FBMC transmitter. At the receiver side, equalization can be performed to retrieve the conveyed data, or alternatively one may deploy precoding at the transmitter instead (ROTTENBERG et al., 2017).

Despite being possible to combine FBMC to other schemes, they tend to impose drawbacks, which is the case of the Generalized Spatial Modulation. In this scheme, the antenna activation pattern is used to convey additional information. Hence, only a fraction of the antennas is activated at the same time, requiring less RF chains (YANG et al., 2016). However, the symbol period is much longer in multicarrier systems, thus all antennas tend to remain active, requiring that the number of RF chains is equal to the number of transmitting antennas. For this reason, spatial modulation and even Media-Based-MIMO (NARESH; CHOCKALINGAM, 2017; KHANDANI, 2014) schemes are recommended for single carrier transmission.

In order to present the basic operation of MIMO-FBMC via V-BLAST topology, let us extend the Single-Input Single-Output (SISO) description carried out previously. In a MIMO-FBMC V-BLAST system with N_T transmitting antennas and N_R receiving antennas the signal received at the ith receiving antenna can be written as

$$x^{(i)}[k] = \sum_{l=1}^{N_T} h^{(i,l)}[k,\ell] * s^{(l)}[k] + \eta^{(i)}[k], \tag{2.38}$$

where $h^{(i,l)}[k,\ell]$ is the the ℓ-th tap channel impulse response between lth transmitting and the ith receiving antenna on the instant k. After passing through the FBMC analysis filter

bank, the following symbols are obtained:

$$y_{m,n}^{(i)} = \left\langle x^{(i)}[k], p_{m,n}[k] \right\rangle . \tag{2.39}$$

By assuming that each subchannel is flat and the channel coherence time is long enough to be greater than a transmission frame in an FBMC system, one can establish the following relationship between the received and transmitted symbols:

$$\mathbf{y}_{m,n} = \mathbf{H}_m \left(\mathbf{a}_{m,n} + j\hat{\mathbf{a}}_{m,n} \right) + \boldsymbol{\eta}_{m,n}, \tag{2.40}$$

where

$$\mathbf{y}_{m,n} = \begin{bmatrix} y_{m,n}^{(1)} & y_{m,n}^{(2)} & \cdots & y_{m,n}^{(N_R)} \end{bmatrix}^T, \tag{2.41}$$

$$\mathbf{H}_m = \begin{bmatrix} H_m^{(1,1)} & H_m^{(1,2)} & \cdots & H_m^{(1,N_T)} \\ H_m^{(2,1)} & H_m^{(2,2)} & \cdots & H_m^{(2,N_T)} \\ \vdots & \vdots & \ddots & \vdots \\ H_m^{(N_R,1)} & H_m^{(N_R,2)} & \cdots & H_m^{(N_R,N_T)} \end{bmatrix}, \tag{2.42}$$

$$\mathbf{a}_{m,n} = \begin{bmatrix} a_{m,n}^{(1)} & a_{m,n}^{(2)} & \cdots & a_{m,n}^{(N_T)} \end{bmatrix}^T, \tag{2.43}$$

$$\hat{\mathbf{a}}_{m,n} = \begin{bmatrix} \hat{a}_{m,n}^{(1)} & \hat{a}_{m,n}^{(2)} & \cdots & \hat{a}_{m,n}^{(N_T)} \end{bmatrix}^T, \tag{2.44}$$

and

$$\boldsymbol{\eta}_{m,n} = \begin{bmatrix} \eta_{m,n}^{(1)} & \eta_{m,n}^{(2)} & \cdots & \eta_{m,n}^{(N_R)} \end{bmatrix}^T. \tag{2.45}$$

Also, the entries of $\mathbf{H}_m$ are

$$H_m^{(i,l)} = \sum_{\ell=0}^{\infty} h^{(i,l)}[\ell] e^{-j\frac{2\pi}{M}m\ell}. \tag{2.46}$$

Since eq. (2.40) is a classical per subcarrier representation of MIMO systems, there is a vast number of detection techniques that can be deployed in order to retrieve $\mathbf{a}_{m,n}$. For further details on channel estimation, equalization, and detection for MIMO systems, refer to Chapter 4.

2.3.3 An Overview

As pointed out previously, providing a detailed survey on FBMC systems is outside the scope of this work. Furthermore, this work focuses on the design of prototype filters, which will be discussed more carefully throughout the remainder of the text. Thus, Table 2.1 synthesizes relevant references, constituting an essential collection of works recommended for current and future direction in FBMC research.

Table 2.1 A small collection of relevant FBMC references

Topic	Reference	Description
Projects	(VIHOLAINEN et al., 2009)	The Phydias project is devoted to develop FBMC technologies capable of enabling emerging wireless systems with dynamic spectrum access.
	(SCHELLMANN, 2015)	The Metis project aims to develop radio access technologies for 5G. In particular, such project considered FBMC as a possible waveform to be deployed in 5G due to its synchronization and channel spread robustness.
FBMC Basics	(BOROUJENY, 2011) (BOROUJENY, 2014)	Both works provide a complete overview on FBMC systems, highlighting their features, advantages, drawbacks and perspectives of deployment in 5G systems and other wireless systems to come.
	(SIOHAN; LACAILLE, 1999) (SIOHAN et al., 2002)	Classical works that describe very precisely and comprehensibly the FBMC multiplexing scheme. An essential read for FBMC studies.
	(FANG et al., 2013) (WALDHAUSER et al., 2006)	Survey papers that provide a comparison between FBMC, OFDM and other filtered based multicarrier systems.
	(WUNDER et al., 2014)	This paper discusses non-orthogonal waveforms candidates for 5G systems, highlighting requirements to allow a more flexible radio access.
Prototype Filters	(SAHIN et al., 2014)	A solid and comprehensive survey on prototype filters is provided in this work.
	(FLOCH et al., 1995)	Proposition of the Isotropic Orthogonal-Transform Algorithm (IOTA), which is used to create Extended Gaussian Functions (EGF) from Gaussian pulses.
	(SIOHAN; ROCHE, 1998) (SIOHAN; ROCHE, 2000)	A closed form expression is proposed to generate EGF instead of using the IOTA.
	(MARTIN, 1998) (MIRABBASI; MARTIN, 2003) (BELLANGER, 2001)	These works develop prototype filters designed using the frequency sampling technique. The resulting prototype filter presents fast spectrum decay, low sidelobes and near-perfect symbol reconstruction.
	(SLEPIAN; POLLAK, 1961) (LANDAU; POLLAK, 1961) (LANDAU; POLLAK, 1962) (SLEPIAN, 1964) (SLEPIAN, 1978)	This series of paper provides a detailed study on the Prolate Spheroidal Wave Functions and Sequences, which are signals capable of providing the lowest out-of-band energy emission.

Table 2.1 A small collection of relevant FBMC references

Topic	Reference	Description
	(VAHLIN; HOLTE, 1994) (VAHLIN; HOLTE, 1996)	Aiming to provide near-perfect symbol reconstruction and desirable spectrum features, the Optimal Finite Duration Pulse prototype filter is derived by using discrete spheroidal wave sequences.
	(HAAS; BELFIORE, 1997) (PRAKASH; REDDY, 2013)	Prototype filter options created from Hermite polynomials.
Channel Equalization	(IHALAINEN et al., 2011)	A multi-tap channel equalizer is proposed using the frequency-sampling technique, which enables subcarriers to be equalized independently in a low rate. Such design incorporates the usage of MIMO systems, whereas the ZF and the MMSE solutions are provided. This paper basically can be considered the evolution of (IHALAINEN et al., 2005) and (IHALAINEN et al., 2006)
	(IKHLEF; LOUVEAUX, 2009a)	This work proposes a MMSE channel equalizer for FBMC systems. Such methodology equalizes all subcarriers adjointly in time domain.
	(IKHLEF; LOUVEAUX, 2009b)	An extention of (IKHLEF; LOUVEAUX, 2009a) is presented enabling the equalization in MIMO systems.
	(BALTAR et al., 2009)	A Decision Feedback Equalizer (DFE) using adjacent carrier interference canceling is proposed for FBMC systems.
	(WALDHAUSER et al., 2008a)	The adaptive algorithm Least Mean-Square (LMS) is deployed to equalize FBMC systems. As many works from this author, adjacent carrier interference canceling is applied.
	(WALDHAUSER et al., 2008b)	An MMSE equalizer is developed in frequency domain. In this case, equalization of a given subcarrier takes into account only adjacent subcarriers, differently from (IKHLEF; LOUVEAUX, 2009a), where all subcarriers are equalized adjointly.
	(CHEN; MAEHARA, 2017)	Similar to the equalizer presented in (BALTAR et al., 2009), authors proposed and enhanced MMSE-DFE by adding extra filtering for further subcarrier interference suppression.
	(NDO et al., 2012)	Differently from previous works, the proposed equalizer takes into account the typically discarded imaginary symbol interference in order to improve equalization performance.

Table 2.1 A small collection of relevant FBMC references

Topic	Reference	Description
	(LIN et al., 2005)	Wiener filtering is deployed to equalize FBMC symbols. A study on the effects of the length of the filtering is also provided.
Channel Estimation	(LÉLÉ et al., 2008a)	A channel estimation methodology using scattered pilots is provided.
	(LÉLÉ et al., 2008c)	The Interference Approximation Method and Pair of Pilots channel estimation techniques are proposed.
	(KATSELIS et al., 2011) (KOFIDIS et al., 2013)	A review of preamble-based channel estimators for FBMC systems. This work studies both SISO and MIMO channel estimation for FBMC systems.
	(CUI et al., 2016)	The scattered pilots channel estimation is improved by using coded pilots.
	(ALDABABSEH; JAMOOS, 2014)	Kalman filtering is deployed to estimate channels in FBMC systems.
	(KONG et al., 2014)	Channel estimation on FBMC systems with cyclic prefix is discussed. In this sense, weighted least square and pairs of pilots are extended for CP-FBMC usages.
MIMO-FBMC	(AMINJAVAHERI et al., 2017)	A prototype filter designed for MIMO systems.
	(ROTTENBERG et al., 2017)	A study of MIMO-FBMC systems including Precoding and Decoding techniques.
	(KOFIDIS; KATSELIS, 2011)	Preamble-based channel estimation for MIMO systems operating under V-BLAST.
	(FARHANG et al., 2014)	A survey on MIMO-FBMC systems including Precoding and Decoding techniques.

3 Prototype Filters

This chapter provides a brief study of prototype filters for FBMC systems. Although there is a large number of functions or sequences that can be deployed as prototype filters, few of them stand out in FBMC applications. Thus, this chapter covers the most relevant and well-known prototype filter options for FBMC systems. Additionally, different figures of merit are presented to evaluate and compare the performance between different prototype filters. Hence, this chapter establishes the necessary framework for designing prototype filters for FBMC systems, which will be the subject of the next chapters.

3.1 Figures of Merit

In this section, we present figures of merit to evaluate the performance of prototype filters from different perspectives. Since these metrics are very concise, they are useful for selecting and designing prototype filters. In particular, the parameters herein presented describes the spectrum leakage, time-frequency localization, and reconstruction capabilities of a prototype filter, as shown in the sequel.

3.1.1 Signal-to-Interference Ratio

According to (5.7), the choice of the prototype filter impacts the symbol estimation at the receiver side, as self-interference arises. Hence, considering the scenario depicted in Figure 2.2, the estimated symbols experience a Signal-to-Interference Ratio (SIR) expressed by

$$\mathrm{SIR} = \frac{1}{\sum\limits_{(m,n)\neq(m_0,n_0)} \mathrm{Re}\left\{\langle p_{m,n}[k] \, | p_{m_0,n_0}[k] \rangle\right\}^2}, \tag{3.1}$$

which can be used to quantify the symbol reconstruction quality. Typically, prototype filters are designed to provide a SIR level of dozens of dBs, as can be observed for example in Table II of (MARTIN, 1998). Indeed, there are some other alternatives such as the maximum distortion parameter of Section V of (SIOHAN; LACAILLE, 1999) and the prototype filter noise floor of eq. (4) of (BELLANGER, 2001), which describe the self-interference of the prototype filter similarly to eq. (3.1).

3.1.2 In and Out-of-Band Energy

Another concern that arises when designing prototype filters for multicarrier applications is the amount of energy emitted outside the passband. Low OoB energy emission ensures high energy efficiency and low interference to adjacent bands, which are desirable

features a Cognitive Radio must comply when adapting itself for opportunistic spectrum usage (KUMAR; TYAGI, 2016).

The energy contained within the frequency range $|\omega| \leq \omega_c$ can be defined as

$$E(\omega_c) = \frac{1}{2\pi} \int_{-\omega_c}^{\omega_c} \left| P(e^{j\omega}) \right|^2 d\omega, \tag{3.2}$$

where $P(e^{j\omega})$ is the Discrete-Time Fourier Transform (DTFT) of $p[k]$. Typically, ω_c is set to $1/M$ as it is the subcarrier frequency separation.

More conveniently, eq. (3.2) may be expressed in matrix form, by defining the vector

$$\mathbf{p} = \begin{bmatrix} p[0] & p[1] & \cdots & p[L_p - 1] \end{bmatrix}^T \tag{3.3}$$

and the entries of the matrix $\mathbf{\Gamma}(\omega_c)$ as (VAIDYANATHAN, 1993)

$$[\mathbf{\Gamma}(\omega_c)]_{k,l} = \frac{\omega_c}{\pi} \operatorname{sinc}\left[(k-l) \frac{\omega_c}{\pi} \right]. \tag{3.4}$$

Thus, the In-Band (IB) energy can be evaluated through

$$E(\omega_c) = \mathbf{p}^T \mathbf{\Gamma}(\omega_c) \mathbf{p}, \tag{3.5}$$

while the total energy of the filter can be expressed as

$$E(\pi) = \mathbf{p}^T \mathbf{p} \tag{3.6}$$

and the energy outside the frequency range $|\omega| \leq \omega_c$, or OoB energy, is evaluated by

$$\overline{E}(\omega_c) = \mathbf{p}^T \left[\mathbf{I} - \mathbf{\Gamma}(\omega_c) \right] \mathbf{p}. \tag{3.7}$$

3.1.3 Maximum Sidelobe Level

As suggested by the name, the Maximum Sidelobe Level (MSL) measures the ratio between the maximum sidelobe of $|P(e^{j\omega})|^2$ and the main lobe level, which can be defined as

$$\text{MSL} = \frac{\max\limits_{\omega \in \mathbb{W}} \left| P(e^{j\omega}) \right|^2}{|P(e^{j0}))|^2}, \tag{3.8}$$

where

$$\mathbb{W} = \left\{ \omega \in \mathbb{R} \,\middle|\, \omega > 0, \quad \frac{d}{d\omega} |P(e^{j\omega})|^2 = 0 \right\}. \tag{3.9}$$

This measurement can be used to describe the interference level a system deploying $p[k]$ may generate in adjacent bands.

3.1.4 Heisenberg Factor

As a large amount of telecommunication systems operates under significant time and Doppler spreads, their pulse shaping is expected to be well localized in order to deal with such a harsh environment. Hence, it is highly desirable to deploy prototype filters with low time and frequency spreads, which are defined, respectively, as

$$D_k^2 = \sum_{k=-\infty}^{\infty} \underline{k}^2 \, |p[k]|^2 \tag{3.10}$$

and

$$D_f^2 = \int_{-1/2}^{1/2} f^2 \left| P(e^{j2\pi f}) \right|^2 df. \tag{3.11}$$

For convenience, let us also define

$$D_\tau = T_s D_k \tag{3.12}$$

and

$$D_\nu = \frac{D_f}{T_s} \tag{3.13}$$

as the time and frequency spreads of the prototype filter normalized by its sampling period.

Unfortunately, a prototype filter cannot be designed to achieve an arbitrary time-frequency localization, as time and frequency spreads are conflicting goals. Indeed, this statement is known as the Heisenberg Uncertainty Principle, described by the inequality (CALVES; VILBE, 1992)

$$0 \leq \xi \leq 1, \tag{3.14}$$

where ξ is the Heisenberg parameter, defined by

$$\xi = \frac{1}{4\pi D_k D_f} = \frac{1}{4\pi D_\tau D_\nu}. \tag{3.15}$$

Notice that well-localized pulses in frequency and time can achieve close to unit ξ, while poorly located pulses may achieve near-null values of ξ. As an example, the optimal pulse in terms of time-frequency concentration is Gaussian with $\xi = 1$, while $\xi = 0$ for a DC waveform.

As an alternative, the pulse concentration can be analyzed graphically via the ambiguity function. Since it is not a figure of merit *per se*, Appendix F offers some background on the ambiguity function to avoid disrupting the content of this chapter. Additionally, Appendix F includes the ambiguity function contour plots of all the prototype filters analyzed in this work.

3.2 Prototype Filters

This section presents popular prototype filters choices. We cover classic filter designs used in communications systems as the Square-Root Raised Cosine (SRRC), passing to

prototype filter designs dedicated for filtered multicarrier systems. Since this work is not intended to be a survey on prototype filters, we provide only prominent filter designs. Some of them have been highlighted as candidates to be deployed in FBMC systems to come, as remarked in (DOHLER; NAKAMURA, 2016). Nevertheless, we can point out some more recent developments on the design of prototype filters, which include the works (PRAKASH; REDDY, 2013) and (AMINJAVAHERI et al., 2017). Furthermore, the survey presented by Sahin et al. (2014) is a reliable and recommended reference that deals almost exclusively with prototype filters.

Since this work focuses on discrete signal processing, prototype filters will be described predominately as discrete signals. Also, in order to corroborate the explanation of the prototype filter designs, their impulse and frequency responses are presented considering $M = 32$, $K = 4$ and $L_p = 129$. Notice that the choice $M = 32$ allows a better spectrum visualization as the passband of the filter lies typically around $1/M$ and the normalized frequency range is $f \in [-1/2, +1/2]$. Moreover, the overlapping factor $K = 4$ is considered an excellent value, as it provides a contained spectrum and a reasonable output latency, defined in eq. (2.12). Finally, by taking $L_p = KM + 1$, one can omit the input delay added to the FBMC receiver, as Δ_β can be set to zero, reducing the complexity of the FBMC receiver marginally. Notice that the discussion and performance comparison of the presented prototype filters is carried out on the next section, as the analysis becomes much more fluid once the filter designs and figures of merit are already defined.

3.2.1 Square-Root Raised Cosine

Typically, the Raised-Cosine (RC) filter is deployed in the transmitter to minimize the ISI by complying with the Nyquist criterion (PROAKIS; MANOLAKIS, 2000). However, as a typical communication link requires filtering at both the transmitter and receiver, it is interesting to split these properties along both communication sides. These features are met by the SRRC, as its squared spectrum coincides with the RC one. By properly sampling and time-shifting the continuous SRRC impulse response becomes (BOROUJENY, 2011)

$$p[k] = \frac{\frac{4r}{M}\underline{k}\cos\left[\frac{\pi(1+r)}{M}\underline{k}\right] + \sin\left[\frac{\pi(1-r)}{M}\underline{k}\right]}{\frac{\pi}{M}\underline{k}\left[1-\left(\frac{4r}{M}\underline{k}\right)^2\right]}, \tag{3.16}$$

where r is the roll-off factor, which is a measure of bandwidth excess.

Figure 3.1 depicts the impulse and frequency responses[1] for SRRCs with roll-off factors of 0.25 and 0.75. As r increases, one can observe the spectrum expanding, while the impulse response shrinks. Notice that, SRRCs are not popular choices for prototype filters in FBMC, as they cannot offer high-performance symbol reconstruction or outstanding

[1]The terms spectrum frequency response are usual terminology. However, the exact term for the spectrum representation used in this chapter is Periodogram, i.e., the squared DTFT of $p[k]$.

spectrum features, even when r is optimized. However, the idea behind the SRRCs have inspired the use of Nyquist ISI criteria in other prototype filters design.

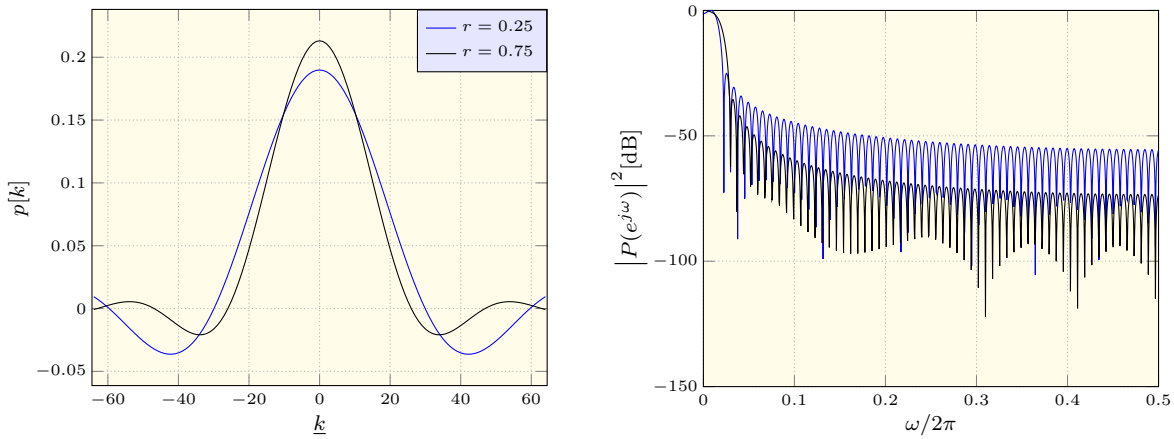

(a) Impulse Response **(b)** Frequency Response

Figure 3.1 SRRC prototype filter ($K = 4$, $M = 32$, and $L_p = 129$)

3.2.2 Gaussian Function

Gaussian functions are among the most critical functions in science. They are deployed in different fields such as quantum mechanics, filtering in signal processing and most notably in statistics. Concerning their usage as a prototype filter, let us present the continuous Gaussian function as

$$g_\alpha(t) = (2\alpha)^{1/4} e^{-\pi\alpha t^2}, \tag{3.17}$$

where α is the spreading factor. In terms of spectrum analysis, Gaussian functions preserve their form in both frequency and time domains, as the Fourier transform of $g_\alpha(t)$ yields another Gaussian function. Hence, Gaussian functions are capable of delivering an isotropic time-frequency response if $\alpha = 1$. Despite being elementary, Gaussian functions are not deployed as prototype filters in FBMC systems as they do not take into account the operational requirements of such systems. Nevertheless, it is essential to present the Gaussian functions as they are the basis of other prototype filters.

Figure 3.2 depicts the frequency and impulse responses for Gaussian prototype filters with three different spreading factors. Noticeably, the bell-shape of the frequency response cannot be observed due to the log scale of the plot. Also, the sidelobes and the frequency response floor show up due to windowing effects. As the spreading factor increases, the Gaussian pulse becomes narrower, while the spectrum expands throughout the frequency domain.

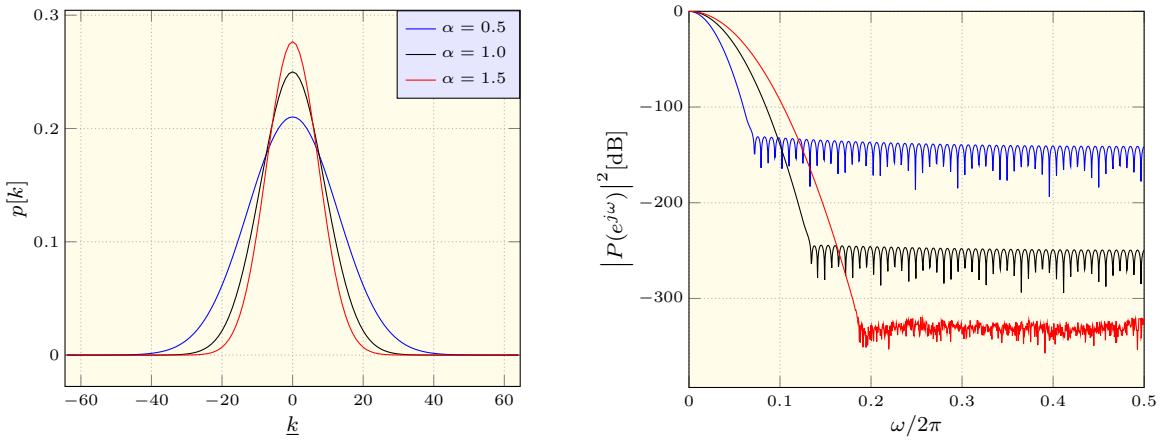

(a) Impulse Response **(b)** Frequency Response

Figure 3.2 Gaussian prototype filter ($K = 4$, $M = 32$, and $L_p = 129$)

3.2.3 Extended Gaussian Function

Originally, the Extended Gaussian Function (EGF) was designed to be generated by deploying the Isotropic Orthogonal Transform Algorithm (IOTA) (FLOCH et al., 1995)

$$\mathcal{O}_a\left\{x(t)\right\} = \frac{x(t)}{\sum_{i=-\infty}^{\infty} \left|x(t-ai)\right|^2} \tag{3.18}$$

on a Gaussian function in both time and frequency domains. The IOTA is a transformation capable of creating orthogonal pulses, as proved in Appendix C. Hence, the continuous representation for EGF is

$$p(t) = \mathcal{F}^{-1}\left\{\mathcal{O}_{\tau_0}\left\{\mathcal{F}\left\{\mathcal{O}_{\nu_0}\left\{g_\alpha(t)\right\}\right\}\right\}\right\}, \tag{3.19}$$

where $\mathcal{F}\{\cdot\}$ is the Fourier transform operator, τ_0 is the signaling interval and ν_0 is the subcarrier spacing, which must comply with $\tau_0\nu_0 = 1/2$ for FBMC systems. In order to obtain the discrete version of an EGF, one can sample it properly. Fortunately, an analytic expression for (3.19) is provided in eq. (3) of (SIOHAN; ROCHE, 1998):

$$\begin{aligned} p[k] = \frac{1}{2}\sum_{\ell=1}^{\ell_k} \overline{d}_{\ell,\alpha,\nu_0} \left[e^{-\pi\alpha\left(\frac{2\tau_0}{M}-\frac{\ell}{\nu_0}\right)^2} + e^{-\pi\alpha\left(\frac{2\tau_0}{M}+\frac{\ell}{\nu_0}\right)^2} \right] \\ \times \sum_{m=1}^{m_k} \overline{d}_{m,\frac{1}{\alpha},\nu_0} \cos\left(2\pi m \frac{k}{\tau_0}\right), \end{aligned} \tag{3.20}$$

where the values $\overline{d}_{m,\frac{1}{\alpha},\nu_0}$ are available in Table A.1 of (SIOHAN; ROCHE, 2000). Despite being an approximation, authors claim that the proposed formula is capable of achieving an accuracy of 10^{-19}, which goes beyond the machine epsilon of a double data type, *i.e.*, $\approx 10^{-16}$.

Figure 3.3 exemplifies EGFs with the preset introduced previously. By comparing Figures 3.3 and 3.2, one can observe that the IOTA changes the Gaussian waveforms

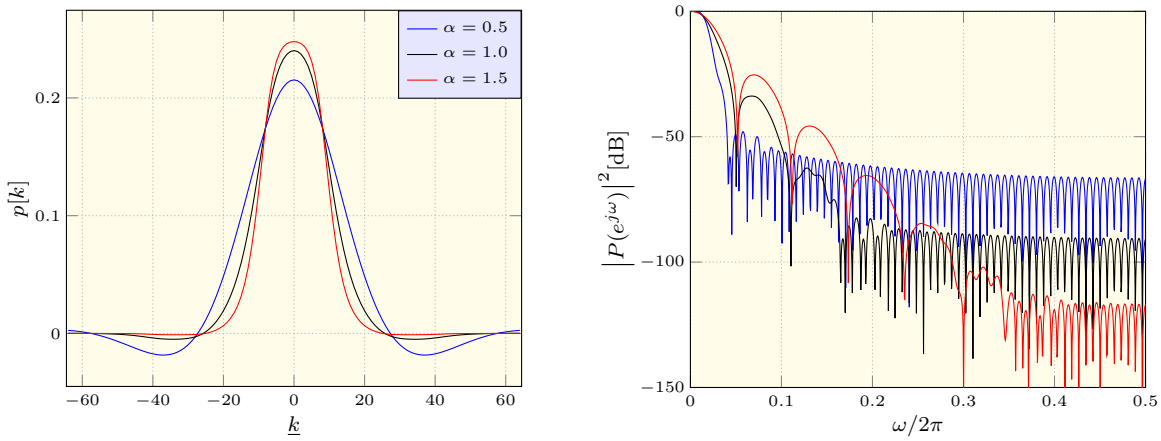

(a) Impulse Response **(b)** Frequency Response

Figure 3.3 EGF prototype filter ($K = 4$, $M = 32$, and $L_p = 129$)

dramatically in both time and frequency domains. The passband is reduced considerably, approaching $1/M$, *i.e.*, the normalized frequency separation between adjacent subcarriers. Still, EGFs offer neither low OoB emission nor fast spectrum decay compared to other prototype filters. However, by tuning α, one can control the trade-off between reconstruction and spectrum features.

3.2.4 Hermite Filter Prototype Filter

The Hermite filter was proposed by Haas and Belfiore (1997) and is composed by a superposition of normalized Hermite functions, defined in Appendix D.2. This prototype filter can be defined as

$$p(t) = \sum_{\ell=0}^{N_H-1} H_{4\ell}\mathcal{H}_{4\ell}(t) \tag{3.21}$$

where $H_{4\ell}$ are the filter weights and $\mathcal{H}_{4\ell}(t)$ is the Hermite function. Since Hermite functions are orthogonal, they are proper for building the prototype filter through superposition. Despite being defined as a continuous function, one can easily sample eq. (3.21) to obtain the discrete representation.

In contrast to other methods, the Hermite prototype filter is designed based on the ambiguity function of eq. (3.21), which can be expressed by

$$\begin{aligned} A(\tau,\nu) = \sum_{\ell=0}^{N_H-1} H_{4\ell}^2 A_{4\ell,4\ell}(\tau,\nu) + \sum_{\ell=0}^{N_H-2}\sum_{i=\ell+1}^{N_H-1} H_{4\ell}H_{4i}\Big[&\mathrm{Re}\left\{A_{4\ell,4i}(\tau,\nu)\right\}\left(1-e^{j2\pi\nu\tau}\right) \\ &+ j\mathrm{Im}\left\{A_{4\ell,4i}(\tau,\nu)\right\}\left(1+e^{j2\pi\nu\tau}\right)\Big], \end{aligned} \tag{3.22}$$

where

$$A_{m,n}(\tau,\nu) = 2^{\frac{m+n-1}{2}}\pi^{\frac{m-n}{2}} n! e^{-\frac{\pi}{2}(\tau^2+\nu^2)}(\tau+j\nu)^{m-n} e^{j\pi\tau\nu} L_n^{(m-n)}\left[\pi\left(\tau^2+\nu^2\right)\right] \tag{3.23}$$

is the cross ambiguity function of two Hermite functions and $L_\ell^{(i)}(x)$ denotes the generalized Laguerre polynomial, defined in Appendix D.3.

In order to satisfy orthogonality between adjacent channels, the Hermite prototype filter requires the following constraints:

$$\begin{cases} A(0,0) & = 1 \\ A(\sqrt{2},0) & = 0 \\ A(\sqrt{2},\sqrt{2}) & = 0 \\ A(2\sqrt{2},0) & = 0 \\ A(2\sqrt{2},\sqrt{2}) & = 0 \end{cases}. \tag{3.24}$$

Since the set of constraints in eq. (3.24) is symmetric in time and frequency, the ambiguity function of the resulting filter is expected to be isotropic, as shown in Figure F.4.

By solving the non-linear system in eq. (3.24), the prototype filter weights $H_{4\ell}$ can be obtained. Indeed, Haas and Belfiore (1997) originally solved eq. (3.24) considering the superposition of $N_H = 5$ Hermite functions, resulting in the weights presented in Table A.2.

Despite imposing stringent orthogonality constraints that lead to a high symbol reconstruction performance, the Hermite design does not take into account spectrum concerns. Hence, spectrum containment is not expected to be among the best options. Furthermore, one can observe that the Hermite design is similar to the EGF but much less flexible as spectrum features can still be tuned by α.

Figure 3.4 depicts both the impulse and frequency response of the Hermite design. Notice that the impulse response of the Hermite filter is similar to the EGF with $\alpha = 1$. However, the Hermite filter presents a slightly superior frequency response performance, which is as expected since the EGF deploys the IOTA procedure, while the Hermite filter is bound by ambiguity constraints, which are used to define lower frequency and time spreads.

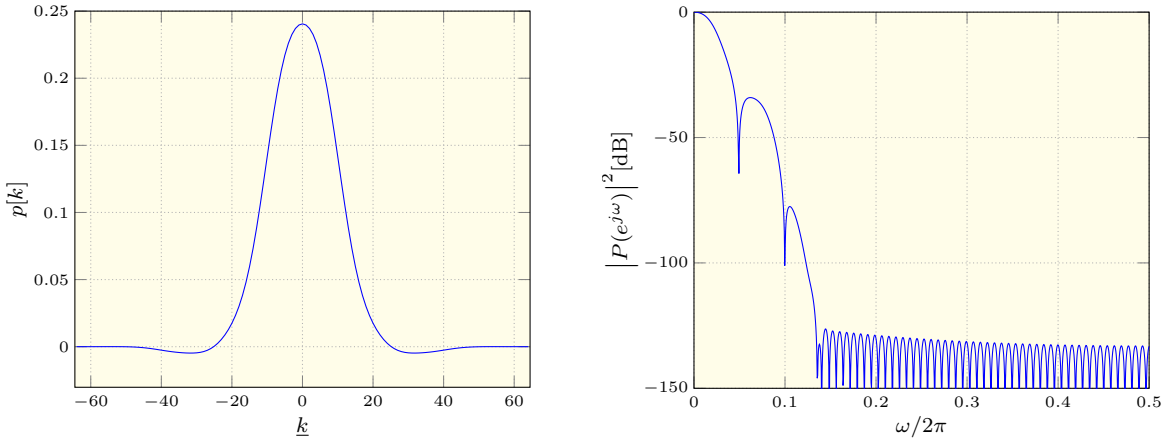

(a) Impulse Response **(b)** Frequency Response

Figure 3.4 Hermite prototype filter ($K = 4$, $M = 32$, and $L_p = 129$)

3.2.5 Mirabbasi-Martin Prototype Filter

To ensure fast spectrum decay throughout the stopband region, the Mirabbasi-Martin prototype filter (MARTIN, 1998) focuses on minimizing the discontinuity in their boundaries, while maintaining desirable reconstruction features for multicarrier applications and ensuring a smooth pulse variation. This design uses the frequency sampling technique, where the filter weights are samples of the frequency response of the prototype filter (BELORUTSKY; SAVINYKH, 2016). Such a methodology is also adopted in window projects, *e.g.,* Hamming and Blackman. Nonetheless, these pulses are not optimized for multicarrier applications.

Due to its fast spectrum decay and high performance for data reconstruction, Mirabbasi-Martin prototype becomes the primary choice for the Phydias project (VIHOLAINEN et al., 2009), which aims to enable FBMC applications in wireless systems to come. Indeed, such a filter is also known as the PHYDIAS filter when $K = 4$. Curiously, both Martin and Bellanger have achieved the same design, with the same filter coefficients, as can be observed in Section V of (BELLANGER, 2001) and in Table I of (MARTIN, 1998). The Mirabbasi-Martin prototype filter can be written as

$$p[k] = k_0 + 2\sum_{\ell=1}^{K-1} k_\ell \cos\left(\frac{2\pi\ell}{KM}k\right), \tag{3.25}$$

where the coefficients k_ℓ are available in Table A.3.

Figure 3.5 depicts the impulse and frequency response of the Mirabbasi-Martin design. One of the most remarkable features of Mirabbasi-Martin design is its very fast spectrum decay and low-level sidelobes. Hence, such filter is one of, if not the, most widespread prototype filter for FBMC systems.

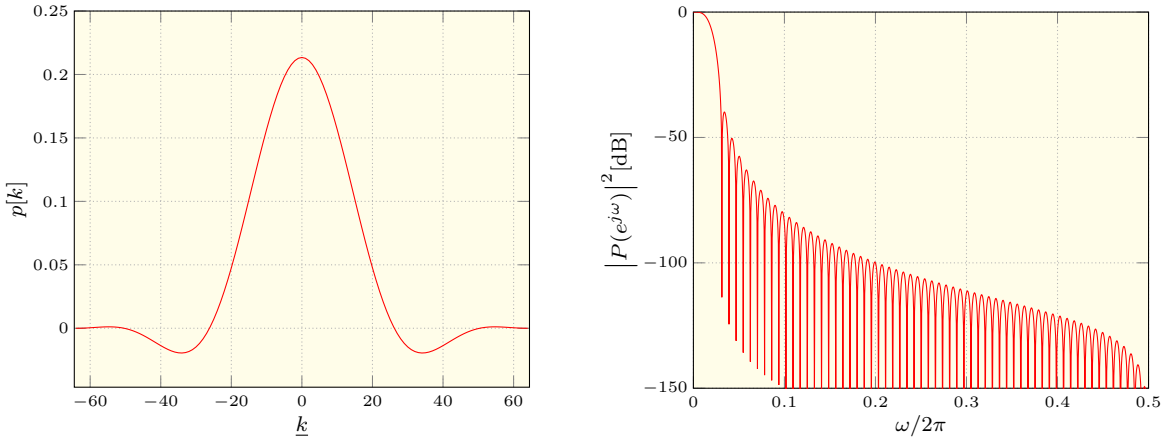

(a) Impulse Response **(b)** Frequency Response

Figure 3.5 Mirabbasi-Martin prototype filter ($K = 4$, $M = 32$, and $L_p = 129$)

3.2.6 Discrete Prolate Spheroidal Sequences

The Prolate filter is a classic design that aims to maximize the energy within its passband region. This design can be expressed by the following optimization problem:

$$\begin{aligned} \boldsymbol{\psi}_{0,\omega_s} = \underset{\mathbf{p}}{\text{argmax}} \quad & \mathbf{p}^H \boldsymbol{\Gamma}(\omega_s)\mathbf{p} \\ \text{s.t.} \quad & \mathbf{p}^H\mathbf{p} = 1. \end{aligned} \tag{3.26}$$

Since $\boldsymbol{\Gamma}(\omega_s)$ is symmetric, a straightforward solution comes by recalling the Rayleigh-Ritz Theorem (HORN; JOHNSON, 1985), which guarantees the solution of (3.26) to be the eigenvector associated with the largest eigenvalue of $\boldsymbol{\Gamma}(\omega_s)$. By denoting $\gamma_0 \geq \gamma_1 \geq \cdots \geq \gamma_{L_p-1} > 0$ the eigenvalues of $\boldsymbol{\Gamma}(\omega_s)$, and $\boldsymbol{\psi}_{i,\omega_s}$ the eigenvector associated to γ_i, the solution of (3.26) is

$$\boldsymbol{\psi}_{0,\omega_s} = \begin{bmatrix} \psi_{0,\omega_s}[0] & \psi_{0,\omega_s}[1] & \cdots & \psi_{0,\omega_s}[L_p-1] \end{bmatrix}^T. \tag{3.27}$$

Physically, γ_i represents the energy of $\psi_{i,\omega_s}[k]$ within $|\omega| \leq \omega_c$, thus

$$0 \leq \gamma_i \leq 1. \tag{3.28}$$

Consequently, the sequence $\psi_{0,\omega_s}[k]$ is the most selective filter for (3.26). It is also noteworthy mentioning that, the remaining filters $\psi_{i,\omega_s}[k]$ are local optima, possessing less energy within their passband than $\psi_{0,\omega_s}[k]$. Indeed, the orthogonal family $\psi_{i,\omega_s}[k]$ is also known as the Discrete Prolate Spheroidal Sequences (DPSS) or the Slepian series (SLEPIAN, 1978). Interestingly, the Slepian series is an excellent choice to interpolate smooth functions [2], making it suitable for low OoB energy emission.

Figure 3.6 illustrates the impulse and frequency response of DPSSs with $\omega_s = 2\pi/M$. Due to the IB energy maximization goal, one can observe that the spectrum of $\psi_{0,\omega_s}[k]$ decays very abruptly around $1/M$. Also, $\psi_{0,\omega_s}[k]$ resembles a Gaussian function, which leads to near-optimal ξ. Notice that the sequences ψ_{i,ω_s}, with $i \neq 0$, cannot be deployed as prototype filters in FBMC systems as they are not low pass filters. However, the complete Slepian set may be used to design other prototype filters, as discussed in the next subsection.

3.2.7 Optimal Finite-Duration Pulse

As stated previously, the Prolate design is optimal in terms of minimizing the energy outside the passband. However, symbol reconstruction requirements are not taken into account in this design. From this perspective, (VAHLIN; HOLTE, 1994) propose the OFDP design by deploying the Slepian sequence to provide a filter with low OoB emission and competent symbol reconstruction capability. The OFDP can be written as

$$p[k] = \sum_i \alpha_{2i}\psi_{2i,2\pi/M}[k], \tag{3.29}$$

[2] refer to table 2 of (C.MOORE; CADA, 2004)

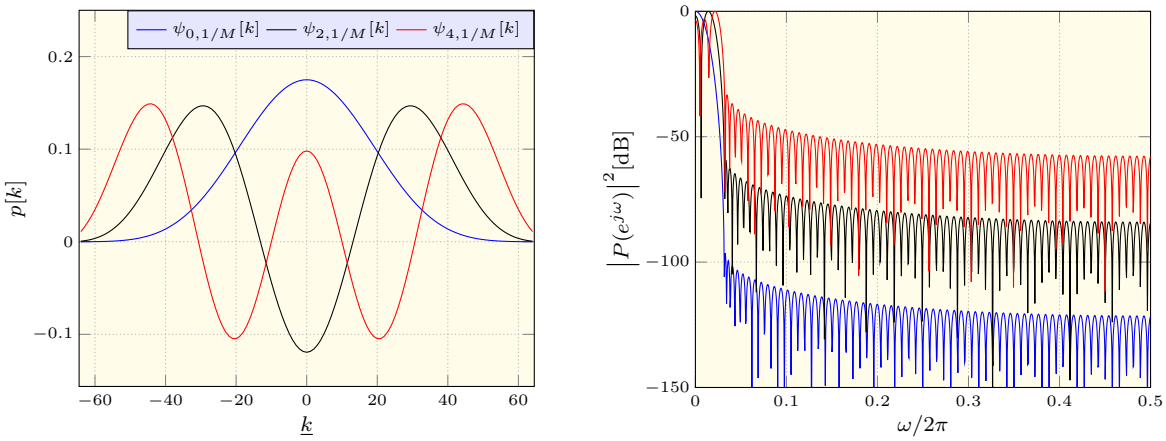

(a) Impulse Response **(b)** Frequency Response

Figure 3.6 DPSS prototype filter ($K = 4$, $M = 32$, and $L_p = 129$)

where the coefficients α_{2i} can be found in Table A.4. Since the IB energy of $\psi_{2i,2\pi/M}$, *i.e.*, γ_{2i}, decays at a high rate as can be observed in Figures 3 and 4 of (SLEPIAN, 1978), truncation on α_{2i} is acceptable for solving the problem.

Both the impulse and frequency responses of the OFDP prototype filter are presented in Figure 3.7. After combining several DPSSs, the OFDP spectrum displays inferior spectrum compared to the generator sequences. Nevertheless, since the OFDP accounts for symbol reconstruction constraints, it delivers a far better symbol estimation, as will become clear in the next section. The OFDP design also displays a more contained spectrum than the EGF and the SRRC. However, the Mirabbasi-Martin prototype filter still overperforms the OFDP, as the former presents a far faster spectrum decay.

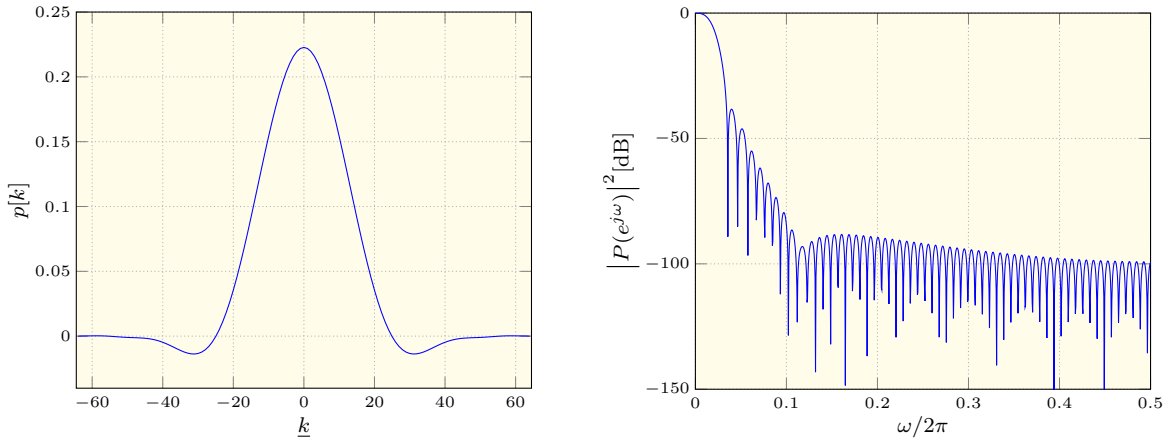

(a) Impulse Response **(b)** Frequency Response

Figure 3.7 OFDP prototype filter ($K = 4$, $M = 32$, and $L_p = 129$)

3.2.8 Window-Based Designs

The idea behind window-based designs is the combination of a truncated sinc filter and a window to compose a prototype filter. The sinc filter delivers a near-rectangular

frequency response due to truncation effects. On the other hand, windows are classically used in Fourier spectral analysis as a mean to control the trade-off between the sidelobe levels and the main lobe spread (HARRIS, 1978). In this sense, the window-based prototype filter can be described as (VIHOLAINEN et al., 2009)

$$p[k] = w[k]\,\mathrm{sinc}\left[\frac{\omega_c}{\pi}\underline{k}\right], \tag{3.30}$$

where ω_c is the cutoff frequency of the filter and $w[k]$ is the window. Popular windows are the rectangular, triangular or Bartlett, Hanning, Hamming and Kaiser. Since this work will not discuss all available windows in literature, we recommend Chapter 7 of (POULARIKAS, 1998) as a consulting material that covers a large number of windows. Nevertheless, Table 3.1 offer windows that can be deployed to build different prototype filters via the window-based design. Notice that, in Table 3.1, υ is the window parameter and $I_0(x)$ is the 0th order modified Bessel Function.

Table 3.1 Window examples

Window type	**Expression**
Rectangular	$w[k] = 1$
Triangular	$w[k] = 1 - 2\dfrac{\lvert\underline{k}\rvert}{L_p}$
Parabolic	$w[k] = 1 - \left(2\dfrac{\underline{k}}{L_p}\right)^2$
Hann	$w[k] = \dfrac{1}{2}\left[1 + \cos\left(\dfrac{2\pi}{L_p}\underline{k}\right)\right]$
Hamming	$w[k] = 0.54 - 0.46\cos\left(\dfrac{2\pi}{L_p}\underline{k}\right)$
Blackman	$w[k] = 0.42 + 0.50\cos\left(\dfrac{2\pi}{L_p}\underline{k}\right) + 0.08\cos\left(\dfrac{4\pi}{L_p}\underline{k}\right)$
Riemann	$w[k] = \mathrm{sinc}\left(\dfrac{2}{L_p}\underline{k}\right)$
Poisson	$w[k] = \exp\left(-\dfrac{2\upsilon}{L_p}\underline{k}\right)$
Hann-Poisson	$w[k] = \dfrac{1}{2}\left[1 + \cos\left(\dfrac{2\pi}{L_p}\underline{k}\right)\right]\exp\left(-\dfrac{2\upsilon}{L_p}\underline{k}\right)$
Cauchy	$w[k] = \dfrac{1}{1 + \left(\dfrac{2\upsilon}{L_p}\underline{k}\right)^2}$
Gaussian	$w[k] = \exp\left[-\dfrac{1}{2}\left(\dfrac{2\upsilon}{L_p}\underline{k}\right)^2\right]$
Kaiser	$w[k] = \dfrac{1}{I_0(\pi\upsilon)} I_0\left[\pi\upsilon\sqrt{1 - \left(\dfrac{2}{L_p}\underline{k}\right)^2}\right]$

Tuckey	$w[k] = \begin{cases} 1, & \lvert\underline{k}\rvert \leq L_p/2 \\ \frac{1}{2}\left[1+\cos\left(\pi\frac{\underline{k}-\upsilon L_p/2}{(1-\upsilon)L_p/2}\right)\right], & \text{otherwise} \end{cases}$

It is noteworthy mentioning that eq. (3.30) cannot be deployed plainly, as ω_c should be optimized in order to meet FBMC requirements. Hence, a line search to determine the most suitable ω_c can be carried out in order to provide a filter with high reconstruction features or low sidelobes, for example. Notice however that some window designs will require the optimization of an extra parameter, which is the case of Kaiser windows.

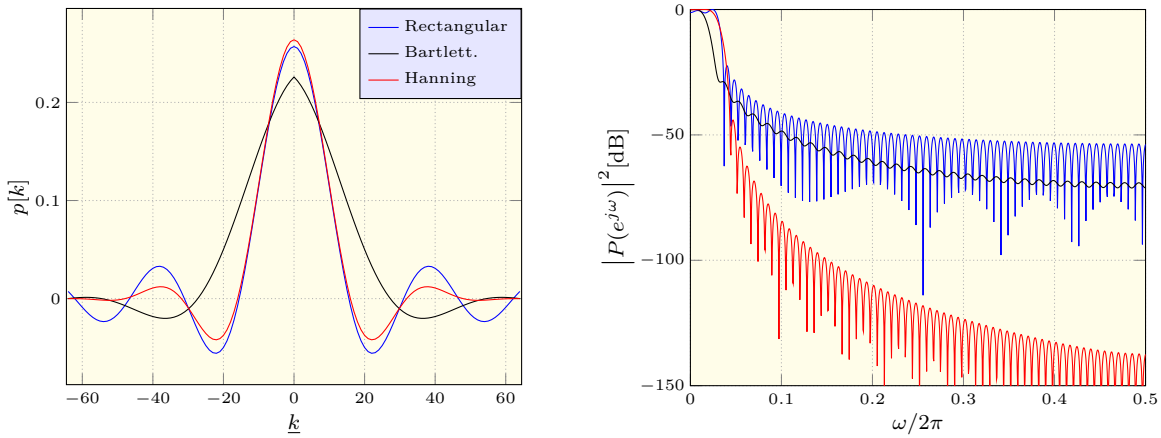

(a) Impulse Response **(b)** Frequency Response

Figure 3.8 Windowed prototype filters ($K = 4$, $M = 32$, and $L_p = 129$)

3.3 Performance Comparison

With the prototype filters and figures of merit presented, let us proceed with a discussion/comparison between the filter designs presented in this Chapter. In this sense, Table 3.2 presents all the aforementioned prototype filter and their respective performance, according to the figures of merit presented in this chapter. In order to complement the analysis herein conducted, Appendix G offers an alternative graphical representation of Table 3.2, which should yield a more intuitive analysis.

In terms of SIR, the EGF, Hermite, OFDP, and Mirabbasi-Martin designs display a reliable performance. Interestingly, one can tune the spreading factor of the EGF in order to control its SIR, making such designs very popular, especially in works that discuss channel estimation in FBMC systems. Other prototype filters present a considerably lower performance, making them unreliable choices for FBMC systems.

Concerning the MSL, one can observe that the Gaussian function and the DPSSs can offer low sidelobe levels. Although such filters present desirable spectrum performance,

they cannot deliver high SIR levels. Thus, Gaussian and DPSSs are considered impractical for FBMC multiplexing. Furthermore, the sidelobes of the Gaussian prototype filters only arise due to truncation effects.

The OoB energy $\overline{E}(1/M)$ is a distinct feature of both DPSSs and Mirabbasi-Martin designs. DPSSs offer low OoB energy emission for obvious reasons, as they are optimized for such purpose. On the other hand, the design proposed by Mirabbasi and Martin (2003) imposes fast spectrum decays for frequencies beyond $1/M$, leading to reasonable low OoB emissions. Curiously, OFDP shows an inferior OoB performance, even deploying DPSSs, which are, technically, the optimal sequences in terms of OoB.

Gaussian function, EGF, and Hermite prototype filter and DPSS0 present near-optimal pulse localization, as presented in Table 3.2. However, OFDP and Martin designs still offer reasonable pulse localization. Noticeably, the DPSS0 displays a near-unity ξ, as its pulse shape resembles a Gaussian function.

It is also noteworthy mentioning that the Hermite prototype filter is similar to the EGF with $\alpha = 1$, as both present isotropic responses and comparable performance. However, EGF is a more flexible design as one can control the SIR level and the spectrum of prototype filter by tuning α.

Table 3.2 Performance comparison of different Prototype Filter

Prototype	SIR[dB]	MSL[dB]	$\overline{E}(1/M)$[dB]	ξ	D_τ	D_ν
SRRC $r = 0.25$	17.5547	−25.0921	−31.7994	0.64680	0.57482	0.21404
SRRC $r = 0.75$	31.9021	−35.5074	−40.7018	0.86452	0.39284	0.23432
Gaussian $\alpha = 0.5$	10.6439	−131.061	−34.0588	1.00000	0.39894	0.19947
Gaussian $\alpha = 1.0$	21.2614	−245.060	−19.1404	1.00000	0.28209	0.28209
Gaussian $\alpha = 1.5$	10.6291	−303.104	−11.1737	1.00000	0.19947	0.39894
EGF $\alpha = 0.5$	33.7097	−58.208	−33.9538	0.87809	0.39618	0.22875
EGF $\alpha = 1.0$	60.4696	−33.8005	−19.6972	0.97697	0.2854	0.28541
EGF $\alpha = 1.5$	87.6698	−25.337	−14.7721	0.93878	0.24516	0.34576
Hermite	80.6075	34.0765	−20.1922	0.97965	0.2850	0.2850
DPSS0	3.85353	−96.4343	−96.3026	0.99853	0.56716	0.14051
DPSS2	1.45332	−59.2371	−60.0297	0.19888	1.2705	0.31494
DPSS4	3.50401	−33.3621	−33.0074	0.10804	1.7168	0.42903
OFDP	59.8554	−38.3323	−35.4478	0.93352	0.34659	0.24595
Martin	65.2550	−39.8603	−45.6141	0.88389	0.3882	0.23192
Rectangular	15.7067	−22.4116	−16.7218	0.43412	0.44382	0.41302
Bartlett	27.7637	−28.7543	−29.4394	0.86902	0.39518	0.23172
Hamming	16.5366	−44.0683	−15.9394	0.71223	0.29251	0.38197

In order to complement the numerical results herein presented, readers can refer to the Appendices for supplementary numerical results. Appendix F presents the ambiguity function plots of the prototype filters presented throughout this work. Additionally, Appendix G presents spider plots of the performance of the prototype filters studied in this work.

3.4 Conclusions

Through the analysis of Table 3.2, we can conclude that the EGF, Hermite, Martin, and OFDP designs are the most promising designs to be deployed in FBMC systems. Indeed, the same conclusion has been widely widespread throughout other works, since they are the predominant prototype filters deployed in FBMC systems. Unfortunately, pure DPSSs offer outstanding spectrum features that outperform other prototype filters, but it lacks SIR performance, compromising its reliability considerably. From this perspective, Chapters 5 and 6 are devoted to the design of prototype filters capable of achieving superior performance compared to those found in the literature.

4 Channel Estimation and Equalization

Since wireless channels can affect the received signal considerably, extra processing is demanded to deal with this effect. From this perspective, this chapter focuses on signal processing techniques to overcome such issue, *i.e.*, channel estimation and equalization. Notice that channel estimation alone does not compensate the channel effect *per se*, but it is a requirement to execute channel equalization and symbol detection. Since wireless channels distort the transmitted signal differently in each frequency, proper frequency compensation must be performed to enable symbol reconstruction at the receiver side. Thus, this chapter presents a brief introduction of both channel estimation and equalization techniques for FBMC systems, considering SISO and MIMO structures.

4.1 Channel Estimation

Channel estimation plays an important role when reconstructing a message transmitted through a wireless channel. In the presence of fading, channel frequency response distorts the transmitted data, requiring channel compensation, *i.e.*, equalization at the receiver. Thus, the receiver requires the knowledge of the Channel State Information (CSI) to design a proper equalization in order to retrieve the transmitted data. By distributing data through different subchannels, multicarrier systems can be designed to make each subchannel frequency flat, making equalization considerably easier. Hence, multicarrier systems can deploy single-tap equalizers, also making channel estimation easier, as only one channel coefficient must be estimated for each subcarrier.

Since OFDM is an orthogonal scheme, channel estimation is straightforward as each subcarrier frequency response can be estimated as proceeded in single carrier transmission. In short, the transmitter sends a pilot sequence known by the receiver and, at the receiver side, the signal is divided by its respective pilot, generating the channel estimate. Unfortunately, OFDM channel estimation techniques cannot be deployed directly in FBMC systems. Since FBMC is orthogonal only in the real field, intrinsic imaginary interference is expected and must be appropriately dealt with for a successful channel estimation.

Generally speaking, channel estimation for FBMC systems can be categorized into two main groups: preamble-based and scattered-based estimation. As the name suggests, preamble-based channel estimation deploys a pilot preamble at the beginning of each transmission frame to enable channel estimation. Many authors have proposed different preamble-based methods aiming to reduce the interference and or the length of the preamble. For example, Lélé et al. (2008a) deploys guard symbols to protect the pilot

symbols from imaginary interference, whereas (AMINI; FARHANG-BOROUJENY, 2010; SAEEDI-SOURCK et al., 2013) aim to reduce intrinsic imaginary interference by inserting null pilot-symbols. As an alternative, scattered-pilot channel estimation mixes pilots with data symbols throughout a transmission frame. The most straightforward option to reduce interference generated by scattered-pilots is disabling the data symbols surrounding pilot symbols. Indeed, such an approach is a poor choice since spectral efficiency is considerably compromised. From this perspective, Stitz et al. (2010) proposes the Auxiliary Pilot method. This method deploys a dummy symbol in an adjacent position to the pilot, aiming to cancel its imaginary interference. Another scattered-pilot approach is developed by Lélé et al. (2008c), in which pilots are surrounded by data symbols coded in such a manner to reduce the interference experienced by the pilot symbol. A more sophisticated approach is proposed by Cui et al. (2016), which combines auxiliary pilots with the coding methodology proposed by Lélé et al. (2008c) and is known as the Coded Auxiliary Pilot channel estimation.

Despite the large number of options, FBMC channel estimators can be overperformed by their OFDM counterparts. Aiming to overcome the imaginary interference, FBMC channel estimators are prone to suffer from performance losses. For example, the usage of auxiliary pilots increases the power required to transmit pilots and dummy symbols. Moreover, depending on the prototype filter, coded scattered-pilots can demand large code matrices to mitigate the interference, increasing the computational complexity dramatically. As a final example, the deployment of long guard periods can jeopardize spectral efficiency.

From this perspective, this section discusses the most classical preamble-based channel estimators for FBMC systems, *i.e.*, POP and IAM. Initially, preamble-based channel estimators are presented for SISO systems and are extended for MIMO usage in the sequel. Since this is not the main topic of the work, this chapter does not intend to offer an in-depth survey on FBMC channel estimators. Hence, this section introduces the basic idea behind FBMC channel estimation, which is primordial for understanding the overall operation of FBMC systems.

4.1.1 Pilot Transmission and Imaginary Interference

In order to discuss channel estimation methods for FBMC systems, let us first discuss how pilots are transmitted and how imaginary interference takes place at the receiver side. Notice that such a discussion is primordial for understanding how each channel estimation works and how they behave.

4.1.1.1 Pilot Transmission

First, recall the multiplexed FBMC signal described in eq. (2.8), *i.e.*,

$$s[k] = \sum_{n=-\infty}^{\infty} \sum_{m=0}^{M-1} b_{m,n} p_{m,n}[k], \tag{4.1}$$

where $b_{m,n}$ is the pilot symbol for the mth subcarrier of the nth time-slot. By correlating the received signal $s[k]$ with the pulse $p_{m_0,n_0}[k]$, we can retrieve b_{m_0,n_0}:

$$\langle s[k], p_{m_0,n_0}[k] \rangle = b_{m_0,n_0} + \sum_{(m,n)\neq(m_0,n_0)} b_{m,n} \langle p_{m,n}[k], p_{m_0,n_0}[k] \rangle . \tag{4.2}$$

Up to this point, attention was concentrated only on the FBMC multiplexing. However, the channel effect can affect the overall signal considerably at the reception if the channel is frequency-selective. Thus, by adding the channel effect into eq. (4.1), the received signal is given by

$$x[k] = \sum_{\ell} h[\ell] s[k-\ell] + \eta[k], \tag{4.3}$$

where $h[\ell]$ is the channel frequency response of the mth subcarrier and $\eta[k]$ is the additive noise. For simplicity, consider that each subchannel is time-invariant and frequency-flat. Thus, eq. (4.3) can be rewritten as

$$x[k] = \sum_{n=-\infty}^{\infty} \sum_{m=0}^{M-1} H_m b_{m,n} p_{m,n}[k], + \eta[k], \tag{4.4}$$

where

$$H_m = \sum_{\ell} h[\ell] e^{-j\frac{2\pi}{M} m\ell} \tag{4.5}$$

is the frequency response of the mth subcarrier. Despite $x[k]$ representing the overall received signal, it is far more useful and efficient to process the received signal at a lower rate. In order to obtain the received signal at a lower rate, one can deploy an analysis filter bank, which outputs

$$y_{m_0,n_0} = \langle x[k], p_{m_0,n_0}[k] \rangle \tag{4.6}$$

for the m_0th subcarrier of the n_0th time-slot.

4.1.1.2 Imaginary interference

As one can observe in eq. (4.2), both real and imaginary interference takes place when the receiver reconstructs the pilot sequence. However, real interference is negligible with the deployment of prototype filters with high SIR levels. On the other hand, imaginary interference is intrinsic, and its level is much higher than real interference. Thus, by ignoring the real self-interference of eq. (4.2), the following approximation can be derived:

$$\langle s[k], p_{m_0,n_0}[k] \rangle \approx b_{m_0,n_0} + j\hat{b}_{m_0,n_0}, \tag{4.7}$$

where

$$\hat{b}_{m_0,n_0} = \mathrm{Im}\left\{ \sum_{(m,n)\neq(m_0,n_0)} b_{m,n} \left\langle p_{m,n}[k], p_{m_0,n_0}[k] \right\rangle \right\} \tag{4.8}$$

is the imaginary interference experienced by the reconstructed symbol of the m_0th subcarrier of the n_0th time-slot. By analyzing eq. (4.8), one can observe that the imaginary interference $\hat{b}_{m_0,n_0}$ is directly related to its adjacent symbols and the prototype filter itself. However, such interference is suppressed by taking the real part of the desired symbol, as depicted in Figures 2.2 and 2.8.

By adapting the results provided by Kofidis et al. (2013), the imaginary interference generated by a_{m_0,n_0} to its direct neighborhood is

$$\breve{b}_{m_0+1,n_0} = +ja_{m_0,n_0} e^{-j\frac{2\pi}{M}\frac{L_p-1}{2}} \sum_{k=0}^{L_p-1} p^2[k] e^{j\frac{2\pi}{M}k}, \tag{4.9}$$

$$\breve{b}_{m_0-1,n_0} = -ja_{m_0,n_0} e^{-j\frac{2\pi}{M}\frac{L_p-1}{2}} \sum_{k=0}^{L_p-1} p^2[k] e^{j\frac{2\pi}{M}k}, \tag{4.10}$$

$$\breve{b}_{m_0,n_0+1} = +ja_{m_0,n_0}(-1)^{m_0} \sum_{k=M/2}^{L_p-1} p[k]p\left[k-\frac{M}{2}\right], \tag{4.11}$$

$$\breve{b}_{m_0-1,n_0-1} = +ja_{m_0,n_0}(-1)^{m_0} \sum_{k=M/2}^{L_p-1} p[k]p\left[k-\frac{M}{2}\right], \tag{4.12}$$

$$\breve{b}_{m_0-1,n_0-1} = -a_{m_0,n_0}(-1)^{m_0} e^{-j\frac{2\pi}{M}\frac{L_p-1}{2}} \sum_{k=M/2}^{L_p-1} p[k]p\left[k-\frac{M}{2}\right] e^{j\frac{2\pi}{M}k}, \tag{4.13}$$

$$\breve{b}_{m_0-1,n_0+1} = -a_{m_0,n_0}(-1)^{m_0} e^{-j\frac{2\pi}{M}\frac{L_p-1}{2}} \sum_{k=M/2}^{L_p-1} p[k]p\left[k-\frac{M}{2}\right] e^{j\frac{2\pi}{M}k}, \tag{4.14}$$

$$\breve{b}_{m_0+1,n_0-1} = -a_{m_0,n_0}(-1)^{m_0} e^{-j\frac{2\pi}{M}\frac{L_p-1}{2}} \sum_{k=M/2}^{L_p-1} p[k]p\left[k-\frac{M}{2}\right] e^{j\frac{2\pi}{M}k}, \tag{4.15}$$

$$\breve{b}_{m_0+1,n_0+1} = -a_{m_0,n_0}(-1)^{m_0} e^{-j\frac{2\pi}{M}\frac{L_p-1}{2}} \sum_{k=M/2}^{L_p-1} p[k]p\left[k-\frac{M}{2}\right] e^{j\frac{2\pi}{M}k}, \tag{4.16}$$

where one can observe both even and odd symmetry in the interference elements. Thus, by combining such eq. (4.9)-(4.16), one can estimate the imaginary interference at any given position, provided the prototype filter and the adjacent pilot symbols are known.

It is also noteworthy mentioning that, by combining (4.6) and (4.7), the output of the analysis filter bank can be written as

$$y_{m_0,n_0} \approx H_m \left(b_{m_0,n_0} + j\hat{b}_{m_0,n_0} \right) + \eta_{m_0,n_0}, \tag{4.17}$$

where

$$\eta_{m_0,n_0} = \left\langle \eta[k], p_{m_0,n_0}[k] \right\rangle. \tag{4.18}$$

4.1.2 POP Channel Estimation

The POP is one of the simplest methods for channel estimation in FBMC systems. In this method, two adjacent pilot symbols are processed in order t generate the channel estimate. Consider the reception of two adjacent symbols y_{m_1,n_1} and y_{m_2,n_2} in a noiseless scenario, which can be described by

$$\begin{cases} y_{m_1,n_1} = H_{m_1}\left(b_{m_1,n_1} + j\hat{b}_{m_1,n_1}\right) \\ y_{m_2,n_2} = H_{m_2}\left(b_{m_2,n_2} + j\hat{b}_{m_2,n_2}\right) \end{cases}. \tag{4.19}$$

The POP method assumes and requires that $H_{m_1} \approx H_{m_2}$. Notice that such an assumption is entirely plausible if the pair of pilots are sequential and transmitted over the same subchannel, *e.g.*, y_{m_1,n_1} and y_{m_1,n_1+1}. In this case, the POP requires only that each subchannel is invariant during the transmission of the pair of pilots.

If eq. (4.19) is split into real and imaginary parts, one can derive the system

$$\begin{cases} \mathrm{Re}\{y_{m_1,n_1}\} = \left(b_{m_1,n_1} - \mathcal{R}\hat{b}_{m_1,n_1}\right)\mathrm{Re}\{H_{m_1}\} \\ \mathrm{Im}\{y_{m_1,n_1}\} = \left(\mathcal{R}b_{m_1,n_1} - \hat{b}_{m_1,n_1}\right)\mathrm{Re}\{H_{m_1}\} \\ \mathrm{Re}\{y_{m_2,n_2}\} = \left(b_{m_2,n_2} - \mathcal{R}\hat{b}_{m_2,n_2}\right)\mathrm{Re}\{H_{m_1}\} \\ \mathrm{Im}\{y_{m_2,n_2}\} = \left(\mathcal{R}b_{m_2,n_2} - \hat{b}_{m_1,n_2}\right)\mathrm{Re}\{H_{m_1}\} \end{cases}, \tag{4.20}$$

where

$$\mathcal{R} = \frac{\mathrm{Im}\{H_{m_1}\}}{\mathrm{Re}\{H_{m_1}\}}. \tag{4.21}$$

By combining eq. (4.20) and (4.21), one can observe that the real part of the channel estimate is given by

$$\mathrm{Re}\left\{\hat{H}_{m_1}\right\} = \frac{\mathrm{Re}\{y_{m_1,n_1}\} + \mathcal{R}\mathrm{Im}\{y_{m_1,n_1}\}}{b_{m_1,n_1}(1+\mathcal{R}^2)}, \tag{4.22}$$

the imaginary part of the channel estimate is given by

$$\mathrm{Im}\left\{\hat{H}_{m_1}\right\} = \mathcal{R}\mathrm{Re}\left\{\hat{H}_{m_1}\right\} \tag{4.23}$$

and the ratio between the imaginary and real parts of the channel is:

$$\mathcal{R} = \frac{b_{m_2,n_2}\mathrm{Re}\{y_{m_1,n_1}\} - b_{m_1,n_1}\mathrm{Re}\{y_{m_2,n_2}\}}{b_{m_1,n_1}\mathrm{Re}\{y_{m_2,n_2}\} - b_{m_2,n_2}\mathrm{Re}\{y_{m_1,n_1}\}}. \tag{4.24}$$

At this point, it becomes clear that the POP method does not require the estimation of the imaginary interference at the receiver side. Therefore, computational complexity is reduced considerably. However, one must recall that POPs is not intended for time-variant and/or non-flat channels, as it assumes that the pair of pilots are faded by the same channel coefficient.

As an example, Figure 4.1 depicts the recommended preamble for POP channel estimation (LÉLÉ et al., 2008a). Notice that the pilot is sent during the first time-slot, whereas its pair is a null symbol transmitted during the second time-slot. Thus, the correspondent pair also serves as a guard interval to mitigate the interference level generated by the data symbols.

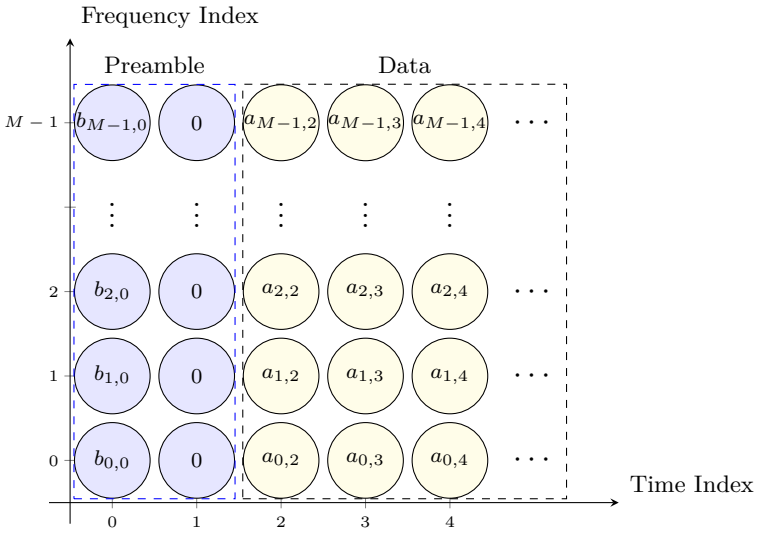

Figure 4.1 POP preamble, where $b_{m,0} = -b_{m-1,0}$ and $b_{0,0} = \pm \max\left(\mathcal{A}_{N_p}\right)$

4.1.3 IAM-1 Channel Estimation

By analyzing eq. (4.17), one can conclude that

$$\begin{aligned} \hat{H}_m &= \frac{y_{m_0,n_0}}{b_{m_0,n_0} + j\hat{b}_{m_0,n_0}} \\ &= H_m + \frac{\eta_{m_0,n_0}}{b_{m_0,n_0} + j\hat{b}_{m_0,n_0}} \end{aligned} \tag{4.25}$$

is the most straightforward solution. Nevertheless, it is noteworthy mentioning that such a channel estimate requires the evaluation of the imaginary interference elements $\hat{b}_{m_0,n_0}$. Fortunately, the imaginary interference can be evaluated with the aid of eq. (4.9)-(4.16). However, the downside of IAM-1 is the high computational complexity for long pilot sequences and/or a large number of subcarriers. Another interesting point to notice is the fact that high imaginary interference levels can mitigate the noise effect, as the noise power in eq. (4.25) is inversely proportional to $b_{m_0,n_0} + j\hat{b}_{m_0,n_0}$.

Differently from FBMC, OFDM channel estimation is straightforward given its full orthogonality that does not add any additional interference. As discussed previously, FBMC systems are orthogonal in the real field and intrinsic imaginary interference always takes place during symbol reconstruction. Thus, such interference must be taken into account in order to estimate the channel state properly.

A large variety of IAM schemes is available in the specialized literature. However, their main differences lie on their pilot preamble. One of the most straightforward solutions is proposed by Lélé et al. (2008a) and consists of deploying PAM symbols during three time-slots. Such a preamble/method is known as the IAM-1 and is depicted in Figure (4.2). Notice that such a preamble takes three time-slots, which is equivalent to 3/2 OFDM symbols[1].

[1] Recall that one OFDM symbol is equivalent to two FBMC. Hence, 3 FBMC

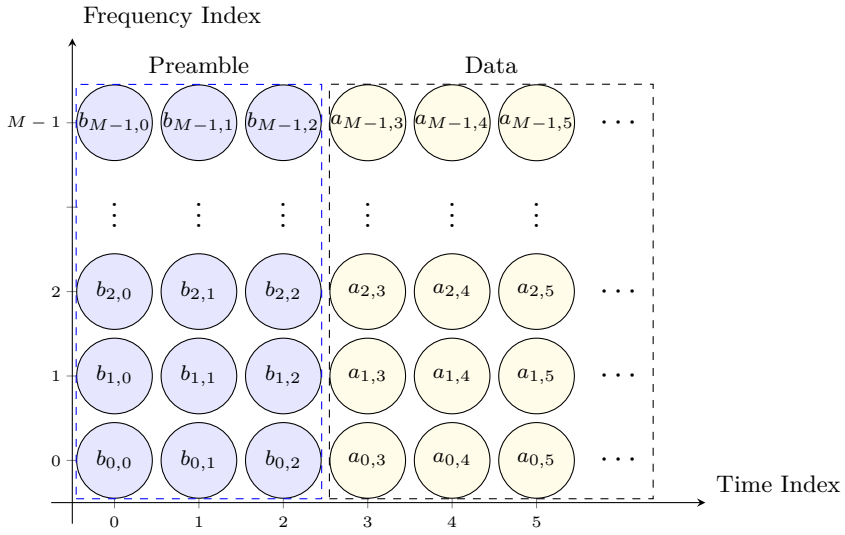

Figure 4.2 IAM-1 preamble, where $b_{m,n} \in \mathcal{A}_{N_p}$

4.1.4 IAM-2 Channel Estimation

As an alternative, (LÉLÉ et al., 2008a) also suggests the IAM-2 method, which deploys a preamble composed by three time-slots with null symbols at the first and third time-slots. For the second slot, the sign of each symbol alternates through all the subcarriers, *i.e.*, $b_{m,1} = -b_{m-1,1}$. In order to mitigate the noise effect, the pilot level is set to the maximum value allowed by the system, which is constrained by the modulation order of the system, *i.e.*, $b_{m,1} = \pm \max\left(\mathcal{A}_{N_p}\right)$.

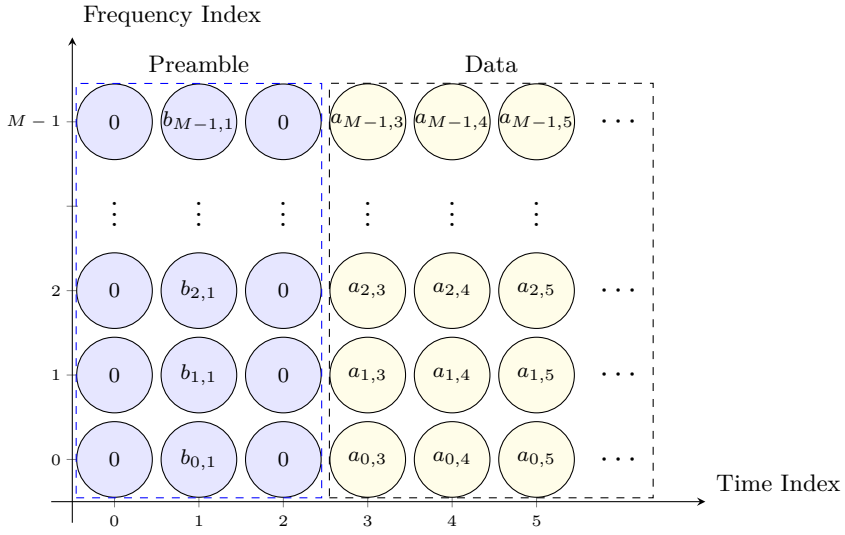

Figure 4.3 IAM-2 preamble, where $b_{m,1} = -b_{m-1,1}$ and $b_{0,1} = \pm \max\left(\mathcal{A}_{N_p}\right)$

Interestingly, the deployment of the preamble depicted in Figure 4.3 nullify the imaginary interference experienced by the pilots transmitted in the second time-slot. Since

the interference is negligible, *i.e.*, $\hat{b}_{m,1} \approx 0$, the channel estimation becomes

$$\begin{aligned} \hat{H}_m &= \frac{y_{m_0,n_0}}{b_{m_0,n_0}} \\ &= H_m + \frac{\eta_{m_0,n_0}}{b_{m_0,n_0}}, \end{aligned} \tag{4.26}$$

which does not require the estimation of the interference term $\hat{b}_{m,1}$. Despite the complexity reduction, the imaginary interference or pseudo-pilots can be evaluated offline before the channel estimation. Thus, there is no computational complexity overhead for this method. However, the main disadvantage of the IAM-2 preamble is the high PAPR of the multiplexed signal $s[k]$, as the pilots in the second time-slot are periodically distributed through all the subcarriers. Therefore, the IAM-2 performance can be significantly limited depending on the power amplifier deployed by the FBMC system.

4.1.5 IAM-R, IAM-I and IAM-C

The most straightforward way to improve the performance of IAM-2 channel estimation is to improve the Signal-to-Noise Ratio (SNR) level of the estimation proposed in eq. (4.25). This can be achieved by increasing the level of the imaginary interference $\hat{b}_{m_0,n_0}$. In order to increase the level of the pseudo-pilot $\hat{b}_{m_0,n_0}$, the second time-slot of the IAM-2 (Figure 4.3) preamble must be optimized. In this sense, (LÉLÉ et al., 2008b) proposes the IAM-R method, which is the IAM-2 method with a re-optimized preamble.

Further improvements are proposed by Lélé et al. (2008d) and are achieved by also allowing imaginary pilots in the preamble. The method known as IAM-I allows random N_p-PAM symbols in the second time-slots under some rules:

i) the symbols in the preamble are organized throughout the subcarriers in triples;

ii) each triple has the same magnitude, but their sign is randomly chosen;

iii) the central term of the triple is always imaginary, while the remaining symbols are real.

Thus by deploying the aforementioned method, the SNR of the channel can be increased, leading to performance improvements over other IAM channel estimation methods.

Another SNR improvement can be achieved by deploying the IAM-C preamble, which is also proposed by Lélé et al. (2008d). In this method, the preamble is very similar to the IAM-R preamble. However, imaginary symbols are introduced in the same positions described in the IAM-I preamble.

Despite improving the SNR, the IAM-R, IAM-I and IAM-C tend to present a poor PAPR performance as remarked by Kofidis and Katselis (2011). This behavior is caused by the increase of the pseudo-pilot level and the deterministic and/or periodic nature of the preambles. Notice that the PAPR effects are more evident in IAM-R and IAM-C due

to the deterministic nature of their preamble. On the other hand, the PAPR effects of the IAM-I are milder due to their random nature. However, it is noteworthy mentioning that despite being less recurrent, high PAPR realization still occur in the IAM-I pilot signal.

In order to provide a more comprehensive overview of the available preambles for FBMC channel estimation, Table 4.1 summarizes the aforementioned methods. Thus, such a table presents the length of the preamble, the number of guard symbols, the definition of the preamble and an illustrative example with $M = 8$ and 2-PAM or 4-PAM random symbols.

Finally, one can extend the aforementioned preamble-based channel estimation techniques by following the steps described by Kofidis and Katselis (2011) and Kofidis et al. (2013).

Table 4.1 A summary of pilots/preambles deployed in FBMC preamble-based channel estimation, where b is a random N_p-PAM symbol

Method	**Length**	**Guard**	**Definition**	**Example**
POP	2 PAM symbols	1 PAM symbols	$b_{m,n} = \begin{cases} (-1)^m \max\left(\mathcal{A}_{N_p}\right), & m = 0, 1, \cdots M-1, \quad n = 0 \\ 0, & \text{otherwise} \end{cases}$	$+1$ 0 -1 0 $+1$ 0 -1 0 $+1$ 0 -1 0 $+1$ 0 -1 0
IAM-1	3 PAM symbols	0 PAM symbols	$b_{m,n} = \begin{cases} b, & m = 0, 1, \cdots M-1, \quad n = 0, 1, 2 \\ 0, & \text{otherwise} \end{cases}$	$+1$ $+3$ -1 $+3$ $+3$ -1 -1 $+3$ $+3$ $+1$ -3 $+1$ -3 $+1$ $+3$ -1 -1 -1 -1 -3 $+3$ $+1$ -1 $+3$

Table 4.1 A summary of pilots/preambles deployed in FBMC preamble-based channel estimation

Method	Length	Guard	Definition	Example
IAM-2	3 PAM symbols	2 PAM symbols	$b_{m,n} = \begin{cases} (-1)^m, & m = 0, 1, \cdots M-1, \quad n = 1 \\ 0, & \text{otherwise} \end{cases}$	$\begin{matrix} 0 & +1 & 0 \\ 0 & -1 & 0 \\ 0 & +1 & 0 \\ 0 & -1 & 0 \\ 0 & +1 & 0 \\ 0 & -1 & 0 \\ 0 & +1 & 0 \\ 0 & -1 & 0 \end{matrix}$
IAM-R	3 PAM symbols	2 PAM symbols	$b_{m,n} = \begin{cases} \pm \max\left(\mathcal{A}_{N_p}\right), & m = 0, \quad n = 1 \\ \pm \max\left(\mathcal{A}_{N_p}\right), & m = 1, \quad n = 1 \\ -b_{m-2,n}, & m = 2, 3, \cdots M-1, \quad n = 1 \\ 0, & \text{otherwise} \end{cases}$	$\begin{matrix} 0 & +1 & 0 \\ 0 & -1 & 0 \\ 0 & -1 & 0 \\ 0 & +1 & 0 \\ 0 & +1 & 0 \\ 0 & -1 & 0 \\ 0 & -1 & 0 \\ 0 & +1 & 0 \end{matrix}$

Table 4.1 A summary of pilots/preambles deployed in FBMC preamble-based channel estimation

Method	**Length**	**Guard**	**Definition**	**Example**
IAM-I	3 PAM symbols	2 PAM symbols	$b_{m,n} = \begin{cases} j^{\mathrm{mod}(m,2)} b, & m = 0, 1, \cdots M-1, \quad n = 1 \\ 0, & \text{otherwise} \end{cases}$	$\begin{matrix} 0 & +3 & 0 \\ 0 & +j3 & 0 \\ 0 & -3 & 0 \\ 0 & -j1 & 0 \\ 0 & -1 & 0 \\ 0 & -j1 & 0 \\ 0 & +3 & 0 \\ 0 & -j3 & 0 \end{matrix}$
IAM-C	3 PAM symbols	2 PAM symbols	$b_{m,n} = \begin{cases} \pm j^{\mathrm{mod}(m,2)} \max\left(\mathcal{A}_{N_p}\right), & m = 0, \quad n = 1 \\ \pm j^{\mathrm{mod}(m,2)} \max\left(\mathcal{A}_{N_p}\right), & m = 1, \quad n = 1 \\ -b_{m-2,n}, & m = 2, 3, \cdots M-1, \quad n = 1 \\ 0, & \text{otherwise} \end{cases}$	$\begin{matrix} 0 & +1 & 0 \\ 0 & -j & 0 \\ 0 & -1 & 0 \\ 0 & +j & 0 \\ 0 & +1 & 0 \\ 0 & -j & 0 \\ 0 & -1 & 0 \\ 0 & +j & 0 \end{matrix}$

4.1.6 A Brief Numeric Comparison

In this section, we offer a brief numeric comparison between the FBMC channel estimation methods presented throughout this section. The methods will be compared according to their achieved channel estimate Normalized Mean-Squared Error (NMSE), defined by

$$\text{NMSE}_H = \frac{1}{M}\sum_{m=0}^{M-1}\mathbb{E}\left[\frac{\left|\hat{H}_m - H_m\right|^2}{\left|H_m\right|^2}\right], \tag{4.27}$$

under the simulation scenario described in Table 4.2. For further reference, we also include the Least Squares (LS) channel estimation performance for OFDM. Notice that the chosen scenario deploys an FBMC system with $M = 64$ subcarriers, an overlapping factor of $K = 4$ and a Mirabasi-Martin prototype filter. Alternatively, the OFDM system deploys almost the same parameters, except the usage of a CP of length $M/8$. Finally, the adopted channel is frequency-flat for each subchannel, where the coherence band is three times larger than the subcarrier bandwidth.

Table 4.2 Parameters deployed for the channel MSE numeric comparison

FBMC	SISO	
	$M = 64$, $K = 4$, $L_p = 257$	
	No CP	
	Mirabbasi-Martin Prototype Filter	
	POP, IAM-1, IAM-2, IAM-R, IAM-I and IAM-C Channel Estimation	
OFDM	SISO	
	$M = 64$	
	12.5% of CP	
	LS Channel Estimation	
Channel	Rayleigh	
	Exponential PDP (CHAYAT, 1997)	$\mathbb{E}\left[\lvert h[k]\rvert^2\right] = \frac{1-e^{-1/\tau_{\text{rms}}}}{e^{-(1+10\tau_{\text{rms}})/\tau_{\text{rms}}}} e^{-\ell/\tau_{\text{rms}}}$
		$\ell = 0, 1, \cdots 10\tau_{\text{rms}}$
	90th Percentile Coherence Band (HAMPTON, 2014, eq. (4.31))	$B_{c,90} = 1/(50\tau_{\text{rms}})$
	Subchannel band	$B_{sc} = 2/M$
	Selectivity Index	$\eta_B = B_{c,90}/B_{sc} = 3$

Figure 4.4 depicts the NMSE performance of both FBMC and OFDM channel estimators under the scenario described in Table 4.2. The performance achieved by most FBMC estimators is superior under low to moderate SNR levels. In this case, the IAM-2, IAM-I, IAM-R and the IAM-C channel estimators outperform the OFDM reference due to the their optimized preambles, which are optimized to increase the power of the pseudo-pilot and improve the SNR without the need of extra transmission power. However, an NMSE performance floor is established under high SNR for IAM channel estimators due to the intrinsic interference generated by adjacent pilots and/or data symbols. Unlike the noise, the effect of the intrinsic interference cannot be eliminated by an SNR increase, establishing

an NMSE floor for the IAM methods. Despite presenting an inferior performance compared to most IAM estimators for low to moderate SNR, the POP scheme does not depend on the evaluation of imaginary interference terms and presents a milder performance degradation in high SNR levels.

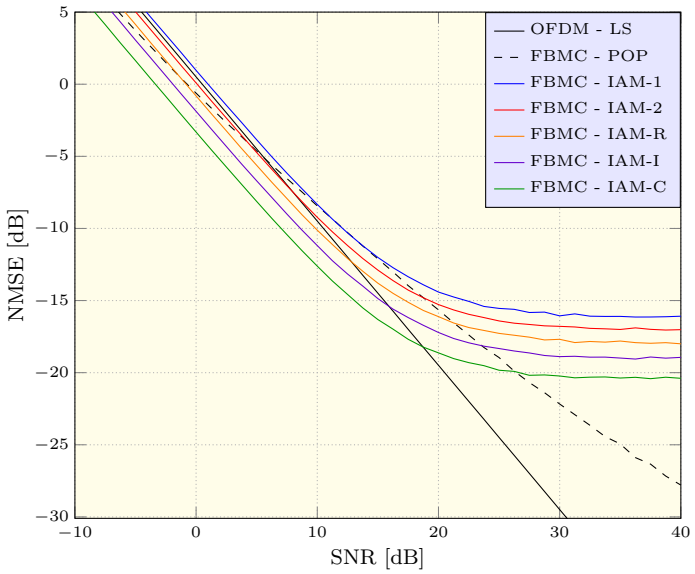

Figure 4.4 Channel estimate NMSE for FBMC and OFDM systems

4.2 Equalization

This section discusses how to proceed with channel equalization in FBMC systems through basic, but effective techniques. As the wireless channel tends to distort the transmitted signal significantly, compensation is required to enable symbol reconstruction at the receiver side. In order to execute such compensation, channel estimates are required and can be obtained via the methods discussed in the previous section of this chapter. Hence, this section presents channel equalization for both SISO and MIMO systems operating with FBMC multiplexing, which is executed after channel estimation at the receiver side.

4.2.1 Equalization Detection for SISO Systems

In order to nullify the channel effects, one can perform the single-tap ZF equalization

$$\tilde{a}_{m,n} = \mathrm{Re}\left\{\frac{y_{m,n}}{H_m}\right\}. \tag{4.28}$$

Notice that the post equalized symbol is still affected by the interference, which can be eliminated by considering only the real part of $y_{m,n}/H_m$. Alternatively, a multi-tap equalization can be proceeded if the subchannels are not flat. In this sense, equalization

can be proceed at a low rate using $y_{m,n}$ (IHALAINEN et al., 2011), i.e.,

$$\tilde{a}_{m,n} = \mathrm{Re}\left\{ \sum_{\ell=0}^{L_w-1} w_{m,\ell} y_{m,n-\ell} \right\}, \tag{4.29}$$

where $w_{m,i}$ are the weights of an L_w-tap equalizer, which can be optimized according to the ZF or MMSE criteria. Notice that there are several equalization alternatives, including, for example, time-based algorithms (IKHLEF; LOUVEAUX, 2009a) and adaptive filtering schemes (CHEN; MAEHARA, 2017). Unfortunately, each method tends to use different notations, making it difficult to standardize the equalization description.

4.2.1.1 MIMO Detection for Frequency-Flat Subchannels

Provided each subchannel is frequency-flat or even mildly selective, any MIMO detection scheme available from literature can be deployed to reconstruct symbols at the receiver side of a MIMO-FBMC system. Hence, eq. (2.40), *i.e.*,

$$\mathbf{y}_{m,n} = \mathbf{H}_m \left(\mathbf{a}_{m,n} + j\hat{\mathbf{a}}_{m,n} \right) + \boldsymbol{\eta}_{m,n} \tag{4.30}$$

is solved to retrieve the transmitted symbols $\mathbf{a}_{m,n}$. However, one must take into account the imaginary interference $j\hat{\mathbf{a}}_{m,n}$ during the detection procedure. For plain linear processing techniques, imaginary interference can be ignored as it can be vanished after taking the real part of the equalization result. As an example, by taking the real part of the ZF equalization, one can completely eliminate the interference terms $j\hat{\mathbf{a}}_{m,n}$.

Unfortunately, not all detectors can be directly extended for MIMO-FBMC as interference affects the received signal. In this sense, eq. (4.30) can be rewritten as a real system:

$$\underbrace{\begin{bmatrix} \mathrm{Im}\{\mathbf{y}_{m,n}\} \\ \mathrm{Re}\{\mathbf{y}_{m,n}\} \end{bmatrix}}_{\underset{\sim}{\mathbf{y}}_{m,n}} = \underbrace{\begin{bmatrix} \mathrm{Re}\{\mathbf{H}_m\} & \mathrm{Im}\{\mathbf{H}_m\} \\ -\mathrm{Im}\{\mathbf{H}_m\} & \mathrm{Re}\{\mathbf{H}_m\} \end{bmatrix}}_{\underset{\sim}{\mathbf{H}}_m} \underbrace{\begin{bmatrix} \hat{\mathbf{a}}_{m,n} \\ \mathbf{a}_{m,n} \end{bmatrix}}_{\underset{\sim}{\mathbf{a}}_{m,n}} + \underbrace{\begin{bmatrix} \mathrm{Im}\{\boldsymbol{\eta}_{m,n}\} \\ \mathrm{Re}\{\boldsymbol{\eta}_{m,n}\} \end{bmatrix}}_{\underset{\sim}{\boldsymbol{\eta}}_{m,n}}, \tag{4.31}$$

which also brings the advantage of a more standardized presentation. Since the goal of the detection is to retrieve $\mathbf{a}_{m,n}$, $\hat{\mathbf{a}}_{m,n}$ can be ignored by converting eq. (4.31) into a triangular system through the QR decomposition. Hence, applying the QR decomposition into $\underset{\sim}{\mathbf{H}}_m$ leads to:

$$\underset{\sim}{\mathbf{H}}_m = \underset{\sim}{\mathbf{Q}}_m \underset{\sim}{\mathbf{R}}_m, \tag{4.32}$$

where $\underset{\sim}{\mathbf{Q}}_m$ is orthonormal and $\underset{\sim}{\mathbf{R}}_m$upper triangular. Since $\underset{\sim}{\mathbf{Q}}_m$ is orthonormal [2], multiplying it by $\underset{\sim}{\mathbf{y}}_{m,n}$, *i.e.*, $\underset{\sim}{\mathbf{Q}}_m^H \underset{\sim}{\mathbf{y}}_{m,n}$ leads to the block-wise system:

$$\underset{\sim}{\mathbf{Q}}_m^H \underset{\sim}{\mathbf{y}}_{m,n} = \begin{bmatrix} \mathbf{y}_{m,n}^{(a)} \\ \underset{\sim}{\mathbf{y}}_{m,n} \end{bmatrix} = \begin{bmatrix} \mathbf{R}_m^{(a)} & \mathbf{R}_m^{(b)} \\ \mathbf{0} & \underset{\sim}{\mathbf{R}}_m \end{bmatrix} \begin{bmatrix} \hat{\mathbf{a}}_{m,n} \\ \mathbf{a}_{m,n} \end{bmatrix} + \begin{bmatrix} \boldsymbol{\eta}_{m,n}^{(a)} \\ \underset{\sim}{\boldsymbol{\eta}}_{m,n} \end{bmatrix}. \tag{4.33}$$

[2] $\underset{\sim}{\mathbf{Q}}_m^H \underset{\sim}{\mathbf{Q}}_m = \mathbf{I}$

Therefore, such a procedure isolates the signal from the interference and the system

$$\underset{\sim}{\mathbf{y}}_{m,n} = \underset{\sim}{\mathbf{R}}_m \mathbf{a}_{m,n} + \underset{\sim}{\boldsymbol{\eta}}_{m,n} \tag{4.34}$$

can be solved through classical MIMO detection.

Aiming to provide a brief overview of MIMO detection, Table 4.3 presents classical and prominent MIMO detectors. Notice that some detectors presented in Table 4.3 were adapted for MIMO-FBMC usage, but can be easily modified for MIMO-OFDM operation. Further details on MIMO detection are provided in (KOBAYASHI et al., 2014) and (KOBAYASHI et al., 2015). Moreover, Appendix H.7 presents scripts for some detectors displayed in Table 4.3.

Table 4.3 MIMO-FBMC detection

Detector	**Details**
ML (CHANG; CHANG, 2017)	The ML detector is the optimum solution for solving (2.40) and can be described by: $\tilde{\mathbf{a}} = \underset{\mathbf{a}_{m,n}}{\operatorname{argmin}} \quad \left\| \underset{\sim}{\mathbf{y}}_{m,n} - \underset{\sim}{\mathbf{R}}_m \mathbf{a}_{m,n} \right\|^2$ $\text{s.t.} \quad \mathbf{a}_{m,n} \in \mathcal{A}_{N_p}^{N_T}.$ Such a detector evaluates $\left\| \underset{\sim}{\mathbf{y}}_{m,n} - \underset{\sim}{\mathbf{R}}_m \mathbf{a}_{m,n} \right\|^2$ considering all combinations of $\mathbf{a}_{m,n}$, choosing the option with the smallest norm. Since there are $N_p^{N_T}$ combinations, the complexity increases dramatically for large MIMO systems.
SD (HASSIBI; VIKALO, 2005) (AGRELL et al., 2002)	The SD is a tree search algorithm with near-ML performance and reduced complexity. It ignores less likely candidates that are outside of a sphere of radius d, which is based on the SNR of the signal, *i.e.*, $\tilde{\mathbf{a}} = \underset{\mathbf{a}_{m,n}}{\operatorname{argmin}} \quad \left\| \underset{\sim}{\mathbf{y}}_{m,n} - \underset{\sim}{\mathbf{R}}_m \mathbf{a}_{m,n} \right\|^2$ $\text{s.t.} \quad \left\| \underset{\sim}{\mathbf{y}}_{m,n} - \underset{\sim}{\mathbf{R}}_m \mathbf{a}_{m,n} \right\|^2 < d^2$ $\mathbf{a}_{m,n} \in \mathcal{A}_{N_p}^{N_T}.$ Since it ignores less likely symbol candidates, complexity can be reduced significantly, especially in high SNR scenarios.
K-Best (MONDAL et al., 2008) (WONG et al., 2002)	In order to reduce complexity, K-Best considers only the K most probable symbol candidates for each antenna. Hence, K^{N_t} combinations are tested rather than $N_p^{N_t}$. However, K must be chosen properly to provide low to moderate complexity, while not degrading error rate performance. Unlike SD, K-Best search presents a constant computational load and uniform data path computation.

Detector	**Details**
SDP-Based Detector (LUO et al., 2010) (MYAMOTO; ABRÃO, 2013) (NEGRÃO et al., 2016)	By observing that $$\left\| \underset{\sim}{\mathbf{y}}_{m,n} - \underset{\sim}{\mathbf{R}}_m \mathbf{a}_{m,n} \right\|^2 \propto \begin{bmatrix} \mathbf{a}_{m,n}^T & 1 \end{bmatrix} \underbrace{\begin{bmatrix} \underset{\sim}{\mathbf{R}}_m^T \underset{\sim}{\mathbf{R}}_m & -\underset{\sim}{\mathbf{R}}_m^T \underset{\sim}{\mathbf{y}}_{m,n} \\ -\underset{\sim}{\mathbf{y}}_{m,n}^T \underset{\sim}{\mathbf{R}}_m & 0 \end{bmatrix}}_{\mathbf{L}} \underbrace{\begin{bmatrix} \mathbf{a}_{m,n} \\ 1 \end{bmatrix}}_{\mathbf{v}},$$ one can recast the ML problem to be solved via SDP: $$\begin{aligned} \tilde{\mathbf{V}} = \underset{\mathbf{V}}{\text{argmin}} \quad & \text{Tr}\left(\mathbf{LV}\right) \\ \text{s.t.} \quad & \min\left\{\mathcal{A}_{N_p}\right\}^2 \mathbf{1} \leq \text{diag}(\mathbf{V}) \leq \max\left\{\mathcal{A}_{N_p}\right\}^2 \mathbf{1} \\ & [\mathbf{V}]_{N_T+1,N_T+1} = 1 \\ & \mathbf{V} \succeq 0, \end{aligned}$$ where $\mathbf{V} = \mathbf{v}\mathbf{v}^T$. Notice that the problem described previously is a relaxed version as the rank-1 constraint is substituted by the semi-positiveness requirement. Since $\tilde{\mathbf{V}} = \tilde{\mathbf{v}}\tilde{\mathbf{v}}^T$ contains the transmitted symbols, one must decouple the desired vector. Two possible choices to decouple symbols are the rank-1 approximation and the Gaussian randomization.
ZF (BAI; CHOI, 2014) (WINTERS et al., 1994)	One of the simplest linear detectors for MIMO V-BLAST systems, the ZF deploys the Moore-Penrose pseudo-inverse matrix to estimate the transmitted symbols: $$\begin{aligned} \tilde{\mathbf{a}}_{m,n} &= \text{Re}\left\{\mathbf{H}_m^{\dagger} \mathbf{y}_{m,n}\right\} \\ &= \text{Re}\left\{\left(\mathbf{H}_m^H \mathbf{H}_m\right)^{-1} \mathbf{H}_m^H \mathbf{y}_{m,n}\right\}. \end{aligned}$$
MMSE (BAI; CHOI, 2014) (WINTERS et al., 1994)	Aiming to improve the ZF performance, MMSE takes into account the noise effect on the overall transmission: $$\tilde{\mathbf{a}}_{m,n} = \text{Re}\left\{\left(\mathbf{H}_m^H \mathbf{H}_m + \frac{N_0}{E_s}\mathbf{I}\right)^{-1} \mathbf{H}_m^H \mathbf{y}_{m,n}\right\}.$$
SIC-Based Detectors (WUBBEN et al., 2001)	The strategy of SIC-based detectors is to use the triangular system $$\underset{\sim}{\mathbf{y}}_{m,n} = \underset{\sim}{\mathbf{R}}_m \mathbf{a}_{m,n} + \underset{\sim}{\boldsymbol{\eta}}_{m,n}$$ to detect symbols and cancel interference. Hence, the last symbol is detected, sliced and its interference is removed on the next layers. This procedure is repeated upwards until all symbols are detected, and is known as the ZF-SIC detector. Notice that the SIC procedure can also be deployed with the MMSE metric by deploying the extended channel matrix $\begin{bmatrix} \underset{\sim}{\mathbf{H}}_m^T & \sqrt{N_0/E_s}\mathbf{I}_{N_T} \end{bmatrix}^T$.
OSIC-Based Detectors (WUBBEN et al., 2003) (KOBAYASHI; ABRÃO, 2016)	The main difference between SIC and OSIC detectors is the deployment of the ordered QR decomposition. Through this modified decomposition, symbols with higher SNR are detected first, reducing error propagation and improving performance.

Detector	Details
LR-Based Detectors (MA; ZHANG, 2008) (WUBBEN et al., 2004) (LENSTRA et al., 1982)	By deploying the Lenstra-Lenstra-Lovász (LLL) algorithm, the receiver can detect symbols with a near-orthogonal channel matrix $$\underset{\sim}{\tilde{\mathbf{R}}}_m = \underset{\sim}{\mathbf{R}}_m \underset{\sim}{\mathbf{T}}_m,$$ where $\underset{\sim}{\mathbf{T}}_m$ is a unimodular matrix, *i.e.*, a matrix with integer entries and a determinant with unitary absolute values, $\left\lvert \underset{\sim}{\mathbf{T}}_m \right\rvert \in \{\pm 1, \pm j\}$. Hence, eq. (2.40) can be rewritten as: $$\begin{aligned} \underset{\sim}{\mathbf{y}}_{m,n} &= \underset{\sim}{\mathbf{R}}_m \mathbf{a}_{m,n} + \underset{\sim}{\boldsymbol{\eta}}_{m,n} \\ &= \underset{\sim}{\mathbf{R}}_m \underset{\sim}{\mathbf{T}}_m \left(\underset{\sim}{\mathbf{T}}_m^{-1} \mathbf{a}_{m,n} \right) + \underset{\sim}{\boldsymbol{\eta}}_{m,n} \\ &= \underset{\sim}{\tilde{\mathbf{R}}}_m \mathbf{z}_{m,n} + \underset{\sim}{\boldsymbol{\eta}}_{m,n}. \end{aligned}$$ Eq. (4.3) can be solved with linear detection. As an example, the ZF solution for eq. (4.3) is $$\tilde{\mathbf{z}}_{m,n} = \underset{\sim}{\tilde{\mathbf{R}}}_m^{\dagger} \underset{\sim}{\mathbf{y}}_{m,n}.$$ After the equalization LR-symbols are quantized and converted back to their original domain. It is noteworthy mentioning that LR can also be combined with MMSE metric as well as other detection techniques such as SIC, OSIC, and Chase-list.
Chase List-Based Detectors (WATERS; BARRY, 2005)	Similar to SIC-based detectors, the Chase List repeats the detection considering different last-antenna symbols candidates $[\mathbf{a}_{m,n}]_{N_T}$. Since the last element of $\mathbf{a}_{m,n}$ is more prone to generate a higher error propagation, repeating its detection can minimize errors. Since it is a relatively simple detector, it can also be combined with both LR and SIC techniques.

4.2.1.2 Multi-tap MIMO Equalization

For frequency-flat subchannels scenarios, the previous MIMO detectors are suitable for reconstructing data at the receiver side. However, they may present deficient performance when operating under frequency-selective subchannels. As an alternative to circumvent such a issue, the FBMC system can operate using a multi-tap equalizer. By deploying multiple taps, such equalizers can overcome subchannel selectivity. From this perspective, multi-tap equalization is a flexible choice, enabling the receiver to choose the number of taps properly accordingly to the frequency selectivity of each subchannel.

In particular, for FBMC systems, Ihalainen et al. (2011) propose a multi-tap equalizer based on the frequency sampling technique. The frequency sampling technique sets the equalizer coefficients properly to assume a value to compensate the frequency response in specific target points. Despite its flexibility, the multi-tap equalizer proposed by Ihalainen et al. (2011) cannot be combined with all of the detection methods presented previously, as only linear methods are compatible.

For the sake of simplicity, let us describe the multi-tap MIMO equalizer considering an odd length L_w. In this sense, the goal is to design a series of L_w matrices to equalize

the received signal $\mathbf{y}_{m,n}$:

$$\tilde{\mathbf{a}}_{m,n} = \mathrm{Re}\left\{ \sum_{\ell=0}^{L_w-1} \mathbf{W}_{m,\ell} \mathbf{y}_{m,n-\ell} \right\}, \tag{4.35}$$

where $\mathbf{W}_{m,i}$ are the taps of the equalizer. In particular, Ihalainen et al. (2011) proposed a design where the equalizer is based on L_w frequency points for each subchannel. Hence, each subchannel is divided into L_w evenly distributed frequency target points

$$\mathbf{H}_{m,(\ell)}, \quad \ell = 0, 1, \cdots L_w - 1, \tag{4.36}$$

which are used to design the frequency-domain equalization matrices $\mathbf{G}_{m,(\ell)}$. Two possible and popular equalization matrices are the ZF

$$\mathbf{G}^{\mathrm{ZF}}_{m,(\ell)} = \left(\mathbf{H}^H_{m,(\ell)} \mathbf{H}_{m,(\ell)} \right)^{-1} \mathbf{H}^H_{m,(\ell)} \tag{4.37}$$

and the MMSE

$$\mathbf{G}^{\mathrm{MMSE}}_{m,(\ell)} = \left(\mathbf{H}^H_{m,(\ell)} \mathbf{H}_{m,(\ell)} + \frac{N_0}{E_s} \mathbf{I}_{N_T} \right)^{-1} \mathbf{H}^H_{m,(\ell)}. \tag{4.38}$$

The final step of the design is the conversion of the matrices $\mathbf{G}_{m,(\ell)}$ into $\mathbf{W}_{m,\ell}$. Unfortunately, plain Discrete Fourier Transform (DFT) cannot be deployed as the equalization of each subchannel is evaluated individually. Such conversion must be proceeded through the linear transformation

$$\begin{bmatrix} \mathbf{W}_{m,0} \\ \mathbf{W}_{m,1} \\ \vdots \\ \mathbf{W}_{m,L_w} \end{bmatrix} = \begin{bmatrix} \mathbf{D}_{11} & \mathbf{D}_{1,2} & \cdots & \mathbf{D}_{1,L_w} \\ \mathbf{D}_{21} & \mathbf{D}_{2,2} & \cdots & \mathbf{D}_{2,L_w} \\ \vdots & \vdots & \ddots & \vdots \\ \mathbf{D}_{L_w,1} & \mathbf{D}_{L_w,2} & \cdots & \mathbf{D}_{L_w,L_w} \end{bmatrix}^{-1} \cdot \begin{bmatrix} \mathbf{G}_{m,(0)} \\ \mathbf{G}_{m,(1)} \\ \vdots \\ \mathbf{G}_{m,(L_w-1)} \end{bmatrix}, \tag{4.39}$$

where

$$\mathbf{D}_{\ell,k} = \exp\left[-j \frac{2\pi}{L_w + 1} \frac{(L_w - 1 - 2\ell)(L_w - 1 - 2k)}{4} \right] \mathbf{I}_{N_T}. \tag{4.40}$$

4.3 Conclusions

Throughout this Chapter, it was possible to understand how imaginary interference affects the transmission of FBMC directly, leading to incompatibilities between signal processing techniques of FBMC and OFDM systems. In particular, this Chapter discussed preamble-based channel estimation techniques, channel equalization, and MIMO detection for FBMC systems. In this sense, it was observed that channel estimation in FBMC has its peculiarities and different mechanisms to minimize the interference during the signal processing. Moreover, this Chapter also introduced a MIMO detection strategy to estimate the transmitted symbols from the imaginary interference, enabling full compatibility of classical MIMO detectors for FBMC systems. Nevertheless, such an advantage comes at the price of a higher complexity since a pre-processing stage that requires a matrix decomposition carried out before MIMO-FBMC symbol detection.

5 OFDP-SDP Design

In this chapter, we propose a prototype filter design that deploys DPSSs as its basis and takes into account near-perfect symbol reconstruction and OoB energy suppression as the optimization criteria. Since the proposed filters share some features with the OFDP, they will be referred to as the OFDP-SDP prototype filter. Despite sharing similarities, the proposed methodology aims to design prototype filters via convex optimization. More specifically, the prototype filter design is stated as a non-convex QCQP, which is relaxed into an SDP for a more straightforward solution.

In particular, we aim to design short length prototype filters ($K \leq 3$) with near-perfect symbol reconstruction with the aid of SDP. The deployment of short length prototype filters is a twofold gain. First, shorter pulses introduce a lower delay at the output of an FBMC system, as highlighted in eq. (26) of (SIOHAN et al., 2002). Second, longer prototype filters may generate interference that spans several adjacent symbols, degrading the overall performance. An example of such behavior is the Interference Approximation Method and the Pair of Pilots (LÉLÉ et al., 2008a) channel estimation for FBMC systems. Their performance is affected by adjacent interference produced by the prototype filter. Numerical results show that prototype filters derived via the SDP problem provides a much better symbol reconstruction compared with other filters such as the EGF.

5.1 Proposed Design

This Chapter proposes a design, which reinterprets and extends the OFDP design introduced by Vahlin and Holte (1994). In short, the OFDP design aims to provide the optimal filter in terms of OoB emission, while taking into account perfect reconstruction of the transmitted data. At this point, it is important to highlight some features and flaws of the original design. Originally, the resulting OFDP is obtained by sampling a continuous sum of Prolate Functions. Also, the resulting optimization problem is solved by using the Euler-Lagrange equation. Specifically, one must solve the set of equations (indexed by the pairs (m, n))

$$\begin{aligned} &2\int_{-T}^{T} p(t)\frac{\sin\left[\frac{2\pi}{\tau_0}(t-s)\right]}{\pi(t-s)}dt \\ &= \sum_{m,n} \lambda_{m,n}\left[p(t-n\tau_0)+p(t+n\tau_0)\right]\cos\left(\frac{4\pi}{\tau_0}mt\right) \end{aligned} \tag{5.1}$$

where

$$p(t) = \sum_{\ell} \alpha_{2\ell}\psi_{2\ell}(t), \tag{5.2}$$

α_ℓ are the filter weights, $\psi_{2\ell}$ are prolate functions, T is the continuous pulse length, τ_0 is the FBMC signaling interval.

However, a more in-depth analysis reveals that perfect reconstruction, modeled by an equality constraint, cannot be achieved. Indeed, the equality constraint for perfect reconstruction is assumed for modeling the problem. Nonetheless, such a constraint is violated, as the authors measure an interference level on the resulting OFDP. Furthermore, as the formulated problem is not convex, there is no guarantee that the provided solution is a global optimum.

5.1.1 Objective Function

In order to obtain an even-symmetric prototype filter around $(L_p - 1)/2$, let us consider the matrix

$$\boldsymbol{\Psi} = \begin{bmatrix} \boldsymbol{\psi}_{0,2\pi/M} & \boldsymbol{\psi}_{2,2\pi/M} & \cdots & \boldsymbol{\psi}_{2(N-1),2\pi/M} \end{bmatrix} \tag{5.3}$$

to be the concatenation of N even indexed Slepian sequences. Through such a matrix, we define the resulting prototype filter as the linear transformation

$$\mathbf{p} = \boldsymbol{\Psi}\mathbf{c}, \tag{5.4}$$

where

$$\mathbf{c} = \begin{bmatrix} c_0 & c_1 & \cdots & c_{N-1} \end{bmatrix}^T \tag{5.5}$$

is the vector containing the weights of the prototype filter.

Consequently, we can define the objective function of the OFDP problem as

$$\overline{E}(\omega_c) = \mathbf{c}^T \boldsymbol{\Psi}^T \left[\mathbf{I}_{L_p} - \boldsymbol{\Gamma}\left(\omega_c\right) \right] \boldsymbol{\Psi}\mathbf{c}. \tag{5.6}$$

Hence, by taking (5.6) as the objective function, we aim to determine the weights c_{2i} which minimize the OoB energy emission.

5.1.2 FBMC Symbol Interference

In order to design an FBMC prototype filter with near-perfect reconstruction properties, let us recall that symbol reconstruction in a noiseless scenario may be proceeded through

$$\begin{aligned} \tilde{a}_{m_0,n_0} &= \mathrm{Re}\left\{ \langle s[k], p_{m_0,n_0}[k] \rangle \right\} \\ &= a_{m_0,n_0} + \sum_{(m,n)\neq(m_0,n_0)} a_{m,n} \mathrm{Re}\left\{ \langle p_{m,n}[k] \, | p_{m_0,n_0}[k] \rangle \right\}. \end{aligned} \tag{5.7}$$

Noticeably, eq. (5.7) highlights the presence of self-interference, which should be minimized in order to enable data reconstruction at an FBMC receiver. In this sense, let us define

the interference terms

$$\begin{aligned}\epsilon_{m,n} &= \mathrm{Re}\left\{\langle p_{m,n}[k]\,|p_{0,0}[k]\rangle\right\} \\ &= \cos\left[\tfrac{\pi}{2}(m+n)\right]\sum_{k=-\infty}^{\infty} p\left[k-n\frac{M}{2}\right]p[k]\cos\left(\frac{2\pi}{M}m\underline{k}\right).\end{aligned} \tag{5.8}$$

Due to the characteristics of (5.8), one can enumerate the following properties:

$$\epsilon_{m,n} = \begin{cases} 1 & m=n=0 & \text{(5.9a)}\\ 0, & |n| > \left\lceil \frac{L_p}{M/2}\right\rceil - 1 & \text{(5.9b)}\\ 0, & \text{odd } m+n & \text{(5.9c)}\\ \epsilon_{m,-n} & & \text{(5.9d)}\\ -\epsilon_{M-m,n}, & 1 \le m \le M/2-1. & \text{(5.9e)}\end{cases}$$

Eq. (5.9a) is the energy of the prototype pulse $p[k]$. $\epsilon_{m,n}$ is null since $p[k]$ has a finite length of L_p, as prescribed by (5.9b). The terms $\epsilon_{m,n}$ are also null for odd $m+n$, given the phase-shift $e^{j\pi/2(m+n)}$ adopted in eq. (2.8). Finally, the symmetric features of (5.8) render both properties (5.9d) and (5.9e).

Considering the properties described in eq. (5.9a) to (5.9e), we can define the set of pairs

$$\mathcal{E} = \left\{ (m,n) \;\middle|\; \begin{array}{l} 0 \le m \le M/2 \\ 0 \le n \le \left\lceil \frac{Lp-1}{M/2}\right\rceil - 1 \\ m+n \text{ even} \\ m+n \neq 0 \end{array} \right\}, \tag{5.10}$$

as the set of non-redundant interference elements $\epsilon_{m,n}$ of $p[k]$. Thus, $\mathcal{E}$ is the smallest set of double capable of representing the SIR provided in (3.1).

5.1.3 Interference Constraints

As the OFDP design takes into account the reconstruction features in an FBMC transmission, such concern must be incorporated into the optimization problem. In this sense, let us define the time-shift operator $\mathbf{\Pi}_n$, which is a nilpotent matrix with entries

$$[\mathbf{\Pi}_n]_{i,j} = \begin{cases} 1, & j = i + nM/2 \\ 0, & \text{otherwise} \end{cases}. \tag{5.11}$$

We also define the diagonal matrix $\mathbf{\Sigma}_m$ with entries

$$[\mathbf{\Sigma}_m]_{k,k} = \cos\left[\frac{2\pi}{M}m\underline{k}\right]. \tag{5.12}$$

Through eq. (5.11) and (5.12), the interference elements $\epsilon_{m,n}$ can be rewritten in matrix form as

$$\epsilon_{m,n} = \cos\left[\frac{\pi}{2}(m+n)\right]\mathbf{p}^T\left(\mathbf{\Sigma}_m\mathbf{\Pi}_n\right)\mathbf{p}. \tag{5.13}$$

Conveniently, one can take advantage of (5.9d) and rewrite eq. (5.13) as

$$\epsilon_{m,n} = \cos\left[\frac{\pi}{2}(m+n)\right]\mathbf{p}^T\left(\frac{\mathbf{\Pi}_n^T\mathbf{\Sigma}_m^T + \mathbf{\Sigma}_m\mathbf{\Pi}_n}{2}\right)\mathbf{p}. \tag{5.14}$$

Since $\epsilon_{m,n}$ is obtained from a symmetric matrix, such a matrix is guaranteed to present a real spectrum, which is desirable for the optimization problem.

As a final step, we combine the linear transformation (5.4) with eq. (5.14) in order to provide the final form for the interference elements

$$\epsilon_{m,n} = \cos\left[\frac{\pi}{2}(m+n)\right]\mathbf{c}^T\mathbf{\Psi}^T\left(\frac{\mathbf{\Pi}_n^T\mathbf{\Sigma}_m^T + \mathbf{\Sigma}_m\mathbf{\Pi}_n}{2}\right)\mathbf{\Psi}\mathbf{c}. \tag{5.15}$$

5.1.4 Resulting Optimization Problem

Considering both the IB energy and the interference elements, the proposed design can be described by the following optimization problem:

$$\begin{aligned}
\mathbf{c}^* = \underset{\mathbf{c}}{\operatorname{argmin}} \quad & \mathbf{c}^T\mathbf{\Psi}^T\left[\mathbf{I}_{L_p} - \mathbf{\Gamma}(\omega_c)\right]\mathbf{\Psi}\mathbf{c} \\
\text{s.t.} \quad & \left|\mathbf{c}^T\mathbf{\Psi}^T\left(\frac{\mathbf{\Pi}_n^T\mathbf{\Sigma}_m^T + \mathbf{\Sigma}_m\mathbf{\Pi}_n}{2}\right)\mathbf{\Psi}\mathbf{c}\right| \leq \epsilon_0 \\
& (m,n) \in \mathcal{E} \\
& \mathbf{c}^T\mathbf{c} = 1.
\end{aligned} \tag{5.16}$$

Through the optimization problem (5.16), the vector $\mathbf{c}$ must be optimized in order to minimize the OoB band emission, while tolerating a maximum interference level ϵ_0, which controls the interference level, and hence the SIR expressed in (3.1). An additional equality constraint is required in order to make the prototype filter energy unitary; otherwise, the solution assumes the trivial form $\mathbf{c} = \mathbf{0}_{N\times 1}$.

Unfortunately, the optimization problem (5.16) is a non-convex QCQP, as the equality constraint is not affine and the inequality constraints do not compose a convex set of functions, given the absolute value inequalities. Hence, there may be multiple local optimums, making it hard to solve such a problem efficiently. In fact, applying the Karush-Kuhn-Tucker (KKT) conditions to a non-convex QCQP may not even lead to a local optimum (LU et al., 2011).

In order to circumvent the non-convexity of (5.16), one can recast such a problem as the following SDP:

$$\begin{aligned}
\tilde{\mathbf{C}}^* = \underset{\mathbf{C}}{\operatorname{argmin}} \quad & \operatorname{Tr}\left\{\mathbf{\Psi}^T\left[\mathbf{I}_{L_p} - \mathbf{\Gamma}(\omega_c)\right]\mathbf{\Psi}\mathbf{C}\right\} \\
\text{s.t} \quad & \left|\operatorname{Tr}\left[\mathbf{\Psi}^T\left(\frac{\mathbf{\Pi}_n^T\mathbf{\Sigma}_m^T + \mathbf{\Sigma}_m\mathbf{\Pi}_n}{2}\right)\mathbf{\Psi}\mathbf{C}\right]\right| \leq \epsilon_0 \\
& (m,n) \in \mathcal{E} \\
& \operatorname{Tr}(\mathbf{C}) = 1 \\
& \mathbf{C} \succeq 0.
\end{aligned} \tag{5.17}$$

After obtaining the SDP solution of (5.17), namely $\tilde{\mathbf{C}}^* = \tilde{\mathbf{c}}^* \left(\tilde{\mathbf{c}}^*\right)^T$, the actual solution $\tilde{\mathbf{c}}^*$ must be extracted. Notice however that $\tilde{\mathbf{C}}^*$ is not guaranteed to be a rank-1 matrix, making such problem a relaxation. Two popular choices to extract the solution from $\tilde{\mathbf{C}}^*$ are the rank-1 approximation and the Gaussian Randomization (PALOMAR; ELDAR, 2009). Through the rank-1 approximation, the principal component of $\tilde{\mathbf{C}}^*$ is extracted from the solution $\tilde{\mathbf{c}}^*$. In other words, $\tilde{\mathbf{c}}^*$ is the eigenvector associated with the largest eigenvalue of $\tilde{\mathbf{C}}^*$. As an alternative, the Gaussian randomization takes samples from a Gaussian random vector with a null mean and $\tilde{\mathbf{C}}^*$ covariance, $\mathbf{x}_i \sim \mathcal{N}(\mathbf{0}, \tilde{\mathbf{C}}^*)$, choosing as the solution the feasible sample with the lowest cost. As expected, the Gaussian randomization presents a massive and unpractical computational cost in large scale problems, as one must sort and check the sample vector feasibility. Since c_i is a continuous variable it is very hard to pick up a feasible sample vector randomly. Notice that the Gaussian randomization is more commonly applied in optimization problems with discrete variables, *e.g*, a Boolean Quadratic Problem, where a feasible candidate can be easily generated by rounding the vector sample. Hence, the rank-1 approximation is a better trade-off in terms of complexity and the quality of the solution, provided $\tilde{\mathbf{C}}^*$ is a low-rank matrix.

Since the optimization problem (5.17) is a relaxation of (5.16), there is no guarantee of achieving the optimal solution. However, SDP relaxation has been applied successfully in many problems related to communication systems and signal processing, besides being efficiently solved in polynomial time (LUO et al., 2010; MATTINGLEY; BOYD, 2010). Furthermore, interpreting the OFDP problem as an SDP may provide flexibility in such a design, since other constraints and modifications can be incorporated. Typically, SDP problems are solved efficiently by recasting them as Second-Order Cone Program (SOCP) and deploying specialized interior-point algorithms (LOBO et al., 1998).

5.1.5 Complexity of the OFDP Design

Concerning the size of the optimization problem (5.17), one may immediately observe N variables and one equality constraint. Furthermore, the number of pairs contained in the set $\mathcal{E}$ is

$$|\mathcal{E}| = \frac{1}{2}\left(\frac{M}{2}+1\right)\left\lceil\frac{L_p}{M/2}\right\rceil - 1. \tag{5.18}$$

This implies that the optimization problem (5.17) presents $2\,|\mathcal{E}|$ inequality constraints. Hence the worst case complexity order required to solve (5.17) is

$$\mathcal{O}\left\{\max\left[N,\ \left(\frac{M}{2}+1\right)\left\lceil\frac{L_p}{M/2}\right\rceil - 1\right]^4 \sqrt{N}\log\left(\frac{1}{\kappa}\right)\right\}, \tag{5.19}$$

where κ is the solution accuracy (LUO et al., 2010). Although the problem posed in (5.17) can be solved reasonably fast, the computation time is not a critical exceedingly concern, as this optimization problem can be solved offline and prior to the operation of the FBMC system.

5.2 Numerical Results

The numerical results presented herein were obtained with the aid of the modeling framework CVX (GRANT; BOYD, 2014) in conjunction with the solver MOSEK 8.0 (APS, 2017). Specifically, MOSEK solves SDP problems by deploying the primal-dual interior-point method algorithm described in (ANDERSEN et al., 2003), which is based on the Nesterov-Todd method (TODD et al., 1998). Other solver options such as Sedumi and SDPT3 are also embedded into CVX, but our tests showed them to be less stable and slower than MOSEK. Also, given the low complexity costs, we extracted the final solution of the SDP problem by using the rank-1 approximation, as the principal component of $\tilde{\mathbf{C}}^*$ always presented more than 97% of the energy of such a matrix.

As stated previously, this chapter focuses on prototype filters with shorter lengths, *e.g.*, $K \leq 2$. However, the developed methodology was extended for comparison purposes. Therefore, the numerical results herein presented take into account $L_p = KM$ samples, where the overlapping factor is $K = \{1, 2, 3\}$. Indeed, we have extended the analysis for the condition $K = 3$ to evaluate the effectiveness of the proposed design methodology. Furthermore, we set a stringent tolerable interference level of $\epsilon_0 = 10^{-12}$ in order to provide a near-perfect symbol reconstruction. Since our proposed design application is focused on multicarrier application, a straightforward choice for the cutoff frequency is $\omega_c = 2\pi/M$ where the short prototype filter condition applies. Also, the optimization problem will be solved for different numbers of subcarriers, $M = \{8, 16, 32, 64, 128\}$ as the performance of prototype filters based on DPSSs varies significantly depending on the number of subcarriers[1]. Table 5.1 summarizes all the parameters values deployed in the numerical analysis, whereas Appendix A presents the weights obtained for each optimization setup.

Table 5.1 Optimization setup for different overlapping factors K

Parameter	K		
	1	2	3
ϵ_0	10^{-12}	10^{-12}	10^{-12}
ω_c	$\frac{2\pi}{M}$	$\frac{2\pi}{M}$	$\frac{2\pi}{M}$
N	$\frac{KM}{2}$	$\frac{KM}{2}$	8

In the following subsections, we present both the impulse and frequency responses for the proposed design, the OFDP and the EGF. Furthermore, aiming to conduct a proper numeric comparison, we present the SIR, MSL, D_τ, D_ν, the Heisenberg factor and the out of band energies for $2\pi/M$ and $4\pi/M$ for the three prototype filter options.

[1] This behavior was observed in Table II of (SIOHAN et al., 2002)

5.2.1 Prototype Filters with $K = 1$

Figure 5.1 presents both the impulse and frequency responses of the proposed prototype filter design and the EGF for an overlapping factor of $K = 1$. Notice that the latter prototype filter was chosen for this comparison as it is regarded as one of the leading choices in FBMC systems to come due to its high symbol reconstruction capability, tuned by the spreading factor α (DOHLER; NAKAMURA, 2016). Unfortunately, (VAHLIN; HOLTE, 1994) did not provide the prototype filter weights for $K = 1$, and the description of the solution of the optimization problem lacks the information needed to remount the exact scenario idealized by the authors. Hence, the OFDP provided by the original design could not be simulated.

In terms of performance, one can observe in Tables 5.2 and 5.3 that the proposed OFDP-SDP design achieved a much higher SIR than the EGF while maintaining similar spectral performance. Furthermore, it is noteworthy mentioning that the SIR levels vary according to the number of subcarriers in both OFDP-SDP and EGF cases.

5.2.2 Prototype Filters with $K = 2$

Noticeably, the original and the proposed OFDP designs present similar pulse shapes for $K = 2$, as one can observe in Figure 5.2. However, differences in the power spectrum are noticeable, especially for the first sidelobes, as presented in Figure 5.2b.

Despite their near-identical aspect, the OFDP and the proposed solution perform differently in terms of symbol reconstruction, as can be observed in Tables 5.5 and 5.6. First, it can be observed that the proposed prototype filter achieves a much higher SIR than the OFDP design, whereas the MSL perfomance is slightly inferior. Regarding the remaining figures of merit, substantial differences cannot be observed. By analyzing Table 5.4, one can conclude that the EGF presents a large spread in the frequency domain, which is a consequence of its symbol reconstruction quality. Furthermore, one can observe that the EGF presented similar MSL levels, a near-optimal Heisenberg factor and slightly higher OoB emissions.

5.2.3 Prototype Filters with $K = 3$

Figures 5.3a and 5.3b present both the impulse and frequency responses for the OFDP, OFDP-SDP and the EGF with an overlapping factor of $K = 3$. Differently from the previous case ($K = 2$), the OFDP and the proposed prototype filter presented significant differences in the impulse and frequency responses. Notice that the frequency response of the proposed filter presents a faster decay up to $\omega/2\pi = 0.05$ while presenting a slower decay for $\omega/2\pi \geq 0.05$. Furthermore, one can observe that the EGF presents a much larger OoB emission in comparison to the other solutions.

Tables 5.5 and 5.6 presents the performance of the OFDP designs and the EGF. In general, both prototype filters achieve similar performances when it comes to the OoB energy and the MSL. However, the OFDP obtained via SDP achieves a far superior SIR, enabling such a pulse to operate over any SNR, without adding any negative impact on the data transmission of an FBMC system. Provided α is appropriately tuned, the EGF may present a high SIR level, even surpassing the original OFDP design. Nevertheless, an EGF prototype filter with a high spreading factor may present a low performance in terms of spectrum containment, as both the IB energy and the MSL levels are relatively high.

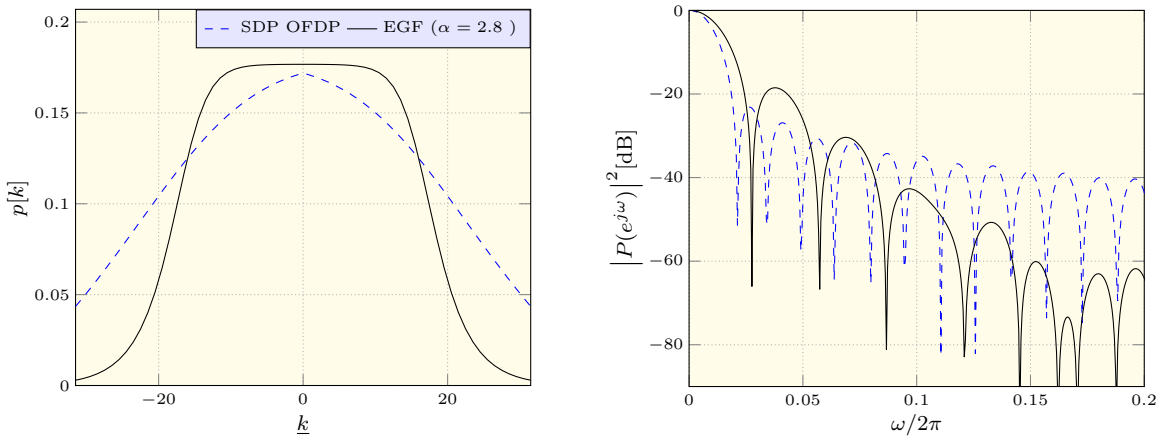

(a) Impulse Response **(b)** Frequency Response

Figure 5.1 Time and frequency representations for OFDP and EGF pulses ($K = 1$, $M = 64$, and $L_p = 64$)

Table 5.2 EGF performance for $K = 1$

M	SIR[dB]	MSL[dB]	D_τ	D_ν	ξ	$\overline{E}\left(\frac{2\pi}{M}\right)$[dB]	$\overline{E}\left(\frac{4\pi}{M}\right)$[dB]
8	77.112	-18.178	0.220	0.454	0.796	-10.793	-17.798
16	78.966	-18.235	0.216	0.471	0.778	-10.580	-17.364
32	80.582	-18.234	0.216	0.472	0.777	-10.574	-17.367
64	81.796	-18.229	0.216	0.472	0.776	-10.570	-17.371
128	82.598	-18.227	0.216	0.473	0.775	-10.568	-17.372

Table 5.3 Proposed prototype filter performance for $K = 1$

M	SIR[dB]	MSL[dB]	D_τ	D_ν	ξ	$\overline{E}\left(\frac{2\pi}{M}\right)$[dB]	$\overline{E}\left(\frac{4\pi}{M}\right)$[dB]
8	262.901	-22.758	0.289	0.329	0.837	-17.707	-24.218
16	262.414	-23.060	0.287	0.376	0.738	-17.336	-23.052
32	266.396	-23.135	0.287	0.450	0.616	-17.246	-22.797
64	264.591	-23.153	0.287	0.570	0.486	-17.224	-22.736
128	246.974	-23.158	0.287	0.755	0.368	-17.218	-22.721

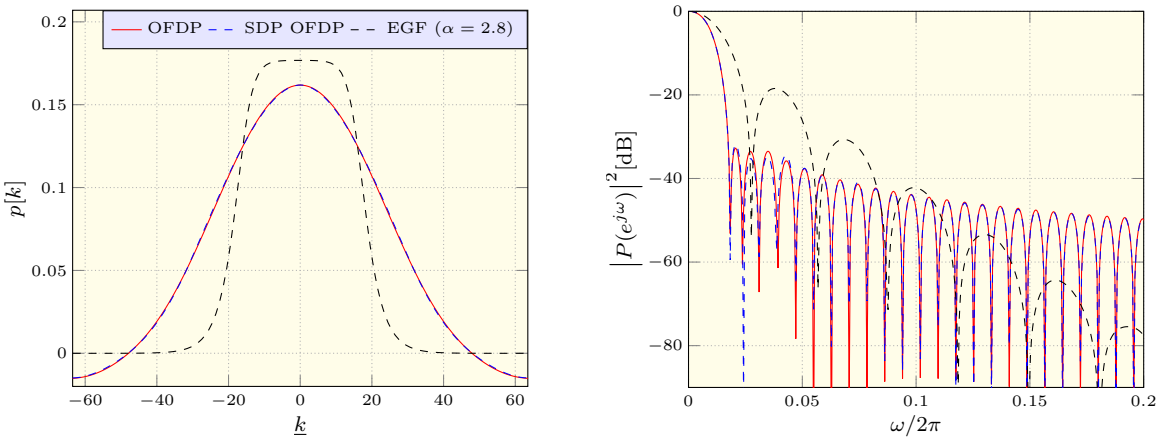

(a) Impulse Response **(b)** Frequency Response

Figure 5.2 Time and frequency representations for OFDP and EGF pulses ($K = 2$, $M = 64$, and $L_p = 128$)

Table 5.4 EGF performance for $K = 2$

M	SIR[dB]	MSL[dB]	D_τ	D_ν	ξ	$\overline{E}\left(\frac{2\pi}{M}\right)$[dB]	$\overline{E}\left(\frac{4\pi}{M}\right)$[dB]
8	77.777	-18.143	0.220	0.454	0.796	-10.789	-17.784
16	77.522	-18.181	0.216	0.471	0.778	-10.581	-17.337
32	77.380	-18.181	0.216	0.472	0.777	-10.579	-17.333
64	77.290	-18.182	0.216	0.472	0.777	-10.579	-17.333
128	77.250	-18.182	0.216	0.472	0.777	-10.579	-17.333

Table 5.5 OFDP performance for $K = 2$

M	SIR[dB]	MSL[dB]	D_τ	D_ν	ξ	$\overline{E}\left(\frac{2\pi}{M}\right)$[dB]	$\overline{E}\left(\frac{4\pi}{M}\right)$[dB]
8	45.408	-32.653	0.329	0.265	0.911	-27.093	-31.245
16	75.576	-32.717	0.328	0.274	0.883	-26.870	-30.673
32	57.915	-32.727	0.328	0.290	0.837	-26.816	-30.555
64	55.934	-32.748	0.328	0.317	0.765	-26.802	-30.526
128	55.498	-32.748	0.328	0.366	0.662	-26.799	-30.519

Table 5.6 Proposed prototype filter performance for $K = 2$

M	SIR[dB]	MSL[dB]	D_τ	D_ν	ξ	$\overline{E}\left(\frac{2\pi}{M}\right)$[dB]	$\overline{E}\left(\frac{4\pi}{M}\right)$[dB]
8	247.429	-31.463	0.328	0.267	0.909	-27.072	-31.281
16	242.197	-31.790	0.328	0.274	0.884	-26.946	-30.749
32	245.090	-31.865	0.328	0.288	0.840	-26.918	-30.640
64	250.045	-31.883	0.328	0.315	0.770	-26.911	-30.614
128	253.981	-31.887	0.328	0.362	0.670	-26.910	-30.607

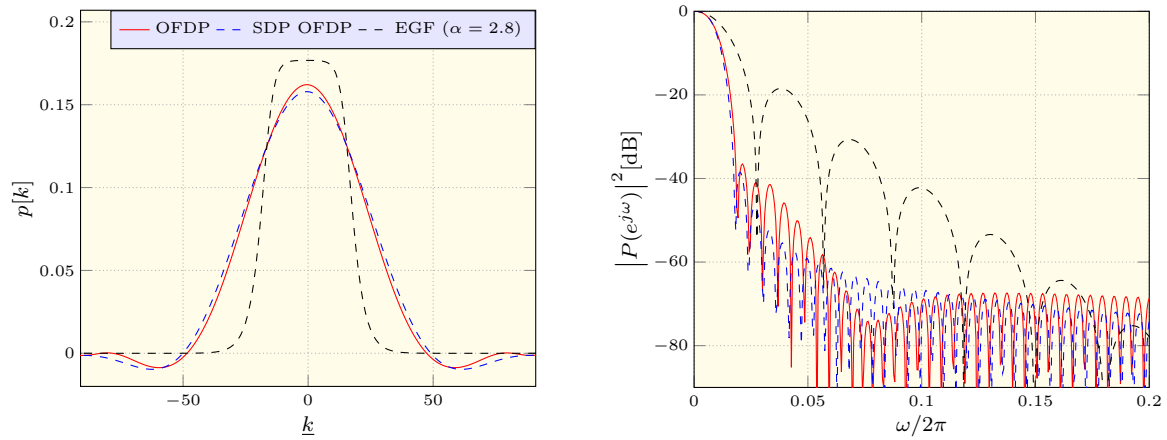

(a) Impulse Response **(b)** Frequency Response

Figure 5.3 Time and frequency representations for OFDP and EGF pulses ($K = 3$, $M = 64$, $L_p = 192$)

Table 5.7 EGF performance for $K = 3$

M	SIR[dB]	MSL[dB]	D_τ	D_ν	ξ	$\overline{E}\left(\frac{2\pi}{M}\right)$[dB]	$\overline{E}\left(\frac{4\pi}{M}\right)$[dB]
8	80.951	-18.141	0.220	0.454	0.796	-10.789	-17.784
16	81.172	-18.180	0.216	0.471	0.778	-10.580	-17.330
32	81.202	-18.180	0.216	0.472	0.777	-10.578	-17.333
64	81.209	-18.181	0.216	0.472	0.777	-10.578	-17.333
128	81.209	-18.181	0.216	0.472	0.777	-10.578	-17.333

Table 5.8 OFDP performance for $K = 3$

M	SIR[dB]	MSL[dB]	D_τ	D_ν	ξ	$\overline{E}\left(\frac{2\pi}{M}\right)$[dB]	$\overline{E}\left(\frac{4\pi}{M}\right)$[dB]
8	42.293	-36.733	0.325	0.257	0.952	-29.312	-44.557
16	65.697	-36.582	0.324	0.259	0.948	-29.228	-43.620
32	54.571	-36.546	0.324	0.259	0.947	-29.207	-43.443
64	52.806	-36.537	0.324	0.260	0.945	-29.202	-43.401
128	52.420	-36.535	0.324	0.261	0.941	-29.200	-43.391

Table 5.9 Proposed prototype filter performance for $K = 3$

M	SIR[dB]	MSL[dB]	D_τ	D_ν	ξ	$\overline{E}\left(\frac{2\pi}{M}\right)$[dB]	$\overline{E}\left(\frac{4\pi}{M}\right)$[dB]
8	44.833	-51.884	0.381	0.234	0.894	-41.569	-42.987
16	49.593	-41.020	0.368	0.238	0.909	-39.727	-46.567
32	58.907	-38.758	0.347	0.246	0.932	-35.524	-51.111
64	58.135	-38.510	0.344	0.248	0.934	-34.997	-51.736
128	57.932	-38.510	0.344	0.248	0.933	-34.958	-51.856

5.3 Conclusions

In this Chapter, we have proposed a methodology to design prototype filters deploying DPSSs and the relaxation of a QCQP problem into SDP. Initially, the designed prototype filters were expected to perform similarly to OFDPs as both pulses deploy DPSSs and share the same optimization criteria. Nevertheless, numerical results demonstrate that our methodology achieved a far superior SIR than OFDP provided by the original work, while maintaining similar spectrum features for small overlapping factors, *i.e.*, $K = \{1, 2\}$. On the other hand, superior spectrum features were achieved by our design for K = 3. Hence, such a design can be useful not only for the OFDP filter design, as it can be extended by modifying the optimization problem or even the set of sequences to compose the prototype filter.

6 Convex Optimization Prototype Filter Design

Following the concepts presented in the previous chapter, we now propose a prototype filter design deploying convex optimization instead of relying on SDP relaxation. Instead of only taking into account symbol reconstruction constraints, the methodology introduced in this chapter also considers spectrum. Initially, the proposed design is written as a non-convex QCQP which is relaxed into a convex QCQP guided by a line search. As a result, we deploy the proposed method to design three prototype filters that provide high-performance symbol reconstruction and superior spectrum features. Numerical results corroborate the effectiveness of the proposed filters by analyzing them from the perspective of different metrics.

6.1 Proposed Design

In this section, we develop a methodology for designing prototype filters via convex optimization. Through this design, we aim to minimize the OoB energy emission, while providing a high-performance symbol reconstruction and maintaining a fast spectrum decay. The description of the proposed design begins by defining the filter expression as a linear transformation. In the sequel, we provide the objective function expression, *i.e.*, the OoB energy. Furthermore, we present a full discussion on the FBMC interference elements, which are used to ensure a high SIR prototype filter. The constraints required to achieve a prototype filter with fast spectrum decay are also offered. Finally, we cast the problem as a non-convex QCQP, which, in its turn, is relaxed into a convex QCQP guided by a line search. Since we aim to deploy convex optimization techniques in our design, we provide a brief proof of the convexity of each component of the optimization problem.

6.1.1 Filter Expression

In order to model the prototype filter, let us define the matrix

$$\mathbf{F} = \begin{bmatrix} \mathbf{f}_0 & \mathbf{f}_1 & \cdots & \mathbf{f}_{N-1} \end{bmatrix}. \tag{6.1}$$

to be the aggregation of N sequences, where

$$\mathbf{f}_i = \begin{bmatrix} f_i[0] & f_i[1] & \cdots & f_i[L_p - 1] \end{bmatrix}^T \tag{6.2}$$

is a vector with unitary norm $\|\mathbf{f}_i\|_2 = 1$. Hence, let us express the prototype filter as the linear transformation

$$\mathbf{p} = \mathbf{F}\mathbf{c}, \tag{6.3}$$

where

$$\boldsymbol{c} = \begin{bmatrix} c_0 & c_1 & \cdots & c_{N-1} \end{bmatrix}^T \tag{6.4}$$

are the coefficients to be optimized.

Throughout this chapter, we consider two families of sequences to be deployed as $f_i[k]$[1]. First, we consider $f_i[k]$ as the DPSS, *i.e.*,

$$f_i[k] = \psi_{2i,\omega_s}[k]. \tag{6.5}$$

As an alternative, a family of cosine sequences can also be deployed:

$$f_i[k] = \begin{cases} \dfrac{1}{\sqrt{KM+1}}, & i = 0 \\ \sqrt{\dfrac{2}{KM+2}} \cos\left(\dfrac{2\pi i}{KM}\underline{k}\right), & i = 1, 2, \cdots N-1 \end{cases}. \tag{6.6}$$

As a result, N does not need to assume a large value, as high values of N may increase the frequency content in the OoB region. Therefore, it can also be noted that the deployment of the linear transformation (6.3) is fortunate as it reduces the number of variables from L_p to N, where, in general, $N << L_p$.

6.1.2 Energy Expression

By combining eq. (3.7) and (6.3), one may rewrite the energy concentrated within the stopband region as

$$\overline{E}(\omega_c) = \mathbf{c}^T \underbrace{\mathbf{F}^T \left[\mathbf{I}_{L_p} - \mathbf{\Gamma}(\omega_c)\right] \mathbf{F}}_{\mathbf{Q}_0} \mathbf{c}, \tag{6.7}$$

which is an appropriate choice as it is a quadratic convex function, given $\mathbf{Q}_0$ is a positive semidefinite matrix. A straightforward way of proving that $\mathbf{Q}_0$ is positive semidefinite is by recalling that $\overline{E}(\omega_c)$ is an energy measurement, *i.e.*, a non-negative value. Thus, if $\overline{E}(\omega_c)$ is non-negative, $\mathbf{Q}_0$ is positive semidefinite. Since $\mathbf{Q}_0$ is positive semidefinite, eq. (6.7) is convex (LU et al., 2011, sec. 1).

6.1.3 FBMC Interference Elements

As observed in eq. (5.7), the quality of the symbol reconstruction depends on the prototype filter, which needs to be designed to provide low distortion levels and enable near-perfect reconstruction. To simplify the representation of the interference for our problem, let us define

$$\begin{aligned} \epsilon_{m,n} &= \mathrm{Re}\left\{\langle p_{m,n}[k] \, | p_{0,0}[k] \rangle\right\} \\ &= \cos\left(\phi_{m,n}\right) \sum_{k=-\infty}^{\infty} p\left[k - n\frac{M}{2}\right] p[k] \cos\left(\frac{2\pi}{M} m\underline{k}\right) \end{aligned} \tag{6.8}$$

[1] One can deploy other sequences as long as they are (near) orthogonal, symmetrical around $(L_p - 1)/2$.

as the distortion or interference introduced by the symbol $a_{m,n}$ to the symbol $a_{0,0}$.

Based on (6.8), five straightforward, yet very useful, properties can be listed:

i $\epsilon_{0,0}$ represents the pulse energy;

ii $\epsilon_{m,n}$ is an even sequence concerning the index n, *i.e.*, $\epsilon_{m,n} = \epsilon_{m,-n}$;

iii $\epsilon_{m,n}$ is odd circular symmetric concerning the index m, *i.e.*, $\epsilon_{m,n} = -\epsilon_{M-m,n}$, for $1 \leq m \leq M/2 - 1$;

iv Given the finite length of the prototype filter, $\epsilon_{m,n} = 0$ for $|n| > \left\lceil \frac{L_p}{M/2} \right\rceil - 1$;

v Given the cosine term, $\epsilon_{m,n} = 0$ case $m + n$ is odd.

Thus, taking into account properties ii, iii and iv, let us define

$$\mathcal{E} = \left\{ (m,n) \left| \begin{array}{l} 0 \leq m \leq M/2 \\ 0 \leq n \leq \left\lceil \frac{Lp-1}{M/2} \right\rceil - 1 \\ m+n \text{ even} \\ m+n \neq 0 \end{array} \right. \right\} \tag{6.9}$$

to be the set of distortion elements $\epsilon_{m,n}$ which are not strictly null, but can eventually become zero, or assume a negligible value depending on the prototype filter design. Given the symmetry of $\epsilon_{m,n}$, we omitted the redundant elements in order to propose an efficient optimization problem.

6.1.3.1 Matrix Form

In order to model the interference elements $\epsilon_{m,n}$ in matrix form, two matrices need to be defined. First,

$$[\mathbf{\Pi}_n]_{i,j} = \begin{cases} 1, & j = i + nM/2 \\ 0, & \text{otherwise} \end{cases} \tag{6.10}$$

are the entries of the nilpotent matrix $\mathbf{\Pi}_n$, responsible for shifting the sequence $p[k]$ by $nM/2$ samples. The second matrix, $\mathbf{\Sigma}_m$, incorporates the cosine term of the summation of eq. (6.8) and is defined as

$$\mathbf{\Sigma}_m = \text{diag}\left\{ \cos\left(\frac{2\pi}{M} m \underline{k} \right) \right\}_{k=0,1,\cdots,L_p-1}. \tag{6.11}$$

Initially, we can rewrite eq. (6.8) as

$$\epsilon_{m,n} = \mathbf{p}^T \underbrace{\left[\cos(\phi_{m,n}) \mathbf{\Sigma}_m \mathbf{\Pi}_n \right]}_{\mathbf{Q}_{m,n}^{(0)}} \mathbf{p}. \tag{6.12}$$

Notice that since $\mathbf{\Sigma}_m$ is diagonal and $\mathbf{\Pi}_n$ is nilpotent, $\mathbf{Q}_{m,n}^{(0)}$ is also nilpotent for $n \neq 0$. Conversely, case $n = 0$, the spectrum of $\mathbf{Q}_{m,n}^{(0)}$ lies on the diagonal of $\mathbf{\Sigma}_m$, as $\mathbf{\Sigma}_m$ is diagonal

and $\mathbf{\Pi}_0 = \mathbf{I}_{L_p}$. Thus, $\mathbf{Q}_{m,n}^{(0)}$ is not a set of semipositive matrices making $\epsilon_{m,n}$ to be a non-convex set.

For a better manipulation in the optimization problem to come, $\epsilon_{m,n}$ can be expressed using a Hermitian symmetric matrix. By noting that $\epsilon_{m,-n} = \mathbf{p}^T \left(\mathbf{Q}_{m,n}^{(0)}\right)^T \mathbf{p}$ and $\epsilon_{m,-n} = \epsilon_{m,n}$, eq. (6.8) can be expressed as

$$\epsilon_{m,n} = \mathbf{p}^T \underbrace{\left[\frac{\mathbf{Q}_{m,n}^{(0)} + \left(\mathbf{Q}_{m,n}^{(0)}\right)^T}{2}\right]}_{\mathbf{Q}_{m,n}^{(1)}} \mathbf{p}. \tag{6.13}$$

Since $\mathbf{Q}_{m,n}^{(1)}$ is a Hermitian matrix, it yields real eigenvalues. Unfortunately, the exact eigenvalues of $\mathbf{Q}_{m,n}^{(1)}$, given $n \neq 0$, cannot be tracked analytically. However, one can observe that

$$\sum_{\ell} \left| \left[\mathbf{Q}_{m,n}^{(1)}\right]_{i,\ell} \right| \leq 1, \quad i \neq \ell. \tag{6.14}$$

Hence, the Gershgorin Theorem (HORN; JOHNSON, 1985) guarantees that the eigenvalues are within the interval

$$\rho\left(\mathbf{Q}_{m,n}^{(1)}\right) \in [-1, 1] \tag{6.15}$$

In terms of the coefficients c_i, the interference element $\epsilon_{m,n}$ can be written as

$$\begin{aligned} \epsilon_{m,n} &= \mathbf{c}^T \mathbf{F}^T \mathbf{Q}_{m,n}^{(1)} \mathbf{F} \mathbf{c} \\ &= \mathbf{c}^T \mathbf{Q}_{m,n}^{(2)} \mathbf{c}. \end{aligned} \tag{6.16}$$

Again, $\mathbf{Q}_{m,n}^{(2)}$ is Hermitian and with eigenvalues that cannot be defined analytically for any pair (m, n). Nevertheless, one can also realize that $\rho\left(\mathbf{Q}_{m,n}^{(2)}\right) \in [-1, 1]$, by analyzing the numerical radius of $\mathbf{Q}_{m,n}^{(2)}$.

6.1.3.2 Self-Interference Constraints

In order to manage the self-interference level generated by the prototype filter, the proposed problem is constrained to a maximum interference level of ϵ_0

$$|\epsilon_{m,n}| = \left|\mathbf{c}^T \mathbf{Q}_{m,n}^{(2)} \mathbf{c}\right| \leq \epsilon_0, \quad (m, n) \in \mathcal{E}. \tag{6.17}$$

Notice that the absolute value must be taken, since $\epsilon_{m,n}$ can assume both real and negative values. Unfortunately, the constraint presented in (6.17) is non-convex since $+\mathbf{Q}_{m,n}^{(2)}$ and $-\mathbf{Q}_{m,n}^{(2)}$ cannot be positive semidefinite simultaneously.

6.1.3.3 Eigenvalues Shift

The eigenvalues of $\mathbf{Q}_{m,n}^{(2)}$ can be manipulated by adding the term $\delta_\rho \mathbf{c}^T \mathbf{F}^T \mathbf{F} \mathbf{c}$ and subtracting δ_ρ from eq. (6.17), leading to

$$\begin{cases} \mathbf{c}^T \left[+\mathbf{Q}_{m,n}^{(2)} + \delta_\rho \mathbf{F}^T \mathbf{F}\right] \mathbf{c} - \delta_\rho \leq \epsilon_0 \\ \mathbf{c}^T \left[-\mathbf{Q}_{m,n}^{(2)} + \delta_\rho \mathbf{F}^T \mathbf{F}\right] \mathbf{c} - \delta_\rho \leq \epsilon_0 \end{cases}, \quad (m, n) \in \mathcal{E}, \tag{6.18}$$

which is valid if, and only if, the energy of the prototype filter is unitary, *i.e.*, $\mathbf{c}^T\mathbf{F}^T\mathbf{F}\mathbf{c} = 1$. In order to provide a more compact notation, let us rewrite eq. (6.18) as

$$\begin{cases} \mathbf{c}^T\mathbf{Q}_{m,n}^{(3a)}\mathbf{c} \leq \epsilon_0 + \delta_\rho \\ \mathbf{c}^T\mathbf{Q}_{m,n}^{(3b)}\mathbf{c} \leq \epsilon_0 + \delta_\rho \end{cases}, \tag{6.19}$$

where

$$\mathbf{Q}_{m,n}^{(3a)} = +\mathbf{Q}_{m,n}^{(2)} + \delta_\rho\mathbf{F}^T\mathbf{F} \tag{6.20}$$

and

$$\mathbf{Q}_{m,n}^{(3b)} = -\mathbf{Q}_{m,n}^{(2)} + \delta_\rho\mathbf{F}^T\mathbf{F}. \tag{6.21}$$

Considering the spectrum of $\mathbf{Q}_{m,n}^{(2)}$ and that both $\mathbf{F}^T\mathbf{F}$ and $\mathbf{Q}_{m,n}^{(2)}$ are Hermitian, one can easily observe that

$$\rho\left(\mathbf{Q}_{m,n}^{(3a)}\right) \in \left[\delta_\rho\rho_{\min}\left(\mathbf{F}^T\mathbf{F}\right) - 1, \delta_\rho\rho_{\max}\left(\mathbf{F}^T\mathbf{F}\right) + 1\right] \tag{6.22}$$

by recalling the Weyl's Inequality. A particular case takes place if $\mathbf{F}$ is orthonormal, where

$$\rho\left(\mathbf{Q}_{m,n}^{(3a)}\right) \in \left[\delta_\rho - 1, \delta_\rho + 1\right], \tag{6.23}$$

which is the case if $\mathbf{F}$ is a Slepian basis, as defined in eq. (6.5). However, if $\mathbf{F}$ is composed by a cosine sequences, as the ones in eq. (6.6), such matrix is only near-orthogonal, making the eigenvalues of $\mathbf{F}^T\mathbf{F}$ very close to the unit. Hence, there exists a non-negative value of δ_ρ which shifts all eigenvalues of $\mathbf{Q}_{m,n}^{(3a)}$ to a positive value, making this matrix positive semidefinite. Similarly, we can also conclude that $\mathbf{Q}_{m,n}^{(3b)}$ is also positive definite for a given value of δ_ρ. Hence, both entries of eq. (6.19) are convex, as both $\mathbf{Q}_{m,n}^{(3a)}$ and $\mathbf{Q}_{m,n}^{(3b)}$ are positive semidefinite (BOYD; VANDENBERGHE, 2004).

6.1.4 Spectrum Decay

As practical FBMC systems deploy windowed pulses, spectrum decay may stagnate, specially if the boundaries of the prototype filter are not null. Thus, the samples at the boundaries of the prototype filter should assume values as low as possible to ensure a fast spectrum decay. In this sense, let us define

$$p[k] = \mathbf{c}^T\mathbf{u}_k, \tag{6.24}$$

where

$$\mathbf{u}_k = \begin{bmatrix} f_0[k] & f_1[k] & \cdots & f_{N-1}[k] \end{bmatrix}^T. \tag{6.25}$$

Thus, at the boundaries of the filter, we impose the constraint

$$\left|\mathbf{c}^T\mathbf{u}_k\right| \leq u_0, \quad k \in \mathcal{K}, \tag{6.26}$$

where $\mathcal{K}$ is the set of indexes of the boundaries samples we wish to limit to a maximum level u_0. Since the prototype filter is symmetrical, *i.e.*, $p[k] = p[Lp - 1 - k]$, one does not need to constraint the amplitude of the pulse from both sides.

6.1.5 Resulting Optimization Problem

By taking eq. (6.7) as the objective function and eqs. (6.19) and (6.26) as constraints, the resulting problem can be written:

$$\begin{aligned} \mathbf{c}^* = \underset{\mathbf{c}}{\operatorname{argmin}} \quad & \mathbf{c}^T\mathbf{Q}_0\mathbf{c} \\ \text{s.t.} \quad & \mathbf{c}^T\mathbf{Q}_{m,n}^{(3a)}\mathbf{c} \leq \epsilon_0 + \delta_\rho, \quad (m,n) \in \mathcal{E} \\ & \mathbf{c}^T\mathbf{Q}_{m,n}^{(3b)}\mathbf{c} \leq \epsilon_0 + \delta_\rho, \quad (m,n) \in \mathcal{E} \\ & \left|\mathbf{u}_k^T\mathbf{c}\right| \leq u_0, \qquad\qquad k \in \mathcal{K} \\ & \mathbf{c}^T\mathbf{F}^T\mathbf{F}\mathbf{c} = 1. \end{aligned} \tag{6.27}$$

Unfortunately, the problem posed in (6.27) is non-convex as the equality constraint is quadratic instead of affine (BOYD; VANDENBERGHE, 2004). Hence, despite

$$E(\pi) = \|\mathbf{p}\|_2^2 = \mathbf{c}^T\mathbf{F}^T\mathbf{F}\mathbf{c}, \tag{6.28}$$

i.e., the prototype filter energy, being a convex function, $\|\mathbf{p}\|_2^2 = 1$ is not a convex constraint, which leads to a non-convex optimization problem. The most straightforward way of solving such a problem is by casting it as an SDP (LU et al., 2011). However, the SDP relaxation requires decoupling the solution through methods such as the rank-1 approximation or the Gaussian randomization. However, rank-1 may provide a poor final solution if the SDP solution is not a low-rank matrix. On the other hand, Gaussian randomization may converge slowly, besides being highly complex as the random vector solution must be projected into the constraints and checked if it is a feasible point. Therefore, this part of the work will focus on a different relaxation approach.

6.1.6 Convex QCQP Relaxation

As an alternative to circumvent the non-convexity of eq. (6.27), let us propose a relaxation in order to obtain a convex QCQP. First, consider the norm inequality

$$\|\mathbf{c}\|_2 \leq \|\mathbf{c}\|_1 \leq \sqrt{N}\,\|\mathbf{c}\|_2\,. \tag{6.29}$$

One can observe that there is a value of ζ such as

$$\|\mathbf{c}\|_2 = \frac{\|\mathbf{c}\|_1}{\zeta}. \tag{6.30}$$

By analyzing (6.29), one can observe that eq. (6.29) is valid for

$$1 \leq \zeta \leq \sqrt{N}. \tag{6.31}$$

Taking the previous observation, we propose exchanging the norm-2 equality constraint by a norm-1 equality

$$\frac{\|\mathbf{c}\|_1}{\zeta} = \frac{\mathbf{1}^T\mathbf{c}}{\zeta}, \tag{6.32}$$

where $\mathbf{1}$ is a vector of ones. Notice that, eq. (6.32) holds if $c_i \geq 0$, which can be obtained by a proper choice of $\mathbf{F}$. As a rule of thumb, $f_i[k]$ is chosen to be symmetrical around $(L_p - 1)/2$, i.e.,

$$[\mathbf{F}]_{\ell,i} = [\mathbf{F}]_{L_p+1-\ell,i}\,, \quad 1 \leq \ell \leq \left\lfloor \frac{L_p}{2} \right\rfloor, \tag{6.33}$$

where $f_i[k] = [\mathbf{F}]_{k+1,i}$ for $0 \leq k \leq L_p - 1$. Also, the central sample of $\mathbf{f}$ must be positive:

$$[\mathbf{F}]_{\left\lceil \frac{L_p}{2} \right\rceil,i} > 0 \tag{6.34}$$

Such features can be observed, for example, in Mirabbasi-Martin, OFDP and Hermite designs if their respective functions are properly scaled.

Therefore, a relaxed QCQP can be cast from eq. (6.27) and (6.32):

$$\begin{aligned} \mathbf{c}(\zeta) = \underset{\mathbf{c}}{\operatorname{argmin}} \quad & \mathbf{c}^T\mathbf{Q}_0\mathbf{c} \\ \text{s.t.} \quad & \mathbf{c}^T\mathbf{Q}_{m,n}^{(3a)}\mathbf{c} \leq \epsilon_0 + \delta, \quad (m,n) \in \mathcal{E} \\ & \mathbf{c}^T\mathbf{Q}_{m,n}^{(3b)}\mathbf{c} \leq \epsilon_0 + \delta, \quad (m,n) \in \mathcal{E} \\ & \left|\mathbf{u}_k^T\mathbf{c}\right| \leq u_0, \qquad\quad k \in \mathcal{K} \\ & \frac{\mathbf{1}^T\mathbf{c}}{\zeta} = 1 \\ & \mathbf{c} \geq \mathbf{0}. \end{aligned} \tag{6.35}$$

The convexity of (6.35) can be guaranteed as the Hessian of both the objective function and the constraints are positive semidefinite, and, also, the equality constraint is affine (LUO et al., 2010). Nevertheless, one must first track the value of ζ^*, for which $\|\mathbf{p}\|_2$ is as close as possible to the unity, leading to a near-optimal solution. In this sense, the associated line search problem

$$\begin{aligned} \zeta^* = \underset{\zeta}{\operatorname{argmin}} \quad & \left|1 - \mathbf{c}^T(\zeta)\mathbf{F}^T\mathbf{F}\mathbf{c}(\zeta)\right|^2 \\ \text{s.t.} \quad & 1 \leq \zeta \leq \sqrt{N} \end{aligned} \tag{6.36}$$

can be performed to track the optimal value of ζ. One can observe that the line search posed in eq. (6.36) requires the solution/evaluation of eq. (6.35). Also, the objective function of (6.36) must reach very small values to satisfy $\|\mathbf{p}\|_2 = 1$. Hence, once ζ^* is found, the relaxed solution

$$\tilde{\mathbf{c}}^* = \mathbf{c}(\zeta^*) \tag{6.37}$$

is established.

6.2 Numerical Results

In this section, we offer numerical results to corroborate the effectiveness of the proposed filter design methodology. First, we define the optimization setup for three

proposed prototype filters. After that, we provide a brief explanation of the tools deployed to solve the proposed optimization problem. Finally, we offer a performance comparison between the filters obtained through the proposed methodology *versus* the EGF, OFDP and Martin prototype filters.

6.2.1 Optimization Setup

In order to exemplify the effectiveness of the proposed design, we solve (6.36) using three different configurations referred to hereafter as Type-I, Type-II and Type-III prototype filters. All the three set of parameters are summarized in Table 6.1. It is noteworthy mentioning that we choose an overlapping factor $K = 4$, as it enables achieving filters with high performance for both SIR and spectrum measurements. Compared to the previous chapter, which focused on shorter prototype filters with a very high SIR performance the design proposed in this Chapter aims to achieve both a relatively high spectrum and symbol reconstruction performance. Furthermore, $M = 32$ was chosen to enable a better spectrum visualization. However, we must highlight at this point that the proposed design is also capable of handling other values of M.

Type-I configuration deploys $2K$ DPSS with a passband of $\omega_s = 2\pi/M$ to build the prototype filter, reasonably stringent interference tolerance ϵ_0 and near-null border samples. On the other hand, Type-II and Type-III filters are built through the summation of $K+1$ cosines. Type-II imposes a higher reconstruction constraint, while Type-III focuses on a very fast spectrum decay. Furthermore, we set $\delta = 2$ as it can easily make $\mathbf{Q}_{m,n}^{(3a)}$ and $\mathbf{Q}_{m,n}^{(3b)}$ positive semidefinite, according to eq. (6.22). Concerning ω_c, it is noteworthy mentioning that such a parameter is set around $2\pi/M$, given the subcarrier bandwidth and separation. For Type-II and III, we set a more stringent ω_c to reduce the spectrum level within adjacent subcarriers.

Table 6.1 Optimization parameters setup for the proposed method considering $K = 4$, $M = 32$, and $L_p = 129$

Parameter	Type-I	Type-II	Type-III
N	$2K$	$K+1$	$K+1$
ω_c	$\frac{2\pi}{M}$	$\frac{K}{N}\frac{2\pi}{M}$	$\frac{K}{N}\frac{2\pi}{M}$
ϵ_0	$2 \cdot 10^{-4}$	$8 \cdot 10^{-5}$	$2 \cdot 10^{-4}$
u_0	10^{-12}	10^{-12}	10^{-12}
$\mathcal{K}$	$\{0, 1\}$	$\{0\}$	$\{0, 1\}$
δ_ρ	2	2	2
$f_i[k]$	Slepian sequences, eq. (6.5)	Cosine sequences, eq. (6.6)	Cosine sequences, eq. (6.6)

The solution for the proposed design with the configurations described in Table 6.1 takes two phases. First, the master problem (6.36) is solved by using the Golden

search, whereas the slave problem (6.35) was solved through MOSEK 8.0. For this class of problem, MOSEK casts the original QCQP as a SOCP, which is solved by the interior-point algorithm described in (ANDERSEN et al., 2003). In order to achieve an easier implementation, (6.36) was parsed into MATLAB using the modeling language CVX. The solution of the proposed problem, *i.e.*, the weights of the filters, are provided in Appendix B, where some additional observations are offered.

6.2.2 Prototype Filter Performance Analysis

In Fig. 6.1, one can observe both the impulse and frequency responses of the prototype filters obtained via the proposed convex optimization problem. As for the impulse response, all prototype filters are very similar. Nevertheless, the frequency response of Type-I, Type-II and Type-III are very distinguishable, besides presenting small sidelobes and fast spectrum decay. In particular, Type-I and Type-III presented a very expressive spectrum decay, compared with Type-II. However, by promoting a comparison among Type-I, Type-II, Type-III, EGF, OFDP, and Martin prototype filters, one concludes that the proposed pulses achieved a superior spectrum decay with small sidelobes. Indeed, one may also observe that Type-II and Mirabbasi-Martin prototype filters are very similar, but the former presented smaller sidelobes.

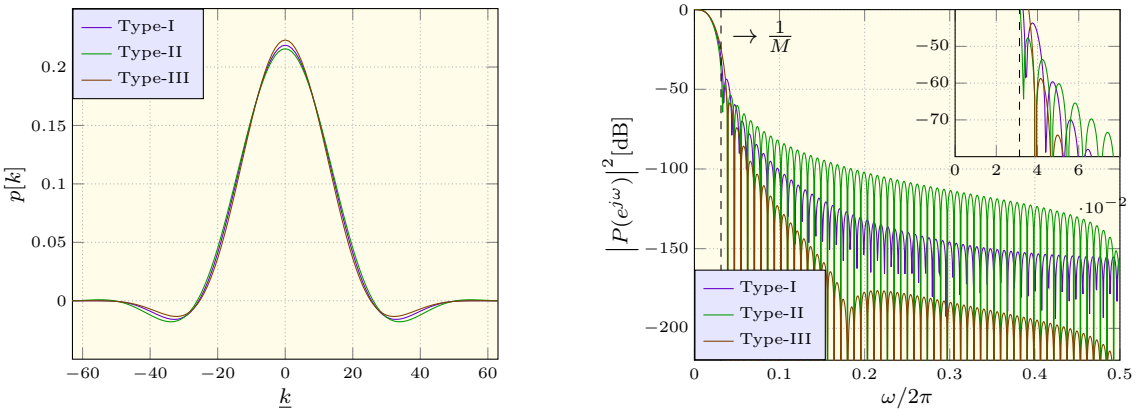

(a) Impulse Response **(b)** Frequency Response

Figure 6.1 Type-I, II and III pulses ($K = 4$, $M = 32$, and $L_p = 129$)

Let us now proceed a more precise analysis by deploying the figures of merit discussed in Section 3.1. In this sense, Table 6.2[2] summarizes the figures of merit of the proposed prototype filters *versus* the EGF, OFDP, and Martin. Initially, one can observe that the EGF design provides a poor spectrum and a variable SIR performance tuned by α. In this sense, high values of α lead to a high SIR but a poorer spectrum, while the opposite holds, where $\alpha = 1$ is typically considered a good trade-off. Moreover, Martin

[2]The best filter value for each parameter is highlighted in green, while the worst is marked in red; the EGF with $\alpha = 1/2$ and $\alpha = 2$ were not marked in red or green due to their poor symbols reconstruction *versus* spectrum performance trade-off.

Filter presents a solid performance, with a high SIR and a good spectrum performance, *i.e.*, small sidelobes, fast energy decay and low frequency spread. However, such filter resulted in the poorest Heisenberg factor. Despite outperforming the EGF in terms of spectrum, the OFDP design performed poorly, including the OoB energy. Concerning the proposed prototype filters, Type-I delivers a reasonably high SIR and a very competitive spectrum performance. Interestingly, Type-II filter showed a slightly superior performance, in almost all aspects, than Martin prototype filter, making it an attractive choice. It is worth mentioning that Type-II filter spectrum superiority over the Martin prototype filter comes by its slightly reduced passband $\omega_c = \frac{K}{M}\frac{2\pi}{M}$. Furthermore, Type-II filter deploys an extra tone ($N = K + 1$) when compared with the Martin filter (K tones), improving the symbol reconstruction. Finally, Type-III presented a similar SIR performance to Type-I and the smallest MSL. However, the OoB energy $\overline{E}(2\pi/M)$ is among the highest.

Table 6.2 Prototype filters comparison considering $K = 4$, $M = 32$, and $L_p = 129$.

Prototype Filter	SIR[dB]	MSL[dB]	D_k	D_ν	ξ	$\overline{E}\left(\frac{2\pi}{M}\right)$[dB]	$\overline{E}\left(\frac{4\pi}{M}\right)$[dB]
EGF ($\alpha = 1/2$)	33.733	−58.208	0.396	0.229	0.878	−33.954	−48.812
EGF ($\alpha = 2$)	114.481	−21.376	0.228	0.399	0.874	−12.461	−20.670
EGF ($\alpha = 1$)	60.498	−33.801	0.285	0.285	0.976	−19.697	−33.504
Martin	65.237	−39.860	0.388	0.232	0.883	−45.614	−70.604
OFDP	59.865	−38.332	0.346	0.246	0.933	−35.448	−62.288
Type-I	52.746	−43.635	0.364	0.239	0.915	−42.301	−82.958
Type-II	68.090	−47.678	0.379	0.234	0.897	−50.087	−72.934
Type-III	51.252	−58.729	0.348	0.244	0.934	−35.200	−100.569

To complement the OoB energy measurements presented in Table 6.2[3], Fig. 6.2 portrays the OoB energy for a broad range of frequencies. Through such a figure, one can observe how fast the energy decays throughout the spectrum. Hence, faster decays indicate high spectrum efficiency and lower interference to adjacent bands.

6.2.3 BER Performance

As observed previously, the proposed prototype filters can offer high performance in terms of SIR and spectrum containment. However, we also present the performance in terms of BER of an FBMC system in more contemporary application scenarios. In this sense, we chose a point-to-point MIMO-FBMC system (ROTTENBERG et al., 2017) deploying N_t transmit antennas and N_r receive antennas using V-BLAST topology, *i.e.*, spatial multiplexing mode. Furthermore, symbols are equalized via a ZF MIMO equalizer

[3]The best filter for each parameter is highlighted in green, while the worst is marked in red. The EGF with $\alpha = 1/2$ and $\alpha = 2$ were excluded not marked in red or green due to their poor symbol reconstruction versus spectrum performance trade-off.

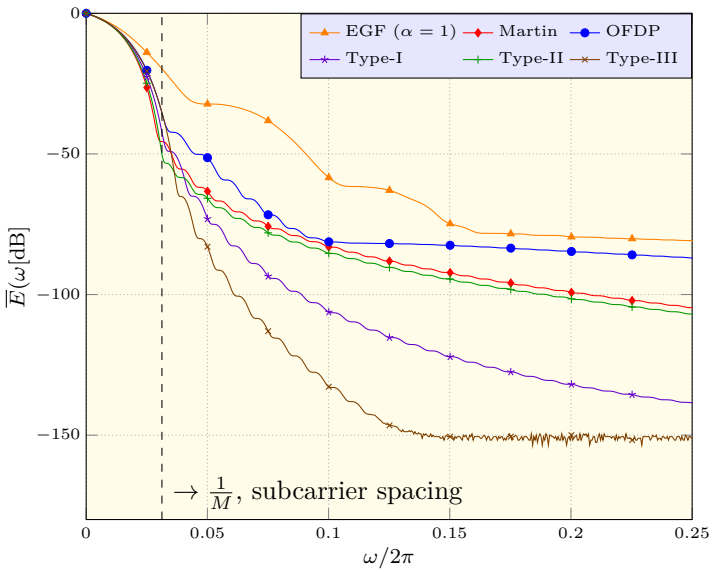

Figure 6.2 OoB Energy emission for prototype filters considering $K = 4$, $M = 32$, and $L_p = 129$

with L_w taps proposed in (IHALAINEN et al., 2011), which is more flexible than other methods such as (CHEN; MAEHARA, 2017) since the equalizer does not require a flat channel response. The performance of the system was evaluated in a frequency-selective Rayleigh channel considering three different scenarios described in Table 6.3. Notice that the radio channel of Scenarios [A] and [C] are reasonably frequency selective, whereas Scenario [B] can be considered frequency flat per subcarrier.

The system herein described operates in a selective Rayleigh channel with an exponential power delay profile (CHO JAEKWON KIM; KANG, 2010) with an RMS delay spread τ_{rms} and no antenna correlation. Considering that each subcarrier takes a band of $B_{sc} = 2/M$ and taking the 90th percentile coherence bandwidth $B_{c,90} = 1/(50\tau_{rms})$, eq. (4.31) of (HAMPTON, 2014), we define the ratio between such numbers to be

$$\eta_B = \frac{B_{c,90}}{B_{sc}}, \tag{6.38}$$

which are used to parameterize the channel selectivity. Furthermore, we make no use of CP in order to provide a higher spectral efficiency.

Fig. 6.3 depicts the BER performance for all configurations and a wide normalized SNR (E_b/N_0) range. Observing the results for Scenario [A], we can conclude that even a 7 taps equalization was unable to compensate the channel effect properly under a high SNR regime, introducing a BER floor. Yet in this configuration, we can also observe that the BER floor level is proportional to D_ν, where, for example, the EGF filter performed poorly due to its higher frequency dispersion. For Scenario [B], all filters performed similarly in the analyzed E_b/N_0 range. Hence, despite differences in terms of the measured SIR, the proposed prototype filters seem to be suitable in practical scenarios. For Scenario [C], diversity improved the BER considerably, making possible the usage of a single tap filter for channel equalization.

At this point, it is noteworthy mentioning that the BER floor can be established in two cases. The first case is the BER floor generated due to the subcarrier frequency selectivity which took place in Scenario [A]. The other BER floor level is dictated by the self-interference of the prototype filter, which can be measured using the SIR parameter. In Scenario [A], one could lower the BER floor level by increasing the number of subcarriers or, conversely, by deploying a longer equalizer. However, such BER floor never surpasses the one dictated by the self-interference of the prototype filter.

Despite possessing different SIR levels, all the prototype filters presented similar BER performance in each analyzed scenario, as depicted in Fig. 6.3. Performance differences in Scenario [B] and [C] should arise only in higher E_b/N_0 level, which would require much more demanding computational resources. However, filters with extremely high SIR levels may not be required as systems typically do not operate in an E_b/N_0 level around $70 - 100$[dB], where self-interference should take place. Despite Type-I and Type-III possessing lower SIR levels, they do not introduce noticeable performance losses in the presented E_b/N_0 range, which covers most practical application scenarios. Thus, the keypoint of this analysis is to demonstrate that the proposed prototype filters impose no symbol reconstruction drawbacks, while offering a considerable spectrum improvement, making them an interesting choice for current and future applications.

6.3 Conclusions

In this chapter, we proposed a prototype filter design framework capable of providing high symbol reconstruction performance and desirable spectral features. The main difference between the proposed design methodology and other available options is its solution method based on convex optimization. In this sense, we were able to write such a complex design

Table 6.3 Prototype filters comparison

System	MIMO V-BLAST, $N_t \times N_r$ (ROTTENBERG et al., 2017)	
	FBMC multiplexing, No CP, $M = 64$, $K = 4$, $L_p = 257$	
	Uncoded 8-PAM, equivalent to 64QAM in OFDM	
	L_w-taps Zero-Forcing Equalizer (IHALAINEN et al., 2011)	
Channel	Rayleigh	
	Exponential PDP (CHAYAT, 1997)	$\mathbb{E}\left[\lvert h[k]\rvert^2\right] = \frac{1 - e^{-1/\tau_{\text{rms}}}}{e^{-(1+10\tau_{\text{rms}})/\tau_{\text{rms}}}} e^{-\ell/\tau_{\text{rms}}}$ $\ell = 0, 1, \cdots 10\tau_{\text{rms}}$
	90th Percentile Coherence Band (HAMPTON, 2014, eq. (4.31))	$B_{c,90} = 1/(50\tau_{\text{rms}})$
	Subchannel band	$B_{sc} = 2/M$
	Selectivity Index	$\eta_B = B_{c,90}/B_{sc}$
Scenario	[A] 4×4, $L_w = 7$, $\eta_B = 3$	
	[B] 4×4, $L_w = 1$, $\eta_B = 30$	
	[C] 4×6, $L_w = 7$, $\eta_B = 3$	

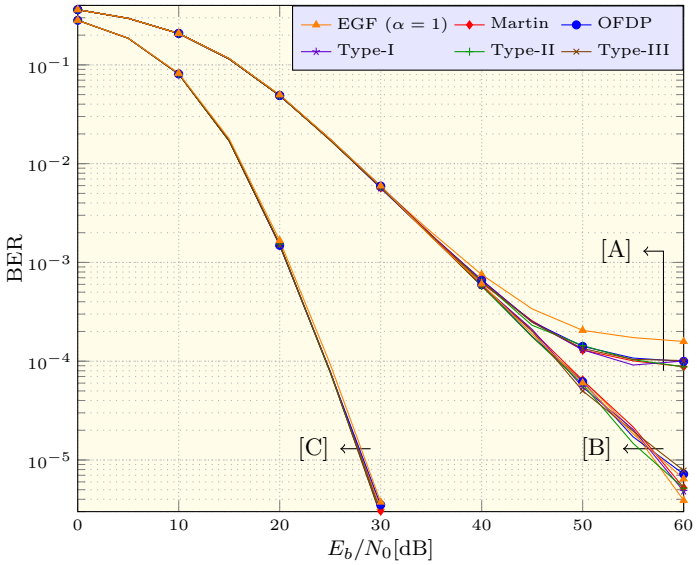

Figure 6.3 BER performance for different prototype filter choices

into a convex QCQP problem guided by a line search, which benefits from powerful available optimization tools. As a result, we proposed three prototype filters. The Type-I and Type-III filters presented very fast spectrum decays, with the MSL ranging from -45 to -58[dB] and reasonably high SIR values. On the other hand, the Type-II filter demonstrated to be slightly superior, in almost all aspects, than the Mirabbasi-Martin design, which is a standard prototype filter choice for FBMC systems. Thus, the proposed design methodology has demonstrated to be both flexible and effective, given the superior spectrum performance achieved by the proposed prototype filters.

7 Theoretical Error Probability of FBMC Systems

As observed in previous Chapters, the prototype filter choice is a critical point to be addressed when designing FBMC systems. Since the deployment of different prototype filters yields different SIR levels, symbol reconstruction performance, *i.e.*, BER performance is expected to be different. Despite the effects of the prototype filter on the overall performance of FBMC transmissions being extensively studied, the provision expressions for Bit Error Probability (BEP) have been ignored so far. This topic remained ignored as prototype filters can be designed to achieve high SIR levels, meaning marginal effects on the BER performance. Moreover, one can also deploy SIR or distortion measurements to assess the effectiveness of the prototype filter on the overall transmission of an FBMC system qualitatively. However, the provision of closed-form BEPs has not been proposed due to their non-trivial solution. From this perspective, the main contribution of this chapter lies in the provision of analytic expressions of BEP for FBMC systems, regardless of the prototype filter option. Hence, as an effective contribution and novelty, we quantify the prototype filter effect on the BER performance of an FBMC system, which was known only qualitatively until now.

7.1 The Single Carrier Case

In order to provide a comprehensive presentation of the subject, let us present first the single carrier case for calculating the BEP of the transmission of PAM symbols. Initially, this section briefly discusses the N_p-PAM modulation. In the sequel, the BEPs are derived considering a single carrier transmission of N_p-PAM symbols over AWGN as well as frequency-flat Rayleigh channels.

7.1.1 PAM Modulation

By deploying PAM, data symbols are constrained to the alphabet

$$\mathcal{A}_{N_p} = \{-N_p + 1, -N_p + 3, \cdots, N_p - 1\}, \tag{7.1}$$

meaning that only the in-phase component is deployed. Furthermore, one can easily infer that each N_p-PAM symbol can deliver

$$N_b = \log_2(N_p) \tag{7.2}$$

bits by using an average symbol energy of

$$E_s = \frac{N_p^2 - 1}{3}. \tag{7.3}$$

7.1.2 BEP for Single Carrier PAM Transmission over AWGN Channels

First, consider the simplest scenario: the transmission of PAM symbols over an AWGN channel. Such a transmission can be modeled as

$$x = a + \eta, \tag{7.4}$$

where a is the transmitted N_p-PAM symbol and η is the additive noise described by the Probability Density Function (PDF)

$$f_\eta(y) = \frac{1}{\sqrt{\pi N_0}}\, e^{-\frac{y^2}{N_0}}, \tag{7.5}$$

where N_0 is the noise power density. Furthermore, one can rewrite the noise power in terms of the normalized SNR γ_b[1] based on eq. (7.2) and (7.3), *i.e.*,

$$N_0 = \frac{N_p^2 - 1}{3 \log_2 N_p \gamma_b}. \tag{7.6}$$

A classical and straightforward approximation for evaluating the BEP of PAM symbols corrupted by additive noise is given by Proakis and Manolakis (2000):

$$P_b^{\text{AWGN,PAM}}(\gamma_b) \approx \frac{2\,(N_p - 1)}{N_p \log_2 N_p} \int_1^\infty f_\eta(z) dz. \tag{7.7}$$

Despite being very simple, eq. (7.7) only considers symbol errors caused by adjacent symbols. Moreover, eq. (7.7) approximates the BEP as the Symbol Error Probability (SEP) divided by the number of bits. Thus, such expression considers that symbols are misestimated at the same rate of the bits.

By solving eq. (7.7) considering an AWGN channel, one can obtain the approximated BEP of an N_p-PAM transmission over an AWGN channel:

$$P_b^{\text{AWGN,PAM}}(\gamma_b) \approx \frac{2\,(N_p - 1)}{N_p \log_2 N_p} Q\left(\sqrt{\frac{6 \log_2 N_p}{N_p^2 - 1} \gamma_b}\right). \tag{7.8}$$

where

$$Q(y) = \frac{1}{\sqrt{2\pi}} \int_y^\infty e^{-\frac{z^2}{2}}\, dz \tag{7.9}$$

is the tail distribution of a standard normal distribution. Notice that an exact BEP expression is far more complex as all error combinations must be taken into account. Fortunately, Cho and Yoon (2002) offer the exact expression considering N_p-PAM Gray coded symbols:

$$P_b^{\text{AWGN,PAM}}(\gamma_b) = \frac{1}{N_p \log_2 N_p} \sum_{k=1}^{\log_2 N_p} \sum_{i=0}^{(1-2^{-k})N_p - 1} w_{i,k,N_p} \int_{2i+1}^\infty f_\eta(z) dz, \tag{7.10}$$

[1] Bit energy per noise energy.

where

$$w_{i,k,N_p} = (-1)^{\lfloor i2^{k-1}/N_p \rfloor} \left(2^{k-1} - \left\lfloor \frac{i2^{k-1}}{N_p} + \frac{1}{2} \right\rfloor \right). \tag{7.11}$$

In particular, the transmission over AWGN channels leads to the exact BEP

$$P_b^{\text{AWGN,PAM}}(\gamma_b) = \frac{2}{N_p \log_2 N_p} \sum_{k=1}^{\log_2 N_p} \sum_{i=0}^{(1-2^{-k})N_p - 1} w_{i,k,N_p} Q\left((2i+1) \sqrt{\frac{6 \log_2 N_p}{N_p^2 - 1} \gamma_b} \right). \tag{7.12}$$

7.1.3 BEP for Single Carrier PAM Transmission over Frequency-Flat Rayleigh Channels

By considering that symbol transmission takes place over frequency-flat Rayleigh channels, the transmission model presented in (7.4) must be rewritten as

$$x = ha + \eta, \tag{7.13}$$

where h is the complex-valued channel coefficient.

Since the channel fades the signal randomly, one must consider all the possible values h can take in order to evaluate the average BEP. Thus, the overall BEP is obtained by the integral

$$P_b^{\text{RAY,PAM}}(\gamma_b) = \int_0^\infty f_{|h|^2}(z, \gamma_b) P_b^{\text{AWGN}}(z) dz, \tag{7.14}$$

where

$$f_{|h|^2}(y, \gamma_b) = \frac{1}{\gamma_b} e^{-\frac{y}{\gamma_b}} u(y). \tag{7.15}$$

is the PDF of the squared channel coefficient for a given normalized SNR γ_b.

By combining and solving eqs. (7.14) and (7.8), it can be concluded that an approximation for the BEP of N_p-PAM symbols transmitted over frequency-flat Rayleigh channels is given by

$$P_b^{\text{RAY,PAM}}(\gamma_b) \approx \frac{N_p - 1}{N_p \log_2 N_p} \left(1 - \frac{\sqrt{\frac{3 \log_2 N_p}{N_p^2 - 1} \gamma_b}}{\sqrt{\frac{3 \log_2 N_p}{N_p^2 - 1} \gamma_b + 1}} \right). \tag{7.16}$$

Similarly, an exact formula can be obtained through eqs. (7.14) and (7.12):

$$P_b^{\text{RAY,PAM}}(\gamma_b) = \frac{1}{N_p \log_2 N_p} \sum_{k=1}^{\log_2 N_p} \sum_{i=0}^{(1-2^{-k})N_p - 1} w_{i,k,N_p} \left(1 - \frac{\sqrt{\frac{3(2i+1)^2 \log_2 N_p}{N_p^2 - 1} \gamma_b}}{\sqrt{\frac{3(2i+1)^2 \log_2 N_p}{N_p^2 - 1} \gamma_b + 1}} \right), \tag{7.17}$$

which was proposed by Lopes et al. (2007).

7.2 The FBMC Case

Based on the foundation provided previously, this section builds up the closed-form BEP expressions for FBMC systems over AWGN and frequency-flat Rayleigh channels.

7.2.1 BEP for FBMC Transmission over AWGN Channels

For the FBMC case over AWGN, one must combine the multiplexed signal with the effect of the additive noise, *i.e.*,

$$x[k] = s[k] + \eta[k], \tag{7.18}$$

where $\eta[k] \sim \mathcal{CN}(0, N_0)$. Hence, the reconstruction of the n_0th symbol of the m_0th subcarrier can be proceeded by combining eqs. (7.18) and (5.7), *i.e.*,

$$\begin{aligned} x_{m_0,n_0} &= \mathrm{Re}\left\{\langle x[k]\,|p_{m_0,n_0}[k]\rangle\right\} \\ &\quad a_{m_0,n_0} \\ &\quad + \sum_{\substack{n\neq n_0 \\ m\neq m_0}} a_{m,n}\epsilon_{m,n} + \mathrm{Re}\left\{\langle \eta[k]\,|\,p_{m_0,n_0}[k]\rangle\right\} \\ &= a_{m_0,n_0} + \epsilon_0 + \eta_0, \end{aligned} \tag{7.19}$$

where ϵ_0 is the overall interference experienced by a_{m_0,n_0}. At this point, one can observe that the easiest option to derive the BEP of an FBMC signal under AWGN signal is achieved by

i. obtaining the PDF of the noise combined with the interference $(\epsilon_0 + \eta_0)$;

ii. deploying eq. (7.7) for an approximate BER expression or (7.12) for the exact BER formula derivation.

7.2.1.1 PDF of the Noise plus Interference

By recalling that the resulting PDF of the sum of two random variables is the convolution of both PDFs, *i.e.*,

$$f_{a+b}(y) = \int_{-\infty}^{\infty} f_a(z) f_b(y-z) dz. \tag{7.20}$$

Thus, since the PDF of the nth PAM symbol of the mth subcarrier is modeled by

$$f_{a_{m,n}}(y) = \frac{1}{N_p} \sum_{a_{m,n}\in\mathcal{A}_{N_p}} \delta\left(y - a_{m,n}\right) \tag{7.21}$$

and $\epsilon_{m,n}$ is deterministic, one may conclude that

$$f_{a_{m,n}\epsilon_{m,n}}(y) = \frac{1}{N_p} \sum_{a_{m,n}\in\mathcal{A}_{N_p}} \delta\left(y - a_{m,n}\epsilon_{m,n}\right). \tag{7.22}$$

Notice that the summation notation adopted in eqs. (7.21) and (7.22) provides a more compact presentation. In this notation, the summation includes all the elements of the N_p-PAM set described in eq. (2.2).

According to eq. (7.19), the interference experienced at the receiver side (ϵ_0) is the combination of adjacent symbols $a_{m,n}$ scaled by their respective interference elements

$\epsilon_{m,n}$. Hence, a series of convolutions must be evaluated in order to evaluate the PDF of ϵ_0, which leads to

$$f_{\epsilon_0}(y) = \frac{1}{N_p^{|\mathcal{E}'|}} \sum_{a_{0,-2K+1} \in \mathcal{A}_{N_p}} \cdots \sum_{a_{M-1,2K-1} \in \mathcal{A}_{N_p}} \delta\left(y - \sum_{(m,n)\in\mathcal{E}'} a_{m,n}\epsilon_{m,n}\right), \tag{7.23}$$

where the last summation includes all the elements of $\mathcal{E}'$, which is defined by

$$\mathcal{E}' = \left\{ \epsilon_{m,n} \;\middle|\; \begin{array}{l} 0 \leq m \leq M-1 \\ |n| \leq \left\lceil \frac{L_p - 1}{M/2} \right\rceil - 1 \\ m+n \text{ even} \\ m+n \neq 0 \end{array} \right\} \tag{7.24}$$

Once more, such a notation was adopted in favor of a more compact presentation. Notice that eq. (7.23) has a large number of coefficients as it takes into account all possible combination of interfering elements $a_{m,n}\epsilon_{m,n}$. In this sense, we limited the last summation to the set $\mathcal{E}'$ in order to ignore null interfering elements and decrease the complexity of the equation.

$$f_{\epsilon_0+\eta_0}(y) = \frac{1}{N_p^{|\mathcal{E}'|}}\sqrt{\frac{1}{2\pi}\frac{6\log_2 N_p}{N_p^2-1}\gamma_b}\sum_{a_{0,-2K+1}\in\mathcal{A}_{N_p}}\cdots\sum_{a_{M-1,2K-1}\in\mathcal{A}_{N_p}}\exp\left[-\frac{6\log_2 N_p}{N_p^2-1}\gamma_b\left(\frac{y-\sum\limits_{(m,n)\in\mathcal{E}'}a_{m,n}\epsilon_{m,n}}{2}\right)^2\right] \tag{7.25}$$

$$P_b^{\text{AWGN,FBMC}}(\gamma_b)\approx\frac{2\left(N_p-1\right)}{N_p^{|\mathcal{E}'|+1}\log_2 N_p}\sum_{a_{0,-2K+1}\in\mathcal{A}_{N_p}}\cdots\sum_{a_{M-1,2K-1}\in\mathcal{A}_{N_p}}Q\left[\sqrt{\frac{6\log_2 N_p}{N_p^2-1}\gamma_b}\left(1-\sum_{(m,n)\in\mathcal{E}'}a_{m,n}\epsilon_{m,n}\right)\right] \tag{7.26}$$

$$P_b^{\text{AWGN,FBMC}}(\gamma_b) = \frac{2}{N_p^{|\mathcal{E}'|+1}\log_2 N_p}\sum_{a_{0,-2K+1}\in\mathcal{A}_{N_p}}\cdots\sum_{a_{M-1,2K-1}\in\mathcal{A}_{N_p}}\sum_{k=1}^{\log_2 N_p}\sum_{i=0}^{(1-2^{-k})N_p-1}w_{i,k,N_p}Q\left[\sqrt{\frac{6\log_2 N_p}{N_p^2-1}\gamma_b}\left(2i+1-\sum_{(m,n)\in\mathcal{E}'}a_{m,n}\epsilon_{m,n}\right)\right] \tag{7.27}$$

$$P_b^{\text{RAY,FBMC}}(\gamma_b) \approx \frac{N_p-1}{N_p^{|\mathcal{E}'|+1}\log_2 N_p}\sum_{a_{0,-2K+1}\in\mathcal{A}_{N_p}}\cdots\sum_{a_{M-1,2K-1}\in\mathcal{A}_{N_p}}\left[1-\left(2i+1-\sum_{(m,n)\in\mathcal{E}'}a_{m,n}\epsilon_{m,n}\right)\sqrt{\frac{\frac{6\log_2 N_p}{N_p^2-1}\gamma_b}{\left(2i+1-\sum\limits_{(m,n)\in\mathcal{E}'}a_{m,n}\epsilon_{m,n}\right)^2\frac{6\log_2 N_p}{N_p^2-1}\gamma_b+1}}\right] \tag{7.28}$$

$$\begin{aligned}P_b^{\text{RAY,FBMC}}(\gamma_b) &= \frac{1}{N_p^{|\mathcal{E}'|+1}\log_2 N_p}\sum_{a_{0,-2K+1}\in\mathcal{A}_{N_p}}\cdots\sum_{a_{M-1,2K-1}\in\mathcal{A}_{N_p}}\sum_{k=1}^{\log_2 N_p}\sum_{i=0}^{(1-2^{-k})N_p-1}w_{i,k,N_p}\\ &\times\left[1-\left(2i+1-\sum_{(m,n)\in\mathcal{E}'}a_{m,n}\epsilon_{m,n}\right)\sqrt{\frac{\frac{6\log_2 N_p}{N_p^2-1}\gamma_b}{\left(2i+1-\sum\limits_{(m,n)\in\mathcal{E}'}a_{m,n}\epsilon_{m,n}\right)^2\frac{6\log_2 N_p}{N_p^2-1}\gamma_b+1}}\right]\end{aligned} \tag{7.29}$$

It is noteworthy mentioning that the increasing number of elements on the PDF of the summation of random variables can be observed in other random processes. For example, this behavior can also be observed on the Bates and Irwin-Hall distributions (MARENGO et al., 2017; BRADLEY; GUPTA, 2002), which consists of the summation of an arbitrary number of uniform random variables.

Since $f_{\epsilon_0}(x)$ is composed exclusively by Dirac delta functions, convolving it with any other function is trivial as the Dirac Function is the neutral element for convolution operation. Thus, the overall PDF of the noise plus interference can be expressed by (7.25). Therefore, by combining eq. (7.25) with eq. (7.7), the approximate BEP for FBMC signals over AWGN is obtained as (7.26). On the other hand, the exact BEP expression is obtained by combining eqs. (7.25) and (7.12), resulting in eq. (7.27).

7.2.2 BEP for FBMC Transmission over Frequency-Flat Rayleigh Channels

The received signal of an FBMC system operating over frequency-flat Rayleigh channels can be expressed as

$$x[k] = \sum_{\ell=0}^{\infty} h[\ell]s[k-\ell] + \eta[k], \tag{7.30}$$

where $h[k]$ is the channel impulse response, which fades the transmitted signal and may introduce frequency selectivity. However, let us consider the simplifying assumption that each subchannel is frequency-flat. Such an assumption is plausible as multicarrier systems are typically designed to enable a simple one-tap per-subchannel equalization. Notice, however, that multi-tap equalizers (IHALAINEN et al., 2005; WALDHAUSER et al., 2008b; IHALAINEN et al., 2011) can be deployed as an alternative in scenarios where the number of subcarriers is insufficient to lead to subchannel frequency-flatness.

Aiming to retrieve the conveyed data, the received signal is pre-processed using the appropriate FBMC pulse, leading to

$$\begin{aligned} x_{m_0,n_0} &= \mathrm{Re}\left\{\langle x[k] \,|\, p_{m_0,n_0}[k]\rangle\right\} \\ &= H_{m_0}\left(a_{m_0,n_0} + \sum_{\substack{n\neq n_0 \\ m\neq m_0}} a_{m,n}\epsilon_{m,n}\right) + \mathrm{Re}\left\{\langle \eta[k] \,|\, p_{m_0,n_0}[k]\rangle\right\} \\ &\approx H_{m_0}\left(a_{m_0,n_0} + \epsilon_0\right) + \eta_0, \end{aligned} \tag{7.31}$$

where H_{m_0} is the frequency response of the m_0th subcarrier. Notice that eq. (7.31) is an approximation, as one must recall that the subchannels were considered frequency-flat. Moreover, eq. (7.31) is composed of the faded symbol plus the interference and the additive noise. From this perspective, the approximate BEP expression for an FBMC system operating over frequency-flat Rayleigh channels can be obtained by integrating eq. (7.14)

considering eq. (7.26), which leads to eq. (7.28), while the exact expression emerges from the integration of eq. (7.14) considering eq. (7.27), yielding (7.29).

7.3 Numerical Results

This section presents the numerical results aiming to demonstrate the effectiveness of the BEP expressions derived throughout this paper. In order to achieve such a goal, we compare the derived BEP expressions with the simulated BER for the OFDM and FBMC setups described in Table 7.1, considering both AWGN and frequency-flat Rayleigh channels. For FBMC, two prototype filter were deployed, the EGF and the Mirabbasi-Martin filter. Notice that the EGF (SIOHAN et al., 2002) was chosen as the prototype filter due to its flexibility, which enables achieving different self-interference levels by tuning the spreading factor α. This feature is useful to test the effectiveness of the derived expressions under very distinct scenarios. In particular, the EGF set with $\alpha = 1.00$ provides a large SIR of 60.49 dB, enabling near-perfect symbol reconstruction. On the other hand, by setting $\alpha = 0.25$, the SIR of the EGF is reduced to 21.27 dB, leading to a poor BER performance. Moreover, the Mirabbasi-Martin prototype filter is also deployed in this comparison as it presents a high spectrum and symbol reconstruction performances. Indeed, such a prototype filter is one of the most popular choices, being recommended in the PHYDIAS project (VIHOLAINEN et al., 2009).

Table 7.1 Parameters for the FBMC system.

Parameter	OFDM	FBMC
Modulation order	64-QAM	8-PAM
Subcarriers, M	16	16
Cyclic Prefix	$M/8$	0
Overlapping factor, K	-	4
Filter length, L_p	-	$MK+1$
Prototype Filter	-	EGF, $\alpha = \{0.25, 1.00\}$, Mirabbasi-Martin

7.3.1 Complexity Considerations

Before presenting the BEP results, let us discuss the complexity of the derived expressions. Despite not relying on complex functions, the main issue of the derived expressions is the large number of terms of the summations. A more careful analysis reveals that the BEP expressions in eq. (7.26), (7.27), (7.28) and (7.29) presents at least $N_p^{|\mathcal{E}|+1}$ terms. Hence, the summation of a huge number of terms is required in

order to provide the theoretical BEP expression. As an example, evaluating the BEP of the reasonably small system portrayed in Table 7.1 would require the evaluation of approximately $3 \cdot 10^{107}$ terms. However, the interference elements $\epsilon_{m,n}$ decay rapidly as shown in Fig. 7.1. Therefore, let us restrain the set $\mathcal{E}$ to the 8 largest elements in order to make the developed expressions feasible and therefore useful. Notice that even with the limited set, the theoretical expressions require the summation of, at least, $16 \cdot 10^6$ elements.

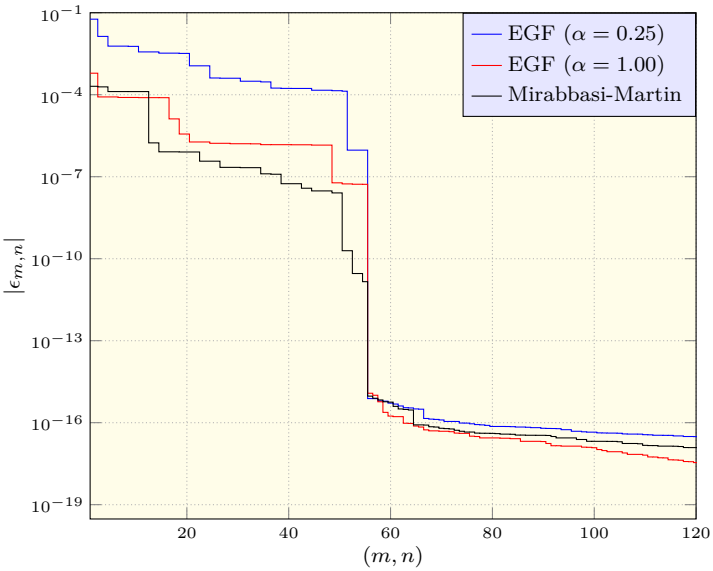

Figure 7.1 Ordered absolute values for the interference elements $\epsilon_{m,n}$ for the FBMC system described in Table 7.1.

7.3.2 BER Performance

In Figures 7.2a and 7.2b, we present both the simulated BER and the theoretical BEP for the FBMC system described in Table 7.1 considering an EGF prototype filter, and AWGN and frequency-flat Rayleigh scenarios. With $\alpha = 1.00$ the FBMC system showed no apparent performance loss, whereas with $\alpha = 0.25$, the BER performance is considerably severed, leading to a BER floor around 10^{-3} in the Rayleigh scenario. Such behavior is established due to the degradation of the prototype filter SIR, which dictates the amount of self-interference generated by the prototype filter. However, it is important to state that the prototype filter SIR improves as α increases, while the spectrum gets increasingly poor. As an example, EGFs with α values of 0.5, 1 and 2 lead to SIR levels of 33.73, 60.49 and 114.48 dB, respectively, whereas the OoB energy emission increases gradually to -33.95, -19.69 and -12.46 dB.

In order to prove the effectiveness of the derived expression for any prototype filter, Figures 7.3a and 7.3b compares the BER with the BEP for an FBMC system deploying a Mirabbasi-Martin prototype filter (MIRABBASI; MARTIN, 2003) and the parameters described in Table 7.1. Once more, the simulation and the analytically results depicted

in Figures 7.3a and 7.3b are very close, proving the effectiveness of the proposed BEP expressions. Moreover, since the Mirabbasi-Martin prototype filter presents a high SIR level, ≈ 65.25 dB, performance losses were not observed in Figures 7.3a and 7.3b.

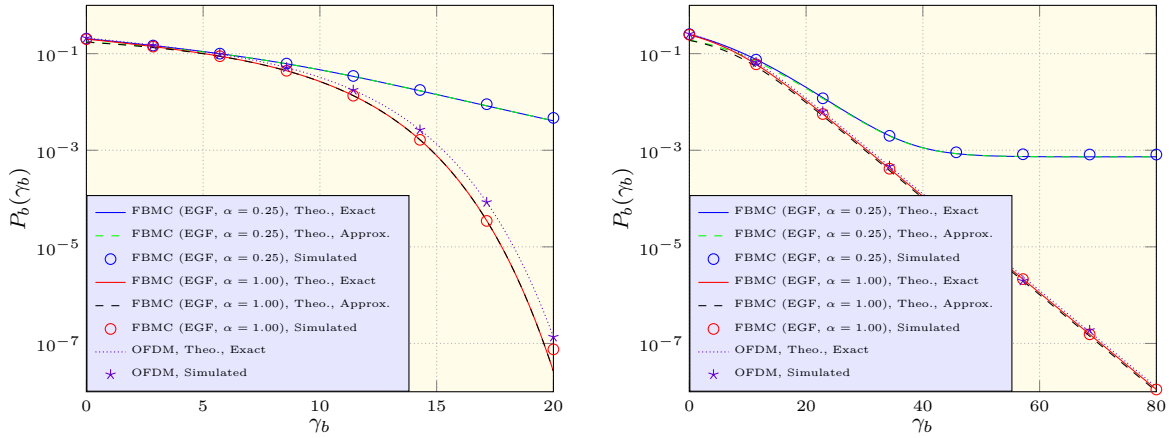

(a) AWGN **(b)** Rayleigh

Figure 7.2 Theoretical and simulated BER for the FBMC system described in Table 7.1 and with EGF prototype filter.

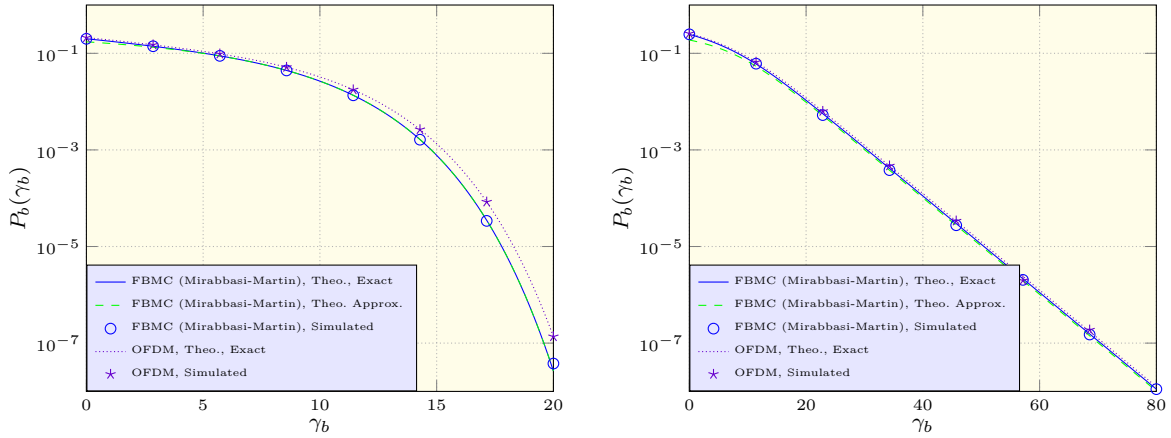

(a) AWGN **(b)** Rayleigh

Figure 7.3 Theoretical and simulated BER for the FBMC system described in Table 7.1 and with Mirabbasi-Martin prototype filter.

Regarding the effectiveness of the derived formulas, one can observe that such expressions are very close to the simulation results. Despite reducing the size of the set $\mathcal{E}$ considerably, such approximation led a small influence on the overall results, as $\epsilon_{m,n}$ elements decay rapidly. Thus, the provided expression demonstrated to be effective to predict the BER performance of FBMC systems operating over AWGN and Rayleigh channels, regardless of the prototype filter choice.

Additionally, one can observe that the numerical results for OFDM match with the BEP expressions provided in section 7.1. Compared to FBMC with EGF with $\alpha = 1$ and Mirabbasi-Martin prototype filters, the BER performance of OFDM presents a small

offset due to the deployment CP, which does not carry actual data, reducing the overall SNR of the signal. On the other hand, prototype filters with low symbol reconstruction performance, *e.g.*, EGF with $\alpha = 0.25$, can limit the BER performance of FBMC systems operating under high SNR regime as observed in Figure 7.2b.

Aiming to complement the numerical results, we analyze the impact of the number of elements of $\mathcal{E}'$ on the proposed BEP formulas. For such an analysis, the system described in Table 7.1 is re-simulated considering an EGF prototype filter with $\alpha = 0.25$ and limiting the number of $e_{m,n}$ to the largest terms with the number o interference elements being limited to $|\mathcal{E}'| = \{1, 2, 4, 8\}$. Since the exact and approximated expressions are very close, we present only the exact BEP expressions. Figures 7.4a and 7.4b presents the AWGN and Rayleigh BEP expressions for different $|\mathcal{E}'|$. As $|\mathcal{E}'|$ increases, the proposed BEP expressions becomes closer and closer to the simulated BER performance. In this case, as $|\mathcal{E}'|$ increases, the BEP performance become higher as more interference elements are accounted in the proposed expression. Moreover, if we consider only $|\mathcal{E}'| = 1$ or 2 interference elements, no BEP floor was established in the simulated γ_b range for Rayleigh channels.

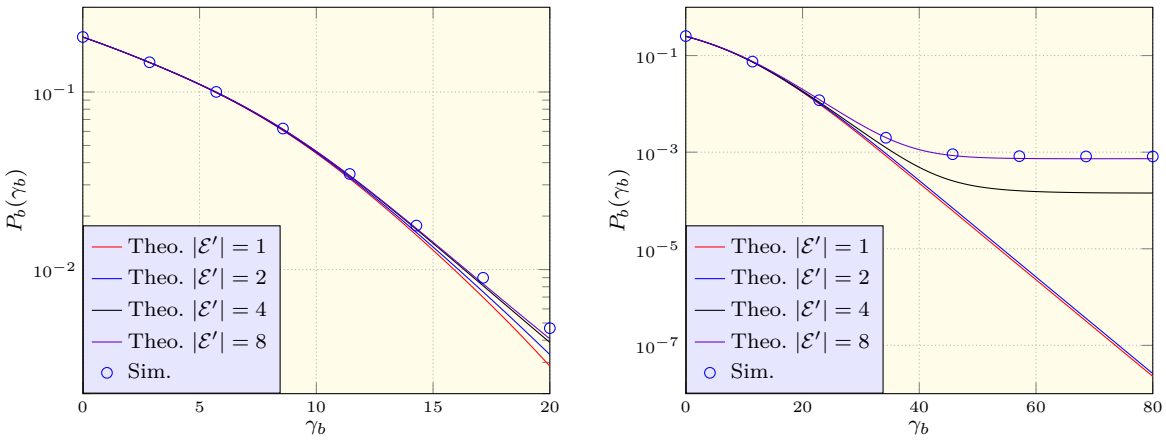

(a) AWGN **(b)** Rayleigh

Figure 7.4 Exact BEP expressions for different $\left||E|'\right|$

7.4 Conclusions

Chapter 7 derived the theoretical BEP expressions for FBMC systems under AWGN and frequency-flat Rayleigh channels, regardless of the prototype filter choice. Despite the required computational processing, the provided formulas are exact. Fortunately, the derived expressions are relatively accurate even when restricting the interference set $\mathcal{E}'$ to the most significant values. Thus, such an approximation does not compromise the final BEP prediction values. From this perspective, the numerical results demonstrate that the proposed BEP expressions can adequately characterize the BER performance of FBMC systems. Therefore, this chapter quantifies the effect of the prototype filter on the overall

BER performance of FBMC systems, which until now was only known qualitatively in terms of dependencies on SIR and distortion measurements.

8 Conclusions and Final Remarks

Chapter 1 briefly introduces 5G requirements, services, and technologies, emphasizing FBMC as a potential 5G waveform. From this perspective, Chapter 2 describes the FBMC multiplexing, including efficient polyphase implementations and their basic formulation for wireless systems. Chapter 3 discusses various prototype filters and their relation with FBMC transmission. In particular, the EGF, OFDP, and Mirabbasi-Martin designs stand out as the most suitable prototype filters for FBMC systems. Closing the first part of this work, Chapter 4 discusses processing techniques for channel estimation and equalization. At this point, it becomes clear that, despite its advantages, FBMC systems are not fully compatible with processing techniques employed in OFDM systems. Furthermore, sophisticated FBMC processing techniques are more complex than OFDM counterparts, *e.g.*, MIMO detection and channel estimation.

Regarding the project of prototype filters, Chapter 5 proposes a more flexible prototype filter design. Initially, this chapter states the filter design problem as the minimization of the OoB energy emission, given reconstruction requirements and energy constraint. Despite the objective function being convex, the constraints are non-convex. Aiming to circumvent the non-convexity, the problem was relaxed into an SDP, resulting in a prototype filter with far superior reconstruction features than other options available in the literature.

Differently from Chapter 5, the design proposed in Chapter 6 focused on providing filters with superior spectrum features. In order to achieve such goal, the design minimizes the OoB energy emission, whereas boundary constraints were deployed to impose fast spectrum decay. Of paramount importance, symbol reconstruction was also taken into account by limiting the amount of self-interference generated by the prototype filter. Moreover, a series of manipulations were conducted to convert the design into a convex-QCQP guided by a line search. Thus, such a design was deployed to create three prototype filters using both cosine and Slepian basis. Initial analysis points out that the proposed filters provide a high-performance spectrum, but their symbol reconstruction capabilities are not among the best. Despite favoring spectrum features over high prototype filter SIR levels, simulations suggested no performance losses when using the proposed prototype filters in a practical wireless application.

In Chapter 7, the effects of the prototype filters on the symbol reconstruction of FBMC systems are discussed. In this sense, Chapter 7 offers exact closed-form BER expressions that include the contribution of the prototype filter on the overall FBMC signal transmission. Despite being exact, simulating such expressions is prohibitive due to the number of terms. However, numerical results show that even with approximations, the overall result is very close to the simulation results.

The overall contributions of this work are the provision of an extensive discussion on FBMC systems and a systematic design methodology of prototype filters. Despite covering a reasonable amount of topics related to FBMC systems, there are many points observed in this thesis that can still be explored to make FBMC systems even more attractive for 5G and wireless systems to come. Hence, future works may explore the following topics:

- **Efficient equalization/detection structures** As observed in 4, OFDM equalization and detection techniques, for both SISO and MIMO systems, are not always applicable for FBMC. Hence, there are many research opportunities to deal with the imaginary interference on FBMC systems and possibly processing techniques combined with polyphase components.
- **Enhanced channel estimation techniques** Similarly to equalization and detection, channel estimation in FBMC systems has its peculiarities and challenges. In this sense, channel estimation techniques for FBMC systems can still improve their performance in terms of spectral efficiency, PAPR and processing complexity.
- **Extensions and modifications of the prototype filter designs proposed in Chapters 5 and 6** The design methodologies proposed in this work can be further explored, aiming to modify the optimization problem to incorporate new constraints bounded to other figures of merit not used in this work. Furthermore, the usage of other families of sequences is yet another possible study extension.
- **Alternative and approximated FBMC BEP expressions** Despite the BEP equations proposed in Chapter 7 being exact, they rely on the summation of a massive number of elements. An interesting possibility is to approximate the interference PDF ϵ_0 aiming to derive closed-form expressions that are less complex than the proposed in this thesis, but yet very close to the actual result.

Bibliography

3GPP. *3GPP TR 36.942 V13.0.0 (2016-01)*. [S.l.], 2016. Cited on page 42.

AGRELL, E.; ERIKSSON, T.; VARDY, A.; ZEGER, K. Closest Point Search in Lattices. *IEEE Transactions on Information Theory*, v. 48, n. 8, p. 2201–2214, August 2002. ISSN 0018-9448. Available from Internet: <https://doi.org/10.1109/TIT.2002.800499>. Cited on page 104.

AL-FUQAHA, A.; GUIZANI, M.; MOHAMMADI, M.; ALEDHARI, M.; AYYASH, M. Internet of Things: a Survey on Enabling Technologies, Protocols, and Applications. *IEEE Communications Surveys Tutorials*, v. 17, n. 4, p. 2347–2376, June 2015. ISSN 1553-877X. Available from Internet: <https://doi.org/10.1109/COMST.2015.2444095>. Cited on page 41.

ALDABABSEH, M.; JAMOOS, A. Estimation of FBMC/OQAM Fading Channels Using Dual Kalman Filters. *The Scientific World Journal*, Hindawi Publishing Corporation, v. 2014, n. Ici, 2014. ISSN 1537744X. Available from Internet: <https://doi.org/10.1155/2014/586403>. Cited on page 72.

AMINI, P.; FARHANG-BOROUJENY, B. Packet Format Design and Decision Directed Tracking Methods for Filter Bank Multicarrier Systems. *Eurasip Journal on Advances in Signal Processing*, v. 2010, n. 1, p. 307983, March 2010. ISSN 1687-6180. Available from Internet: <https://doi.org/10.1155/2010/307983">. Cited on page 90.

AMINJAVAHERI, A.; FARHANG, A.; DOYLE, L. E.; FARHANG-BOROUJENY, B. Prototype Filter Design for FBMC in Massive MIMO Channels. In: *2017 IEEE International Conference on Communications (ICC)*. Paris, France: IEEE, 2017. p. 1–6. Available from Internet: <https://doi.org/10.1109/ICC.2017.7997302>. Cited 2 times on page(s) 72 and 76.

ANATEL. *Portaria Nº 481*. [S.l.], 2015. Cited on page 42.

ANDERSEN, E.; ROOS, C.; TERLAKY, T. On Implementing a Primal-Dual Interior-Point Method for Conic Quadratic Optimization. *Mathematical Programming*, v. 95, n. 2, p. 249–277, February 2003. ISSN 1436-4646. Available from Internet: <https://doi.org/10.1007/s10107-002-0349-3>. Cited 2 times on page(s) 114 and 129.

APS, M. *MOSEK Optimization Toolbox for Matlab Release 8.0.0.94*. Copenhagen, Denmark, 2017. Available from Internet: <https://www.mosek.com/documentation/>. Cited on page 114.

BAI, L.; CHOI, J. *Low Complexity MIMO Detection*. Boston, USA: Springer Publishing Company, Incorporated, 2014. ISBN 1489998241, 9781489998248. Cited on page 105.

BALTAR, L. G.; WALDHAUSER, D. S.; NOSSEK, J. A. MMSE Subchannel Decision Feedback Equalization for Filter Bank Based Multicarrier Systems. In: *2009 IEEE International Symposium on Circuits and Systems*. Taipei, Taiwan: IEEE, 2009. p. 2802–2805. ISSN 0271-4302. Available from Internet: <https://doi.org/10.1109/ISCAS.2009.5118384>. Cited 2 times on page(s) 52 and 71.

BELLANGER, M. G. Specification and Design of a Prototype Filter for Filter Bank Based Multicarrier Transmission. In: *2001 IEEE International Conference on Acoustics, Speech, and Signal Processing. Proceedings*. Salt Lake City, USA: IEEE, 2001. v. 4, p. 2417–2420 vol.4. ISSN 1520-6149. Available from Internet: <https://doi.org/10.1109/ICASSP.2001.940488>. Cited 3 times on page(s) 70, 73, and 81.

BELORUTSKY, R. Y.; SAVINYKH, I. S. Modified Technique of FIR Filter Design by the Frequency Sampling Method. In: *2016 11th International Forum on Strategic Technology (IFOST)*. Novosibirsk, Russia: IEEE, 2016. p. 259–262. Available from Internet: <https://doi.org/10.1109/IFOST.2016.7884100>. Cited on page 81.

BIOGLIO, V.; CONDO, C.; LAND, I. Design of Polar Codes in 5G New Radio. *Corr*, abs/1804.04389, 2018. Available from Internet: <https://dblp.org/rec/bib/journals/corr/abs-1804-04389>. Cited on page 47.

BJÖRNSON, E.; CARVALHO, E. de; SøRENSEN, J. H.; LARSSON, E. G.; POPOVSKI, P. A Random Access Protocol for Pilot Allocation in Crowded Massive MIMO Systems. *IEEE Transactions on Wireless Communications*, v. 16, n. 4, p. 2220–2234, April 2017. ISSN 1536-1276. Available from Internet: <https://doi.org/10.1109/TWC.2017.2660489>. Cited on page 47.

BJÖSRNSON, E.; LARSSON, E. G.; MARZETTA, T. L. Massive MIMO: Ten Myths and One Critical Question. *IEEE Communications Magazine*, v. 54, n. 2, p. 114–123, February 2016. ISSN 0163-6804. Available from Internet: <https://doi.org/10.1109/MCOM.2016.7402270>. Cited on page 45.

BOCCARDI, F.; HEATH, R. W.; LOZANO, A.; MARZETTA, T. L.; POPOVSKI, P. Five Disruptive Technology Directions for 5G. *IEEE Communications Magazine*, v. 52, n. 2, p. 74–80, February 2014. ISSN 0163-6804. Available from Internet: <https://doi.org/10.1109/MCOM.2014.6736746>. Cited on page 51.

BOROUJENY, B. F. OFDM Versus Filter Bank Multicarrier. *IEEE Signal Processing Magazine*, v. 28, n. 3, p. 92–112, May 2011. ISSN 1053-5888. Available from Internet: <https://doi.org/10.1109/MSP.2011.940267>. Cited 2 times on page(s) 70 and 76.

BOROUJENY, B. F. Filter Bank Multicarrier Modulation: a Waveform Candidate for 5G and Beyond. *Advances in Electrical Engineering*, v. 28, n. 3, p. 92–112, May 2014. ISSN 1053-5888. Available from Internet: <http://dx.doi.org/10.1155/2014/482805>. Cited on page 70.

BOYD, S.; VANDENBERGHE, L. *Convex Optimization*. New York, USA: Cambridge University Press, 2004. ISBN 978-0521833783. Available from Internet: <https://doi.org/10.1017/CBO9780511804441>. Cited 2 times on page(s) 125 and 126.

BRADLEY, D. M.; GUPTA, R. C. On the Distribution of the Sum of N Non-Identically Distributed Uniform Random Variables. *Annals of the Institute of Statistical Mathematics*, v. 54, n. 3, p. 689–700, 2002. ISSN 00203157. Available from Internet: <10.1023/A:1022483715767>. Cited on page 141.

BULUSU, S. S. K. C.; SHAIEK, H.; ROVIRAS, D. Reduction of PAPR of FBMC-OQAM Systems by Dispersive Tone Reservation Technique. In: *2015 International Symposium on Wireless Communication Systems (ISWCS)*. Brussels, Belgium: IEEE, 2015. p. 561–565.

Available from Internet: <https://doi.org/10.1109/ISWCS.2015.7454408>. Cited on page 51.

CAI, Y.; QIN, Z.; CUI, F.; LI, G. Y.; MCCANN, J. A. Modulation and Multiple Access for 5G Networks. *IEEE Communications Surveys Tutorials*, v. 20, n. 1, p. 629–646, Firstquarter 2018. ISSN 1553-877X. Available from Internet: <https://doi.org/10.1109/COMST.2017.2766698>. Cited 2 times on page(s) 47 and 48.

CALVES, L. C.; VILBE, P. On the Uncertainty Principle in Discrete Signals. *IEEE Transactions on Circuits and Systems II: Analog and Digital Signal Processing*, v. 39, n. 6, p. 394–395, June 1992. ISSN 1057-7130. Available from Internet: <https://doi.org/10.1109/82.145299>. Cited on page 75.

CARVALHO, E. d.; BJÖRNSON, E.; SøRENSEN, J. H.; POPOVSKI, P.; LARSSON, E. G. Random Access Protocols for Massive MIMO. *IEEE Communications Magazine*, v. 55, n. 5, p. 216–222, May 2017. ISSN 0163-6804. Available from Internet: <https://doi.org/10.1109/MCOM.2017.1600477CM>. Cited on page 46.

CASSIAU, N.; KTENAS, D.; DORE, J. B. Time and Frequency Synchronization for Comp with FBMC. In: *ISWCS 2013: the Tenth International Symposium on Wireless Communication Systems*. Ilmenau, Germany: VDE, 2013. p. 1–5. Cited on page 51.

CHANG, M.; CHANG, W. Maximum-Likelihood Detection for MIMO Systems Based on Differential Metrics. *IEEE Transactions on Signal Processing*, v. 65, n. 14, p. 3718–3732, July 2017. ISSN 1053-587X. Available from Internet: <https://doi.org/10.1109/TSP.2017.2698411>. Cited on page 104.

CHAYAT, N. *Tentative Criteria for Comparison of Modulation Methods*. [S.l.], 1997. Cited 2 times on page(s) 101 and 132.

CHEN, C. W.; MAEHARA, F. An Enhanced MMSE Subchannel Decision Feedback Equalizer with ICI Suppression for FBMC/OQAM Systems. In: *2017 International Conference on Computing, Networking and Communications (ICNC)*. Santa Clara, USA: IEEE, 2017. p. 1041–1045. Available from Internet: <https://doi.org/10.1109/ICCNC.2017.7876278>. Cited 4 times on page(s) 52, 71, 103, and 131.

CHO JAEKWON KIM, W. Y. Y. Y. S.; KANG, C. G. *MIMO-OFDM Wireless Communications with Matlab*. Singapore, Singapore: John Wiley and Sons, 2010. ISBN 978-0470825617. Available from Internet: <https://doi.org/10.1002/9780470825631>. Cited on page 131.

CHO, K.; YOON, D. On the General BER Expression of One- and Two-Dimensional Amplitude Modulations. *IEEE Transactions on Communications*, v. 50, n. 7, p. 1074–1080, July 2002. ISSN 0090-6778. Available from Internet: <https://doi.org/10.1109/TCOMM.2002.800818>. Cited on page 136.

CISCO. *CISCO Visual Networking Index: Forecast and Methodology, 2016 to 2021*. East Lansing, Michigan, 2017. Cited on page 41.

C.MOORE, I.; CADA, M. Prolate Spheroidal Wave Functions, Fourier Analysis, and Uncertainty V: the Discrete Case. *Prolate Spheroidal Wave Functions, An Introduction to the Slepian Series and Its Properties*, v. 16, n. 3, p. 208–230, March 2004. Available from Internet: <https://doi.org/10.1016/j.acha.2004.03.004>. Cited on page 82.

CUI, W.; QU, D.; JIANG, T.; FARHANG-BOROUJENY, B. Coded Auxiliary Pilots for Channel Estimation in FBMC-OQAM Systems. *IEEE Transactions on Vehicular Technology*, v. 65, n. 5, p. 2936–2946, May 2016. ISSN 0018-9545. Available from Internet: <https://doi.org/10.1109/TVT.2015.2448659>. Cited 3 times on page(s) 51, 72, and 90.

DOCOMO. *5G Radio Access: Requirements, Concept and Technologies*. Tokyo, Japan, 2014. Cited on page 41.

DOHLER, M.; NAKAMURA, T. *5G Mobile and Wireless Communications Technology*. New York, USA: Cambridge University Press, 2016. ISBN 978-1107130098. Available from Internet: <https://doi.org/10.1017/CBO9781316417744>. Cited 3 times on page(s) 42, 76, and 115.

DONG, L.; ZHAO, H.; CHEN, Y.; CHEN, D.; WANG, T.; LU, L.; ZHANG, B.; HU, L.; GU, L.; LI, B.; YANG, H.; SHEN, H.; TIAN, T.; LUO, Z.; WEI, K. Introduction on IMT-2020 5G Trials in China. *IEEE Journal on Selected Areas in Communications*, v. 35, n. 8, p. 1849–1866, August 2017. ISSN 0733-8716. Available from Internet: <https://doi.org/10.1109/JSAC.2017.2710678>. Cited 2 times on page(s) 47 and 50.

FANG, J.; YOU, Z.; LU, I. T.; LI, J.; YANG, R. Comparisons of Filter Bank Multicarrier Systems. In: *2013 IEEE Long Island Systems, Applications and Technology Conference (LISAT)*. New York, USA: IEEE, 2013. p. 1–6. Available from Internet: <https://doi.org/10.1109/LISAT.2013.6578232>. Cited on page 70.

FARHANG, A.; MARCHETTI, N.; FIGUEIREDO, F.; MIRANDA, J. P. Massive MIMO and Waveform Design for 5th Generation Wireless Communication Systems. In: *1st International Conference on 5G for Ubiquitous Connectivity*. Akaslompolo, Finland: IEEE, 2014. p. 70–75. Available from Internet: <https://doi.org/10.4108/icst.5gu.2014.258195>. Cited 2 times on page(s) 51 and 72.

FETTWEIS, G. P. The Tactile Internet: Applications and Challenges. *IEEE Vehicular Technology Magazine*, v. 9, n. 1, p. 64–70, March 2014. ISSN 1556-6072. Available from Internet: <https://doi.org/10.1109/MVT.2013.2295069>. Cited on page 41.

FLOCH, B. L.; ALARD, M.; BERROU, C. Coded Orthogonal Frequency Dvision Multiplex. *Proceedings of the IEEE*, v. 83, n. 6, p. 982–996, June 1995. ISSN 0018-9219. Available from Internet: <https://doi.org/10.1109/5.387096>. Cited 2 times on page(s) 70 and 78.

GALLAGER, R. Low-Density Parity-Check Codes. *IRE Transactions on Information Theory*, v. 8, n. 1, p. 21–28, January 1962. ISSN 0096-1000. Available from Internet: <https://doi.org/10.1109/TIT.1962.1057683>. Cited on page 47.

GAO, X.; EDFORS, O.; TUFVESSON, F.; LARSSON, E. G. Massive MIMO in Real Propagation Environments: Do All Antennas Contribute Equally? *IEEE Transactions on Communications*, v. 63, n. 11, p. 3917–3928, November 2015. ISSN 0090-6778. Cited on page 50.

GRANT, M.; BOYD, S. *CVX: Matlab Software for Disciplined Convex Programming, Version 2.1*. 2014. Available from Internet: <http://cvxr.com/cvx>. Cited on page 114.

GUAN, P.; WU, D.; TIAN, T.; ZHOU, J.; ZHANG, X.; GU, L.; BENJEBBOUR, A.; IWABUCHI, M.; KISHIYAMA, Y. 5G Field Trials: OFDM-BASED Waveforms and Mixed

Numerologies. *IEEE Journal on Selected Areas in Communications*, v. 35, n. 6, p. 1234–1243, June 2017. ISSN 0733-8716. Available from Internet: <https://doi.org/10.1109/JSAC.2017.2687718>. Cited 2 times on page(s) 48 and 51.

HAAS, R.; BELFIORE, J.-C. A Time-Frequency Well-Localized Pulse for Multiple Carrier Transmission. *Wireless Personal Communications*, v. 5, n. 1, p. 1–18, July 1997. ISSN 1572-834X. Available from Internet: <https://doi.org/10.1023/A:1008859809455>. Cited 4 times on page(s) 71, 79, 80, and 168.

HAMPTON, J. R. *Introduction to MIMO Communications*. 1. ed. New York, USA: Cambridge University Press, 2014. ISBN 978-1107337527. Available from Internet: <https://doi.org/10.1017/CBO9781107337527>. Cited 3 times on page(s) 101, 131, and 132.

HAN, F. M.; ZHANG, X. D. Hexagonal Multicarrier Modulation: a Robust Transmission Scheme for Time-Frequency Dispersive Channels. *IEEE Transactions on Signal Processing*, v. 55, n. 5, p. 1955–1961, May 2007. ISSN 1053-587X. Available from Internet: <https://doi.org/10.1109/TSP.2006.890884>. Cited on page 62.

HAN, H.; GUO, X.; LI, Y. A High Throughput Pilot Allocation for M2M Communication in Crowded Massive MIMO Systems. *IEEE Transactions on Vehicular Technology*, v. 66, n. 10, p. 9572–9576, October 2017. ISSN 0018-9545. Available from Internet: <https://doi.org/10.1109/TVT.2017.2702604>. Cited on page 47.

HAN, H.; LI, Y.; GUO, X. A Graph-Based Random Access Protocol for Crowded Massive MIMO Systems. *IEEE Transactions on Wireless Communications*, v. 16, n. 11, p. 7348–7361, November 2017. ISSN 1536-1276. Available from Internet: <https://doi.org/10.1109/TWC.2017.2747145>. Cited on page 47.

HARRIS, F. J. On the Use of Windows for Harmonic Analysis with the Discrete Fourier Transform. *Proceedings of the IEEE*, v. 66, n. 1, p. 51–83, January 1978. ISSN 0018-9219. Available from Internet: <https://doi.org/10.1109/PROC.1978.10837>. Cited on page 84.

HASSIBI, B.; VIKALO, H. On the Sphere-Decoding Algorithm I. Expected Complexity. *IEEE Transactions on Signal Processing*, v. 53, n. 8, p. 2806–2818, August 2005. ISSN 1053-587X. Available from Internet: <https://doi.org/10.1109/TSP.2005.850352>. Cited on page 104.

HAYKIN, S. Cognitive Radio: Brain-Empowered Wireless Communications. *IEEE Journal on Selected Areas in Communications*, v. 23, n. 2, p. 201–220, February 2005. ISSN 0733-8716. Available from Internet: <https://doi.org/10.1109/JSAC.2004.839380>. Cited on page 42.

HORN, R. A.; JOHNSON, C. R. *Matrix Analysis*. New York, USA: Cambridge University Press, 1985. ISBN 978-0521305860. Available from Internet: <https://doi.org/10.1017/9781139020411>. Cited 2 times on page(s) 82 and 124.

HWANG, T.; YANG, C.; WU, G.; LI, S.; LI, G. Y. OFDM and Its Wireless Applications: a Survey. *IEEE Transactions on Vehicular Technology*, v. 58, n. 4, p. 1673–1694, May 2009. ISSN 0018-9545. Available from Internet: <https://doi.org/10.1109/TVT.2008.2004555>. Cited on page 48.

IEEE. IEEE Standard for Safety Levels with Respect to Human Exposure to Radio Frequency Electromagnetic Fields, 3 Khz to 300 Ghz. *IEEE Std C95.1-2005 (revision of IEEE Std C95.1-1991)*, p. 1–238, April 2006. Available from Internet: <https://doi.org/10.1109/IEEESTD.2006.99501>. Cited on page 42.

IHALAINEN, T.; IKHLEF, A.; LOUVEAUX, J.; RENFORS, M. Channel Equalization for Multi-Antenna FBMC/OQAM Receivers. *IEEE Transactions on Vehicular Technology*, v. 60, n. 5, p. 2070–2085, June 2011. ISSN 0018-9545. Available from Internet: <https://doi.org/10.1109/TVT.2011.2145424>. Cited 8 times on page(s) 52, 71, 103, 106, 107, 131, 132, and 141.

IHALAINEN, T.; STITZ, T. H.; RENFORS, M. Efficient Per-Carrier Channel Equalizer for Filter Bank Based Multicarrier Systems. In: *2005 IEEE International Symposium on Circuits and Systems*. Kobe, Japan: IEEE, 2005. p. 3175–3178 Vol. 4. ISSN 0271-4302. Available from Internet: <https://doi.org/10.1109/ISCAS.2005.1465302>. Cited 2 times on page(s) 71 and 141.

IHALAINEN, T.; STITZ, T. H.; RINNE, M.; RENFORS, M. Channel Equalization in Filter Bank Based Multicarrier Modulation for Wireless Communications. *Eurasip Journal on Advances in Signal Processing*, v. 2007, n. 1, p. 049389, November 2006. ISSN 1687-6180. Available from Internet: <https://doi.org/10.1155/2007/49389>. Cited on page 71.

IKHLEF, A.; LOUVEAUX, J. An Enhanced MMSE Per Subchannel Equalizer for Highly Frequency Selective Channels for FBMC/OQAM Systems. In: *2009 IEEE 10th Workshop on Signal Processing Advances in Wireless Communications*. Perugia, Italy: IEEE, 2009. p. 186–190. ISSN 1948-3244. Available from Internet: <https://doi.org/10.1109/SPAWC.2009.5161772>. Cited 3 times on page(s) 52, 71, and 103.

IKHLEF, A.; LOUVEAUX, J. Per Subchannel Equalization for MIMO FBMC/OQAM Systems. In: *2009 IEEE Pacific Rim Conference on Communications, Computers and Signal Processing*. Victoria, Canada: IEEE, 2009. p. 559–564. ISSN 1555-5798. Available from Internet: <https://doi.org/10.1109/PACRIM.2009.5291308>. Cited on page 71.

ITU. *Minimum Requirements Related to Technical Performance for IMT-2020 Radio Interfaces*. Geneva, Switzerland, 2017. Available from Internet: <https://www.itu.int/dms_pub/itu-r/opb/rep/R-REP-M.2410-2017-PDF-E.pdf>. Cited on page 43.

KATSELIS, D.; BENGTSSON, M.; ROJAS, C. R.; HJALMARSSONA, H.; KOFIDIS, E. On Preamble-Based Channel Estimation in OFDM/OQAM Systems. In: *2011 19th European Signal Processing Conference*. Catalonia, Spain: [s.n.], 2011. p. 1618–1622. ISSN 2076-1465. Cited on page 72.

KHANDANI, A. K. Media-Based Modulation: Converting Static Rayleigh Fading to AWGN. In: *2014 IEEE International Symposium on Information Theory*. Honolulu, USA: IEEE, 2014. p. 1549–1553. ISSN 2157-8095. Available from Internet: <https://doi.org/10.1109/ISIT.2014.6875093>. Cited on page 68.

KOBAYASHI, R. T.; ABRÃO, T. Ordered MMSE–SIC Via Sorted QR Decomposition in Ill Conditioned Large-Scale MIMO Channels. *Telecommunication Systems*, v. 63, n. 2, p. 335–346, October 2016. ISSN 1572-9451. Available from Internet: <https://doi.org/10.1007/s11235-015-0123-5>. Cited on page 105.

KOBAYASHI, R. T.; CIRIACO, F.; ABRÃO, T. Performance and Complexity Analysis of Sub-Optimum MIMO Detectors Under Correlated Channel. In: *2014 International Telecommunications Symposium (ITS)*. São Paulo, Brasil: [s.n.], 2014. p. 1–5. Available from Internet: <https://doi.org/10.1109/ITS.2014.6948035>. Cited on page 104.

KOBAYASHI, R. T.; CIRIACO, F.; ABRÃO, T. Efficient near-Optimum Detectors for Large MIMO Systems Under Correlated Channels. *Wireless Personal Communications*, v. 83, n. 2, p. 1287–1311, July 2015. ISSN 1572-834X. Available from Internet: <https://doi.org/10.1007/s11277-015-2450-y>. Cited on page 104.

KOFIDIS, E.; KATSELIS, D. Preamble-Based Channel Estimation in MIMO OFDM/O-QAM Systems. In: *2011 IEEE International Conference on Signal and Image Processing Applications (icsipa)*. Kuala Lumpur, Malaysia: [s.n.], 2011. p. 579–584. Available from Internet: <https://doi.org/10.1109/ICSIPA.2011.6144161>. Cited 3 times on page(s) 72, 96, and 97.

KOFIDIS, E.; KATSELIS, D.; RONTOGIANNIS, A. A.; THEODORIDIS, S. Preamble-Based Channel Estimation in OFDM/OQAM Systems: a Review. *Corr*, abs/1303.2136, 2013. Available from Internet: <http://arxiv.org/abs/1303.2136>. Cited 3 times on page(s) 72, 92, and 97.

KONG, D.; XIA, X. G.; JIANG, T.; GAO, X. Channel Estimation in CP-OQAM-OFDM Systems. *IEEE Transactions on Signal Processing*, v. 62, n. 21, p. 5775–5786, 2014. ISSN 1053587X. Available from Internet: <https://doi.org/10.1109/TSP.2014.2356441>. Cited on page 72.

KUMAR, R.; TYAGI, A. Computationally Efficient Mask-Compliant Spectral Precoder for OFDM Cognitive Radio. *IEEE Transactions on Cognitive Communications and Networking*, v. 2, n. 1, p. 15–23, March 2016. Available from Internet: <https://doi.org/10.1109/TCCN.2016.2577039>. Cited 2 times on page(s) 52 and 74.

LANDAU, H. J.; POLLAK, H. O. Prolate Spheroidal Wave Functions, Fourier Analysis, and Uncertainty II. *The Bell System Technical Journal*, v. 40, n. 1, p. 65–84, January 1961. ISSN 0005-8580. Available from Internet: <https://doi.org/10.1002/j.1538-7305.1961.tb03977.x>. Cited on page 70.

LANDAU, H. J.; POLLAK, H. O. Prolate Spheroidal Wave Functions, Fourier Analysis and Uncertainty III: the Dimension of the Space of Essentially Time- and Band-Limited Signals. *The Bell System Technical Journal*, v. 41, n. 4, p. 1295–1336, July 1962. ISSN 0005-8580. Available from Internet: <https://doi.org/10.1002/j.1538-7305.1962.tb03279.x>. Cited on page 70.

LARSSON, E. G.; EDFORS, O.; TUFVESSON, F.; MARZETTA, T. L. Massive MIMO for Next Generation Wireless Systems. *IEEE Communications Magazine*, v. 52, n. 2, p. 186–195, February 2014. ISSN 0163-6804. Available from Internet: <https://doi.org/10.1109/MCOM.2014.6736761>. Cited on page 45.

LÉLÉ, C.; JAVAUDIN, J.-P.; LEGOUABLE, R.; SKRZYPCZAK, A.; SIOHAN, P. Channel Estimation Methods for Preamble-Based OFDM/OQAM Modulations. *Emerging Telecommunications Technologies*, v. 65, n. 5, p. 2936–2946, September 2008. ISSN 0018-9545. Available from Internet: <https://doi.org/10.1109/TVT.2015.2448659>. Cited 7 times on page(s) 51, 72, 89, 93, 94, 95, and 109.

LÉLÉ, C.; JAVAUDIN, J.-P.; LEGOUABLE, R.; SKRZYPCZAK, A.; SIOHAN, P. Channel Estimation Methods for Preamble-Based OFDM/OQAM Modulations. *European Transactions on Telecommunications*, v. 19, n. 7, p. 741–750, 2008. Available from Internet: <https://onlinelibrary.wiley.com/doi/abs/10.1002/ett.1332>. Cited on page 96.

LÉLÉ, C.; LEGOUABLE, R.; SIOHAN, P. Channel Estimation with Scattered Pilots in OFDM/OQAM. In: *2008 IEEE 9th Workshop on Signal Processing Advances in Wireless Communications*. Recife, Brazil: IEEE, 2008. p. 286–290. ISSN 1948-3244. Available from Internet: <https://doi.org/10.1109/SPAWC.2008.4641615>. Cited 3 times on page(s) 51, 72, and 90.

LÉLÉ, C.; SIOHAN, P.; LEGOUABLE, R. 2 Db Better than CP-OFDM with OFDM/OQAM for Preamble-Based Channel Estimation. In: *2008 IEEE International Conference on Communications*. [s.n.], 2008. p. 1302–1306. ISSN 1550-3607. Available from Internet: <https://doi.org/10.1109/ICC.2008.253>. Cited on page 96.

LENSTRA, A. K.; LENSTRA, H. W.; LOVASZ, L. Factoring Polynomials with Rational Coefficients. *Mathematische Annalen*, v. 261, n. 4, p. 515–534, December 1982. ISSN 1432-1807. Available from Internet: <https://doi.org/10.1007/BF01457454>. Cited on page 106.

LIN, G.; LUNDHEIM, L.; HOLTE, N. *On Efficient Equalization for OFDM/OQAM Systems*. Trondheim, Norway, 2005. Available from Internet: <http://citeseerx.ist.psu.edu/viewdoc/summary?doi=10.1.1.487.9194>. Cited on page 72.

LIN, H.; SIOHAN, P. FBMC/COQAM: An Enabler for Cognitive Radio. In: *Cocora 2014: the Fourth International Conference on Advances in Cognitive Radio*. Nice, France: IARIA, 2014. p. 30–34. Cited on page 51.

LIN, J. C. Human Exposure to RF, Microwave, and Millimeter-Wave Electromagnetic Radiation [health Effects]. *IEEE Microwave Magazine*, v. 17, n. 6, p. 32–36, June 2016. ISSN 1527-3342. Available from Internet: <https://doi.org/10.1109/MMM.2016.2538540>. Cited on page 42.

LIU, X.; ZHANG, Q.; QIU, P.; TONG, J.; ZHANG, H.; ZHAO, C.; WANG, J. A 5.16 gbps Decoder ASIC for Polar Code in 16nm Finfet. *Corr*, abs/1807.01451, 2018. Available from Internet: <https://dblp.org/rec/bib/journals/corr/abs-1807-01451>. Cited on page 48.

LOBO, M. S.; VANDENBERGHE, L.; BOYD, S.; LEBRET, H. Applications of Second-Order Cone Programming. *Linear Algebra and Its Applications*, v. 284, n. 1, p. 193 – 228, 1998. ISSN 0024-3795. International Linear Algebra Society (ILAS) Symposium on Fast Algorithms for Control, Signals and Image Processing. Available from Internet: <https://doi.org/10.1016/S0024-3795(98)10032-0>. Cited on page 113.

LOPES, W. T. A.; MADEIRO, F.; ALENCAR, M. S. Closed-Form Expression for the Bit Error Probability of Rectangular QAM Subject to Rayleigh Fading. In: *2007 IEEE 66th Vehicular Technology Conference*. [s.n.], 2007. p. 915–919. ISSN 1090-3038. Available from Internet: <https://doi.org/10.1109/VETECF.2007.200>. Cited on page 137.

LU, C.; FANG, S.-C.; JIN, Q.; WANG, Z.; XING, W. KKT Solution and Conic Relaxation for Solving Quadratically Constrained Quadratic Programming Problems. *SIAM Journal*

on Optimization, v. 21, n. 4, p. 1475–1490, December 2011. Available from Internet: <https://doi.org/10.1137/100793955>. Cited 3 times on page(s) 112, 122, and 126.

LUO, Z. q.; MA, W. k.; SO, A. M. c.; YE, Y.; ZHANG, S. Semidefinite Relaxation of Quadratic Optimization Problems. *IEEE Signal Processing Magazine*, v. 27, n. 3, p. 20–34, May 2010. ISSN 1053-5888. Available from Internet: <https://doi.org/10.1109/MSP.2010.936019>. Cited 3 times on page(s) 105, 113, and 127.

MA, X.; ZHANG, W. Performance Analysis for MIMO Systems with Lattice-Reduction Aided Linear Equalization. *IEEE Transactions on Communications*, v. 56, n. 2, p. 309–318, 2008. ISSN 0090-6778. Available from Internet: <https://doi.org/10.1109/TCOMM.2008.060372>. Cited on page 106.

MARENGO, J. E.; FARNSWORTH, D. L.; STEFANIC, L. A Geometric Derivation of the Irwin-Hall Distribution. *International Journal of Mathematics and Mathematical Sciences*, v. 2017, p. 296–300, 2017. ISSN 16870425. Available from Internet: <https://doi.org/10.1155/2017/3571419>. Cited on page 141.

MARINELLO, J. C.; ABRÃO, T. Collision Resolution Protocol Via Soft Decision Retransmission Criterion. *IEEE Transactions on Vehicular Technology*, v. 68, n. 4, p. 4094–4097, April 2019. ISSN 0018-9545. Available from Internet: <https://doi.org/10.1109/TVT.2019.2898026>. Cited on page 47.

MARTIN, K. W. Small Side-Lobe Filter Design for Multitone Data-Communication Applications. *IEEE Transactions on Circuits and Systems II: Analog and Digital Signal Processing*, v. 45, n. 8, p. 1155–1161, August 1998. ISSN 1057-7130. Available from Internet: <https://doi.org/10.1109/82.718830>. Cited 3 times on page(s) 70, 73, and 81.

MATTINGLEY, J.; BOYD, S. Real-Time Convex Optimization in Signal Processing. *IEEE Signal Processing Magazine*, v. 27, n. 3, p. 50–61, May 2010. ISSN 1053-5888. Available from Internet: <https://doi.org/10.1109/MSP.2010.936020>. Cited on page 113.

MICHELOZZI ALESSANDRA CAPON, U. K. P. Adult and Childhood Leukemia near a High-Power Radio Station in Rome, Italy. *American Journal of Epidemiology*, v. 155, n. 12, p. 1096–1103, June 2002. Available from Internet: <https://doi.org/10.1093/aje/155.12.1096>. Cited on page 42.

MIRABBASI, S.; MARTIN, K. Overlapped Complex-Modulated Transmultiplexer Filters with Simplified Design and Superior Stopbands. *IEEE Transactions on Circuits and Systems II: Analog and Digital Signal Processing*, v. 50, n. 8, p. 456–469, August 2003. ISSN 1057-7130. Available from Internet: <https://doi.org/10.1109/TCSII.2003.813592>. Cited 5 times on page(s) 52, 70, 86, 143, and 168.

MONDAL, S.; SALAMA, K. N.; ALI, W. H. A Novel Approach for K-Best MIMO Detection and Its VLSI Implementation. In: *2008 IEEE International Symposium on Circuits and Systems*. Seattle, USA: [s.n.], 2008. p. 936–939. ISSN 0271-4302. Cited on page 104.

MYAMOTO, A.; ABRÃO, T. SDR Lattice-Reduction-Aided Detector. *IEEE Latin America Transactions*, v. 11, n. 4, p. 1007–1014, June 2013. ISSN 1548-0992. Available from Internet: <https://doi.org/10.1109/TLA.2013.6601743>. Cited on page 105.

NARESH, Y.; CHOCKALINGAM, A. On Media-Based Modulation Using RF Mirrors. *IEEE Transactions on Vehicular Technology*, v. 66, n. 6, p. 4967–4983, June 2017. ISSN

0018-9545. Available from Internet: <https://doi.org/10.1109/TVT.2016.2620989>. Cited on page 68.

NDO, G.; LIN, H.; SIOHAN, P. FBMC/OQAM Equalization: Exploiting the Imaginary Interference. In: *2012 IEEE 23rd International Symposium on Personal, Indoor and Mobile Radio Communications - (PIMRC)*. Sydney, NSW, Australia: IEEE, 2012. p. 2359–2364. ISSN 2166-9570. Available from Internet: <https://doi.org/10.1109/PIMRC.2012.6362751>. Cited on page 71.

NEGRÃO, J.; MUSSI, A.; ABRÃO, T. Semidefinite Relaxation for Large Scale MIMO Detection. In: *XXXIV Simpósio Brasileiro De Telecomunicações (sbrt 20016)*. Santarém, Brasil: [s.n.], 2016. p. 324–328. Cited on page 105.

PALOMAR, D. P.; ELDAR, Y. C. *Convex Optimization in Signal Processing and Communications*. New York, USA: Cambridge University Press, 2009. ISBN 978-0521762229. Available from Internet: <https://doi.org/10.1017/CBO9780511804458>. Cited on page 113.

POULARIKAS, A. *Handbook of Formulas and Tables for Signal Processing*. Boca Raton, USA: CRC Press, 1998. ISBN 9780849385797. Available from Internet: <https://doi.org/10.1201/9781420049701>. Cited on page 84.

PRAKASH, J. A.; REDDY, G. R. Efficient Prototype Filter Design for Filter Bank Multicarrier (FBMC) System Based on Ambiguity Function Analysis of Hermite Polynomials. In: *2013 International Mutli-Conference on Automation, Computing, Communication, Control and Compressed Sensing*. Kottayam, India: IEEE, 2013. p. 580–585. Available from Internet: <https://doi.org/10.1109/iMac4s.2013.6526477>. Cited 2 times on page(s) 71 and 76.

PROAKIS, J. G.; MANOLAKIS, D. G. *Digital Communications*. 4. ed. Upper Saddle River, USA: McGraw-Hill, 2000. ISBN 978-0071181839. Cited 2 times on page(s) 76 and 136.

RAHMATALLAH, Y.; MOHAN, S. Peak-to-Average Power Ratio Reduction in OFDM Systems: a Survey and Taxonomy. *Communications Surveys&tutorials, IEEE*, v. 15, n. 4, p. 1567–1592, 2013. ISSN 1553-877X. Available from Internet: <https://doi.org/10.1109/surv.2013.021313.00164>. Cited on page 51.

RAPPAPORT, T. S.; SUN, S.; MAYZUS, R.; ZHAO, H.; AZAR, Y.; WANG, K.; WONG, G. N.; SCHULZ, J. K.; SAMIMI, M.; GUTIERREZ, F. Millimeter Wave Mobile Communications for 5G Cellular: It Will Work! *IEEE Access*, v. 1, p. 335–349, May 2013. ISSN 2169-3536. Available from Internet: <https://doi.org/10.1109/ACCESS.2013.2260813>. Cited on page 46.

RAPPAPORT, T. S.; XING, Y.; MACCARTNEY, G. R.; MOLISCH, A. F.; MELLIOS, E.; ZHANG, J. Overview of Millimeter Wave Communications for Fifth-Generation (5G) Wireless Networks?with a Focus on Propagation Models. *IEEE Transactions on Antennas and Propagation*, v. 65, n. 12, p. 6213–6230, December 2017. ISSN 0018-926X. Available from Internet: <https://doi.org/10.1109/TAP.2017.2734243>. Cited on page 46.

RICHARDSON, T. Error-Floors of LDPC Codes. In: *Proceedings of the 41st Annual Conference on Communication, Control and Computing*. [S.l.: s.n.], 2003. p. 1426–1435. Cited on page 48.

ROH, W.; SEOL, J. Y.; PARK, J.; LEE, B.; LEE, J.; KIM, Y.; CHO, J.; CHEUN, K.; ARYANFAR, F. Millimeter-Wave Beamforming as An Enabling Technology for 5G Cellular Communications: Theoretical Feasibility and Prototype Results. *IEEE Communications Magazine*, v. 52, n. 2, p. 106–113, February 2014. ISSN 0163-6804. Available from Internet: <https://doi.org/10.1109/MCOM.2014.6736750>. Cited 3 times on page(s) 45, 46, and 50.

ROTTENBERG, F.; MESTRE, X.; HORLIN, F.; LOUVEAUX, J. Single-Tap Precoders and Decoders for Multiuser MIMO FBMC-OQAM Under Strong Channel Frequency Selectivity. *IEEE Transactions on Signal Processing*, v. 65, n. 3, p. 587–600, February 2017. ISSN 1053-587X. Available from Internet: <https://doi.org/10.1109/TSP.2016.2621722>. Cited 4 times on page(s) 68, 72, 130, and 132.

RUSEK, F.; PERSSON, D.; LAU, B. K.; LARSSON, E. G.; MARZETTA, T. L.; EDFORS, O.; TUFVESSON, F. Scaling up MIMO: Opportunities and Challenges with Very Large Arrays. *IEEE Signal Processing Magazine*, v. 30, n. 1, p. 40–60, January 2013. ISSN 1053-5888. Available from Internet: <https://doi.org/10.1109/MSP.2011.2178495>. Cited on page 45.

SAEEDI-SOURCK, H.; SADRI, S.; WU, Y.; FARHANG-BOROUJENY, B. Near Maximum Likelihood Synchronization for Filter Bank Multicarrier Systems. *IEEE Wireless Communications Letters*, v. 2, n. 2, p. 235–238, April 2013. ISSN 2162-2337. Cited on page 90.

SAHIN, A.; GUVENC, I.; ARSLAN, H. A Survey on Multicarrier Communications: Prototype Filters, Lattice Structures, and Implementation Aspects. *IEEE Communications Surveys Tutorials*, v. 16, n. 3, p. 1312–1338, March 2014. ISSN 1553-877X. Available from Internet: <https://doi.org/10.1109/SURV.2013.121213.00263>. Cited 3 times on page(s) 62, 70, and 76.

SCHELLMANN, M. *Mobile and Wireless Communications Enablers for the Twenty-Twenty Information Society (METIS)*. [S.l.], 2015. Cited 2 times on page(s) 51 and 70.

SHAFI, M.; MOLISCH, A. F.; SMITH, P. J.; HAUSTEIN, T.; ZHU, P.; SILVA, P. D.; TUFVESSON, F.; BENJEBBOUR, A.; WUNDER, G. 5G: a Tutorial Overview of Standards, Trials, Challenges, Deployment, and Practice. *IEEE Journal on Selected Areas in Communications*, v. 35, n. 6, p. 1201–1221, June 2017. ISSN 0733-8716. Available from Internet: <https://doi.org/10.1109/JSAC.2017.2692307>. Cited on page 43.

SHEPARD, C.; YU, H.; ANAND, N.; LI, E.; MARZETTA, T.; YANG, R.; ZHONG, L. Argos: Practical Many-Antenna Base Stations. In: *Proceedings of the 18th Annual International Conference on Mobile Computing and Networking*. New York, NY, USA: ACM, 2012. (Mobicom '12), p. 53–64. ISBN 978-1-4503-1159-5. Available from Internet: <http://doi.acm.org/10.1145/2348543.2348553>. Cited on page 50.

SIOHAN, P.; LACAILLE, N. Analysis of OFDM/OQAM Systems Based on the Filterbank Theory. In: *Global Telecommunications Conference, 1999. Globecom '99*. Rio de Janeiro, Brazil: IEEE, 1999. v. 4, p. 2279–2284 vol.4. Available from Internet: <https://doi.org/10.1109/GLOCOM.1999.827610>. Cited 2 times on page(s) 70 and 73.

SIOHAN, P.; ROCHE, C. Analytical Design for a Family of Cosine Modulated Filter Banks. In: *Circuits and Systems, 1998. ISCAS '98. Proceedings of the 1998 IEEE International Symposium On*. Monterey, USA: IEEE, 1998. v. 5, p. 150–153 vol.5. Available from Internet: <https://doi.org/10.1109/ISCAS.1998.694430>. Cited 2 times on page(s) 70 and 78.

SIOHAN, P.; ROCHE, C. Cosine-Modulated Filterbanks Based on Extended Gaussian Functions. *IEEE Transactions on Signal Processing*, v. 48, n. 11, p. 3052–3061, 2000. ISSN 1053587X. Available from Internet: <https://doi.org/10.1109/78.875463>. Cited 3 times on page(s) 70, 78, and 167.

SIOHAN, P.; SICLET, C.; LACAILLE, N. Analysis and Design of OFDM/OQAM Systems Based on Filterbank Theory. *IEEE Transactions on Signal Processing*, v. 50, n. 5, p. 1170–1183, 2002. ISSN 1053587X. Available from Internet: <https://doi.org/10.1109/78.995073>. Cited 7 times on page(s) 58, 60, 65, 70, 109, 114, and 142.

SLEPIAN, D. Prolate Spheroidal Wave Functions, Fourier Analysis and Uncertainty IV: Extensions to Many Dimensions Generalized Prolate Spheroidal Functions. *The Bell System Technical Journal*, v. 43, n. 6, p. 3009–3057, November 1964. ISSN 0005-8580. Available from Internet: <https://doi.org/10.1002/j.1538-7305.1964.tb01037.x>. Cited on page 70.

SLEPIAN, D. Prolate Spheroidal Wave Functions, Fourier Analysis, and Uncertainty V: the Discrete Case. *The Bell System Technical Journal*, v. 57, n. 5, p. 1371–1430, May 1978. ISSN 0005-8580. Available from Internet: <https://doi.org/10.1002/j.1538-7305.1978.tb02104.x>. Cited 3 times on page(s) 70, 82, and 83.

SLEPIAN, D.; POLLAK, H. O. Prolate Spheroidal Wave Functions, Fourier Analysis, and Uncertainty I. *The Bell System Technical Journal*, v. 40, n. 1, p. 43–63, January 1961. ISSN 0005-8580. Available from Internet: <https://doi.org/10.1002/j.1538-7305.1961.tb03976.x>. Cited on page 70.

STITZ, T. H.; IHALAINEN, T.; VIHOLAINEN, A.; RENFORS, M. Pilot-Based Synchronization and Equalization in Filter Bank Multicarrier Communications. *Eurasip Journal on Advances in Signal Processing*, v. 2010, n. 1, p. 741429, February 2010. ISSN 1687-6180. Available from Internet: <https://doi.org/10.1155/2010/741429">. Cited on page 90.

STROHMER, T.; BEAVER, S. Optimal OFDM Design for Time-Frequency Dispersive Channels. *IEEE Transactions on Communications*, v. 51, n. 7, p. 1111–1122, July 2003. ISSN 0090-6778. Available from Internet: <https://doi.org/10.1109/TCOMM.2003.814200>. Cited on page 62.

TODD, M. J.; TOH, K. C.; TUTUNCU, R. H. On the Nesterov–Todd Direction in Semidefinite Programming. *SIAM Journal on Optimization*, v. 8, n. 3, p. 769–796, 1998. Available from Internet: <https://doi.org/10.1137/S105262349630060X>. Cited on page 114.

VAHLIN, A.; HOLTE, N. Optimal Finite Duration Pulses for OFDM. In: *Global Telecommunications Conference, 1994*. San Francisco, USA: IEEE, 1994. p. 258–262. ISBN 078031820X. Available from Internet: <https://doi.org/10.1109/GLOCOM.1994.513418>. Cited 6 times on page(s) 52, 71, 82, 109, 115, and 168.

VAHLIN, A.; HOLTE, N. Optimal Finite Duration Pulses for OFDM. *IEEE Transactions on Communications*, v. 44, n. 1, p. 10–14, 1996. ISSN 00906778. Available from Internet: <https://doi.org/10.1109/26.476088>. Cited on page 71.

VAIDYANATHAN, P. P. *Multirate Systems and Filter Banks*. Upper Saddle River, USA: Prentice-Hall, 1993. ISBN 978-0136057185. Cited 2 times on page(s) 74 and 185.

VIEIRA, J.; MALKOWSKY, S.; NIEMAN, K.; MIERS, Z.; KUNDARGI, N.; LIU, L.; WONG, I.; OWALL, V.; EDFORS, O.; TUFVESSON, F. A Flexible 100-ANTENNA Testbed for Massive MIMO. In: *2014 IEEE Globecom Workshops (GC Wkshps)*. [s.n.], 2014. p. 287–293. ISSN 2166-0077. Available from Internet: <https://doi.org/10.1109/GLOCOMW.2014.7063446>. Cited 2 times on page(s) 45 and 50.

VIHOLAINEN, A.; BELLANGER, M.; HUCHARD, M. *Phydyas 007 - Physical Layer for Dynamic Access and Cognitive Radio*. [S.l.], 2009. Cited 7 times on page(s) 51, 58, 60, 70, 81, 84, and 142.

WALDHAUSER, D. S.; BALTAR, L. G.; NOSSEK, J. A. Comparison of Filter Bank Based Multicarrier Systems with OFDM. In: *Apccas 2006 - 2006 IEEE Asia Pacific Conference on Circuits and Systems*. Singapore, Singapore: IEEE, 2006. p. 976–979. Available from Internet: <https://doi.org/10.1109/APCCAS.2006.342225>. Cited on page 70.

WALDHAUSER, D. S.; BALTAR, L. G.; NOSSEK, J. A. Adaptive Equalization for Filter Bank Based Multicarrier Systems. In: *2008 IEEE International Symposium on Circuits and Systems*. Seattle, USA: IEEE, 2008. p. 3098–3101. ISSN 0271-4302. Available from Internet: <https://doi.org/10.1109/ISCAS.2008.4542113>. Cited on page 71.

WALDHAUSER, D. S.; BALTAR, L. G.; NOSSEK, J. A. MMSE Subcarrier Equalization for Filter Bank Based Multicarrier Systems. In: *2008 IEEE 9th Workshop on Signal Processing Advances in Wireless Communications*. Recife, Brazil: IEEE, 2008. p. 525–529. ISSN 1948-3244. Available from Internet: <https://doi.org/10.1109/SPAWC.2008.4641663>. Cited 2 times on page(s) 71 and 141.

WANG, C.; HAIDER, F.; GAO, X.; YOU, X.; YANG, Y.; YUAN, D.; AGGOUNE, H. M.; HAAS, H.; FLETCHER, S.; HEPSAYDIR, E. Cellular Architecture and Key Technologies for 5G Wireless Communication Networks. *IEEE Communications Magazine*, v. 52, n. 2, p. 122–130, February 2014. ISSN 0163-6804. Available from Internet: <https://doi.org/10.1109/MCOM.2014.6736752>. Cited on page 42.

WANG, J.; JIN, A.; SHI, D.; WANG, L.; SHEN, H.; WU, D.; HU, L.; GU, L.; LU, L.; CHEN, Y.; WANG, J.; SAITO, Y.; BENJEBBOUR, A.; KISHIYAMA, Y. Spectral Efficiency Improvement with 5G Technologies: Results from Field Tests. *IEEE Journal on Selected Areas in Communications*, v. 35, n. 8, p. 1867–1875, August 2017. ISSN 0733-8716. Available from Internet: <https://doi.org/10.1109/JSAC.2017.2713498>. Cited on page 47.

WANG, J.; JIN, A.; SHI, D.; WANG, L.; HU, L.; GU, L.; BENJEBBOUR, A. Field Trials on Spectral Efficiency Improvement in Massive MIMO Systems. In: *2018 IEEE 87th Vehicular Technology Conference (VTC Spring)*. [s.n.], 2018. p. 1–5. ISSN 2577-2465. Available from Internet: <https://doi.org/10.1109/VTCSpring.2018.8417817>. Cited 2 times on page(s) 47 and 48.

WANG, L. C.; RANGAPILLAI, S. A Survey on Green 5G Cellular Networks. In: *2012 International Conference on Signal Processing and Communications (SPCOM)*. Bangalore, India: IEEE, 2012. p. 1–5. ISSN 2165-0608. Available from Internet: <https://doi.org/10.1109/SPCOM.2012.6290252>. Cited on page 42.

WATERS, D. W.; BARRY, J. R. The Sorted-QR Chase Detector for Multiple-Input Multiple-Output Channels. In: *IEEE Wireless Communications and Networking Confer-*

ence, 2005. [s.n.], 2005. v. 1, p. 538–543 Vol. 1. ISSN 1525-3511. Available from Internet: <https://doi.org/10.1109/WCNC.2005.1424558>. Cited on page 106.

WINTERS, J. H.; SALZ, J.; GITLIN, R. D. The Impact of Antenna Diversity on the Capacity of Wireless Communication Systems. *IEEE Transactions on Communications*, v. 42, n. 234, p. 1740–1751, February 1994. ISSN 0090-6778. Available from Internet: <https://doi.org/10.1109/TCOMM.1994.582882>. Cited on page 105.

WOLNIANSKY, P.; FOSCHINI, G.; GOLDEN, G.; VALENZUELA, R. V-BLAST: An Architecture for Realizing Very High Data Rates over the Rich-Scattering Wireless Channel. In: *International Symposium on Signals, Systems, and Electronics, 1998. ISSSE 98. 1998 URSI.* Pisa, Italy: IEEE, 1998. p. 295–300. Available from Internet: <https://doi.org/10.1109/ISSSE.1998.738086>. Cited on page 68.

WONG, K. wai; TSUI, C. ying; CHENG, R. S. .; MOW, W. ho. A VLSI Architecture of a K-Best Lattice Decoding Algorithm for MIMO Channels. In: *2002 IEEE International Symposium on Circuits and Systems. Proceedings (cat. No.02ch37353).* [s.n.], 2002. v. 3, p. III–III. Available from Internet: <https://doi.org/110.1109/ISCAS.2002.1010213>. Cited on page 104.

WUBBEN, D.; BOHNKE, R.; KUHN, V.; KAMMEYER. MMSE Extension of V-BLAST Based on Sorted QR Decomposition. In: *Vehicular Technology Conference, 2003. VTC 2003-FALL. 2003 IEEE 58th.* Orlando, USA: IEEE, 2003. v. 1, p. 508–512 Vol.1. ISSN 1090-3038. Available from Internet: <https://doi.org/10.1109/VETECF.2003.1285069>. Cited on page 105.

WUBBEN, D.; BOHNKE, R.; KUHN, V.; KAMMEYER, K. . Near-Maximum-Likelihood Detection of MIMO Systems Using MMSE-BASED Lattice- Reduction. In: *2004 IEEE International Conference on Communications (IEEE Cat. No.04ch37577).* [s.n.], 2004. v. 2, p. 798–802 Vol.2. Available from Internet: <https://doi.org/10.1109/ICC.2004.1312611>. Cited on page 106.

WUBBEN, D.; BOHNKE, R.; RINAS, J.; KUHN, V.; KAMMEYER, K. D. Efficient Algorithm for Decoding Layered Space-Time Codes. *Electronics Letters*, v. 37, n. 22, p. 1348–1350, October 2001. ISSN 0013-5194. Available from Internet: <https://doi.org/10.1049/el:20010899>. Cited on page 105.

WUNDER, G.; JUNG, P.; KASPARICK, M.; WILD, T.; SCHAICH, F.; CHEN, Y.; BRINK, S. T.; GASPAR, I.; MICHAILOW, N.; FESTAG, A.; MENDES, L.; CASSIAU, N.; KTENAS, D.; DRYJANSKI, M.; PIETRZYK, S.; EGED, B.; VAGO, P.; WIEDMANN, F. 5GNOW: Non-Orthogonal, Asynchronous Waveforms for Future Mobile Applications. *IEEE Communications Magazine*, v. 52, n. 2, p. 97–105, February 2014. ISSN 0163-6804. Available from Internet: <https://doi.org/10.1109/MCOM.2014.6736749>. Cited 2 times on page(s) 48 and 70.

YANG, P.; XIAO, Y.; GUAN, Y. L.; HARI, K. V. S.; CHOCKALINGAM, A.; SUGIURA, S.; HAAS, H.; RENZO, M. D.; MASOUROS, C.; LIU, Z.; XIAO, L.; LI, S.; HANZO, L. Single-Carrier Spatial Modulation: a Promising Design for Large-Scale Broadband Antenna Systems. *IEEE Communications Surveys Tutorials*, PP, n. 99, p. 1–1, February 2016. ISSN 1553-877X. Available from Internet: <https://doi.org/10.1109/COMST.2016.2533580>. Cited on page 68.

ZHANG, L.; XIAO, P.; ZAFAR, A.; QUDDUS, A. u.; TAFAZOLLI, R. FBMC System: An Insight into Doubly Dispersive Channel Impact. *IEEE Transactions on Vehicular Technology*, v. 66, n. 5, p. 3942–3956, May 2017. ISSN 0018-9545. Available from Internet: <https://doi.org/10.1109/TVT.2016.2602096>. Cited on page 52.

Annex

ANNEX A – Prototype Filter Weights

A.1 Extended Gaussian Function

The weights used to generate EGFs is obtained via

$$\overline{d}_{k,\alpha,\nu_0} = \sum_{\ell=0}^{\ell_k} b_{k,\ell} e^{-\frac{\pi\alpha}{2\nu_0^2}(2\ell+k)}, \tag{A.1}$$

where the weights $b_{k,\ell}$ are found in Table A.1. Moreover, b_{k,ℓ_k} is the last element provided on the kth row of Table A.1.

Table A.1 EGF weights $b_{k,\ell}$ (SIOHAN; ROCHE, 2000)

k	$b_{k,0}$	$b_{k,1}$	$b_{k,2}$	$b_{k,3}$	$b_{k,4}$	$b_{k,5}$	$b_{k,6}$	$b_{k,7}$
0	$+1$	$+\frac{3}{4}$	$+\frac{105}{64}$	$+\frac{675}{256}$	$+\frac{76233}{16384}$	$+\frac{457107}{65536}$	$+\frac{12097169}{1048576}$	$+\frac{7054315}{4194304}$
1	-1	$-\frac{15}{8}$	$-\frac{219}{64}$	$-\frac{6055}{1024}$	$-\frac{161925}{16384}$	$-\frac{2067909}{1301072}$	$-\frac{26060847}{1048576}$	
2	$+\frac{3}{4}$	$+\frac{19}{16}$	$+\frac{1545}{512}$	$+\frac{9765}{2048}$	$+\frac{596277}{65536}$	$+\frac{3679941}{262144}$	$+\frac{394159701}{16777216}$	
3	$-\frac{5}{8}$	$-\frac{123}{128}$	$-\frac{2289}{1024}$	$-\frac{34871}{8192}$	$-\frac{969375}{131072}$	$-\frac{51182445}{4194304}$		
4	$+\frac{35}{64}$	$+\frac{213}{256}$	$+\frac{7797}{4096}$	$+\frac{56163}{16384}$	$+\frac{13861065}{2097152}$	$+\frac{87185895}{8388608}$		
5	$-\frac{63}{128}$	$-\frac{763}{1024}$	$-\frac{13875}{8192}$	$-\frac{790815}{262144}$	$-\frac{23600537}{4194304}$			
6	$+\frac{231}{512}$	$+\frac{1395}{2048}$	$+\frac{02281}{131072}$	$+\frac{1434705}{524288}$	$+\frac{85037895}{16777216}$			
7	$-\frac{429}{1024}$	$-\frac{20691}{32768}$	$-\frac{374325}{262144}$	$-\frac{5297445}{2097152}$				
8	$+\frac{6435}{16384}$	$+\frac{38753}{65536}$	$+\frac{1400487}{1048576}$	$+\frac{989593}{4194304}$				
9	$-\frac{12155}{32768}$	$-\frac{146289}{262144}$	$-\frac{2641197}{2097152}$					
10	$+\frac{46189}{131072}$	$+\frac{277797}{524288}$	$+\frac{20050485}{16777216}$					
11	$-\frac{88179}{262144}$	$-\frac{2120495}{4194304}$						
12	$+\frac{676039}{2097152}$	$+\frac{4063017}{8388608}$						
13	$-\frac{1300075}{4194304}$							
14	$+\frac{5014575}{16777216}$							

A.2 Hermite Prototype Filter

Table A.2 Hermite prototype filter weights (HAAS; BELFIORE, 1997)

n	H_n
0	1
4	$-1.9324881 \cdot 10^{-3}$
8	$-7.3110588 \cdot 10^{-6}$
12	$-3.154209 \cdot 10^{-9}$
16	$+9.663413 \cdot 10^{-12}$

A.3 Mirabbasi-Martin Prototype Filter

Table A.3 Mirabbasi-Martin prototype filter weights (MIRABBASI; MARTIN, 2003)

K	k_0	k_1	k_2	k_3	k_4	k_5	k_6	k_7
3	1	−0.9114	+0.4114					
4	1	−0.9719	+0.7071	−0.2351				
6	1	−0.9972	+0.9413	−0.7071	+0.3373	−0.0744		
8	1	−0.9998	+0.9315	−0.9270	+0.7071	−0.3748	+0.1168	−0.0152

A.4 Optimal Finite-Duration Pulse

Table A.4 OFDP prototype filter weights (VAHLIN; HOLTE, 1994)

K	α_0	α_2	α_4	α_6	α_8	α_{10}	α_{12}	α_{14}	α_{16}	α_{18}
2	0.9785	0.2055	−0.0113	0.0147	−0.0007					
3	0.9395	0.3282	0.0927	0.0308	−0.0015	−0.0024	0.0039	0.0002	−0.0034	
4	0.9126	0.3841	0.1329	0.0426	0.0144	0.0005	−0.0052	−0.0019	0.0013	0.0010

Appendix

APPENDIX A – Prototype Filter Weights for OFDP-SDP Design

Table A.1 OFDP-SDP Filter Weights for $K = 1$

i	c_i $(M = 8)$	c_i $(M = 16)$	c_i $(M = 32)$	c_i $(M = 64)$	c_i $(M = 128)$
0	+0.999997	+0.999989	+0.999986	+0.999985	+0.999985
2	+0.000546	+0.000922	+0.001017	+0.001041	+0.001047
4	+0.002061	+0.002888	+0.003051	+0.003089	+0.003098
6	+0.001153	+0.001315	+0.001367	+0.001381	+0.001385
8	+0.000000	+0.002069	+0.002025	+0.002010	+0.002007
10	+0.000000	+0.002003	+0.002121	+0.002136	+0.002140
12	+0.000000	+0.001457	+0.001721	+0.001763	+0.001772
14	+0.000000	+0.000934	+0.001320	+0.001374	+0.001386
16	+0.000000	+0.000000	+0.001021	+0.001080	+0.001093
18	+0.000000	+0.000000	+0.000804	+0.000867	+0.000881
20	+0.000000	+0.000000	+0.000642	+0.000710	+0.000724
22	+0.000000	+0.000000	+0.000517	+0.000590	+0.000605
24	+0.000000	+0.000000	+0.000417	+0.000498	+0.000512
26	+0.000000	+0.000000	+0.000334	+0.000424	+0.000439
28	+0.000000	+0.000000	+0.000262	+0.000365	+0.000380
30	+0.000000	+0.000000	+0.000189	+0.000317	+0.000333
32	+0.000000	+0.000000	+0.000000	+0.000277	+0.000293
34	+0.000000	+0.000000	+0.000000	+0.000243	+0.000260
36	+0.000000	+0.000000	+0.000000	+0.000215	+0.000232
38	+0.000000	+0.000000	+0.000000	+0.000191	+0.000208
40	+0.000000	+0.000000	+0.000000	+0.000170	+0.000188
42	+0.000000	+0.000000	+0.000000	+0.000152	+0.000170
44	+0.000000	+0.000000	+0.000000	+0.000136	+0.000155
46	+0.000000	+0.000000	+0.000000	+0.000122	+0.000142
48	+0.000000	+0.000000	+0.000000	+0.000109	+0.000130
50	+0.000000	+0.000000	+0.000000	+0.000098	+0.000119
52	+0.000000	+0.000000	+0.000000	+0.000087	+0.000110
54	+0.000000	+0.000000	+0.000000	+0.000078	+0.000102
56	+0.000000	+0.000000	+0.000000	+0.000068	+0.000094
58	+0.000000	+0.000000	+0.000000	+0.000059	+0.000088
60	+0.000000	+0.000000	+0.000000	+0.000050	+0.000082
62	+0.000000	+0.000000	+0.000000	+0.000038	+0.000076
64	+0.000000	+0.000000	+0.000000	+0.000000	+0.000071
66	+0.000000	+0.000000	+0.000000	+0.000000	+0.000067
68	+0.000000	+0.000000	+0.000000	+0.000000	+0.000062
70	+0.000000	+0.000000	+0.000000	+0.000000	+0.000059
72	+0.000000	+0.000000	+0.000000	+0.000000	+0.000055
74	+0.000000	+0.000000	+0.000000	+0.000000	+0.000052
76	+0.000000	+0.000000	+0.000000	+0.000000	+0.000049
78	+0.000000	+0.000000	+0.000000	+0.000000	+0.000046
80	+0.000000	+0.000000	+0.000000	+0.000000	+0.000043
82	+0.000000	+0.000000	+0.000000	+0.000000	+0.000041
84	+0.000000	+0.000000	+0.000000	+0.000000	+0.000039
86	+0.000000	+0.000000	+0.000000	+0.000000	+0.000037
88	+0.000000	+0.000000	+0.000000	+0.000000	+0.000035
90	+0.000000	+0.000000	+0.000000	+0.000000	+0.000033

92	+0.000000	+0.000000	+0.000000	+0.000000	+0.000031
94	+0.000000	+0.000000	+0.000000	+0.000000	+0.000029
96	+0.000000	+0.000000	+0.000000	+0.000000	+0.000028
98	+0.000000	+0.000000	+0.000000	+0.000000	+0.000026
100	+0.000000	+0.000000	+0.000000	+0.000000	+0.000025
102	+0.000000	+0.000000	+0.000000	+0.000000	+0.000024
104	+0.000000	+0.000000	+0.000000	+0.000000	+0.000022
106	+0.000000	+0.000000	+0.000000	+0.000000	+0.000021
108	+0.000000	+0.000000	+0.000000	+0.000000	+0.000020
110	+0.000000	+0.000000	+0.000000	+0.000000	+0.000019
112	+0.000000	+0.000000	+0.000000	+0.000000	+0.000017
114	+0.000000	+0.000000	+0.000000	+0.000000	+0.000016
116	+0.000000	+0.000000	+0.000000	+0.000000	+0.000015
118	+0.000000	+0.000000	+0.000000	+0.000000	+0.000014
120	+0.000000	+0.000000	+0.000000	+0.000000	+0.000013
122	+0.000000	+0.000000	+0.000000	+0.000000	+0.000011
124	+0.000000	+0.000000	+0.000000	+0.000000	+0.000010
126	+0.000000	+0.000000	+0.000000	+0.000000	+0.000008

Table A.2 OFDP-SDP Filter Weights for $K = 2$

i	c_i $(M = 8)$	c_i $(M = 16)$	c_i $(M = 32)$	c_i $(M = 64)$	c_i $(M = 128)$
0	+0.977436	+0.978410	+0.978645	+0.978704	+0.978718
2	+0.210571	+0.205923	+0.204784	+0.204501	+0.204430
4	−0.009941	−0.010711	−0.010889	−0.010933	−0.010943
6	+0.011468	+0.012209	+0.012336	+0.012365	+0.012372
8	−0.006107	−0.004729	−0.004353	−0.004258	−0.004235
10	−0.001618	−0.003866	−0.004273	−0.004366	−0.004388
12	+0.002843	+0.001523	+0.001120	+0.001017	+0.000992
14	+0.000442	+0.002290	+0.002335	+0.002336	+0.002335
16	+0.000000	+0.001078	+0.001399	+0.001465	+0.001481
18	+0.000000	+0.000050	+0.000376	+0.000454	+0.000473
20	+0.000000	−0.000200	−0.000144	−0.000104	−0.000093
22	+0.000000	+0.000131	−0.000155	−0.000181	−0.000186
24	+0.000000	+0.000336	+0.000096	+0.000026	+0.000010
26	+0.000000	+0.000030	+0.000290	+0.000244	+0.000231
28	+0.000000	+0.000042	+0.000256	+0.000291	+0.000293
30	+0.000000	+0.000047	+0.000072	+0.000163	+0.000183
32	+0.000000	+0.000000	−0.000058	−0.000000	+0.000019
34	+0.000000	+0.000000	−0.000022	−0.000064	−0.000063
36	+0.000000	+0.000000	+0.000090	−0.000006	−0.000025
38	+0.000000	+0.000000	+0.000115	+0.000088	+0.000067
40	+0.000000	+0.000000	+0.000029	+0.000117	+0.000118
42	+0.000000	+0.000000	−0.000033	+0.000063	+0.000086
44	+0.000000	+0.000000	+0.000015	−0.000012	+0.000012
46	+0.000000	+0.000000	+0.000068	−0.000032	−0.000033
48	+0.000000	+0.000000	+0.000022	+0.000011	−0.000015
50	+0.000000	+0.000000	−0.000017	+0.000060	+0.000036
52	+0.000000	+0.000000	+0.000034	+0.000060	+0.000066
54	+0.000000	+0.000000	+0.000015	+0.000016	+0.000048
56	+0.000000	+0.000000	+0.000007	−0.000019	+0.000005
58	+0.000000	+0.000000	+0.000013	−0.000009	−0.000021
60	+0.000000	+0.000000	+0.000008	+0.000028	−0.000007
62	+0.000000	+0.000000	+0.000007	+0.000043	+0.000026
64	+0.000000	+0.000000	+0.000000	+0.000020	+0.000043
66	+0.000000	+0.000000	+0.000000	−0.000010	+0.000028

68	+0.000000	+0.000000	+0.000000	−0.000009	−0.000001
70	+0.000000	+0.000000	+0.000000	+0.000017	−0.000014
72	+0.000000	+0.000000	+0.000000	+0.000031	−0.000001
74	+0.000000	+0.000000	+0.000000	+0.000013	+0.000022
76	+0.000000	+0.000000	+0.000000	−0.000008	+0.000030
78	+0.000000	+0.000000	+0.000000	−0.000003	+0.000015
80	+0.000000	+0.000000	+0.000000	+0.000018	−0.000005
82	+0.000000	+0.000000	+0.000000	+0.000020	−0.000010
84	+0.000000	+0.000000	+0.000000	+0.000001	+0.000004
86	+0.000000	+0.000000	+0.000000	−0.000007	+0.000020
88	+0.000000	+0.000000	+0.000000	+0.000009	+0.000020
90	+0.000000	+0.000000	+0.000000	+0.000017	+0.000006
92	+0.000000	+0.000000	+0.000000	+0.000003	−0.000007
94	+0.000000	+0.000000	+0.000000	−0.000005	−0.000004
96	+0.000000	+0.000000	+0.000000	+0.000009	+0.000009
98	+0.000000	+0.000000	+0.000000	+0.000011	+0.000017
100	+0.000000	+0.000000	+0.000000	−0.000002	+0.000011
102	+0.000000	+0.000000	+0.000000	+0.000002	−0.000001
104	+0.000000	+0.000000	+0.000000	+0.000010	−0.000006
106	+0.000000	+0.000000	+0.000000	−0.000001	+0.000002
108	+0.000000	+0.000000	+0.000000	+0.000004	+0.000012
110	+0.000000	+0.000000	+0.000000	+0.000004	+0.000012
112	+0.000000	+0.000000	+0.000000	+0.000002	+0.000003
114	+0.000000	+0.000000	+0.000000	+0.000003	−0.000005
116	+0.000000	+0.000000	+0.000000	+0.000002	−0.000002
118	+0.000000	+0.000000	+0.000000	+0.000002	+0.000008
120	+0.000000	+0.000000	+0.000000	+0.000002	+0.000011
122	+0.000000	+0.000000	+0.000000	+0.000002	+0.000005
124	+0.000000	+0.000000	+0.000000	+0.000002	−0.000003
126	+0.000000	+0.000000	+0.000000	+0.000001	−0.000003
128	+0.000000	+0.000000	+0.000000	+0.000000	+0.000005
130	+0.000000	+0.000000	+0.000000	+0.000000	+0.000009
132	+0.000000	+0.000000	+0.000000	+0.000000	+0.000005
134	+0.000000	+0.000000	+0.000000	+0.000000	−0.000002
136	+0.000000	+0.000000	+0.000000	+0.000000	−0.000002
138	+0.000000	+0.000000	+0.000000	+0.000000	+0.000004
140	+0.000000	+0.000000	+0.000000	+0.000000	+0.000008
142	+0.000000	+0.000000	+0.000000	+0.000000	+0.000004
144	+0.000000	+0.000000	+0.000000	+0.000000	−0.000002
146	+0.000000	+0.000000	+0.000000	+0.000000	−0.000002
148	+0.000000	+0.000000	+0.000000	+0.000000	+0.000004
150	+0.000000	+0.000000	+0.000000	+0.000000	+0.000007
152	+0.000000	+0.000000	+0.000000	+0.000000	+0.000002
154	+0.000000	+0.000000	+0.000000	+0.000000	−0.000002
156	+0.000000	+0.000000	+0.000000	+0.000000	+0.000000
158	+0.000000	+0.000000	+0.000000	+0.000000	+0.000005
160	+0.000000	+0.000000	+0.000000	+0.000000	+0.000005
162	+0.000000	+0.000000	+0.000000	+0.000000	−0.000000
164	+0.000000	+0.000000	+0.000000	+0.000000	−0.000002
166	+0.000000	+0.000000	+0.000000	+0.000000	+0.000003
168	+0.000000	+0.000000	+0.000000	+0.000000	+0.000005
170	+0.000000	+0.000000	+0.000000	+0.000000	+0.000001
172	+0.000000	+0.000000	+0.000000	+0.000000	−0.000002
174	+0.000000	+0.000000	+0.000000	+0.000000	+0.000001
176	+0.000000	+0.000000	+0.000000	+0.000000	+0.000004
178	+0.000000	+0.000000	+0.000000	+0.000000	+0.000002
180	+0.000000	+0.000000	+0.000000	+0.000000	−0.000002

182	+0.000000	+0.000000	+0.000000	+0.000000	+0.000001
184	+0.000000	+0.000000	+0.000000	+0.000000	+0.000004
186	+0.000000	+0.000000	+0.000000	+0.000000	+0.000002
188	+0.000000	+0.000000	+0.000000	+0.000000	−0.000001
190	+0.000000	+0.000000	+0.000000	+0.000000	+0.000001
192	+0.000000	+0.000000	+0.000000	+0.000000	+0.000003
194	+0.000000	+0.000000	+0.000000	+0.000000	+0.000000
196	+0.000000	+0.000000	+0.000000	+0.000000	−0.000001
198	+0.000000	+0.000000	+0.000000	+0.000000	+0.000003
200	+0.000000	+0.000000	+0.000000	+0.000000	+0.000002
202	+0.000000	+0.000000	+0.000000	+0.000000	−0.000001
204	+0.000000	+0.000000	+0.000000	+0.000000	+0.000001
206	+0.000000	+0.000000	+0.000000	+0.000000	+0.000002
208	+0.000000	+0.000000	+0.000000	+0.000000	−0.000001
210	+0.000000	+0.000000	+0.000000	+0.000000	+0.000001
212	+0.000000	+0.000000	+0.000000	+0.000000	+0.000002
214	+0.000000	+0.000000	+0.000000	+0.000000	−0.000001
216	+0.000000	+0.000000	+0.000000	+0.000000	+0.000002
218	+0.000000	+0.000000	+0.000000	+0.000000	+0.000001
220	+0.000000	+0.000000	+0.000000	+0.000000	+0.000000
222	+0.000000	+0.000000	+0.000000	+0.000000	+0.000001
224	+0.000000	+0.000000	+0.000000	+0.000000	+0.000000
226	+0.000000	+0.000000	+0.000000	+0.000000	+0.000001
228	+0.000000	+0.000000	+0.000000	+0.000000	+0.000001
230	+0.000000	+0.000000	+0.000000	+0.000000	+0.000001
232	+0.000000	+0.000000	+0.000000	+0.000000	+0.000001
234	+0.000000	+0.000000	+0.000000	+0.000000	+0.000001
236	+0.000000	+0.000000	+0.000000	+0.000000	+0.000001
238	+0.000000	+0.000000	+0.000000	+0.000000	+0.000001
240	+0.000000	+0.000000	+0.000000	+0.000000	+0.000001
242	+0.000000	+0.000000	+0.000000	+0.000000	+0.000000
244	+0.000000	+0.000000	+0.000000	+0.000000	+0.000000
246	+0.000000	+0.000000	+0.000000	+0.000000	+0.000000
248	+0.000000	+0.000000	+0.000000	+0.000000	+0.000000
250	+0.000000	+0.000000	+0.000000	+0.000000	+0.000000
252	+0.000000	+0.000000	+0.000000	+0.000000	+0.000000
254	+0.000000	+0.000000	+0.000000	+0.000000	+0.000000

Table A.3 OFDP-SDP Filter Weights for $K = 3$

i	c_i $(M = 8)$	c_i $(M = 16)$	c_i $(M = 32)$	c_i $(M = 64)$	c_i $(M = 128)$
0	+0.957496	+0.956053	+0.949855	+0.948972	+0.948899
2	+0.288312	+0.292721	+0.308339	+0.310240	+0.310387
4	−0.004557	+0.014057	+0.050492	+0.055095	+0.055532
6	+0.005317	+0.004917	+0.011235	+0.011967	+0.012007
8	−0.004371	−0.006708	−0.004763	−0.004522	−0.004468
10	+0.001670	−0.001909	−0.001761	−0.001571	−0.001533
12	−0.002147	+0.002055	+0.001068	+0.001016	+0.001001
14	+0.001722	+0.001718	+0.000328	+0.000293	+0.000285

APPENDIX B – Prototype Filter Weights for QCQP Design

The weights of the proposed prototype filter are presented in Table B.1.

Table B.1 Filter weights for Type-I, Type-II and Type-III configurations with $K = 4$, $M = 32$, $L_p = KM + 1$

	Type-I	**Type-II**	**Type-III**
c_0	$9.179317816790 \cdot 10^{-1}$	$5.016511380872 \cdot 10^{-1}$	$4.993086025524 \cdot 10^{-1}$
c_1	$3.802162534407 \cdot 10^{-1}$	$6.897038048179 \cdot 10^{-1}$	$6.777473126670 \cdot 10^{-1}$
c_2	$1.077526750194 \cdot 10^{-1}$	$5.039449735142 \cdot 10^{-1}$	$5.037266848356 \cdot 10^{-1}$
c_3	$2.456277538185 \cdot 10^{-2}$	$1.795258480584 \cdot 10^{-1}$	$2.213401597940 \cdot 10^{-1}$
c_4	$4.639914990515 \cdot 10^{-3}$	$9.191524770412 \cdot 10^{-3}$	$4.093046350246 \cdot 10^{-2}$
c_5	$1.306778847145 \cdot 10^{-3}$		
c_6	$1.577770437750 \cdot 10^{-3}$		
c_7	$3.721905313771 \cdot 10^{-4}$		

In particular, if $\mathbf{F}$ is taken as a cosine basis (Type-II and Type-III) scaling the number of subcarriers for a given overlapping factor K is an easier task due to the frequency sampling feature of such basis. In this sense, even if the coefficients provided in Table B.1 are derived for a specific value of M, one can still scale the prototype filter for larger values of M. This can be achieve by correctly scaling the frequency components via

$$p[k] = \sum_{i=0}^{N-1} c'_i \cos\left(\frac{2\pi}{KM} i\underline{k}\right), \tag{B.1}$$

where

$$c'_i = \begin{cases} 1, & i = 0 \\ \sqrt{\dfrac{2L_p}{L_p+1}}\dfrac{c_i}{c_0}, & \text{otherwise} \end{cases}. \tag{B.2}$$

APPENDIX C – IOTA: Orthogonality Proof

First, let us apply the orthogonalization operator (3.18) on a continuous function $x(t)$, i.e.,

$$y(t) = \mathcal{O}_{\tau_0} x(t). \tag{C.1}$$

The operator $\mathcal{O}_{\tau_0}$ divides the original function by a summation of shifted versions, leading to the interesting property

$$\begin{aligned}\sum_{n=-\infty}^{\infty} |y(t-n\tau_0)|^2 &= \frac{1}{\tau_0} \sum_{n=-\infty}^{\infty} \frac{|x(t-n\tau_0)|^2}{\sum_{\ell=-\infty}^{\infty} |x(t-n\tau_0-\ell\tau_0)|^2} \\ &= \frac{1}{\tau_0} \frac{\sum_{n=-\infty}^{\infty} |x(t-n\tau_0)|^2}{\sum_{\ell=-\infty}^{\infty} |x(t-\ell\tau_0)|^2} \\ &= \frac{1}{\tau_0}.\end{aligned} \tag{C.2}$$

By convoluting eq. (C.2) with a Dirac Comb, one may conclude that

$$\left[\sum_{n=-\infty}^{\infty} \delta(t-n\tau_0)\right] * |y(t)|^2 = \frac{1}{\tau_0}. \tag{C.3}$$

If the Fourier transform is applied to eq. (C.3), one can observe that

$$\left[\frac{1}{\tau_0} \sum_{n=-\infty}^{\infty} \delta(t-n/\tau_0)\right] \mathcal{F}\left\{|y(t)|^2\right\} = \frac{1}{\tau_0}\delta(\nu). \tag{C.4}$$

By observing that $\mathcal{F}\left\{|y(t)|^2\right\} = A_y(0,\nu)$ and making $\nu = m/\tau_0$ in eq. (C.4), the following eq. may be derived:

$$A_y(0, m/\tau_0) = 0. \tag{C.5}$$

Further manipulations can be carried out if one recalls that $\tau_0\nu_0 = 1/2$:

$$A_y(0, 2m\nu_0) = 0. \tag{C.6}$$

Hence, if one applies the operator $\mathcal{O}_{\tau_0}$ in time domain, the original signal will be orthogonal in the frequency domain. Similarly, if one applies the orthogonalization operator in the frequency domain, one may conclude that

$$A'_y(2n\tau_0, 0) = 0, \tag{C.7}$$

which is basically the Nyquist ISI criteria. Therefore, the complete IOTA implementation provide a prototype filter that yields

$$A_p(2n\tau_0, 2m\nu_0) = 0, \tag{C.8}$$

which can provide perfect symbol reconstruction if, and only if, the prototype filter is a non-truncated continuous function.

APPENDIX D – Functions Definition

D.1 Tail Distribution Function

The Q-Function or tail distribution function describes the probability of a normal random variable with null mean and unitary variance, $X \sim \mathcal{N}(0,1)$, assuming a value larger than x, i.e.,

$$Q(x) = \Pr\left(X > x\right), \tag{D.1}$$

which leads to the integral form:

$$Q(x) = \frac{1}{\sqrt{2\pi}} \int_x^\infty \exp\left(-\frac{t^2}{2}\right) dt. \tag{D.2}$$

Similarly, to the Q-Function, the complementary error function also describe probabilities related to normal random variables. But in this case, with a random variable of variance 1/2, leading to the relation

$$\operatorname{erfc}(x) = 1 - 2Q\left(\sqrt{2}x\right), \tag{D.3}$$

or

$$Q(x) = \frac{1}{2} - \operatorname{erfc}\left(\frac{x}{\sqrt{2}}\right), \tag{D.4}$$

Notice that authors deploy both the complementary error function and the Q-Function and the choice of one or another is a mere preference matter.

D.2 Hermite Functions

Let us define the Hermite function through the recursive formula

$$\mathcal{H}_n(x) = \exp\left(-\frac{x}{2}\right) \frac{d^n}{dx^n} \exp\left(-x^2\right), \tag{D.5}$$

which, in contrast, is different from Hermite polynomials by a $e^{-x^2/2}$ factor.

For convenience, let us also define the normalized Hermite function as

$$\mathcal{H}'_n(x) = \mathcal{H}_n\left(\sqrt{2\pi}x\right), \tag{D.6}$$

which aids the description of the Hermite prototype filter. Moreover, we also provide the closed form expression for the normalized Hermite functions for $n \in \{0, 4, 8, 12\}$ in Table D.1

Table D.1 Normalized Hermite Functions $\mathcal{H}'_n(x)$ for $n \in \{0, 4, 8, 12\}$

n	$\mathcal{H}'_n(x)$
0	$16\exp\left(-\pi x^2\right)\left(4\pi^2x^4 - 6\pi x^2 + 3/4\right)$
4	$256\exp\left(-\pi x^2\right)\left(16\pi^4x^8 - 112\pi^3x^6 + 210\pi^2x^4 - 105\pi x^2 + 105/16\right)$
8	$4096\exp\left(-\pi x^2\right)\left(64\pi^6x^{12} - 1056\pi^5x^{10} + 5940\pi^4x^8 - 13860\pi^3x^6 + 51975/4\pi^2x^4 - 31185/8\pi x^2 + 10395/64\right)$
12	$65536\exp\left(-\pi x^2\right)\left(256\pi^8x^{16} - 7680\pi^7x^{14} + 87360\pi^6x^{12} - 480480\pi^5x^{10} + 1351350\pi^4x^8 - 1891890\pi^3x^6 + 1182431.25\pi^2x^4 - 253378.125\pi x^2 + 2027025/256\right)$

D.3 Generalized Laguerre Polynomials

The generalized or associated Laguerre polynomials is the family of orthogonal polynomials that are the solution of

$$x\frac{d^2y}{dx^2} + (\alpha + 1 - x)\frac{dy}{dx} + ny = 0, \tag{D.7}$$

which is a second order differential equation known as Laguerre's equation. The solution of (D.7) can be obtained via the recursive formula

$$L_n^\alpha(x) = \frac{1}{n!}e^{-x}x^{-\alpha}\frac{d^n}{dx^n}\left(x^{n+\alpha}e^{-x}\right), \tag{D.8}$$

known as Rodrigues Formula. Fortunately, a closed form expression is available:

$$L_n^\alpha(x) = \sum_{\ell=0}^{n}\frac{(-1)^\ell x^\ell}{\ell!(n-\ell)!}\prod_{i=\ell+1}^{n}(i+\alpha). \tag{D.9}$$

APPENDIX E – Multirate Processing Basics

In this section, basics on multirate processing are presented aiming to aid readers to deploy such concepts on signal processing of FBMC systems.

E.1 Expansion/Up-Sampling

An expander is a device capable of increasing the rate of its input signal. The representation of the such a device is presented in Figure E.1 and its output can be written as

$$y[k] = \begin{cases} x\left[\frac{k}{N}\right], & k = iN, \text{ where } i \in \mathbb{Z} \\ 0, & \text{otherwise} \end{cases}, \tag{E.1}$$

where $x[k]$ is the input signal, $y[k]$ is the output signal and N is an integer that represents the expansion rate of the block. By analyzing eq. (E.1), the expander block increases the rate of the input signal by inserting $N-1$ zeroes between samples of $x[k]$.

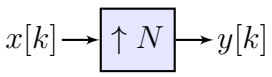

Figure E.1 Expander Block Diagram

E.1.1 Example I

As an example, Figure E.2 depicts the expansion of a triangular pulse with $N = 2$. Notice that the expander inserts one null point between each pair of adjacent samples of the input signal, as highlighted in blue.

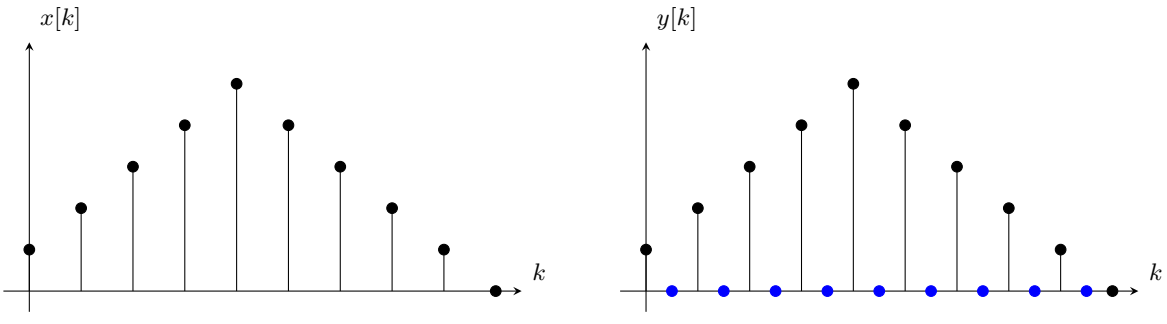

(a) Input signal **(b)** Output signal

Figure E.2 Up-sampling example for $N = 2$

E.1.2 Z-Transform and Spectrum

Concerning the spectrum, one can observe that the Z-Transform of the output signal of an expander is

$$\begin{aligned} Y(z) &= \sum_{\ell=-\infty}^{\infty} y\left[\ell\right] z^{-\ell} \\ &= \sum_{\ell=-\infty}^{\infty} x\left[\frac{\ell}{N}\right] z^{-\ell}\Big|_{\ell \leftarrow N\ell} \\ &= \sum_{\ell=-\infty}^{-\infty} x\left[\frac{\ell}{N}\right] \left(z^{N}\right)^{\ell} \\ &= X\left(z^{N}\right). \end{aligned} \tag{E.2}$$

By recalling that the DFT can be easily obtained from eq. (E.2) by making $z = e^{j\omega}$, one can also observe that the spectrum period becomes $2\pi/N$. Hence, the spectrum of the output signal is compressed throughout the frequency domain. In order to illustrate such behavior, Figure E.3 exemplifies how a input signal with a triangular spectrum is affected by the expansion procedure. It is worthy note mentioning that Figures E.2 and E.3 are not related directly as the triangular shape was used in both cases for simplicity.

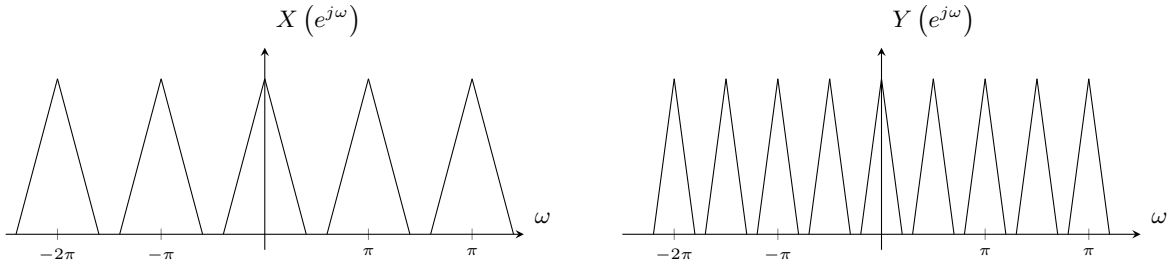

(a) Input signal **(b)** Output signal

Figure E.3 Spectrum for an up-sampler with $N = 2$

E.2 Decimation/Down-Sampling

Conversely from the expansion/up-sampling, the decimation procedure reduces the number of samples, *i.e.*,

$$y[k] = x[Mk], \tag{E.3}$$

where $x[k]$ is the input signal, $y[k]$ is the output signal and M is an integer that represents the decimation rate of the block. Hence, by analyzing eq. (E.3), one can infer that the decimator takes only one sample of M sequential samples, whereas the remaining samples are discarded.

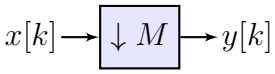

Figure E.4 Decimator Block Diagram

E.2.1 Example II

Figure E.5 depicts the decimation procedure applied, once more, to a triangular input signal. Since the decimation rate is $M = 2$, the decimator block eliminates the odd indexed samples highlighted in red.

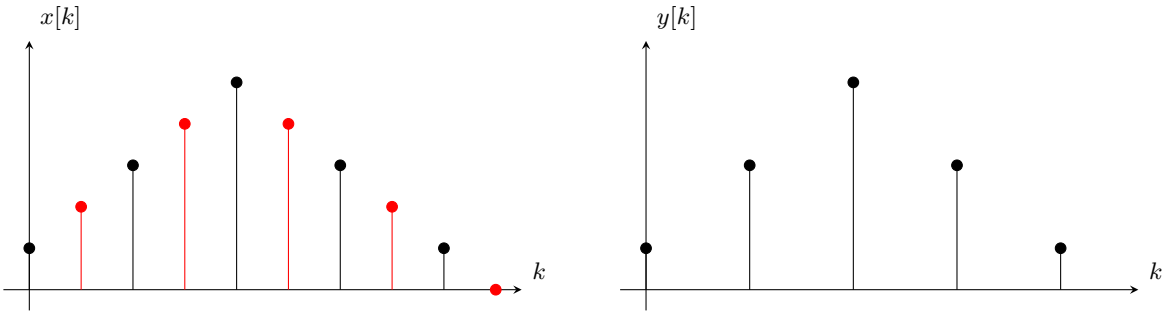

(a) Input signal **(b)** Output signal for $M = 2$

Figure E.5 Down-sampling example

E.2.2 Z-Transform and Spectrum

In order to obtain the spectrum of the decimated signal, let us multiply the input signal by a Dirac comb with a a rate of M samples:

$$x'[k] = x[k] \sum_{\ell=-\infty}^{\infty} \delta\left(k - M\ell\right). \tag{E.4}$$

By deploying the Dirac comb, samples that would be discarded by the decimator are zeroed prior to the decimation procedure itself. Despite $x[k]$ and $x'[k]$ being different, their decimation lead to the same result. As a second step, eq. (E.4) can be rewritten by using the Discrete Fourier Series (DFS) representation for the Dirac comb

$$x'[k] = x[k] \sum_{m=0}^{M-1} e^{j\frac{2\pi}{M}mk}. \tag{E.5}$$

Since eq. (E.5) can be interpreted as the sum of M frequency shifts (modulation) of $x[k]$, the Z-transform of $x'[k]$ can be expressed as: (E.5):

$$X'(z) = \frac{1}{M} \sum_{m=0}^{M-1} X\left(ze^{-\frac{2\pi}{M}m}\right). \tag{E.6}$$

By considering $x'[k]$ the expanded signal of $y[k]$, one can observe that:

$$X'(z) = Y(z^M), \tag{E.7}$$

as presented previously in eq. (E.2). Therefore, by using the dual form of eq. (E.7), *i.e.*,

$$Y(z) = X(z^{1/M}), \tag{E.8}$$

the decimated signal of $x[k]$ can be written as

$$Y(z) = \frac{1}{M} \sum_{m=0}^{M-1} X\left(z^{1/M} e^{-j\frac{2\pi}{M}m}\right) \tag{E.9}$$

Differently from the expander, the spectrum of the output signal of a decimator spreads throughout the frequency domain. Figure E.6 depicts how the decimator affects the spectrum of a input signal with a triangular spectrum.

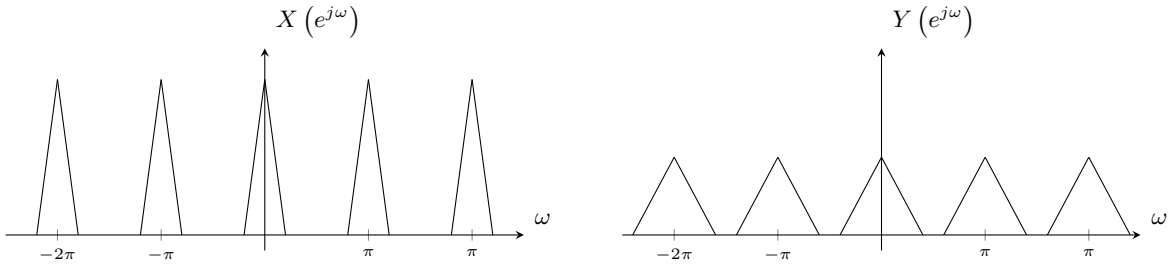

(a) Input signal **(b)** Output signal

Figure E.6 Spectrum for an down-sampler with $M = 2$

E.3 Polyphase Decomposition

Through the Polyphase Decomposition, a digital filter of length L_p can be split into M filters with a lower number of taps. In this sense, let us apply the Z-Transform of $p[k]$:

$$P(z) = \sum_{k=0}^{L_p-1} p[k] z^{-k}. \tag{E.10}$$

By deploying the Polyphase Decompostion, the Z-Transform of the filter can be written as

$$P(z) = \sum_{m=0}^{M-1} G_m(z^M) z^{-m}, \tag{E.11}$$

where

$$G_m(z) = \sum_{\ell=0}^{K-1} p[m + \ell M] z^{-\ell}. \tag{E.12}$$

Notice that such a procedure split the original filter into M filters of length $\lfloor L_p/M \rceil$, which is particularly advantageous for implementing filter-banks efficiently.

E.4 Noble Identities

According to the Noble identities (VAIDYANATHAN, 1993), one can reverse the order of the filtering and the expander/decimator, as illustrated in Figures E.7 and E.8.

(a) Implementation 1 **(b)** Implementation 2

Figure E.7 Down-sampling Noble identities

(a) Implementation 1 **(b)** Implementation 2

Figure E.8 Up-sampling Noble identities

APPENDIX F – Ambiguity Function

The ambiguity function of a pulse $p(t)$ is a bi dimensional function that describes the effects of a Doppler shift ν on a receiver equipped with a matched filter, which can be described by

$$A_p(\tau,\nu) = \int_{-\infty}^{\infty} p(t)p^*(t-\tau)e^{-j2\pi\nu\tau}dt. \tag{F.1}$$

An useful interpretation comes by visualizing the ambiguity function as a auto-correlation function that covers both the time and frequency domains. In fact, it is easy to observe that $A_p(\tau,0)$ is the auto-correlation of a pulse $p(t)$, while $A_p(0,0)$ describes the total power of the prototype filter. Also, the ambiguity function can be used to describe the Nyquist ISI criteria as $A_p(n\tau_0,0) = \delta(n)$ coincides with such constraint.

As an alternative use, the ambiguity function can be deployed to visualize the time-frequency spreading features of a prototype function. In this sense, a prototype filter can be considered well-contained in time if its ambiguity function experiences a fast decay around $\tau = 0$. Similarly, if $A_p(\tau,\nu)$ falls quickly along the ν-axis, then $p(t)$ presents a concentrated spectrum. However, as pointed out, prototype filters cannot be concentrated in both frequency and time domains according to the Heisenberg Uncertainty Principle. Hence, optimal concentration on both time and frequency domains occurs when $\xi = 1$. In this sense, if one normalizes both ν and τ axis, the ambiguity function will yields an isotropic response for near unitary ξ prototype filters.

In the following sections, we provide the contour plot of the prototype filters discussed in Chapter 3. Ten plot levels are displayed in an Hue, Saturation, Value (HSV) color gradient for each ambiguity function plot, where the preset levels are shown when

$$A_p(\tau,\nu) \in \{0.0316, 0.0458, 0.0664, 0.0962, 0.1395, 0.2021, 0.2929, 0.4244, 0.6150, 0.8913\}.$$

Also, the axis of $A_p(\tau,\nu)$ are normalized with τ_0 and ν_0 in order to provide a better ambiguity function visualization.

F.1 Squared-Root-Raised-Cosine

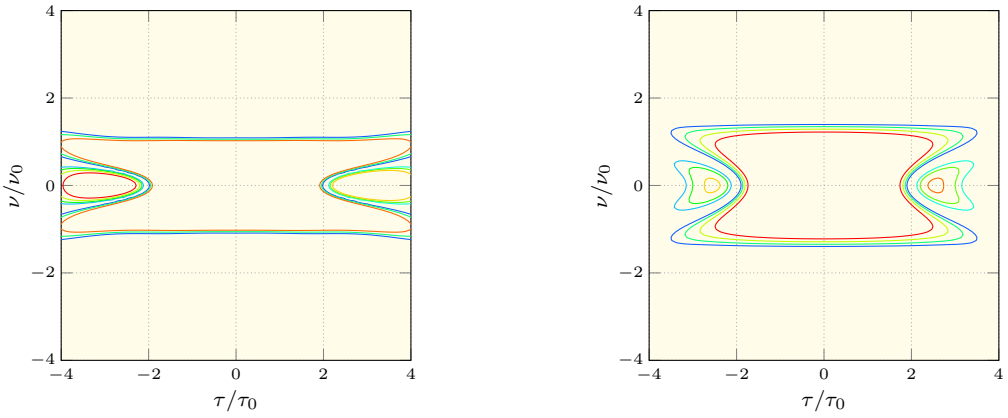

(a) $r = 0.25$ **(b)** $r = 0.75$

Figure F.1 Ambiguity function for SRRC prototype filters ($K = 4$, $M = 32$, and $L_p = 129$)

F.2 Gaussian Function

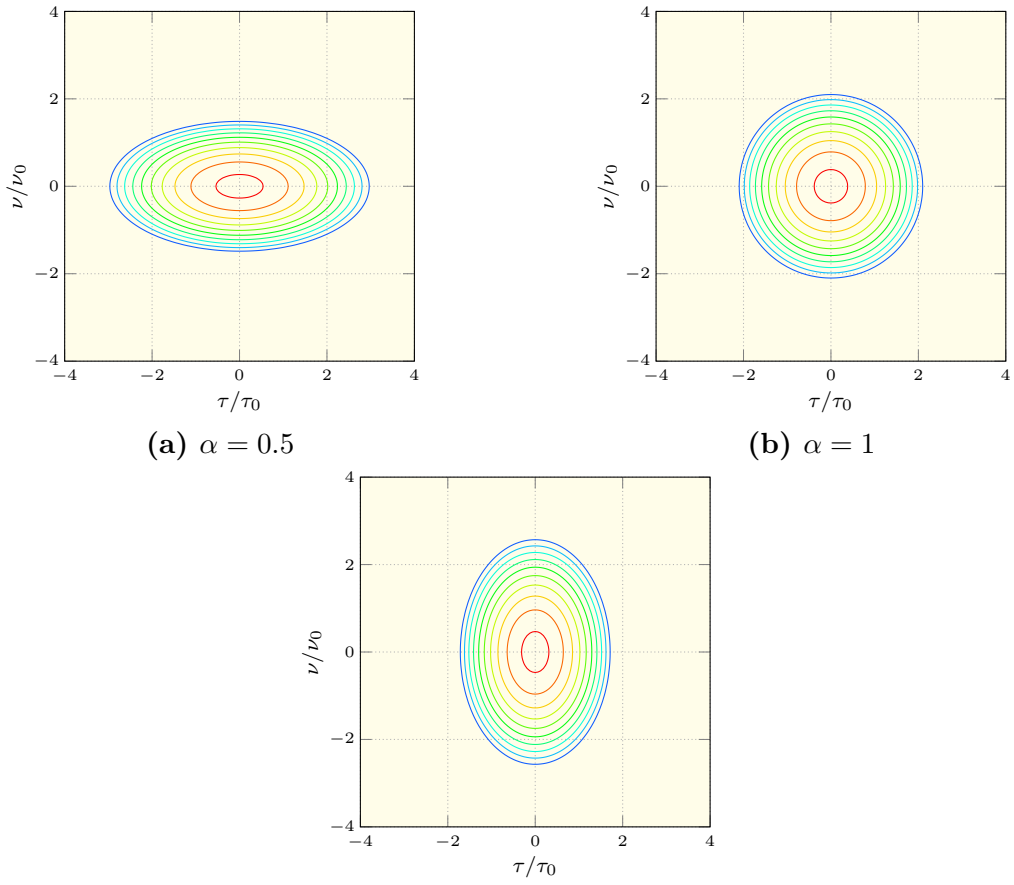

(a) $\alpha = 0.5$ **(b)** $\alpha = 1$

(c) $\alpha = 1.5$

Figure F.2 Ambiguity function for Gaussian prototype filters ($K = 4$, $M = 32$, and $L_p = 129$)

F.3 Extended Gaussian Function

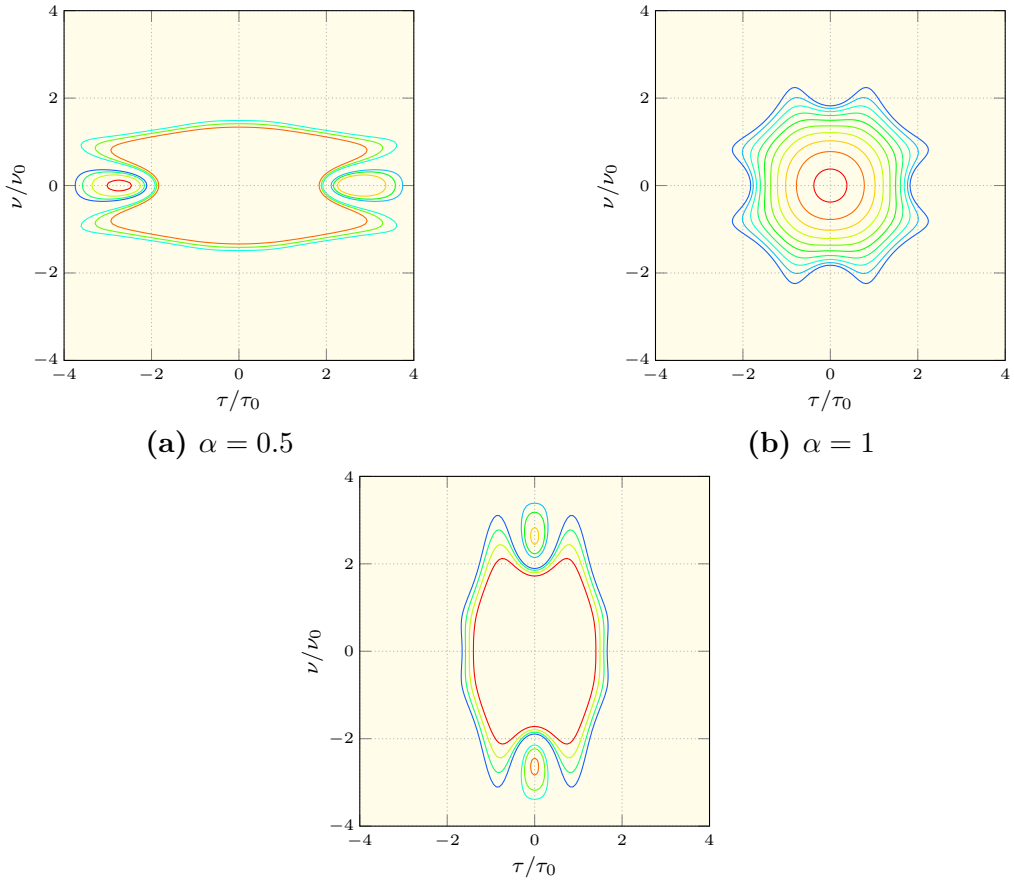

(a) $\alpha = 0.5$

(b) $\alpha = 1$

(c) $\alpha = 1.5$

Figure F.3 Ambiguity function for EGF prototype filters ($K = 4$, $M = 32$, and $L_p = 129$)

F.4 Hermite Prototype Filter

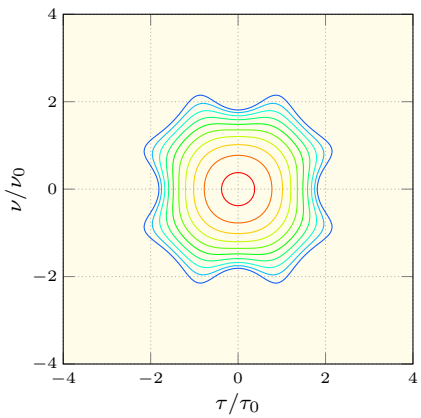

Figure F.4 Ambiguity function for Hermite prototype filter ($K = 4$, $M = 32$, and $L_p = 129$)

F.5 Discrete Prolate Spheroidal Sequences

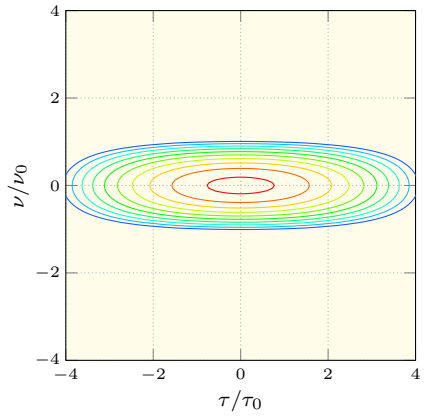

Figure F.5 Ambiguity function for DPSS prototype filters ($K = 4$, $M = 32$, and $L_p = 129$)

F.6 Optimal Finite-Duration Pulse

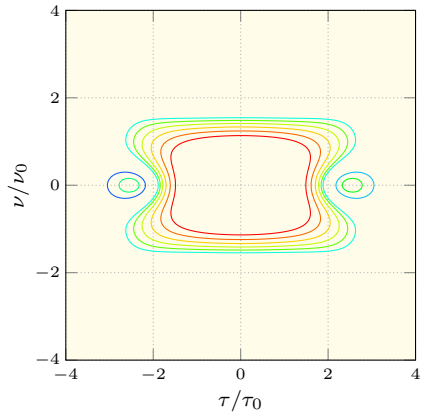

Figure F.6 Ambiguity function for OFDP prototype filter ($K = 4$, $M = 32$, and $L_p = 129$)

F.7 Mirabbasi-Martin Prototype Filter

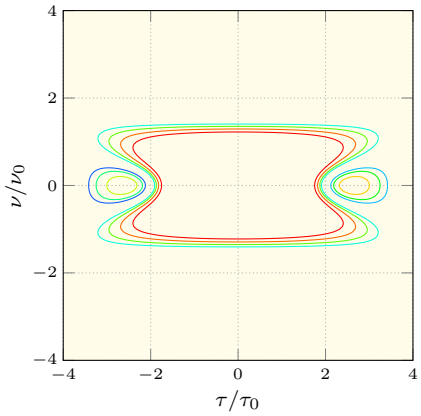

Figure F.7 Ambiguity function for Mirabbasi-Martin prototype filter ($K = 4$, $M = 32$, and $L_p = 129$)

F.8 Windowed Designs

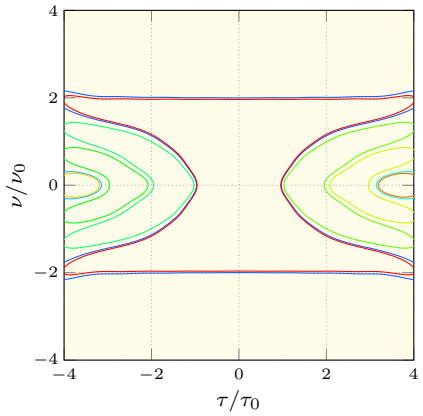

(a) Rectangular window

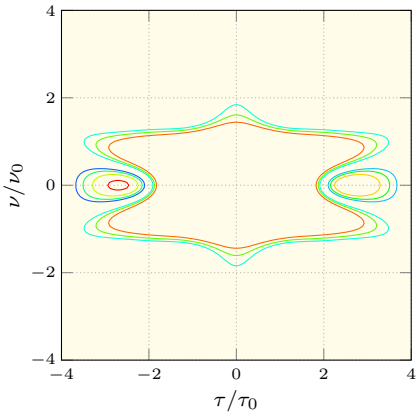

(b) Triangular window

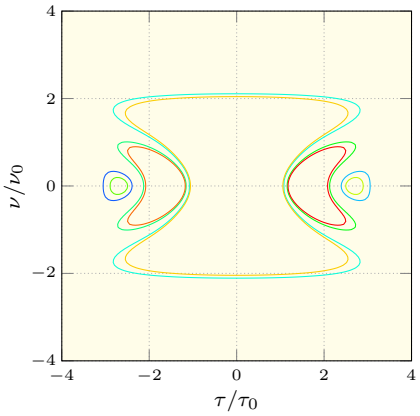

(c) Hanning window

Figure F.8 Ambiguity function for windowed prototype filters ($K = 4$, $M = 32$, and $L_p = 129$)

F.9 OFDP-SDP

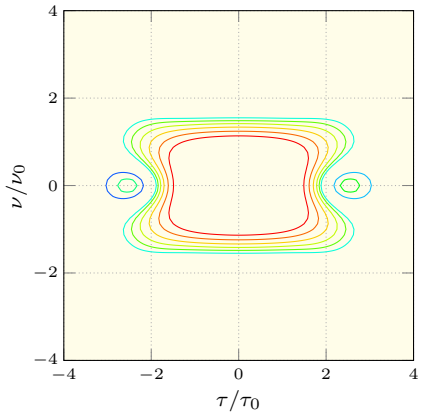

Figure F.9 Ambiguity function for OFDP-SDP prototype filter ($K = 3$, $M = 32$, and $Lp = 96$)

F.10 Type-I Prototype Filter

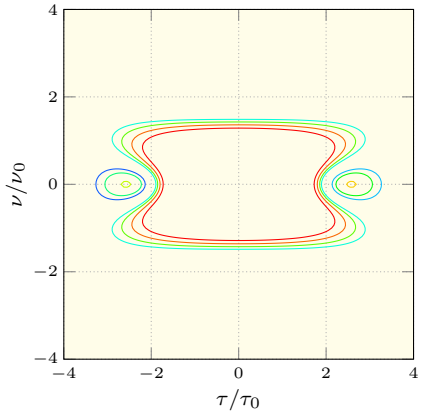

Figure F.10 Ambiguity function for Type-I prototype filter ($K = 4$, $M = 32$, and $L_p = 129$)

F.11 Type-II Prototype Filter

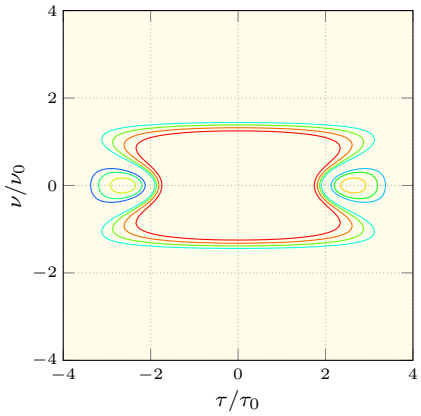

Figure F.11 Ambiguity function for Type-II prototype filter ($K = 4$, $M = 32$, and $L_p = 129$)

F.12 Type-III Prototype Filter

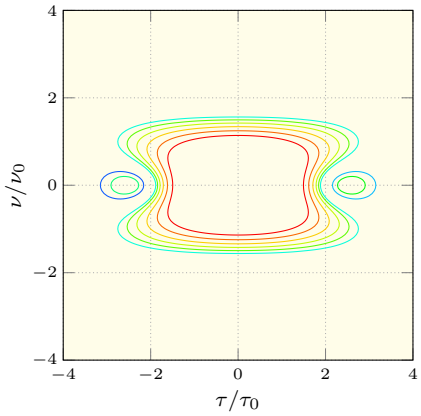

Figure F.12 Ambiguity function for Type-III prototype filter ($K = 4$, $M = 32$, and $L_p = 129$)

APPENDIX G – Performance Spider Plots

In order to complement the numerical results presented in Chapter 3, the following figures in this appendix constitute an alternative representation of Table 3.2. In this sense, spider plots, also known as radar charts, are used to display the performance of each prototype filter discussed in Chapter 3. A spider plot is a multi-axis plot used to characterize the parameters or behavior of a given set of data. In this case, we aim to present the performance of each prototype filter in terms of SIR, MSL, OoB energy, Heisenberg factor and time and frequency spreads. Notice, however, that such parameters are remapped to represent performance in an increasing way. Hence, larger areas covered by a spider plot mean higher global filter performance.

G.1 Squared-Root-Raised-Cosine

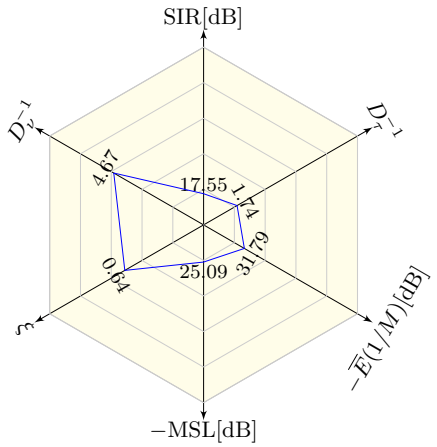

(a) $r = 0.25$

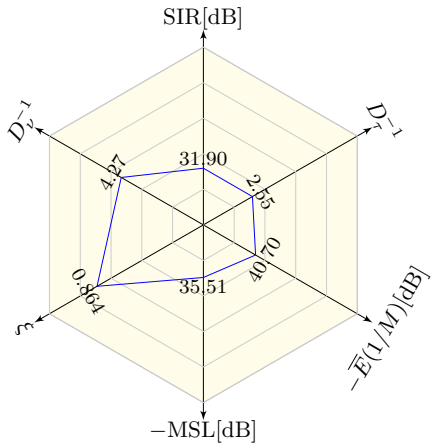

(b) $r = 0.75$

Figure G.1 Performance spider plots for SRRC prototype filters ($K = 4$, $M = 32$, and $L_p = 129$)

G.2 Gaussian Function

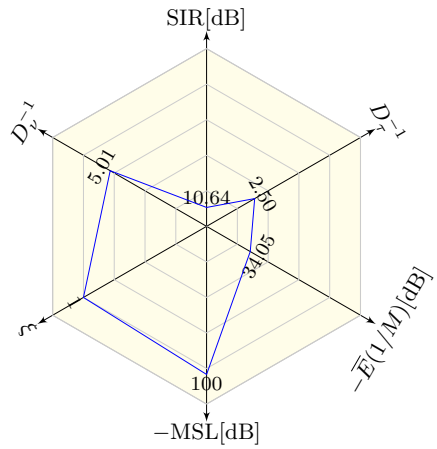

(a) $\alpha = 0.5$

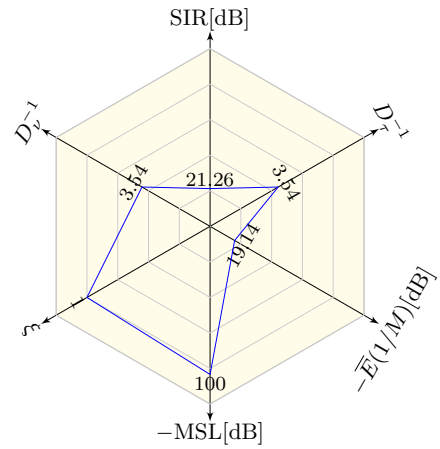

(b) $\alpha = 1$

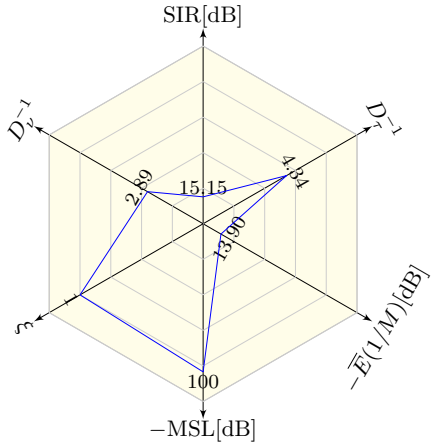

(c) $\alpha = 1.5$

Figure G.2 Performance spider plots for Gaussian prototype filters ($K = 4$, $M = 32$, and $L_p = 129$)

G.3 Extended Gaussian Function

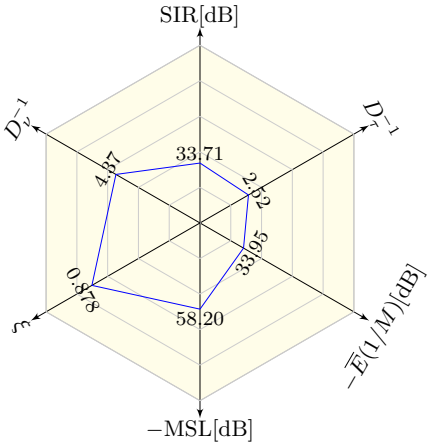

(a) $\alpha = 0.5$

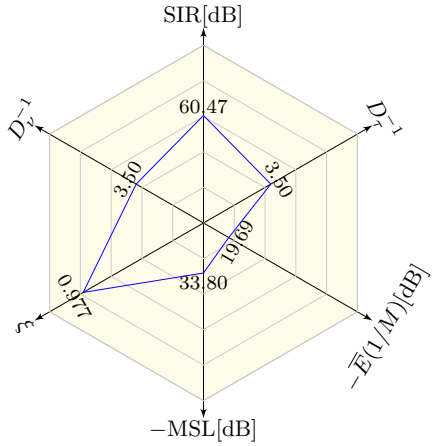

(b) $\alpha = 1$

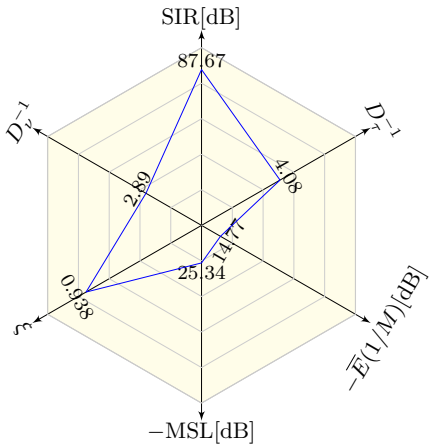

(c) $\alpha = 1.5$

Figure G.3 Performance spider plots for EGF prototype filters ($K = 4$, $M = 32$, and $L_p = 129$)

G.4 Hermite Prototype Function

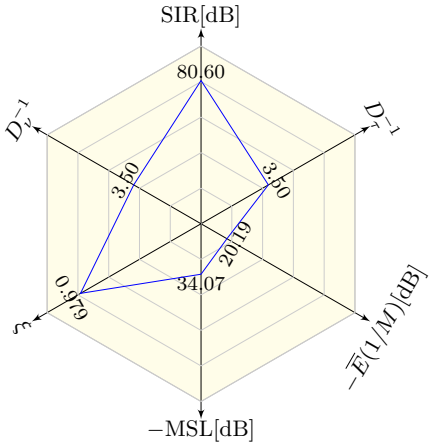

Figure G.4 Performance spider plots for Hermite prototype filter ($K = 4$, $M = 32$, and $L_p = 129$)

G.5 Discrete Prolate Spheroidal Sequence

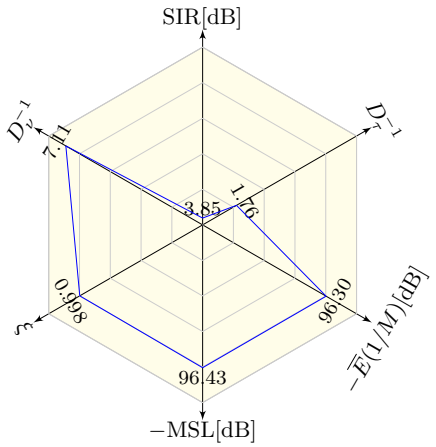

Figure G.5 Performance spider plots for DPSS prototype filters ($K = 4$, $M = 32$, and $L_p = 129$)

G.6 Optimal Finite-Duration Pulse

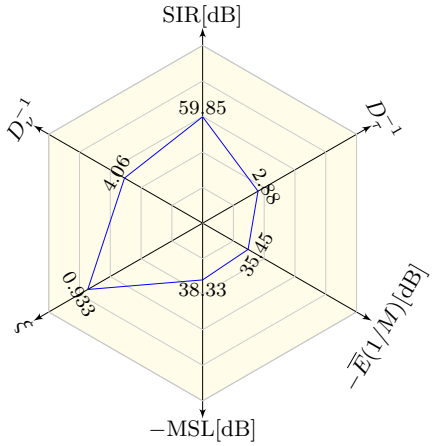

Figure G.6 Performance spider plots for OFDP prototype filter ($K = 4$, $M = 32$, and $L_p = 129$)

G.7 Mirabbasi-Martin Prototype Filter

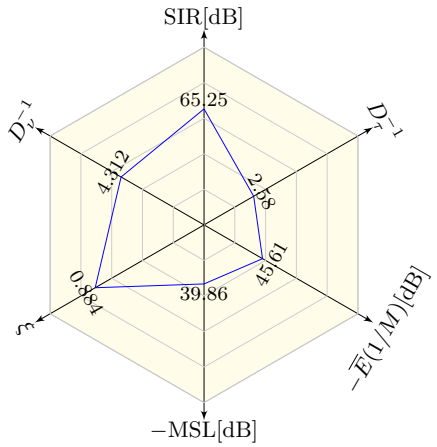

Figure G.7 Performance spider plots for Mirabbasi-Martin prototype filter ($K = 4$, $M = 32$, and $L_p = 129$)

G.8 Windowed Designs

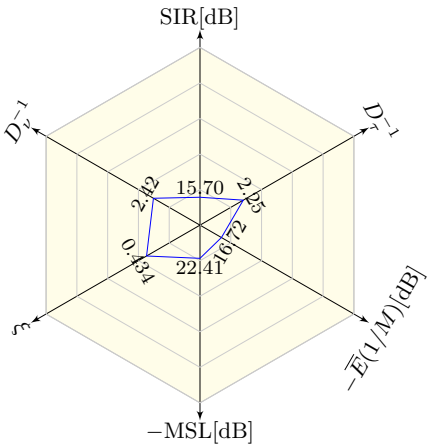

(a) Rectangular window

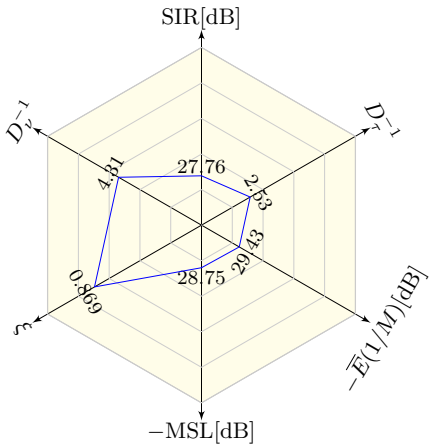

(b) Triangular window

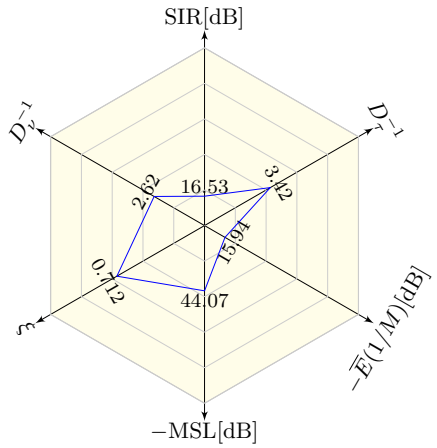

(c) Hanning window

Figure G.8 Performance spider plots for windowed prototype filters ($K = 4$, $M = 32$, and $L_p = 129$)

G.9 OFDP-SDP

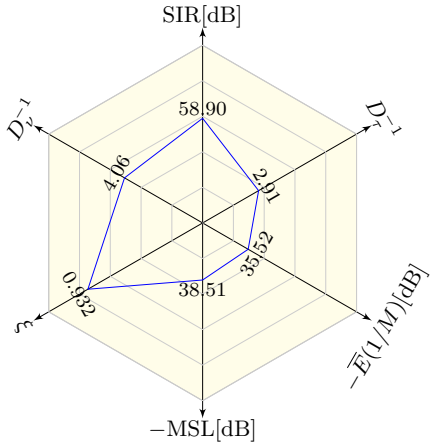

Figure G.9 Performance spider plots for OFDP-SDP prototype filter ($K = 3$, $M = 32$ and $Lp = 96$)

G.10 Type-I Prototype Filter

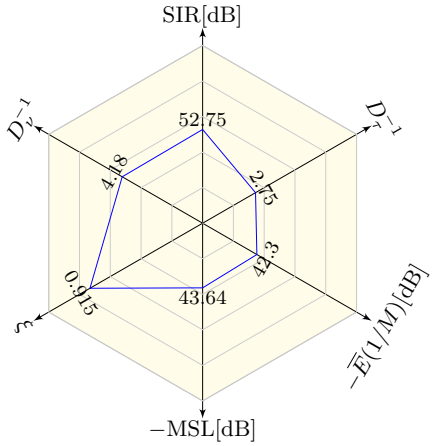

Figure G.10 Performance spider plots for Type-I prototype filter ($K = 4$, $M = 32$ and $L_p = 129$

G.11 Type-II Prototype Filter

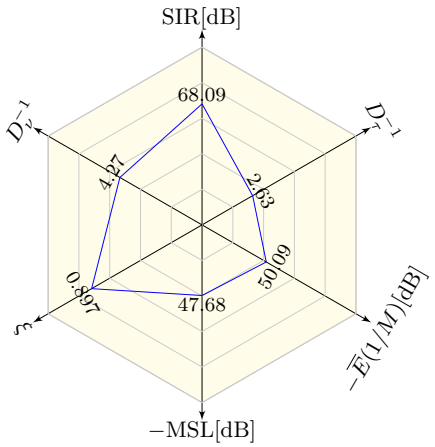

Figure G.11 Performance spider plots for Type-II prototype filter ($K = 4$, $M = 32$, and $L_p = 129$)

G.12 Type-III Prototype Filter

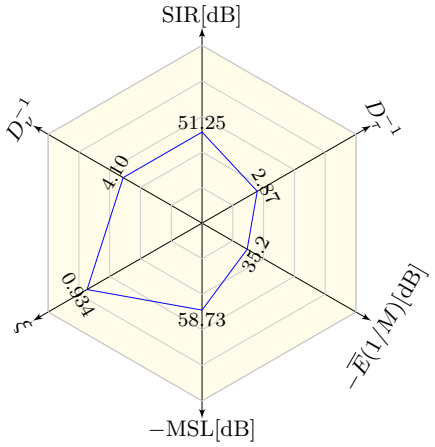

Figure G.12 Performance spider plots for Type-III prototype filter ($K = 4$, $M = 32$, and $L_p = 129$)

APPENDIX H – MATLAB Scripts

H.1 FBMC Transmultiplexer Scripts

H.1.1 Traditional Implementation

Script H.1 Matlab script for a classical FBMC implementation

```
function fbmc_transmux
%% Description: traditional FBMC transmux implementation

%% Basic Parameters
M   = 64;                                                   %% Number of subcarriers
K   = 4;                                                    %% Overlapping factor
Nq  = 64;                                                   %% Modulation order (QAM)
Nd  = 1000;                                                 %% Number of QAM symbols
Lp  = M*K + 1;                                              %% Fitler length
p   = proto_egf( M, K, Lp, 1.00, 1/sqrt(2), 1/sqrt(2));     %% Prototype filter

%% Filter bank
Lp       = length(p);                                       %% Filter length
g        = fbmc_bank( M, p );                               %% Filter bank
[Da,Db]  = fbmc_delay_eval( Lp, M, K );                     %% Delay net
Phi      = 1i.^hankel( 0:M-1, M-1:M-1+2*Nd-1 );             %% Phase shift

%% Transmux
d  = qammod( randi([0 Nq-1], [M Nd]), Nq, 0, 'gray' );      %% QAM data
a  = reshape( [real(d);imag(d)], [M 2*Nd] );                %% QAM staggering
b  = a .* Phi;                                              %% Phase-shifted PAM symbols
s  = fbmc_synthesis( b, g );                                %% Synthesis
xd = circshift( s, [0 Db] );                                %% Receiver delay
y  = mc_fbmc_analysis( xd, g );                             %% Analysis
yd = circshift( y, [0 -Da] );                               %% Output "delay" shift
ah = real( yd(:,1:2*Nd) .* conj(Phi) );                     %% Remove phase shift
dh = ah(:,1:2:end) + 1i*ah(:,2:2:end);                      %% De-staggering
end
```

H.1.2 Polyphase Implementation

Script H.2 Matlab script for a polyphase FBMC implementation

```
function fbmc_transmux_poly
%% Description: polyphase FBMC transmux implementation

%% Basic Parameters
M  = 64;                                                %% Number of subcarriers
K  = 4;                                                 %% Overlapping factor
Nq = 64;                                                %% Modulation order (QAM)
Nd = 1000;                                              %% Number of QAM symbols
Lp = M*K + 1;                                           %% Fitler length
p  = proto_egf( M, K, Lp, 1.00, 1/sqrt(2), 1/sqrt(2));  %% Prototype filter

%% Filter bank
Lp      = length(p);                                    %% Filter length
Gz2     = fbmc_bank_poly( p, M );                       %% Polyphase filterbank
[Da,Db] = fbmc_delay_eval( Lp, M, K );                  %% Delay net
Phi     = 1i.^hankel( 0:M-1, M-1:M-1+2*Nd-1 );          %% Phase shift

%% Transmux
d  = qammod( randi([0 Nq-1], [M Nd]), Nq, 0, 'gray' );  %% QAM data
a  = reshape( [real(d);imag(d)], [M 2*Nd] );            %% QAM staggering
b = a .* Phi;                                           %% Phase-shifted PAM symbols
s  = fbmc_synthesis_poly( b, Gz2 );                     %% Synthesis
xd = circshift( s, [0 Db] );                            %% Receiver delay
y  = fbmc_analysis_poly( xd, Gz2 );                     %% Analysis
yd = circshift( y, [0 -Da] );                           %% Output "delay" shift
ah = real( yd(:,1:2*Nd) .* conj(Phi) );                 %% Remove phase shift
dh = ah(:,1:2:end) + 1i*ah(:,2:2:end);                  %% De-staggering
end
```

H.1.3 Filter Bank Functions

Script H.3 Matlab script for generating a FBMC filter bank

```
function g = fbmc_bank( M, p )
%% Description: filter bank
%       Output: g, filter bank
%        Input: M, number of subcariers
%               p, filter length

%% Filter length
Lp = length(p);

%% Synthesis filter
g = zeros(M,Lp);
k = 0:(Lp-1);
for m = 1:M
    g(m,:) = p .* exp( 1i*2*pi*(m-1)/M* ( k-(Lp-1)/2 ) ) ;
end

end
```

Script H.4 Matlab script for generating the polyphase components of a FBMC filter bank

```
function [Gz2,Gz] = fbmc_bank_poly( p, M )
%% Description: evaluates the polyphase components of a prototype filter p
%       Output: Gz2, polyphase components of p
%               Gz,  polyphase components of p
%        Input: p,   prototype filter
%               M,   number of subcariers

%% Filter length
Lp = length(p);

%% Polyphase components G(z)
Gz = zeros( M, ceil(Lp/M) );
for m = 0:M-1
    temp = p( m+1:M:end );
    Gz(m+1,1:length(temp)) = temp;
end

%% Polyphase components G(z^2)
Gz2            = zeros(M,2*ceil(Lp/M));
Gz2(:,1:2:end) = Gz;
end
```

H.1.4 Delay and Latency Functions

Script H.5 Matlab script for evaluating the Δ_α and Δ_β

```
function [Da,Db] = mc_fbmc_delay_eval( Lp, M, K )
%% Description: generates the EGF prototype filter with a spreading factor alpha
%       Output: Da, latency
%               Db, input delay
%        Input: Lp, filter length
%               M,  number of subcariers
%               K,  overlapping factor

%% Delay and latency evaluation
if Lp > M*K +1
    Db = M-mod(Lp,M*K)+1;
    Da = ( Lp - 1 + Db )/ (M/2);

else
    Db = -(Lp-M*K-1);
    Da = 2*K;
end
end
```

H.1.5 FBMC Synthesis Functions

Script H.6 Matlab script for synthesizing a FBMC signal

```
function s = fbmc_synthesis( b, g )
%% Description: FBMC signal synthesis
%       Output: s, FBMC signal
%        Input: b, input phase-shifted PAM symbols
%               g, polyphase components of p

%% Input sizes
[M,Nsymb] = size(b);
Lp = size( g, 2 );

%% Symbol expansion
b_exp = kron( b, [1 zeros(1,M/2-1)] );

%% Synthesis filtering
s = zeros( 1, Lp + M/2*(Nsymb) -1 );
for m = 1:M
    s =  s + conv( g(m,:), b_exp(m,:) );
end
end
```

Script H.7 Matlab script for synthesizing a FBMC signal via polyphase components

```
function s = fbmc_synthesis_poly( b, Gz2 )
%% Description: FBMC signal synthesis
%       Output: s,   FBMC signal
%        Input: b,   input phase-shifted PAM symbols
%               Gz2, polyphase components of p

%% Sizes
[M,N] = size(b);
Lp    = sum(sum(Gz2(:,1:2:end)~=0));

%% Synthesis
s    = zeros( 1, (N+2*ceil(Lp/M)-1)*M/2 );
Phi0 = repmat( exp(-1i*2*pi/M*[0:M-1]'*(Lp-1)/2), [1 N] );
x1   = ifft( M * b .* Phi0, M, 1);
for m = 1:M
    temp2 = zeros( 1, (N+2*ceil(Lp/M)-1)*M/2 );
    temp2(1:M/2:end) = conv(x1(m,:),Gz2(m,:));
    s = s + circshift( temp2, [0 m-1] );
end
end
```

H.1.6 FBMC Analysis Functions

Script H.8 Matlab script for analyzing a FBMC signal

```
function bh = fbmc_analysis( xd, g )
%% Description: FBMC signal synthesis
%       Output: bh, estimated phase-shifted PAM symbol
%        Input: xd, input FBMC signal properly with a proper delay
%               g,  filter bank

%% Input sizes
[M,Lp] = size(g);

%% Analysis
bh_exp = zeros( M, length(xd)+Lp-1 );
for m = 1:M
    bh_exp(m,:) = conv( xd, fliplr( conj(g(m,:)) ) );
end
bh     = bh_exp( :,1:(M/2)^1:end );
end
```

Script H.9 Matlab script for analyzing a FBMC signal via polyphase components

```
function bh = fbmc_analysis_poly(xd,Gz2)
%% Description: FBMC signal analysis
%       Output: bh,  estimated phase-shifted PAM symbol
%        Input: xd,  input FBMC signal properly with a proper delay
%               Gz2, polyphase components of p

%% Sizes
M  = size(Gz2,1);
Lp = sum(sum(Gz2(:,1:2:end)~=0));

%% Synthesis
b0 = zeros(M,round(length(xd)/(M/2))+2*ceil(Lp/M)-1);
for m = 1:M
    temp = circshift( xd, [0 m-1] );
    b0(m,:) = conv( temp(1:M/2:end), Gz2(m,:) );
end
Phi0 = repmat( exp(-1i*2*pi/M*[0:M-1]'*(Lp-1)/2), [1 ...
    round(length(xd)/(M/2))+2*ceil(Lp/M)-1] );
bh = M * ifft( b0,M,1 ) .* Phi0;
end
```

H.2 Prototype Filter Scripts

Script H.10 Matlab script for generating a SRRC prototype filter

```
function p = proto_srrc( M, Lp, r )
%% Description: generates the Square-Root Raised Cosine prototype filter
%       Output: p,  prototype filter
%        Input: M,  number of subcariers
%               Lp, filter length
%               r,  roll-off factor

%% Pulse evaluation
k           = ( -(Lp-1)/2:(Lp-1)/2 );
p           = ( 4*r/M*k.*cos( pi*(1+r)/M*k ) + sin( pi*(1-r)/M*k ) ) ...
            ./ ( ( 1 - (4*r/M*k).^2 ) .* pi/M .*k );
p(k==0)     = (pi+r*(4-pi)) / pi;
p(k==+M/2) = 2*M * ( cos(pi*r/2)-2*r*sin(pi*r/2) ) / ( pi*M*(1-4*r^2) );
p(k==-M/2) = 2*M * ( cos(pi*r/2)-2*r*sin(pi*r/2) ) / ( pi*M*(1-4*r^2) );

%% Energy Normalization
p = p / norm( p );
end
```

Script H.11 Matlab script for generating a Mirabbasi-Martin prototype filter

```
function p = proto_martin( M, K, Lp )
%% Description: generates the Mirabbasi-Martin prototype filter
%       Output: p, prototype filter
%        Input: M, number of subcariers
%               K, overlapping factor
%              Lp, filter length

%% Weights
switch K
    case 3
        k = [1 -.91143783 +.41143783];
    case 4
        k = [1 -.97195983 .70710681 -.23514695];
    case 5
        k = [1 -.99184131 +.86541624 -.50105361 +.12747868];
    case 6
        k = [1 -.99722723 +.94136732 -.70710681 +.3373834 -.07441672];
    case 8
        k = [1 -.99988389 +.99315513 -.92708081 ...
               +.70710681 -.37486154 +.11680273 -.01523841];
end

%% Puse Evaluation
p = ones(1,Lp);
n = (0:Lp-1) - (Lp-1)/2;
for ii = 2:K
    p = p + 2 * abs(k(ii)) * cos( 2*pi*n/(K*M) * (ii-1));
end

%% Energy Normalization
p = p / norm( p );
end
```

Script H.12 Matlab script for generating a DPSS prototype filter

```
function p = proto_prolate( Lp, fc, n )
%% Description: generates the DPSS prototype filter
%        Output: p,  prototype filter
%         Input: Lp, filter length
%                fc, cut-off frequency        [0,1]
%                n, p is the n-th DPSS        [1,Lp]

%% Slepian Matrix
wc = 2*pi*fc/1;
P  = zeros(Lp,Lp);
for k = 1:Lp
    for l = 1:Lp
        P(k,l) = sinc( ((k-1)-(l-1))*wc/pi ) * wc/pi;
    end
end

%% Slepian Series
[p,~] = eig( P );
p = fliplr(p);

%% Energy Normalization
p = p(:,n).';
if sum(p)<0
   p = -p;
end

%% Energy Normalization
p = p/norm(p);
end
```

Script H.13 Matlab script for generating a OFDP prototype filter

```
function p = proto_ofdp( M, K, Lp )
%% Description: generates the OFDP prototype filter
%        Output: p, prototype filter
%         Input: M, number of subcariers
%                K, overlapping factor
%               Lp, filter length

%% Weights
switch K
    case 2
        a = [.9785 .2055 -.0113 .0147 -.0007 -.0033 -.0012];
    case 3
        a = [.9395 .3282  .0927 .0308 -.0015 -.0024 .0039 .0002 -.0034];
    case 4
        a = [.9126 .3841 .1329 .0426 .0144 .0005 -.0052 -.0019 .0013 .0010];
end

%% Slepian Series
f = dpss( Lp, Lp/M, 2*length(a) ).';

%% Pulse evaluation
p = zeros( 1, Lp );
for ii = 1:length(a)
    phi = f(2*(ii-1)+1,:) * (-1)^(ii-1);
    phi = phi / sqrt(phi*phi');
    p = p +  a(ii)*phi;

end

%% Energy Normalization
p = p / norm( p );
end
```

Script H.14 Matlab script for generating a Gaussian prototype filter

```
function p = proto_exp( M, Lp, alpha )
%% Description: generates the EGF prototype filter with a spreading factor alpha
%        Output: p,      prototype filter
%         Input: M,      number of subcariers
%                K,      overlapping factor
%                Lp,     filter length
%                alpha,  spreading factor

%% Sampling period
Ts = sqrt(2) / (M/2);

%% Time
t = (-(Lp-1)/2:(Lp-1)/2) * Ts;

%% Pulse eval
p = ( 2*alpha )^.25 * exp( -pi * alpha * t.^2 );

%% Energy Normalization
p = p / norm( p );
end
```

Script H.15 Matlab script for generating a EGF prototype filter

```
function z = proto_egf(M,Lp,alpha,v0,t0)
%% Description: generates the EGF prototype filter with a spreading factor alpha
%       Output: p,      prototype filter
%        Input: M,      number of subcariers
%               K,      overlapping factor
%               Lp,     filter length
%               alpha,  spreading factor
%               v0,     FBMC frequency separation
%               t0,     FBMC time separation
%                       notice that t0*v0=1/2

%% Sampling interval
Ts = t0 / (M/2);
t  = ( -(Lp-1)/2:(Lp-1)/2 ) * Ts;

%% Pulse evaluation
y = zeros(1,Lp);
for l = 0:14
    y = y + dh(l,1/alpha,t0) * cos( 2*pi*l*t/t0 );
end
z = zeros(1,Lp);
for k = 0:14
    z = z + 1/2 * dh(k,alpha,v0) *( g(alpha,t+k/v0) + g(alpha,t-k/v0)  ) ;
end
z = z .* y;

%% Normalization
z = z / norm(z);
end

function ga = g(alpha,t)
    ga = (2*alpha)^.25 * exp( -pi*alpha*t.^2 );
end

function d = dh( k, alpha, v0 )

b = [               1              3/4            105/64           675/256        76233/16384       457107/65536    12097169/1048576  7054315/4194304;
                   -1            -15/8           -219/64         -6055/1024       -161925/16384   -2067909/1301072   -26060847/1048576                0;
                  3/4             19/16          1545/512          9765/2048        596277/65536     3679941/262144  394159701/16777216                0;
                 -5/8          -123/128         -2289/1024        -34871/8192      -969375/131072  -51182445/4194304                   0                0;
                35/64           213/256          7797/4096        56163/16384    13861065/2097152   87185895/8388608                   0                0;
             -63/128          -763/1024        -13875/8192     -790815/262144  -23600537/4194304                   0                   0                0;
             231/512          1395/2048       202281/131072    1434705/524288  85037895/16777216                   0                   0                0;
          -429/1024        -20691/32768     -374325/262144   -5297445/2097152                   0                   0                   0                0;
          6435/16384         38753/65536    1400487/1048576     989593/4194304                   0                   0                   0                0;
       -12155/32768      -146289/262144    -2641197/2097152                   0                   0                   0                   0                0;
       46189/131072       277797/524288   20050485/16777216                   0                   0                   0                   0                0;
      -88179/262144    -2120495/4194304                   0                   0                   0                   0                   0                0;
     676039/2097152     4063017/8388608                   0                   0                   0                   0                   0                0;
   -1300075/4194304                   0                   0                   0                   0                   0                   0                0;
   5014575/16777216                   0                   0                   0                   0                   0                   0                0 ...
            ];

K  = 14;
jk = floor( (K-k)/2 );
d  = 0;
for j = 0:jk
    d = d + b(k+1,j+1) * exp( -pi*alpha/(2*v0^2) * (2*j+k) );
end
end
```

Script H.16 Matlab script for generating a window based prototype filter

```
function p = proto_sinc( Lp, fc, w )
%% Description: generates a window based prototype filter
%        Output: p,  prototype filter
%         Input: Lp, number of subcariers
%                w,  window

%% Sinc Filter
k = (0:Lp-1) - (Lp-1)/2;
h = sinc( 2 * fc * k );

%% Prototype Filter
p = w .* h;

%% Energy Normalization
p = p / norm( p );
end
```

Script H.17 Matlab script for generating a Hermite prototype filter

```
function h = proto_hermite(M,K,Lp)
%% Description: generates the Hermite prototype filter
%        Output: p, prototype filter
%         Input: M, number of subcariers
%                K, overlapping factor
%               Lp, filter length

%% Sampling time
t0 = 1/sqrt(2);
Ts = t0 / (M/2);
t = ((0:Lp-1) - (Lp-1)/2) * Ts;

%% Pulse Evaluation
h = +1.0000000e-0  *       exp(-pi*t.^2) ...
    -1.9324881e-3  *    16*exp(-pi*t.^2).* ( 4*pi^2*t.^4 -6*pi*t.^2 +3/4 ) ...
    -7.3110588e-6  *   256*exp(-pi*t.^2).* ( 16*pi^4*t.^8 -112*pi^3*t.^6 ...
        +210*pi^2*t.^4 -105*pi*t.^2 +105/16 ) ...
    -3.1542096e-9  *  4096*exp(-pi*t.^2).* ( 64*pi^6*t.^12 -1056*pi^5*t.^10 ...
        +5940*pi^4*t.^8 -13860*pi^3*t.^6 +51975/4*pi^2*t.^4 -31185/8*pi*t.^2 +10395/64 )...
    +9.6634138e-13 * 65536*exp(-pi*t.^2).* ( 256*pi^8*t.^16 -7680*pi^7*t.^14 ...
        +87360*pi^6*t.^12 -480480*pi^5*t.^10 +1351350*pi^4*t.^8 -1891890*pi^3*t.^6 ...
        +1182431.25*pi^2*t.^4 -253378.125*pi*t.^2 +2027025/256 );

%% Pulse Normalization
h = h/norm(h);
end
```

H.3 Prototype Filter Merit Figures Scripts

Script H.18 Matlab script example for evaluating the performance of a Mirabbasi-Martin prototype filter

```
function merit_example
%% Description: SIR evaluation of a Martin prototype filter

%% Prototype filter
M  = 64;
K  = 4;
Lp = K*M + 1;
p = proto_martin( M, K, Lp );

%% Figures of merit
SIR          = mc_fbmc_merit_sir( p, M )
MSA          = mc_fbmc_merit_msa( p )
EO           = mc_fbmc_merit_oob( p, 1/M )
[xi,Dk,Dnu] = mc_fbmc_merit_heisen( p )
end
```

Script H.19 Matlab script example for evaluating the SIR of a prototype filter

```
function SIR_db = fbmc_merit_sir( p, M )
%% Description: returns the SIR of a prototype filter p
%       Output: SIR_db, prototype filter SIR
%        Input: p,      prototype filter
%               M,      number of subcarriers

%% Evaluation of the interference elements
e = mat_interf_elements( p, M );

%% SIR evaluation
SIR_db = 10*log10( 1 / ( sum(e(:).^2)-1 ) );
end
```

Script H.20 Matlab script example for evaluating the MSL of a prototype filter

```
function MSA_db = fbmc_merit_msa( p )
%% Description: returns the MSA of a prototype filter p
%        Output: SIR_db, prototype filter SIR
%         Input: p,      prototype filter
%                M,      number of subcarriers

%% PSD evaluation
NFFT  = 4096;
Pf    = abs( fftshift( fft( p, NFFT ) ) ).^2;
Pf    = Pf / max(Pf);
Pf_db = 10*log10(Pf);

%% MSA eval
Ph  = Pf_db( length(Pf_db)/2:end);
pk = findpeaks(Ph);
pk = pk(pk<-5);
if isempty(pk)
    pk = -inf;
end
MSA_db = -pk(1);
end
```

Script H.21 Matlab script example for evaluating the OoB energy of a prototype filter

```
function Ewc0_db = fbmc_merit_oob( p, fc )
%% Description: returns the OOB energy of a prototype filter p
%        Output: Ewc0_db, OOB energy
%         Input: p,       prototype filter
%                M,       number of subcarriers
%                fc,      cutoff frequency

%% Filter length
Lp = length( p );

%% Slepian matrix
G = mat_gamma( Lp, fc );

%% OOB energy evaluation
Ewc0_db = 10*log10( p(:)' * ( eye(Lp) - G ) * p(:) );
end
```

Script H.22 Matlab script example for evaluating the Heisenberg factor of a prototype filter

```
function [xi,Dk,Df] = fbmc_merit_heisen( p )
%% Description: returns the Heisenberg factor and time/frequency spreads of a pulse p
%       Output: xi, prototype filter Heisenberg factor
%               Dk, time spread
%               Df, frequency spread
%        Input: p,  prototype filter

%% Prototype filter length
Lp = length(p);

%% Energy normalization
p  = p /norm(p);

%% Time index
NFFT = Lp*16+1;
k  = (0:Lp-1) - (Lp-1)/2;

%% Frequency
f = ( (0:NFFT-1)-(NFFT-1)/2 )/(NFFT-1);

%% PSD calc
Pf = zeros(1,NFFT);
for ii = 1:length(p)
    n  = k(ii);
    Pf = Pf + p(ii) * exp( -1i*2*pi*f*n );
end
Pf = real(Pf);

%% Momentuns
mk = sum(  k.*abs(p).^2  );
mf = trapz( f, f.*abs(Pf).^2 );
Dk = sqrt( sum(  (k-mk).^2.*abs(p).^2 ) );
Df = sqrt( trapz( f, (f-mf).^2.*abs(Pf).^2 ) );

%% Heisenberg factor
xi = 1 / (4*pi*Dk*Df);
end
```

H.4 Channel Estimation for FBMC Systems

Script H.23 Matlab script for generating different preambles for channel estimation for FBMC systems

```
function ap = fbmc_ce_pilot_generation( M, ce_method, Nq )
%% Description: IAM-R/I/C channel estimation
%        Output:        ap, pilots
%         Input:         M, number of pilots
%                ce_method, channel estimation method
%                       Nq, QAM modulation order, Np=sqrt(Nq)

switch ce_method
    case 'pop'
        ap = zeros(M,2);
        ap(:,1) = (-1).^mod(1:M,2);
        ap = sqrt(2) * ap;
    case 'iam1'
        ap = pammod( randi([0 sqrt(Nq)-1], [M 3]), sqrt(Nq), 0, 'gray' ) ;
        ap = 1 / sqrt( 1/3*(sqrt(Nq)^2-1) )  * ap;
    case 'iam2'
        ap = zeros(M,3);
        ap(:,2) = (-1).^mod(1:M,2);
        ap = sqrt(3) * ap;
    case 'iamr'
        ap = zeros(M,3);
        AH = hadamard(M);
        ap(:,2) = AH(:,4);
        ap = sqrt(3) * ap;
    case 'iami'
        ap = zeros(M,3);
        p1 = pammod( randi([0 sqrt(Nq)-1], [1 ceil(M/3)]), sqrt(Nq), 0, 'gray' );
        p2 = repmat( p1, [3 1] ) * ( sqrt(Nq)-1 );
        ap(:,2) = p2(1:M).' .* 1i.^mod(0:M-1,3).';
        ap = sqrt(3) * ap / sqrt( 1/3*(sqrt(Nq)^2-1) );
    case 'iamc'
        ap = zeros(M,3);
        AH = hadamard(M);
        ap(:,2) = AH(:,4) .* 1i.^mod(0:M-1,2).';
        ap = sqrt(3) * ap;
end
end
```

Script H.24 Matlab script for POP channel estimation

```
function H = fbmc_ce_pop( x, ap, Phi, p )
%% Description: IAM channel estimation
%       Output: e,      interference elements of p
%        Input: x,      received signal
%               ap,     transmitted pilot sequence
%               p,      prototype filter

%% Sizes
Lp = length(p);
M = size(ap,1);
K = round( Lp/M );

%% Prototype filter normalization
p  = p/norm(p);

%% Pre-processing
[Da,Db] = fbmc_delay_eval( Lp, M, K );                    %% Delay net
Gz2     = fbmc_bank_poly( p, M );                         %% Polyphase filterbank
xd = circshift( x, [0 Db] );                              %% Receiver delay
y  = fbmc_analysis_poly( xd, Gz2 );                       %% Analysis
yd = circshift( y, [0 -Da] );                             %% Output "delay" shift
yd = yd( :,1:size(ap,2) ).*conj(Phi(:,1:size(ap,2)));

%% Channel estimation
H = zeros( M, 1 );
for m = 0:M-1
    y1r = real(yd(m+1,1));
    y1i = imag(yd(m+1,1));
    y2r = real(yd(m+1,2));
    y2i = imag(yd(m+1,2));
    a1  = real(ap(m+1,1));
    a2  = imag(ap(m+1,2));
    C = ( a2*y1r - a1*y2r ) / ( a1*y2i - a2*y1i );
    H(m+1) = ( y1r + C*y1i ) / ( a1 *( 1 + C^2 ));
    H(m+1) = H(m+1) + 1i*C*H(m+1);
end

end
```

Script H.25 Matlab script for IAM-1 channel estimation

```
function H = fbmc_ce_iam1( x, ap, Phi,p )
%% Description: IAM1 channel estimation
%        Output: e,      interference elements of p
%         Input: x,      received signal
%                ap,     transmitted pilot sequence
%                p,      prototype filter

%% Sizes
Lp = length(p);
M = size(ap,1);
K = round( Lp/M );

%% Prototype filter normalization
p  = p/norm(p);
k  = (0:Lp-1) - (Lp-1)/2;

%% Complex Interference elements
e  = zeros( M, round(Lp/(M)) );
for m = 0:M-1
    for n = 0:round(Lp/(M/2)+1)
            p1 = [p zeros(1,Lp)].';
            p2 = circshift([ p .* exp(1i*2*pi/M*m*k)...
                             * exp(1*1i*pi*(m+n)/2) zeros(1,Lp)], [0 M/2*n] ).';
            e(m+1,n+1) = ( p2' * p1 );
    end
end
e = [ e 1*fliplr(e(:,2:end)) ];
e(1,1)=0;

%% Pilot zero-pad, if needed
% ap  = ap .*conj(Phi(:,1:size(ap,2)));
if size(ap,2)<size(e,2)
    ap1 = [ap zeros(M,size(e,2)-size(ap,2))];
else
    ap1 = ap;
end

%% Imaginary pilot interference
[Da,Db] = fbmc_delay_eval( Lp, M, K );                  %% Delay net
Gz2     = fbmc_bank_poly( p, M );                       %% Polyphase filterbank
b       = ap.* Phi(:,1:size(ap,2));                     %% PAM phase-shift
s       = fbmc_synthesis_poly( b, Gz2 );                %% Synthesis filter
sd      = circshift( s, [0 Db] );                       %% Receiver delay
yd0     = fbmc_analysis_poly( sd, Gz2 );                %% Analysis
yd0     = circshift( yd0, [0 -Da] );                    %% Output "delay" shift
yd0     = yd0( :,1:size(ap,2) ).*conj(Phi(:,1:size(ap,2)));
ai      = imag((yd0));

%% Pre-processing
xd = circshift( x, [0 Db] );                            %% Receiver delay
y  = fbmc_analysis_poly( xd, Gz2 );                     %% Analysis
yd = circshift( y, [0 -Da] );                           %% Output "delay" shift
yd = yd( :,1:size(ap,2) ).*conj(Phi(:,1:size(ap,2)));

%% Channel estimation
H = yd(:,2) ./ yd0(:,2);
% H(:,3) = mean(H,2);

end
```

Script H.26 Matlab script for IAM-2 channel estimation

```
function H = fbmc_ce_iam2( x, ap, Phi,p )
%% Description: IAM2 channel estimation
%       Output: e,      interference elements of p
%        Input: x,      received signal
%               ap,     transmitted pilot sequence
%               p,      prototype filter

%% Sizes
Lp = length(p);
M = size(ap,1);
K = round( Lp/M );

%% Prototype filter normalization
p  = p/norm(p);

%% Pre-processing
[Da,Db] = fbmc_delay_eval( Lp, M, K );                  %% Delay net
Gz2     = fbmc_bank_poly( p, M );                       %% Polyphase filterbank
xd = circshift( x, [0 Db] );                            %% Receiver delay
y  = fbmc_analysis_poly( xd, Gz2 );                     %% Analysis
yd = circshift( y, [0 -Da] );                           %% Output "delay" shift
yd = yd( :,1:size(ap,2) ).*conj(Phi(:,1:size(ap,2)));

%% Channel estimation
H = yd(:,2) ./ ap(:,2);
end
```

Script H.27 Matlab script for IAM-R/I/C channel estimation

```
function He = fbmc_ce_iamr( x, ap, Phi, p )
%% Description: IAM-R/I/C channel estimation
%        Output: He,      Channel estimate
%         Input:  x,      received signal
%                ap,      transmitted pilot sequence
%                 p,      prototype filter

%% Sizes
Lp = length(p);
M = size(ap,1);
K = round( Lp/M );

%% Prototype filter normalization
p = p/norm(p);

%% Imaginary pilot interference
[Da,Db] = fbmc_delay_eval( Lp, M, K );                    %% Delay net
Gz2     = fbmc_bank_poly( p, M );                         %% Polyphase filterbank
b       = ap.* Phi(:,1:size(ap,2));                       %% PAM phase-shift
s       = fbmc_synthesis_poly( b, Gz2 );                  %% Synthesis filter
sd      = circshift( s, [0 Db] );                         %% Receiver delay
yd0     = fbmc_analysis_poly( sd, Gz2 );                  %% Analysis
yd0     = circshift( yd0, [0 -Da] );                      %% Output "delay" shift
yd0     = yd0(:,1:size(ap,2)).*conj(Phi(:,1:size(ap,2)));
ai      = imag(yd0);

%% Pre-processing
xd = circshift( x, [0 Db] );                              %% Receiver delay
y  = fbmc_analysis_poly( xd, Gz2 );                       %% Analysis
yd = circshift( y, [0 -Da] );                             %% Output "delay" shift
yd = yd(:,1:size(ap,2)).*conj(Phi(:,1:size(ap,2)));

%% Channel estimation
% He = yd(:,2) ./ (ap(:,2)+1i*ai(:,2));
He = yd(:,2) ./ (yd0(:,2));


end
```

H.5 Error Probability for Single-Carrier Systems

H.5.1 AWGN

Script H.28 Matlab script for evaluating the approximated BER of a single-carrier N_p-PAM transmission over an AWGN channel

```
function Pe = pe_pam_awgn_approximation(ebn0,Np)
%% Description: Approx. BER for PAM transmission over AWGN channel
%       Output: Pe,   bit error probability
%        Input: ebn0, normalized SNR
%              Np,    modulation order

%% Number of bits
Nb = log2(Np);

%% Average Energy
Es = (Np^2-1) / 3;

%% Error probability evaluation
xx = Nb/Es * ebn0;
Pe = 2*(Np-1)/Np/Nb * qfunc( sqrt(2*xx) );
end
```

Script H.29 Matlab script for evaluating the exact BER of a single-carrier N_p-PAM transmission over an AWGN channel

```
function Pe = pe_pam_awgn_exact(ebn0,Np)
%% Description: Exact BER for PAM transmission over rayleigh channel
%       Output: Pe,   bit error probability
%        Input: ebn0, normalized SNR
%              Np,    modulation order

%% Number of bits
Nb = log2(Np);

%% Average Energy
Es = (Np^2-1) / 3;

%% w function
w = @(i,k,Np) (-1)^floor(i*2^(k-1)/Np) * ...
              ( 2^(k-1) - floor(i*2^(k-1)/Np+1/2) );

%% Error probability evaluation
Pe = zeros(size(ebn0));
    for k = 1:Nb
        Pk = zeros(size(ebn0));
        for i = 0:(1-2^-k)*Np-1
            xx = (2*i+1)^2 * Nb/Es * ebn0;
            Pk = Pk + w(i,k,Np) * 2*qfunc( sqrt(2*xx) );
        end
        Pe = Pe + 1/Np/Nb*Pk;
    end
end
```

H.5.2 Rayleigh

Script H.30 Matlab script for evaluating the approximated BER of a single-carrier N_p-PAM transmission over an Rayleigh channel

```
function Pe = pe_pam_ray_approximation(ebn0,Np)
%% Description: Approx. BER for PAM transmission over Rayleigh channel
%       Output: Pe,   bit error probability
%        Input: ebn0, normalized SNR
%               Np,    modulation order

%% Number of bits
Nb = log2(Np);

%% Average Energy
Es = (Np^2-1) / 3;

%% Error probability evaluation
xx = Nb/Es * ebn0;
Pe = 2*(Np-1)/Np/Nb * 1/2 * ( 1-sqrt(xx)./sqrt(xx+1) );
end
```

Script H.31 Matlab script for evaluating the exact BER of a single-carrier N_p-PAM transmission over an Rayleigh channel

```
function Pe = pe_pam_ray_exact(ebn0,Np)
%% Description: Exact BER for PAM transmission over rayleigh channel
%       Output: Pe,   bit error probability
%        Input: ebn0, normalized SNR
%               Np,    modulation order

%% Number of bits
Nb = log2(Np);

%% Average Energy
Es = (Np^2-1) / 3;

%% w function
w = @(i,k,Np) (-1)^floor(i*2^(k-1)/Np) * ...
              ( 2^(k-1) - floor(i*2^(k-1)/Np+1/2) );

%% Error probability evaluation
Pe = zeros(size(ebn0));
for k = 1:Nb
    Pk = zeros(size(ebn0));
    for i = 0:(1-2^-k)*Np-1
        xx = (2*i+1)^2 * Nb/Es * ebn0;
        Pk = Pk + 1/Np * w(i,k,Np) * ( 1-sqrt(xx)./sqrt(xx+1) );
    end
    Pe = Pe + 1/Nb*Pk;
end
end
```

H.6 Error Probability for FBMC Systems

H.6.1 AWGN

Script H.32 Matlab script for evaluating the approximated BER of an FBMC N_p-PAM transmission over an AWGN channel

```
function Pe = pe_fbmc_awgn_approximation( ebn0, Np, mu )
%% Description: Approx. BER for PAM transmission over AWGN channel
%        Output: Pe,   bit error probability
%         Input: ebn0, normalized SNR
%                Np,    modulation order

%% Number of bits
Nb = log2(Np);

%% Average Energy
Es = (Np^2-1) / 3;

%% Error probability evaluation
Pe = zeros(size(ebn0));
for l = 1:length(mu)
    a = Nb/Es * ebn0;
    c = 1 - mu(l);
    Pe = Pe + 2*(Np-1)/Np/Nb * qfunc( real(c) * sqrt( 2*a )  )  ;
end
Pe = Pe / length(mu);
end
```

Script H.33 Matlab script for evaluating the exact BER of an FBMC N_p-PAM transmission over an AWGN channel

```
function Pe = pe_fbmc_awgn_exact( ebn0, Np, mu )
%% Description: Exact BER for FBMC PAM transmission over AWGN channel
%       Output: Pe,   bit error probability
%        Input: ebn0, normalized SNR
%               Np,   modulation order
%               mu,   symbol+interference elements combinations

%% Number of bits
Nb = log2(Np);

%% Average Energy
Es = (Np^2-1) / 3;

%% W function
w = @(i,k,Np) (-1)^floor(i*2^(k-1)/Np) *...
              ( 2^(k-1) - floor(i*2^(k-1)/Np+1/2) );

%% Error Probability
ebn0 = ebn0(:).';
Pe = zeros(log2(Np),length(ebn0));
for k = 1:log2(Np)
    for i = 0:(1-2^-k)*Np-1
        for l = 1:length(mu)
            a = Nb/Es * ebn0;
            c = (2*i+1) - mu(l);
            Pe(k,:) = Pe(k,:) + w(i,k,Np) * 2*qfunc( c * sqrt( 2*a )  ) ;
        end
    end
end
Pe = sum( Pe, 1 ) / ( Np * log2(Np) * length(mu) );
Pe = real(Pe);
end
```

H.6.2 Rayleigh

Script H.34 Matlab script for evaluating the approximated BER of an FBMC N_p-PAM transmission over an Rayleigh channel

```
function Pe = pe_fbmc_ray_approximation( ebn0, Np, mu )
%% Description: Approx. BER for PAM transmission over Rayleigh channel
%       Output: Pe,   bit error probability
%        Input: ebn0, normalized SNR
%               Np,    modulation order

%% Number of bits
Nb = log2(Np);

%% Average Energy
Es = (Np^2-1) / 3;

%% Error probability evaluation
Pe = zeros(size(ebn0));
for l = 1:length(mu)
    a = Nb/Es * ebn0;
    c = 1 - mu(l);
    Pe = Pe + 2*(Np-1)/Np/Nb * 1/2 * ( 1 - sqrt(a).* real(c) ./ sqrt(a.*c.^2+1) ) ;
end
Pe = Pe / length(mu);
end
```

Script H.35 Matlab script for evaluating the exact BER of an FBMC N_p-PAM transmission over an Rayleigh channel

```
function Pe = pe_fbmc_ray_exact( ebn0, Np, mu )
%% Description: Exact BER for FBMC PAM transmission over Rayleigh channel
%       Output: Pe,   bit error probability
%        Input: ebn0, normalized SNR
%               Np,   modulation order
%               mu,   symbol+interference elements combinations

%% Number of bits
Nb = log2(Np);

%% Average Energy
Es = (Np^2-1) / 3;

%% W function
w = @(i,k,Np) (-1)^floor(i*2^(k-1)/Np) *...
              ( 2^(k-1) - floor(i*2^(k-1)/Np+1/2) );

%% Error Probability
ebn0 = ebn0(:).';
Pe = zeros(log2(Np),length(ebn0));
parfor k = 1:log2(Np)
    for i = 0:(1-2^-k)*Np-1
        for l = 1:length(mu)
            a = Nb/Es * ebn0;
            c = (2*i+1) - mu(l);
            Pe(k,:) = Pe(k,:) + w(i,k,Np) * ( 1 - sqrt(a).*c ./ sqrt(a.*c.^2+1) ) ;
        end
    end
end
Pe = sum( Pe, 1 ) / ( Np * log2(Np) * length(mu) );
Pe = real(Pe);
end
```

H.6.3 Interference Elements

Script H.36 Matlab script for evaluating the interference elements of a given prototype filter

```
function E = calc_ee( p, M )
%% Description: Returns the interference elements of p
%       Output: e,      interference elements of p
%        Input: p,      prototype filter
%               M,      number of subcarriers

%% Filter Normalization
p  = p/norm(p);

%% Filter length and overlaping factor
Lp = length(p);
K  = round(Lp/M);

%% Discrete time indexes
k  = (0:Lp-1) - (Lp-1)/2;

%% Interference matrix eval.
E = zeros(M,4*K-1);
for m = 0:M-1
    for n = -2*K+1:1:2*K-1
        p1 = [p zeros(1,Lp)].';
        p2 = circshift([p.*exp(1i*2*pi/M*m*k)*exp(1i*pi*(m+n)/2) zeros(1,Lp)], [0 ...
            -M/2*n-0]).';
        E(m+1,n+2*K) = real(p2' * p1);
    end
end
end
```

Script H.37 Matlab script for evaluating all the combinations between the interference elements and PAM symbols

```
function mu = calc_mu( ac, E )
%% Description: Exact BER for FBMC PAM transmission over Rayleigh channel
%       Output: mu,   symbol+interference combinations
%        Input: ac,   Modulation Alphabet
%               E,    FBMC interference elements
%               mu,   symbol+interference elements combinations
E  = E(:)';

%% Number of interference elements
Ni = length(E);

%% Modulation order
Np = length(ac);

%% Combinations between symbols and interference elements
a  = permn(ac, Ni) .* repmat(E,[Np^Ni 1]);
mu = sum(a,2).';
end
```

H.7 MIMO Detection

H.7.1 ML

Script H.38 Matlab script for the ML detector

```
function sh = mimo_fbmc_sd( H, x, Np, r )
%% Description: SD detector for MIMO-FBMC V-BAST
%        Output: sh, estimated signal
%         Input:  H, channel matrix
%                 x, received signal vector
%                Np, modulation order (PAM symbols)
%                 r, sphere squared radius

%% Number of Tx antennas
Nt = size(H,2);

%% Symbol alphabet
c = pammod( 0:(Np-1), Np );

%% Extended real system
H = [real(H) imag(H);-imag(H) real(H)];
x = [imag(x);real(x)];

%% Segregate imaginary interference
[Q,R] = qr(H,0);
y     = Q'*x;
R     = R(end+1-Nt:end,end+1-Nt:end);
y     = y(end+1-Nt:end);

%% SD detection
sh = zeros(Nt,1);
sdc( sh, 0, Nt )

%% Nested SD core function
function sdc( s, e0, l )
%% Description: Recursive SD core function
%         Input:  s, current symbol vector
%                e0, previous squared error
%                 l, current detection layer
for ii = 1:length(c)                              %% SD tree sharch (symbol alphabet)
    s(l) = c(ii);                                 %% Current symbol candidate for the lth layer
    e = e0 + abs( y(l) - R(l,:)*s ).^2;           %% Error evaluation/update
    if( e < r )                                   %% Is the candidate inside the sphere?
        if(l~=1)                                  %% Last detection layer?
            sdc(s,e,l-1);                         %% Run SD for the next layer
        elsh
            r  = e;                               %% Sphere radius update
            sh = s;                               %% New vector solution
        end
    end
end
end
end
```

H.7.2 SD

Script H.39 Matlab script for the SD detector

```
function sh = mimo_fbmc_sd( H, x, Np, r )
%% Description: SD detector for MIMO-FBMC V-BAST
%       Output: sh, estimated signal
%        Input:  H, channel matrix
%                x, received signal vector
%               Np, modulation order (PAM symbols)
%                r, sphere squared radius

%% Number of Tx antennas
Nt = size(H,2);

%% Symbol alphabet
c = pammod( 0:(Np-1), Np );

%% Extended real system
H = [real(H) imag(H);-imag(H) real(H)];
x = [imag(x);real(x)];

%% Segregate imaginary interference
[Q,R] = qr(H,0);
y     = Q'*x;
R     = R(end+1-Nt:end,end+1-Nt:end);
y     = y(end+1-Nt:end);

%% SD detection
sh = zeros(Nt,1);
sdc( sh, 0, Nt )

%% Nested SD core function
function sdc( s, e0, l )
%% Description: Recursive SD core function
%        Input:  s, current symbol vector
%               e0, previous squared error
%                l, current detection layer
for ii = 1:length(c)                              %% SD tree sharch (symbol alphabet)
    s(l) = c(ii);                                 %% Current symbol candidate for the lth layer
    e = e0 + abs( y(l) - R(l,:)*s ).^2;           %% Error evaluation/update
    if( e < r )                                   %% Is the candidate inside the sphere?
        if(l~=1)                                  %% Last detection layer?
            sdc(s,e,l-1);                         %% Run SD for the next layer
        elsh
            r  = e;                               %% Sphere radius update
            sh = s;                               %% New vector solution
        end
    end
end
end
end
```

H.7.3 ZF

Script H.40 Matlab script for the ZF detector

```
function sh = mimo_fbmc_zf( H, x, Np )
%% Description: ZF detector for MIMO-FBMC V-BAST
%       Output: sh, estimated signal
%        Input:  H, channel matrix
%                x, received signal vector
%               Np, modulation order (PAM symbols)

%% ZF detection
sh = inv( H' * H ) * H' * x;

%% PAM slicing
sh = pamdemod( sh, Np, 0, 'gray' );
sh = pammod(   sh, Np, 0, 'gray' );
end
```

Script H.41 Matlab script for the ZF-SIC detector

```
function sh = mimo_fbmc_zf_sic( H, x, Np )
%% Description: ZF-SIC detector for MIMO-FBMC V-BAST
%       Output: sh, estimated signal
%        Input:  H, channel matrix
%                x, received signal vector
%               Np, modulation order (PAM symbols)

%% Number of Tx antennas
Nt = size(H,2);

%% Extended real system
H = [real(H) imag(H);-imag(H) real(H)];
x = [imag(x);real(x)];

%% Segregate imaginary interference
[Q,R] = qr(H,0);
y     = Q'*x;
R     = R(end+1-Nt:end,end+1-Nt:end);
y     = y(end+1-Nt:end);

%% SIC detection
sh = sic( R, y, Np );
end
```

Script H.42 Matlab script for the ZF-OSIC detector

```
function sh = mimo_fbmc_zf_osic( H, x, Np )
%% Description: ZF-OSIC detector for MIMO-FBMC V-BAST
%       Output: sh, estimated signal
%        Input:  H, channel matrix
%                x, received signal vector
%               Np, modulation order (PAM symbols)

%% Number of Tx antennas
Nt = size(H,2);

%% Extended real system
H = [real(H) imag(H);-imag(H) real(H)];
x = [imag(x);real(x)];

%% Segregate imaginary interference
[Q,R,P] = sqrd(H);
y       = Q'*x;
R       = R(end+1-Nt:end,end+1-Nt:end);
P       = P(end+1-Nt:end,end+1-Nt:end);
y       = y(end+1-Nt:end);

%% SIC detection
sh = sic( R, y, Np );

%% Re-ordering
sh = P * sh;
end
```

Script H.43 Matlab script for the ZF-LR-SIC detector

```
function sh = mimo_fbmc_zf_lr_sic( H, x )
%% Description: ZF-LR-SIC detector for MIMO-FBMC V-BAST
%       Output: sh, estimated signal
%        Input:  H, channel matrix
%                x, received signal vector

%% Number of antennas
Nt = size( H,2 );

%% Extended real system
H = [real(H) imag(H);-imag(H) real(H)];
x = [imag(x);real(x)];

%% Segregate imaginary interference
[Q,R] = qr(H,0);
y     = Q'*x;
R     = R(end+1-Nt:end,end+1-Nt:end);
y     = y(end+1-Nt:end);

%% Lattice reduction
[Qr,Rr,T] = clll(eye(Nt),R);

%% SIC detection
y  = Qr' * y;
zh = sic_lr( Rr, T, y );

%% LR domain conversion
sh = T * zh;
end
```

Script H.44 Matlab script for the ZF-LR-OSIC detector

```
function sh = mimo_fbmc_zf_lr_osic( H, x )
%% Description: ZF-LR-OSIC detector for MIMO V-BAST
%        Output: sh, estimated signal
%         Input:  H, channel matrix
%                 x, received signal vector

%% Number of antennas
Nt = size( H,2 );

%% Extended real system
H = [real(H) imag(H);-imag(H) real(H)];
x = [imag(x);real(x)];

%% Segregate imaginary interference
[Q,R,P] = sqrd(H);
y       = Q'*x;
R       = R(end+1-Nt:end,end+1-Nt:end);
P       = P(end+1-Nt:end,end+1-Nt:end);
y       = y(end+1-Nt:end);

%% Lattice reduction
[Qr,Rr,T] = clll(eye(Nt),R);

%% SIC detection
y  = Qr' * y;
sh = sic_lr( Rr, T, y );

%% Re-ordering
sh = P * sh;
end
```

H.7.4 MMSE

Script H.45 Matlab script for the MMSE detector

```
function sh = mimo_fbmc_mmse( H, x, Np, EBN0_db )
%% Description: MMSE detector for MIMO-FBMC V-BAST
%       Output:      sh, estimated signal
%        Input:       H, channel matrix
%                     x, received signal vector
%                    Np, modulation order (PAM symbols)
%               EBN0_db, Eb/N0 in dB

%% Number of TX antennas
Nt = size(H,2);

%% Number of bits per symbol
Nb = log2(Np);

%% Average symbol energy
Es = 2/3 * (Np-1);

%% Noise energy
N0 = Es * Nt / Nb / 10^(EBN0_db/10);

%% MMSE detection
sh = inv( H' * H + N0/Es*eye(Nt) ) * H' * x;

%% PAM slicing
sh = pamdemod( sh, Np, 0, 'gray' );
sh = pammod(   sh, Np, 0, 'gray' );
end
```

Script H.46 Matlab script for the MMSE-SIC detector

```
function sh = mimo_fbmc_mmse_sic( H, x, Np, EBN0_db )
%% Description: MMSE-SIC detector for MIMO-FBMC V-BAST
%        Output:      sh, estimated signal
%         Input:       H, channel matrix
%                      x, received signal vector
%                     Np, modulation order (PAM symbols)
%                EBN0_db, Eb/N0 in dB

%% Number of TX antennas
Nt = size(H,2);

%% Number of bits per symbol
Nb = log2(Np);

%% Average symbol energy
Es = 2/3 * (Np-1);

%% Noise energy
N0 = Es * Nt / Nb / 10^(EBN0_db/10);

%% Number of Tx antennas
Nt = size(H,2);

%% Extended real system
H = [real(H) imag(H);-imag(H) real(H)];
x = [imag(x);real(x)];

%% Extended matrix
H = [H ; sqrt(N0/Es)*eye(2*Nt) ];
x = [x;zeros(2*Nt,1)];

%% Segregate imaginary interference
[Q,R] = qr(H,0);
y     = Q'*x;
R     = R(end+1-Nt:end,end+1-Nt:end);
y     = y(end+1-Nt:end);

%% SIC detection
sh = sic( R, y, Np );
end
```

Script H.47 Matlab script for the MMSE-OSIC detector

```
function sh = mimo_fbmc_mmse_osic( H, x, Np, EBN0_db )
%% Description: MMSE-OSIC detector for MIMO-FBMC V-BAST
%       Output:      sh, estimated signal
%        Input:       H, channel matrix
%                     x, received signal vector
%                    Np, modulation order (PAM symbols)
%               EBN0_db, Eb/N0 in dB

%% Number of TX antennas
Nt = size(H,2);

%% Number of bits per symbol
Nb = log2(Np);

%% Average symbol energy
Es = 2/3 * (Np-1);

%% Noise energy
N0 = Es * Nt / Nb / 10^(EBN0_db/10);

%% Number of Tx antennas
Nt = size(H,2);

%% Extended real system
H = [real(H) imag(H);-imag(H) real(H)];
x = [imag(x);real(x)];

%% Extended matrix
H = [H ; sqrt(N0/Es)*eye(2*Nt) ];
x = [x;zeros(2*Nt,1)];

%% Segregate imaginary interference
[Q,R,P] = sqrd(H);
y       = Q'*x;
R       = R(end+1-Nt:end,end+1-Nt:end);
P       = P(end+1-Nt:end,end+1-Nt:end);
y     = y(end+1-Nt:end);

%% SIC detection
sh = sic( R, y, Np );

%% Re-ordering
sh = P * sh;
end
```

Script H.48 Matlab script for the MMSE-LR-SIC detector

```
function sh = mimo_fbmc_mmse_lr_sic( H, x, Np, EBN0_db )
%% Description: MMSE-LR-SIC detector for MIMO-FBMC V-BAST
%        Output:      sh, estimated signal
%         Input:       H, channel matrix
%                      x, received signal vector
%                     Np, modulation order (PAM symbols)
%                 EBN0_db, Eb/N0 in dB

%% Number of TX antennas
Nt = size(H,2);

%% Number of bits per symbol
Nb = log2(Np);

%% Average symbol energy
Es = 2/3 * (Np-1);

%% Noise energy
N0 = Es * Nt / Nb / 10^(EBN0_db/10);

%% Extended real system
H = [real(H) imag(H);-imag(H) real(H)];
x = [imag(x);real(x)];

%% Extended matrix
H = [H ; sqrt(N0/Es)*eye(2*Nt) ];
x = [x;zeros(2*Nt,1)];

%% Segregate imaginary interference
[Q,R] = qr(H,0);
y     = Q'*x;
R     = R(end+1-Nt:end,end+1-Nt:end);
y     = y(end+1-Nt:end);

%% Lattice reduction
[Qr,Rr,T] = clll(eye(Nt),R);

%% SIC detection
y  = Qr' * y;
zh = sic_lr( Rr, T, y );

%% LR domain conversion
sh = T * zh;
end
```

Script H.49 Matlab script for the MMSE-LR-OSIC detector

```
function sh = mimo_fbmc_mmse_lr_osic( H, x, Np, EBN0_db )
%% Description: MMSE-LR-OSIC detector for MIMO-FBMC V-BAST
%       Output:      sh, estimated signal
%        Input:       H, channel matrix
%                     x, received signal vector
%                    Np, modulation order (PAM symbols)
%               EBN0_db, Eb/N0 in dB

%% Number of TX antennas
Nt = size(H,2);

%% Number of bits per symbol
Nb = log2(Np);

%% Average symbol energy
Es = 2/3 * (Np-1);

%% Noise energy
N0 = Es * Nt / Nb / 10^(EBN0_db/10);

%% Extended real system
H = [real(H) imag(H);-imag(H) real(H)];
x = [imag(x);real(x)];

%% Extended matrix
H = [H ; sqrt(N0/Es)*eye(2*Nt) ];
x = [x;zeros(2*Nt,1)];

%% Segregate imaginary interference
[Q,R,P] = sqrd(H);
y       = Q'*x;
R       = R(end+1-Nt:end,end+1-Nt:end);
P       = P(end+1-Nt:end,end+1-Nt:end);
y       = y(end+1-Nt:end);

%% Lattice reduction
[Qr,Rr,T] = clll(eye(Nt),R);

%% SIC detection
y  = Qr' * y;
zh = sic_lr( Rr, T, y );

%% LR domain conversion
sh = T * zh;

%% Re-ordering
sh = P * sh;
end
```

H.7.5 Auxiliary Functions

Script H.50 Matlab script for the sorted QR decomposition

```
function [Q,R,P] = sqrd(H)
%% Description: sorted QR decomposition for MIMO-FBMC systems
%  Input  H: input matrix
%  Output Q: orthogonal matrix
%         R: upper triangular matrix
%         P: permutation matrix for ordering

%% Number of Tx antennas
Nt = size(H,2);

%% Matrices init.
R = zeros(Nt);
P = eye(Nt);
Q = H;

%% Initial col. norm
E       = sum(abs(Q).^2);
E(1:Nt/2) = 0;

%% SQRD algorithm
for k = 1:Nt
    temp = E;
    temp = temp(k:Nt);
    %% Sorting: weakest channel(H col.) first
    [~,i] =  find( E(:,:)==min(temp) );
    %% Swapping columns
    Q(:,[i k]) = Q(:,[k i]);
    R(:,[i k]) = R(:,[k i]);
    P(:,[i k]) = P(:,[k i]);
    E(:,[i k]) = E(:,[k i]);
    %% Norm of the kth column
    %R(k,k) = sqrt(E(:,k));
    R(k,k) = sqrt(sum(abs(Q(:,k)).^2));
    %% Normalizing kth collumn of Q
    Q(:,k) = Q(:,k)/R(k,k);
    %% Gram-Schimidt process
    for j = k+1:Nt
        R(k,j) = Q(:,k)' * Q(:,j);
        % Removing qk projection from qj vector (orthogonalization process)
        Q(:,j) = Q(:,j) - R(k,j) * Q(:,k);
        E(:,j) = E(:,j) - abs(R(k,j))^2;
    end
end
end
```

Script H.51 Matlab script for the complex LLL algorithm

```
function [Q,R,T] = clll(Q,R)
%% Description: Complex LLL algorithm for lattice reduction
%        Output: Q, LR
%                R, modulation order
%                T, modulation order
%         Input: Q, orthonormal matrix of the channel matrix
%                R, triangular matrix of the channel matrix
Nt = size(Q,2);
d = 3/4;
T = eye(Nt);
k = 2;
while k <= Nt
    for n = k-1:-1:1
        u = round( R(n,k)/R(n,n) );
        if u~=0
            R(1:n,k) = R(1:n,k) - u * R(1:n,n);
            T(:,k)   = T(:,k) - u * T(:,n);
        end
    end
    if d*abs(R(k-1,k-1))^2 > ( abs(R(k,k))^2 + abs(R(k-1,k))^2 )
        R(:,[k k-1]) = R(:,[k-1 k]);
        T(:,[k k-1]) = T(:,[k-1 k]);
        a = R(k-1,k-1) / norm(R(k-1:k,k-1));
        b = R(k,k-1)   / norm(R(k-1:k,k-1));
        O = [a' b; -b a];
        R(k-1:k,k-1:Nt) = O * R(k-1:k,k-1:Nt);
        Q(:,k-1:k) = Q(:,k-1:k) * O';
        k = max(k-1,2);
    else
        k = k + 1;
    end
end
end
```

Script H.52 Matlab script for the SIC

```
function sh = sic( R, y, Np )
%% Description: SIC algorithm
%        Output: sh, estimated signal
%         Input:  R, triangular matrix channel matrix
%                 y, modified recieved signal vector
%                Np, modulation order

%% Number of TX antennas
Nt = size(R,2);

%% SIC
sh = zeros(Nt,1);
sh(Nt) = y(Nt) / R(Nt,Nt);
sh(Nt) = pamdemod( sh(Nt), Np, 0, 'gray' );
sh(Nt) = pammod(   sh(Nt), Np, 0, 'gray' );
for ii = Nt-1 : -1 : 1
    for jj = ii+1:Nt
       sh(ii) = sh(ii) + R(ii,jj) * sh(jj);
    end
    sh(ii) = ( y(ii) - sh(ii) ) / R(ii,ii);
    sh(ii) = pamdemod( sh(ii), Np, 0, 'gray' );
    sh(ii) = pammod(   sh(ii), Np, 0, 'gray' );
end
sh = real(sh);
end
```

Script H.53 Matlab script for the SIC in LR-based detectors

```
function zh = sic_lr( R, T, y )
%% Description: SIC algorithm
%        Output: zh, estimated signal
%         Input:  R, triangular matrix channel matrix
%                 y, modified recieved signal vector
%                Nq, modulation order

%% Number of TX antennas
Nt = size(R,2);

%% LR domain slicing
r  = (1+0*1i) * inv(T) * ones(1*Nt,1);

%% SIC
zh = zeros(Nt,1);
zh(Nt) = y(Nt) / R(Nt,Nt);
zh(Nt) = 2 * round( ( zh(Nt) -  r(Nt) ) / 2 ) + r(Nt);
for ii = Nt-1 : -1 : 1
    for jj = ii+1:Nt
       zh(ii) = zh(ii) + R(ii,jj) * zh(jj);
    end
    zh(ii) = ( y(ii) - zh(ii) ) / R(ii,ii);
    zh(ii) = 2 * round( ( zh(ii) -  r(ii) ) / 2 ) + r(ii);
end
end
```

H.8 Multi-tap MIMO Equalization

Script H.54 Matlab script for multi-tap MIMO equalization using frequency sampling technique

```
function ah = fbmc_eq_mimo_fs( Lw, Ht, y, Phi, g )
%% Description: Multi-tap equalizer for FBMC systems
%        Output: ah, estimated symbols
%         Input: Lw, number of pilots
%                Ht, MIMO channel impulse response
%                 y, received signal
%                 g, filter bank

%% Frequency Sampling FBMC equalization
[M,Nd]      = size(Phi);
Lp          = size(g,2);
K           = round(Lp/M);
[NR,NT,~]   = size(Ht);
Nd          = Nd/2;
D           = dmat(Lw,NT);
Da          = fbmc_delay_eval( Lp, M, K );

%% Eq
ahi = zeros(NT,size(y,2)+Lw-1,M);
ah  = zeros(NT,2*Nd,M);
for m = 1:M
    %% Sub channel fourier
    Hfi = zeros(NR,NT,Lw);
    for ii = 1:NR
        for jj = 1:NT
            ht            = squeeze(Ht(ii,jj,:));
            Hfi(ii,jj,:) = calc_ch(ht(:),m,Lw,g);
        end
    end
    %% Equalizer (freq)
    Wf = zeros(NT*Lw,NR);
    for ii = 1:Lw
       ind = (ii-1)*NT + (1:NT);
       Wf(ind,:) =  ( Hfi(:,:,ii)'*Hfi(:,:,ii) ) \ Hfi(:,:,ii)';
    end
    %% Equalizer (time)
    Wt = D \ Wf;
    %% Convolution
    for ii = 1:Lw
        ind  = (ii-1)*NT + (1:NT);
        ahi(:,:,m) = ahi(:,:,m) + Wt(ind,:) * circshift( [ y(:,:,m) zeros(NR,Lw-1)], ...
            [0 (ii-1)] );
    end
    ahi(:,:,m) = circshift( ahi(:,:,m), [0 -(Lw-1)/2-Da] );
    ah(:,:,m)  = ahi(:,1:2*Nd,m) .* repmat( conj(Phi(m,:)), [NT 1] );
    ah(:,:,m)  = real(ah(:,:,m));
end
end

function [D,A] = dmat(L,NT)
        P = (L-1)/2;
        A = zeros(L,L);
        Omg = 2*pi/(L+1) * (-P:P);
        for jj = 1:L
            A(jj,:) = exp( -1i*(-P:P)*Omg(jj) );
        end
        D = kron( A, eye(NT) );
end

function hf = calc_ch(ht,m,Lw,g)
%%
[M,Lp]  = size(g);
K       = round(Lp/M);
```

```
[~,Db]  = fbmc_delay_eval( Lp, M, K );

%% Signal gen
s = conv( [1 zeros(1,M/2-1)], g(m,:));                          %% Synthesis ...
    (impulse input)
x = conv(s,ht);                                                 %% Transmission

%% No channel
xd1 = circshift( s, [0 Db] );                                   %% Receiver delay
y1  = conv( xd1, conj( fliplr( g(m,:) ) ) );                    %% Analysis
H1 = myfft( y1(1:M/2:end)/2, Lw);

%% No channel
xd2 = circshift( x, [0 Db] );                                    %% Receiver delay
y2  = conv( xd2, conj( fliplr( g(m,:) ) ) );                     %% Analysis
H2 = myfft(y2(1:M/2:end)/2,Lw);

%% Resultant channel
hf = H2./H1;

end

function yf = myfft(y,Lw)
yf = zeros(1,Lw);
Omg = -(Lw-1)/2:(Lw-1)/2;
for kk = 1:length(y)
    yf = yf + y(kk) * exp( -1i*2*pi*(  Omg/(Lw+1) )*(kk-1) );
end
end
```